
**Design, Preparation, and Evaluation of Silk Fibroin
Protein, Peptide, and Peptidomimetic-based
Biomaterials for Drug Delivery and Healthcare
Applications**

A Thesis Submitted for the Degree of

Doctor of Philosophy

By

Biswanath Maity



Bioorganic Chemistry Laboratory, New Chemistry Unit

Jawaharlal Nehru Centre for Advanced Scientific Research

(A Deemed University)

Bengaluru-560064, India

July 2022

Dedicated to my Parents

TABLE OF CONTENTS

Certificate	i
Declaration	iii
Acknowledgements	v
Preface	ix
Chapter 1: Introduction	1
1.1 Peptides and Proteins	3
1.2 Self-Assembly	6
1.3 Self-Assembly of Proteins and Peptides	7
1.4 Hydrogel	9
1.5 Protein-Based Hydrogel	11
1.6 Silk Fibroin	13
1.7 Diabetes Mellitus and Treatments	16
1.8 Insulin	17
1.9 Animal Models in Diabetes Research	19
1.10 Melanin	20
1.11 Wound Healing	20
1.12 Animal Models for Wound Healing	22
1.13 Cell Penetrating Peptides (CPPs)	23
1.14 Peptidomimetics	25
1.15 Cyclic Dipeptides	27
1.16 Objective	28
1.17 References	30
Chapter 2: Injectable Silk Fibroin-based Hydrogel for Sustained Delivery of Insulin in Diabetic Rats	47
2.1 Preparation and Characterization of iSFH	51
2.2 Encapsulation and Sustained Release of Insulin	57
2.3 Cytotoxicity and Hemolysis Study	58
2.4 <i>In vitro</i> Insulin Functional Activity Assay	59

2.5 <i>In Vivo</i> Insulin Delivery in Diabetic Rat	60
2.6 Conclusion	62
2.7 Experimental Methods	63
2.8 Appendix	70
2.9 References	72
Chapter 3: Glucose Responsive Self-Regulated Injectable Silk	77
Fibroin Hydrogel for Insulin Delivery	
3.1 Synthesis and Characterization of Phenylboronic Acid Modified SF	81
3.2 Rheological Analysis	85
3.3 Glucose Responsive Studies	87
3.4 Cytocompatibility and Hemolysis	96
3.5 Conclusion	97
3.6 Experimental Methods	98
3.7 Appendix	102
3.8 References	104
Chapter 4: Antioxidant Silk Fibroin Composite Hydrogel	111
for Rapid Healing of Diabetic Wound	
4.1 Hydrogel Preparation	117
4.2 Morphological Analysis	118
4.3 Conformation Analysis	118
4.4 Mechanical Properties	120
4.5 Swelling Ratio	122
4.6 Antioxidant Assay	122
4.7 Drug Release Profile	123
4.8 Antibacterial Activity	125
4.9 Cytotoxicity Studies	126
4.10 Cell Rescue Studies from Oxidative Stress	127
4.11 <i>In Vitro</i> Cell Migration	129
4.12 <i>In Vivo</i> Wound Healing	131

4.13 Conclusion	138
4.14 Experimental Methods	138
4.15 Appendix	146
4.16 References	148
Chapter 5: Cell Penetrating Peptides Derived from Intrinsically Disordered Ku- Protein for DNA Delivery	155
5.1 Design and Synthesis of IDP-based CPPs	159
5.2 Secondary Structure Analysis	161
5.3 Cytocompatibility Assessment	163
5.4 Cellular Uptake	163
5.5 DNA Binding Studies	164
5.6 Plasmid DNA Transfection	173
5.7 Conclusion	174
5.8 Experimental Methods	175
5.9 Appendix	179
5.10 References	188
Chapter 6: Tumor Microenvironment Sensitive Cell Penetrating Peptidomimetics for Selective Anticancer Drug Delivery	193
6.1 Design and Synthesis of Hkd	197
6.2 Proteolytic Stability	200
6.3 Cell Viability	200
6.4 pH-dependent Cellular Uptake	201
6.5 <i>In Vitro</i> Cytotoxicity of Cpt-Hkd	206
6.6 Conclusion	207
6.7 Experimental Methods	208
6.8 Appendix	218
6.9 References	226
Chapter 7: Conclusions and Future Scope	231
7.1 Conclusions	231
7.2 Future Scope	232

CERTIFICATE

I hereby certify that the work described in the thesis entitled “**Design, Preparation, and Evaluation of Silk Fibroin Protein, Peptide, and Peptidomimetic-based Biomaterials for Drug Delivery and Healthcare Applications**” has been carried out by **Mr. Biswanath Maity** under my supervision at the Bioorganic Chemistry Laboratory, New Chemistry Unit, Jawaharlal Nehru Centre for Advanced Scientific Research (JNCASR), Bengaluru, India and that it has not been submitted elsewhere for the award of any degree or diploma.



Prof. T. Govindaraju
(Research Supervisor)



DECLARATION

I hereby declare that the matter embodied in the thesis entitled “**Design, Preparation, and Evaluation of Silk Fibroin Protein, Peptide, and Peptidomimetic-based Biomaterials for Drug Delivery and Healthcare Applications**” is the resultant of the investigations carried out by me at the Bioorganic Chemistry Laboratory, New Chemistry Unit, Jawaharlal Nehru Centre for Advanced Scientific Research (JNCASR), Bengaluru, India under the supervision of **Prof. T. Govindaraju** and that it has not been submitted elsewhere for the award of any degree or diploma.

In keeping with the general practice in reporting the scientific observations, due acknowledgement has been made whenever the work described is based on the findings of other investigators. Any omission that might have occurred due to oversight or error in judgement is regretted.

Biswanath Maity

Biswanath Maity
(Ph.D Student)



ACKNOWLEDGEMENTS

First and foremost, I would like to express my sincere gratitude to my research supervisor Prof. T. Govindaraju, Bioorganic Chemistry Laboratory, New Chemistry Unit, and School of Advanced Materials (SAMat), JNCASR, for his continuous support, motivation, infinite patience and guidance throughout my Ph.D tenure. It has been a great privilege and honor to be associated with him.

I would like to thank Prof. C. N. R. Rao, FRS, for being the source of inspiration, generous support, and encouragement throughout my stay in JNCASR.

I would like to thank past and present NCU Chairmans for providing the infrastructure and excellent facilities to carry out my research work.

I am thankful to Prof. Jayanta Halder, Prof. Sridhar Rajaram, Prof. Sarit S. Agasti, Prof. Chandrabhas Narayana from JNCASR, Prof. Sidhartha P. Sharma, and Prof. Mahavir Singh from IISc for their valuable courses.

I am thankful to my wonderful lab mates Dr. Maity, Dr. Avinash, Dr. Pandu, Dr. Shivaprasad, Dr. Nagarjun, Dr. Rajasekhar, Dr. Suseela, Dr. Sourav, Dr. Debasis, Mr. Sumon, Mr. Satyajit, Dr. Shadab, Dr. Pardhasaradhi, Dr. Bappa, Dr. Mahesh, Dr. Balachandra, Mr. Madhu, Dr. Lakshmi, Dr. Mouli, Ms. Shardha, Mr. Ashish, Mr. Hariharan, Ms. Dikshaa, Mr. Sabyasachi, Mr. Shivaprasad, Dr. Tanmay, Dr. Ankita, Mr. Nabeel, Ms. Krithi, Mr. Manikandan, Dr. Suresh, Dr. Soumik, Dr. Prayasee, and Ms. Sreyashri for their help and friendly environment in lab. I would like to thank visiting faculties Dr. Hemmant K. Gowda, and Dr. Ramesh for helping me in my work.

I am thankful to Prof. Anuranjan Anand, Dr. R. G. Prakash, and JNCASR Animal House for excellent animal facility.

I thank Prof. E. Eswaramurthy and Ms. Suchismita for DLS experiment. Prof. Jayanta Halder, Rajib, Anton Paar India for Rheology experiment.



I thank Prof. S. N. Bhat for giving me an opportunity to teach undergraduate chemistry laboratory course (POCE).

I sincerely acknowledge the timely help of technical staff Mr. Shiva Kumar (HRMS/MALDI/FTIR), Mr. Mahesh, Mr. Deepak, Mrs. Durgashri (NMR), Mrs. Usha (TEM), Rahul, Meenakshi (FESEM), Dr. Narendra Nala (FACS), Mr. Mune Gowda, and Mr. Dileep (Audio/Visual). I am thankful to Ms. Swetha, Mr. Naveen, Mrs. Ramya, Mrs. Mellissa from NCU office for all their timely help and support.

I thank JNCASR Library, Academic, Administration, Comp Lab, IP cell, Warden, Hostel, Security, Mess Workers, House Keeping Staff, and JNCASR Health Center (Dhanvantari) for providing and maintaining the various facilities that have helped me immensely.

I thank all my friends Arka, Subham, Moinak, Subhajit, Koyel, Sumon, Debasis, Sabya, Paribesh, Arabinda, Brinta, Rajarshi, Soumita, Arjun, Yogendra, Raju, Sresta for their company and support.

I thank all my school and college friends Sourav, Srikanta, Gobinda, Subhasis, Subrata, Gopal, Biswajit, Pintu for their company and support.

I would like to thank Council of Scientific and Industrial Research (CSIR), India for research fellowship to pursue my Ph.D.

Finally, and most importantly, I owe everything to my mother (Bhabani), father (Gopal), brother (Raghu), and sisters (Indrani, Falguni). I thank them for their unconditional love, moral support, and constant encouragement throughout my life. Their love, blessings and affection made me what I am today. I also thank my brothers-in-law (Bibek, and Sudarshan), sister-in-law (Mousumi), nephews (Amit, Asim, Adrij), niece (Rishani) for their love. This thesis is dedicated to my parents for their love and support.



PREFACE

This Ph.D thesis is categorized into six chapters. The objective of the thesis work is to develop and validate the functional properties of protein, and peptides-derived biomaterials in drug delivery and wound healing applications. The introduction Chapter 1 outlines the general structure and functions of the peptide and proteins, and their assembled architectures for biomaterial applications. An overview of the recent developments in the field of peptide and protein-based biomaterial systems is presented. The major emphasis is given to the design strategies utilized for the development of silk fibroin (SF) protein-based hydrogel systems and cell penetrating peptides (CPPs) for healthcare and drug delivery applications.

Chapter 2 deals with the injectable SF hydrogel for sustained insulin delivery in diabetic rats. The potential role of glycols for effective modulation of SF gelation to prepare injectable hydrogel (iSFH) is described. The iSFH exhibits good mechanical strength and mesoporous morphology suitable for insulin encapsulation. The *in vitro* study revealed that iSFH releases the encapsulated insulin in functional active form over 5 days. The biocompatibility and nonhemolytic nature of iSFH support its suitability for further evaluation in live systems. Subcutaneous injection of insulin-iSFH in diabetic Wistar rats developed an active depot underneath the skin, which releases the insulin slowly to restore the physiological glucose homeostasis for 4 days.

In Chapter 3, we discuss the development of glucose responsive self-regulated injectable SF hydrogel for insulin delivery. Hydrogel was fabricated by functionalizing nucleophilic amino acid residues of SF protein with glucose responsive phenylboronic acid. The boronate ester formation between phenylboronic acid and hydroxyl group of serine residue induces SF gelation. The glucose oxidase enzyme was encapsulated inside the hydrogel to induce glucose responsiveness to initiate the degradation of hydrogel to affect the release of insulin. The *in vitro* studies showed that hydrogel releases basal levels of insulin at normoglycemic glucose concentrations, but release rate is enhanced with increasing glucose levels similar to hyperglycemia conditions. The enhanced insulin release kinetics in altered response to hyperglycemia-like conditions revealed pulsatile insulin release behavior of hydrogel. Thus, self-regulated SF hydrogel act as an artificial pancreas to deliver encapsulated insulin in hyperglycemia conditions.

Chapter 4 deals with antioxidant SF composite hydrogel (SFCH) for rapid healing of diabetic wounds. The SFCH dressing is composed of naturally occurring SF protein, antioxidant melanin, and anti-inflammatory isoquinoline natural product berberine. The SFCH scaffolds are highly mesoporous with suitable pore sizes for cellular infiltration and proliferation. *In vitro* studies have revealed that SFCH effectively quenches the reactive species and promotes the cell migration. The wound healing assessment in diabetic type I Wistar rats shows the biocompatible for cellular infiltration and



proliferation. *In vitro* studies have revealed that SFCH effectively quench the reactive species and promotes the cell migration. The wound healing assessment in diabetic type I Wistar rats shows the biocompatible SFCH treatment helps in rapid wound scab formation, and significantly increased the regenerative capacity through promotion of cell migration, tissue re-epithelialization, and collagen deposition.

Chapter 5 present CPPs derived from intrinsically disordered Ku-protein for DNA delivery. We have designed CPPs, Ku-A4 and Ku-P4 from the unstructured tail extension of DNA binding Ku-proteins with repeated AAKKA and PAKKA sequences to enable the delivery of functional biomolecules. The biocompatibility, cellular uptake and DNA binding ability, and further DNA delivery efficacy are studied. Ku-P4 displays good internalization efficacy through the cell membrane. The detailed DNA binding studies show effective condensation of DNA into positively charged polyplex, which effectively penetrates and deliver plasmid DNA inside the cell.

Chapter 6 deals with the study of tumor microenvironment pH responsive cell penetrating peptidomimetics. The designed peptidomimetic Hkd is composed of cyclic dipeptide (CDP)-based unnatural amino acid cyclo (Lys-Asp) (kd) and natural histidine. The rigid CDP unit has multiple hydrogen bonding donor and acceptor sites, protease stability, while histidine has pH responsive charge induction tendency. The pharmacokinetics studies unveiled the serum stability and biocompatibility of Hkd. *In vitro* cellular uptake studies by FACS and confocal microscopy revealed the enhanced peptide uptake at lower pH compared to physiological pH. Cytotoxicity of anticancer drug camptothecin (Cpt) and Cpt-Hkd show that the peptidomimetic fusion decreases the cytotoxicity of the anticancer drug in normal cells. The pH dependent uptake behavior of Hkd is useful in targeting cancer cell microenvironment for selective drug delivery without affecting the normal cells.

In summary, the proposed thesis presents the current developments of protein and peptide-based biomaterial systems and objective of the work in the introduction chapter. The second chapter describes the injectable SF hydrogel and *in vivo* blood glucose-controlled efficacy in diabetic type I Wistar rat model. The third chapter presents the chemically modified injectable SF hydrogel and its glucose responsive insulin release behavior. The fourth chapter deals with evaluation of therapeutic efficacy of multifactorial composite hydrogel in diabetic type I Wistar rat model. The fifth chapter describes the design of biocompatible intrinsically disordered cell penetrating peptides for DNA delivery. The sixth chapter presents the pH responsive cell penetrating peptidomimetics to selectively target the cancer cell microenvironment over normal cells.



Chapter 1

Introduction

1.1 Peptides and Proteins

Peptides and proteins are biomacromolecules made up of amino acids connected through the amide bonds (peptide bonds). They are essential biomolecules with a wide range of biological functions necessary to maintain the normal physiology, growth and survival of the organism. Essential functions carried out by peptides and proteins are catalysis (enzyme), molecular recognition, molecular and ion transport, hormonal activity, immunoprotection, radical scavenging, cytoskeleton structure, and maintenance, among others.¹⁻⁴ These polypeptides are synthesized in living organisms through a multi-step process. Biosynthesis begins with transcription of genetic information coded in DNA to messenger RNA (mRNA). The information coded in mRNA translated into polypeptides (ribosomal machineries) and further undergoes various post-translational modification to adopt the functional three-dimensional structure in endoplasmic reticulum. In nature, another route for peptide synthesis is non-ribosomal peptide synthesis facilitated by peptide synthetase enzymes. The non-ribosomal synthesis mainly results in the production of small indispensable secondary metabolites.⁵⁻⁷

The structural conformation and functionality of protein and peptides depend on the amino acid compositions in the sequence. Amino acids are chemically known aminoalkanoic acids, where amine (-NH₂) and carboxylic acid (-COOH) groups are attached at α -carbon in a specific conformation (L-conformation) with chemically diverse side chains (Figure 1). In nature, twenty proteinogenic amino acids are present, each with its unique side chain functionality, which facilitates characteristic structural and functional properties. Depending on side chain functionality (R), amino acids are categorized as nonpolar (aliphatic and aromatic side chain), polar, and charged amino acids. The molecular structure, three and single-letter abbreviations of natural amino acids are listed in Figure 1.¹⁻⁴

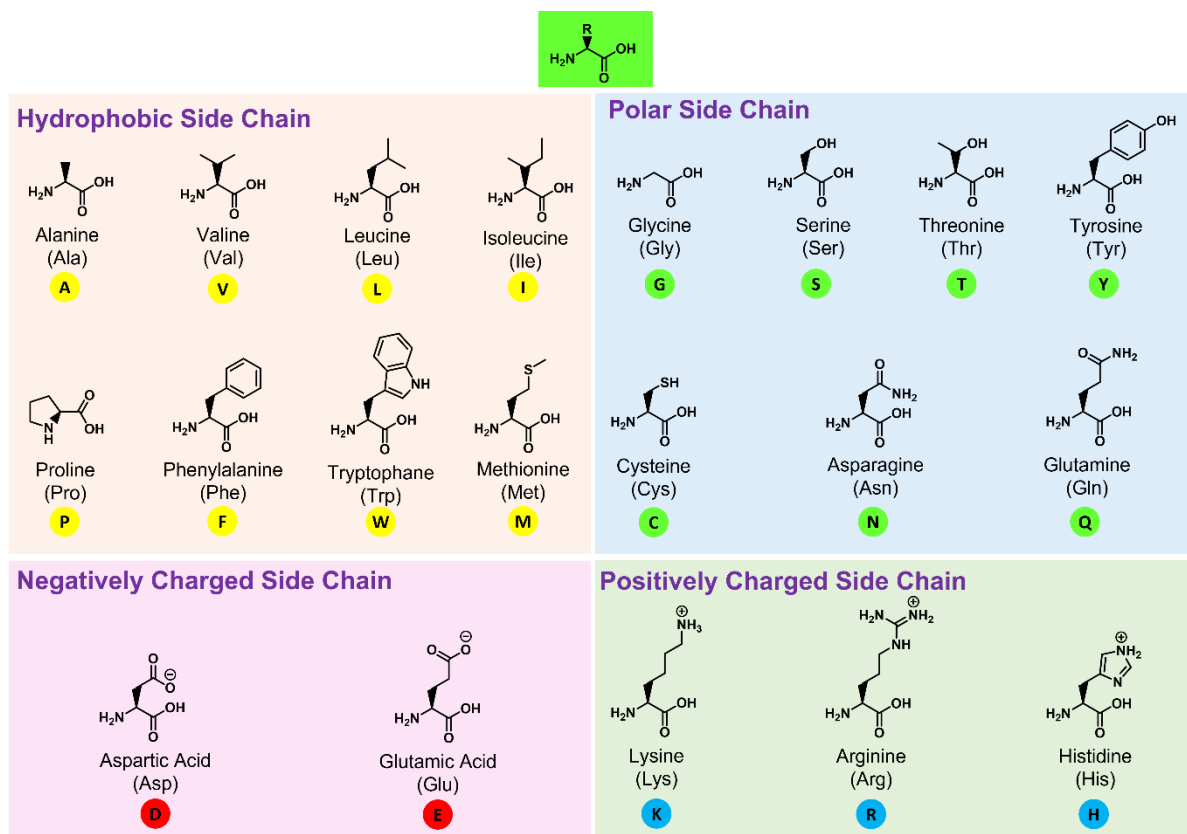


Figure 1. Chemical structures and classification of natural proteogenic amino acids depending on the amino acid side chain nature. Three letter and single letter abbreviations of amino acids are denoted.

Proteins exhibit different levels of organization, namely primary, secondary, tertiary, and quaternary structures.⁴ The primary structure is the amino acid sequence and composition of amino acids, which largely determines the next level of peptide chain organization. The major secondary conformations observed are either α -helical or β -sheet structures. The α -helical secondary structures are driven by intramolecular hydrogen bonding between carbonyl functionality and amide proton. While the β -sheet structures are stabilized by intra- and intermolecular hydrogen bonding, along with other noncovalent interactions depending on the amino acid sequence. Other secondary conformations observed in peptides and proteins include turns and coil conformation.^{1-4,8} The tertiary structure in functional proteins refers to three-dimensional organizations of secondary structural units driven by hydrophobic and hydrophilic

interactions of amino acid side chain leading to the packing of hydrophobic units of peptide chain inside the structure and exposing only hydrophilic groups towards the surface water. The quaternary structure of a protein represents the three-dimensional organization of multi-subunit polypeptides or proteins into a functional conformation. Quaternary structures are stabilized through hydrophobic, electrostatic, disulfide, and salt bridge interactions.^{4,8}

The subtle difference in noncovalent interactions defined by their amino acid composition directs the organization of proteins into globular and fibrous forms with varying structural and functional properties. Globular proteins are polypeptides formed by about 1000 amino acids and involved in cellular biochemical functions. The fibrous proteins are very high molecular weight (up to ~2000 kDa) polypeptides, required for maintaining the structural integrity.^{2,9,10} The intrinsic aggregation propensity of polypeptides is reflected in constructions of marvel materials such as silks under physiological conditions.¹¹⁻¹⁴ On the other hand, misfolding and aggregation of polypeptides and proteins are responsible for pathological outcomes in form of neurodegenerative disorders such as Alzheimer's, Prion, and Parkinson's diseases.¹⁵⁻¹⁹

Inspired by the diverse structures and functions of peptides and proteins, there is an increased interest in developing either natural or synthetic protein and peptide-based materials for a wide range of material and biological applications.²⁰ Peptide-based materials have been used to develop therapeutics, templated synthesis of nanomaterials, drug delivery agents, biomaterials for tissue engineering, and many other biomedical applications.²¹⁻³⁰ The potential advantages of peptide-based materials over other biomolecules include, i) large-scale availability from renewable sources such as biomass and ease of scalable production by genetic engineering or recombinant DNA nanotechnology and chemical synthesis, ii) versatility to modify the structure and function through exchanging the amino acid composition during chemical synthesis, iii) relative stability under ambient conditions as compared to other biomolecules, facilitating the ease of handling, iv) inherent biocompatibility and biodegradability, v)

molecular recognition through non-covalent interactions, vi) inherent aggregation propensity with the availability of diverse chemical functionalities with respect to amino acid composition to modulate physicochemical and biological properties, and vii) aqueous fabrication possibility into various physical formats, including gels, films, nanofibers, foams, porous microsystems, woven, non-woven mats, and nanomaterials.

1.2 Self-Assembly

Self-assembly is the process of spontaneous organization of individual molecular units through noncovalent interactions into ordered structural and functional materials.³¹⁻³³ The molecular recognition between simple building blocks directs the way for association into microscopic or macroscopic objects with nanoscale order. The assembly process is driven by combination of hydrogen bonding, aromatic π - π interactions, van der Waals forces, electrostatic, and ionic interactions.^{34,35} Although these noncovalent interactions are relatively weak individually, the combined coordination of various interactions results in organization of simple blocks into extended structures. This process endorses towards the facile production of desirable functional materials with tailored properties. The nature and functionality of self-assembly outcomes exclusively depends on the information encoded in the individual molecular building blocks. The delicate design of the building blocks can modulate the self-assembly process into controlled molecular architectures with enormous functionality.³⁶ Therefore, the molecular self-assembly is an emerging field of interest across a vast array of molecular perspectives. Various synthetic organic and inorganic building blocks were designed and utilized to prepare self-assembled systems having materials and biological applications.³⁷

Nature, through the billions of years of evolution, is an excellent place to find the inspiration and ideas of self-assembly. Nature employs the self-assembly process to construct its functional biological machinery, including DNA structures, quaternary protein structure, enzymes,

ribosomes, cell membranes, cytoskeleton, extracellular matrix, collagen, and biomineralized materials.³⁸ Inspired by nature, researchers are constantly attempting to harness the complexity of nature and master engineering of biomolecules such as peptides, proteins, and nucleic acids to create new synthetic materials through molecular self-assembly.^{39,40} Utilizing the peptide, protein, and their analogues as molecular building blocks is a promising approach because of its inherent biological relevance to functional and pathological conditions.⁴¹⁻⁴⁸

1.3 Self-Assembly of Proteins and Peptides

Peptides and proteins are the major molecular scaffold-generating building blocks in the biological world. The protein assembly allows constructs in nanoscale, microscale, and macroscale materials with various functional properties in nature.⁴⁹ The self-assembled actin protein fibers provide structural integrity and physical rigidity to cells.^{51,52} The microtubule assembly serves as nanoscopic railways tracks to allow the transport of cargo using the protein motor system.⁵³ Collagen serves as the nanoscale structural blocks of the extracellular matrix and skin integrity.⁵⁴ The macroscopic structures of nails and hairs are assembly products of keratin protein.⁵⁵ The inorganic biological structures of the body systems such as bone, teeth, and animal shells are also directed by the protein templates through specific interaction with calcium or silicon (biomineralization).⁵⁶ Thus, along with distinct functional entities, proteins serve as a template in the biological world. Therefore, protein and its fragment unit peptides are potential building blocks for designing innovative and biocompatible functional materials.⁵⁷ Protein systems are highly complex to utilize as a building block because of their large three-dimensional structure and chemical composition. To enable the facile protein assembly, combined experimental, biophysical, and molecular architectonics strategies have been employed. These tools lead to artificial protein assemblies with unprecedented structure and functionality.

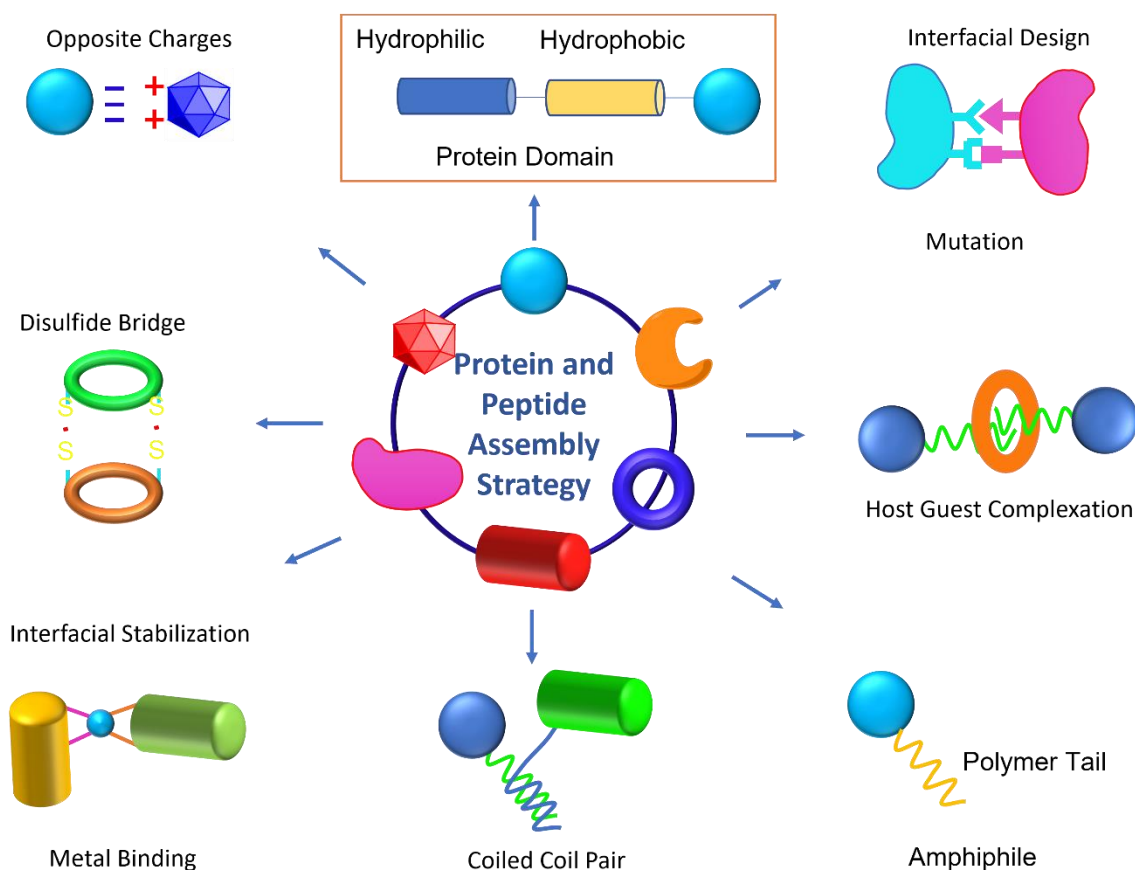


Figure 2. Strategies for protein and peptide assembly formation. Reproduced from reference 49.

Xu et al. engineered oligomeric transmembrane pores assembled in membranes *in vitro* and *in vivo*.⁵⁸ The designed water-soluble hexamer of coiled-coil motifs generates a 12-helix barrel (TMHC6) with the outward-facing residue to promote membrane insertions. The construct was suitably expressed as a hexamer unit in the membrane of *E. coli* and shows ion conductance with higher selectivity for K^+ than Na^+ , due to pore size matching with partially dehydrated K^+ than fully hydrated Na^+ . As molecular recognition is the most straightforward biological function of the protein and protein assembly, Li et al. designed self-assembled antibody nanorings (CSANs) with multiple target sites by fusions of DHFR₂ with single-chain anti-CD3 antibody.⁵⁹ The octavalent anti-CD3 CSANs showed improved binding affinity to CD3 expressing cells compared with the native monoclonal antibody UCHT-1. Der et al. reported the first example of C_2 symmetric enzymatic active protein assembly from helix-turn-helix

domain of the Rab4-binding domain of rabenosyn.⁶⁰ Further incorporation of metal-binding His₄ coordination site at dimeric interface of protein assembly created a stable dimer with high Zn²⁺ affinity at interface. This molecular construct was quite active toward the hydrolysis of the model substrate p-nitro-acetate system with k_{cat}/K_m values of 630 M⁻¹.s⁻¹. Song et al. developed artificial metallo- β -lactamase (Zn₄: C⁹⁶RIDC1₄) through Zn-directed D₂-symmetric tetramer of cyt cb₅₆₂ variant C⁹⁶RIDC1. The C⁹⁶RIDC1 selectively binds to Zn²⁺ and assembled in periplasm of the *E. coli*, which allowed them to survive in a moderate concentration of the β -lactamase antibiotic ampicillin.

1.4 Hydrogel

Hydrogels are water-swollen three-dimensional hydrophilic polymer networks, capable of absorbing large excess of water.⁶¹⁻⁶³ Compared to other classes of synthetic biomaterials, hydrogel can stimulate natural living tissue because of its high-water content inside the matrix, porosity, and softness. The semipermeable hydrogel structure resembled to the native extracellular matrix.⁶⁴ Thus, hydrogels allow the influx and efflux of nutrients, metabolites, and prevent the passage of different immune agents.⁶⁵ Hydrogels are structured through self-assembled architectures of the molecular building blocks in water media. The reversible or physical gels networks are governed through secondary forces such as ionic, hydrogen bonding, and hydrophobic interactions between the molecular entanglement. The physical hydrogel matrix can be easily disassembled by changing the environmental conditions such as pH, ionic strength, and temperature. In chemical gel, networks of covalent bonds join different macromolecular chains with a vast range of functional applicability depending on the functional groups.

The advancement of hydrogel technologies has made a significant contribution to various biomedical applications.⁶⁶ Early studies implicate the usefulness of hydrogel systems for local

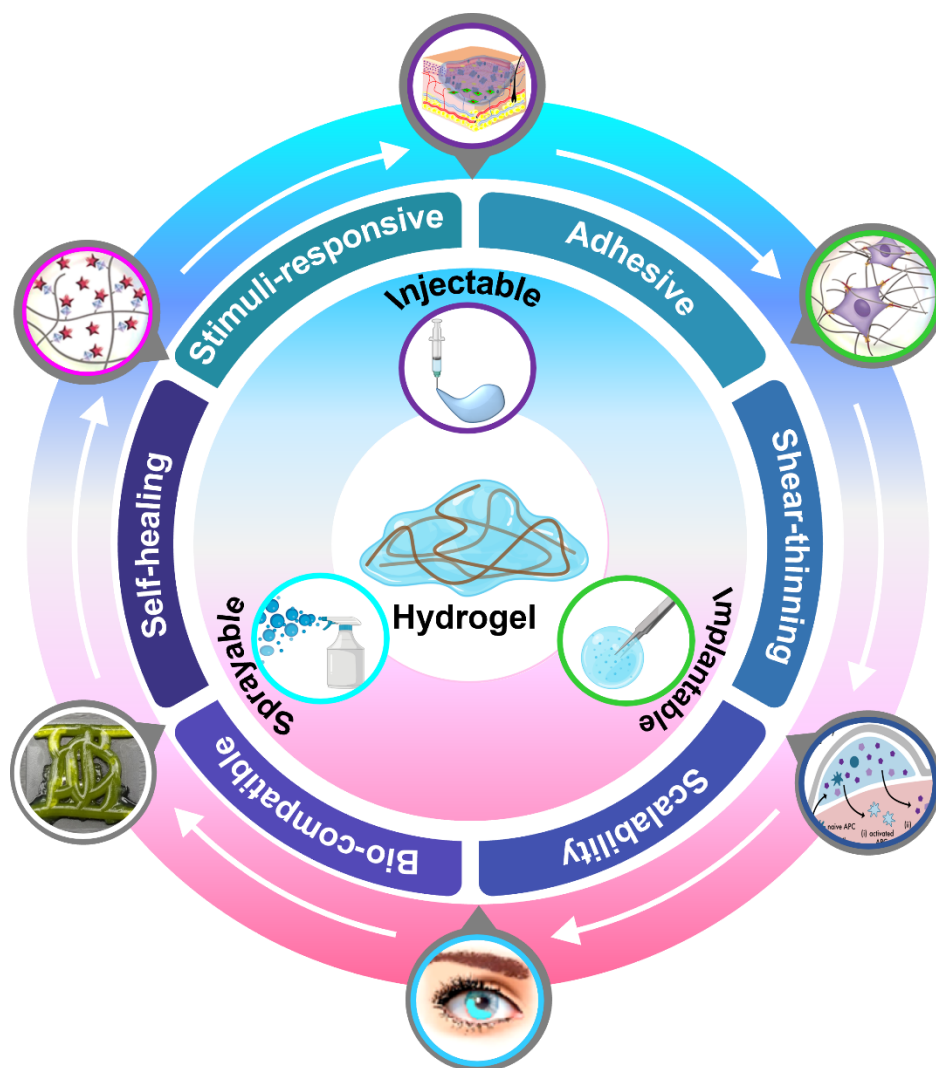


Figure 3. Hydrogel and its vast applications in biology.

and controlled release of bioactive molecules in drug delivery. Hydrogel was recognized as useful scaffold in reconstructive surgeries and became the fundamental tissue engineering technology in regenerative medicine. Hydrogels are extensively used in device coating, soft robotics, environmental engineering, and adoptive cell therapy. High water content in hydrogel makes these materials friendly to biological environment. Although, at the early stage of development, various harsh mechanism of molecular cross-linking was used. But new development of safer noncovalent cross-linking tools triggers the gelation in situ after injection, where several environmental factors of the body, such as physiological temperature, pH, and

ionic strength act as cue to trigger the gelation process.⁶⁷⁻⁶⁹ The noncovalent cross-linked hydrogels showed various exciting properties such as self-healing, comparable mechanical properties to the native tissue, sustainability to natural forces, and body stress in motion.

In recent times, discovery of the shear-thinning hydrogels has advanced the applicability of the hydrogels.^{70,71} The shear-thinning hydrogels were formed through the dynamic and reversible cross-linking between the soluble molecular building blocks.⁷² The dynamic and reversible cross-linking provides unique injectable property to hydrogel and can be injectable even after hydrogel formation, which opens a new frontier of hydrogel technology. These hydrogels can stabilize proteins and cellular cargoes, adhere strongly to the tissues, act as protective barriers, bandages, and coat complex biological geometry.⁷³⁻⁷⁵

The dynamic hydrogels open new translational possibilities by introducing unprecedented functionality into biomaterials. These features include programmable drug release, nanoscale patterning, and stimuli responsive behaviors.⁷⁶ Therefore, interdisciplinary projects require chemists, nanotechnologists, protein engineers, and synthetic biologists to develop sophisticated multifunctional hydrogel for applications. In this regard, programmable bioengineering techniques are leading to smart injectable materials with the potential to release encapsulated drugs based on environmental triggers. With the maturation of these technologies, multifunctional and programable hydrogel may provide the technological foundation for multistage biological events such as tissue regeneration and immunity.⁷⁷⁻⁷⁹

1.5 Protein-Based Hydrogel

The perfect polydispersity, precise control of polymeric units, and fine-tuned molecular level noncovalent interactions make protein an ideal material for tissue engineering and drug delivery applications. The protein-based hydrogel can be prepared using both covalent and noncovalent strategies.⁸⁰ Covalent strategies are stable and responsible for conformational

changes of protein, which are broadly applied to the screening of drug molecules and cell encapsulation. However, hydrogel prepared through noncovalent interactions is injectable and holds promising applications. Chemical reactions utilized for protein-based hydrogel preparation are Michael addition, site-selective conjugations, and enzymatic reactions.⁸¹ The physical protein hydrogel was formed through specific protein-protein, protein-peptide, and protein-polysaccharide interactions.⁸²

Murphy et al. synthesized noncovalent physical hydrogel of calmodulin protein by utilizing its conformational bias in native and Ca²⁺ binding state.⁸³ In calcium-binding state, it exists as extended conformation of dumbbell-shape. This conformation undergoes a rapid transition to collapsed conformation in response to the binding of various small molecule drugs, peptides, and proteins. To assemble the protein hydrogel through a covalent approach, threonine residues of calmodulin was bioengineered with cysteine residue. The engineered protein can be photo cross-linked with the vinyl group of the PEGDA acrylate termini upon UV radiation in collapsed conformations. Francis et al reported the bio-orthogonal conjugation of a polymeric unit at protein terminal to form cross-linked polymeric protein materials.⁸⁴ The polymer-protein cross-linked hydrogel selectively binds and removes heavy metals from water. Enzymatic cross-linking is a mild and selective method for protein hydrogel preparation in 3D cell encapsulations in tissue engineering. Enzymes used for protein cross-linking are phosphopantetheinyl transferase (PPTase), horseradish peroxidase (HRP), and many others.⁸⁵ In addition, bioactive groups can be integrated into the hydrogel system to promote cell spreading and support cell 3D migrations.⁸⁶ The covalent hydrogels are mechanically stronger than the physical hydrogels, whereas physical mixing strategies are biocompatible to cells and therapeutic agents. The mechanical properties of resulting hydrogels can easily be tuned through altering the binding affinity of gelator. The specific protein-protein interactions are extensively applied to design the physiological protein hydrogel system. Tirrell et al. utilized

the coiled-coil interaction between leucine zipper protein domains and pH-dependent interactions to induce the aggregations. The coiled-coil domain of protein backbone can further integrate with polymeric backbone to get polymer-protein hydrogel systems where thermostability and swelling properties could be adjusted by changing the coiled-coil protein pair.^{87,88} Heilshorn et al. have reported two-component hydrogel using tryptophan domain of engineered protein which folds into antiparallel β -sheet structure and binds to proline-rich peptides.⁸⁹

1.6 Silk Fibroin

Silks are fibrous protein polymers spun into fiber by some lepidoptera larvae such as silkworms, scorpions, spiders, mites, and flies.⁹⁰ After biosynthesis in epithelial cells, they are stored in specialized glands and spun into fiber. Each protein differs in terms of composition, structure, and physical properties. Most extensively characterized silks are silkworm silk and spider silk. The cannibalistic nature of spiders limits the large-scale availability of spider silks for biomaterial applications.^{91,92} On the other hand, the domesticated silkworm *Bombyx mori* (*B. mori*) silks are readily available in large scale from sericulture farms. The major structural protein of silkworm silk is silk fibroin (SF), a ~ 400 kDa fibrous protein.^{93,94} SF has unique physicochemical properties, such as modular mechanical strength, water stability, slow degradability, biocompatibility, and low immunogenicity. Generally, silkworm silk was extensively used in textile industries and suture materials in biomedical applications.

The silk fiber produced by the *B. mori* consists of two crystalline SF strands, held together by adhesive sericin protein. The sericin acts as adhesive glue for SF strands and helps to maintain the cocoon structure and protect silk moth from adverse environmental conditions. However, the sticky sericin protein is immunogenic, hence it is removed during the protein extraction process from cocoon. SF is a block co-polymer consisting of highly repetitive primary sequence, which provides the significant homogeneity in secondary

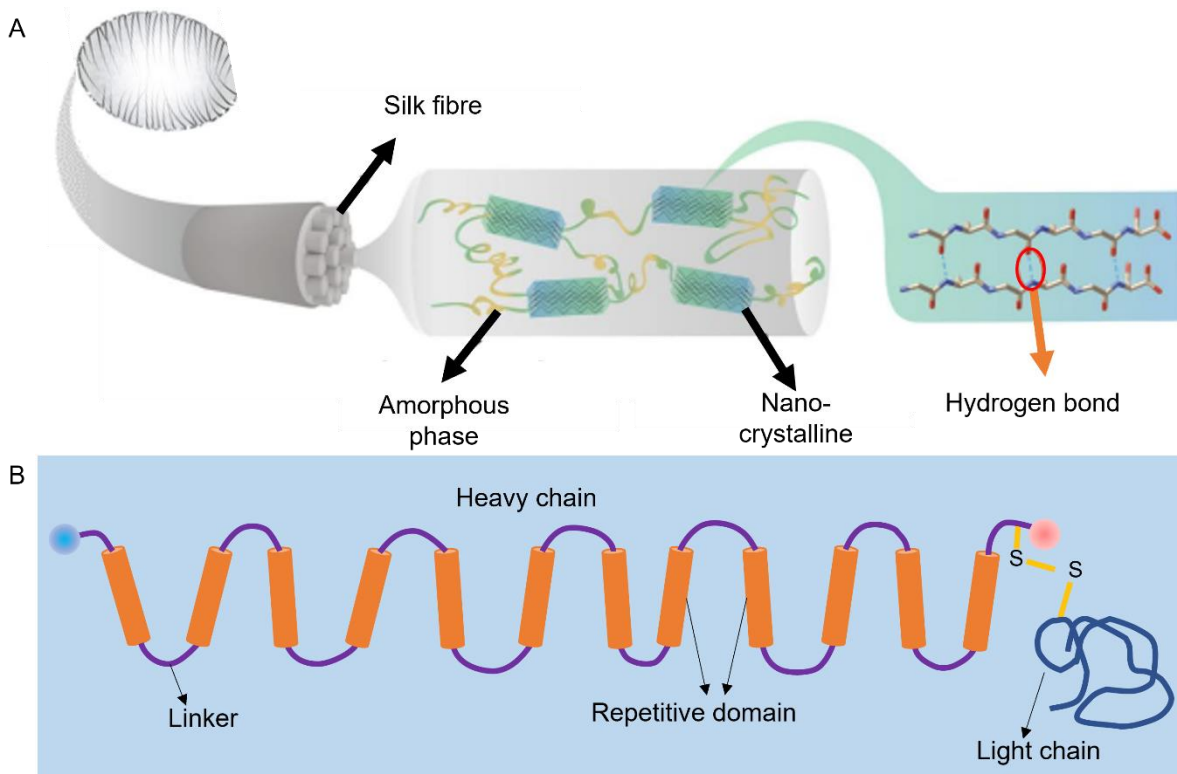


Figure 4. Schematic illustration of cocoon fiber. (A) Cocoon silk fiber and the different phase structure in fiber. Nano-crystalline domain was formed by the hydrogen bonding between β -sheet domains of the protein sequences. (B) Silk fibroin protein with heavy and light chain. Reproduced from reference 99.

structure. The protein strands are made up of large hydrophobic crystalline domains interspaced with short hydrophilic amorphous domains that facilitate the silk assembly and confer strength and resilience to fiber. The hydrophobic domains are composed of crystalline β -sheet content arising from the antiparallel protein chains through extensive hydrogen bonding.^{95,96} Liquid crystalline phases and conformational polymorphism are implicated in biological processing which contribute to the architectural features towards the orientation of β -sheet crystals and fuzzy interspaced between the crystalline and amorphous domain. The hydrophilic domains are bestowed with functionalizable amino acids such as threonine, serine, aspartic acid, glutamic acid, and tyrosine. These amino acid side chains provides the possibility of diverse chemical modifications for requisite biomedical applications. Along with the chemical

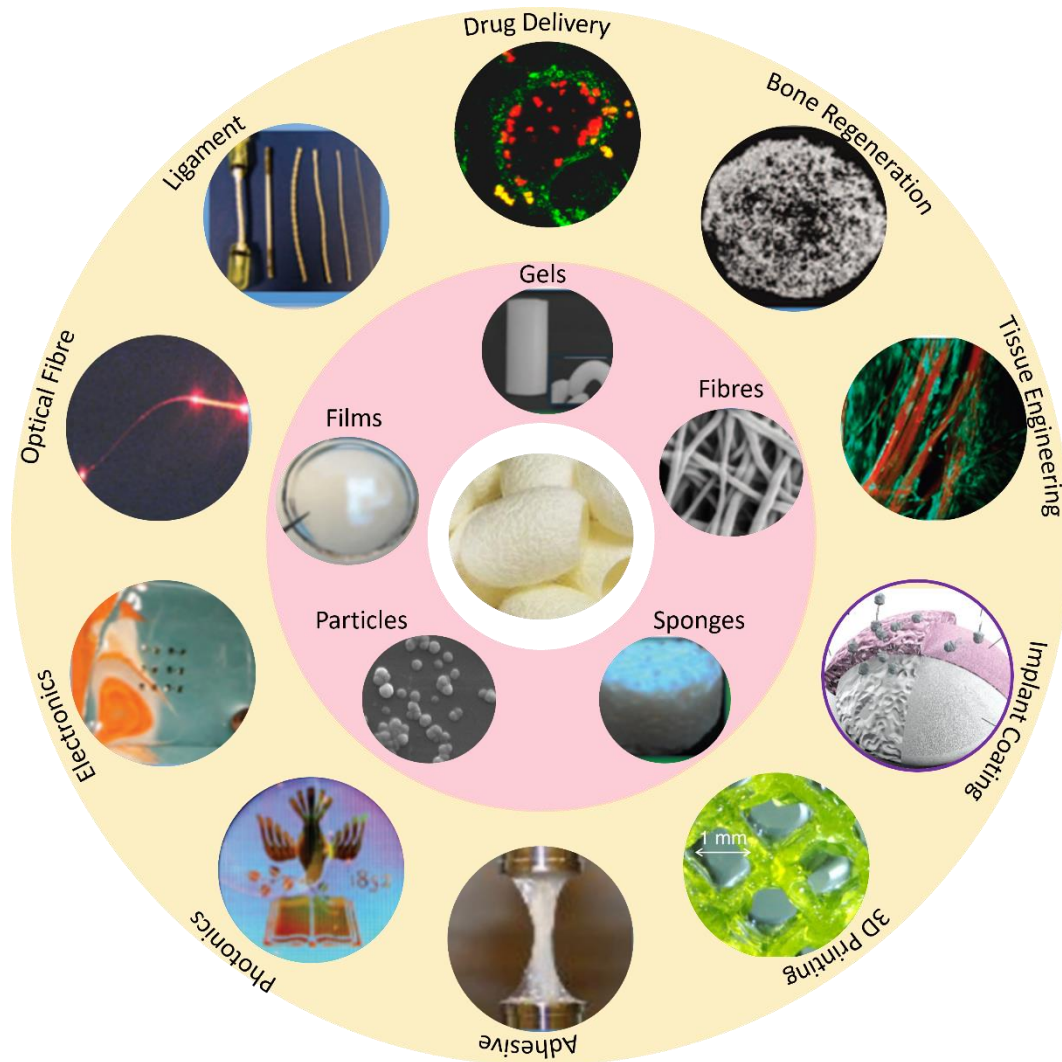


Figure 5. Fabrication of various biomaterials from the regenerated silk fibroin (SF) protein and their applications. Reproduced from reference 100.

modification, physiological and biological properties of SF can be simply modulated through simple physical mixing of desired materials.

The impressive mechanical properties and biocompatibility of SF offer an important set of material options in the field of controlled release, biomaterials, and scaffold generation for tissue engineering.⁹⁷⁻¹⁰⁰ The relative environmental stability, biocompatibility, and genomic control over sequence keeps the opportunity to exploit these protein materials for biomedical applications.¹⁰¹⁻¹⁰⁴ Kaplan et al. have developed various tissue engineering scaffolds which

shows excellent biocompatibility, adhesion, and proliferation of stem cells.^{105,106} They also developed the SF scaffolds for room temperature storage, stabilization of biomolecules for photonic and bioelectronic applications. The self-assembly nature, biocompatibility, and mechanical durability are used for slow, sustained, and controlled release of drugs in drug delivery applications.¹⁰⁷ Recently, SF has been utilized as an edible coating for the storage of perishable fruits.¹⁰⁸ Han et al. have developed a simple protocol for producing intrinsically colored and luminescent SF by feeding the silkworm with dye fluorescein, acridine orange, and rhodamine with the mulberry leaves.¹⁰⁹ These inherently colored SF are a promising candidate for textile and biological applications with the photophysical and real-time monitoring element.¹¹⁰ Moreover, the recombinant SF also holds the applicability in gene delivery, tuneable hydrogel, film, sponge, and 3D printed microtechnology.¹¹¹⁻¹¹⁴

1.7 Diabetes Mellitus and Treatments

The metabolic disease diabetes mellitus is defined chronic medical conditions arises from defective blood glucose regulation of the body.^{115,116} The metabolic abnormality elevated the risk of several long-term complications such as cardiovascular dysfunction, eye damage, kidney dysfunctions, and neurodegenerative diseases. Thus, diabetes is a group of disorders arising from insulin deficiency. Type I diabetes (T1DM) is a genetic disorder caused by the destruction of pancreatic β -cells through humoral and cellular immune factors. The only treatment for T1DM is insulin, and the disease was initially called “insulin dependent diabetes mellitus” (IDDM). The most abundant genetic trait associated with T1DM is human leukocyte antigen class II region.¹¹⁷ Type II diabetes (T2DM) comprises 85% of diabetes arising from insulin resistance or β -cell dysfunctions. The insulin resistance in liver hepatocytes, muscle, and adipocyte cells obstructed the glycogenesis process and leads to persisted hyperglycemia.^{118,119} According to the global estimation, 463 million people are suffering from diabetes which is estimated to reach 700 million by 2045 with 90% T2DM.¹²⁰ The insulin

resistance tendency is partially hereditary, but obesity, aging, and sedentary lifestyle are key risk factors.¹²¹ Insulin resistance enhances insulin demands, subsequently the β -cells overproduces the insulin. But the impaired ability of the β -cell gradually results in transition from prediabetic to diabetic.

There are many treatment options in T2DM to ameliorate insulin sensitivity or enhance insulin production from the β -cells.¹²² In the early stages, altered lifestyle, improved physical activity, and weight loss can help to reduce insulin resistance. Sulfonylurea derivatives are the class of medicine known to increase insulin production from β -cells. Metformin and its derivatives reduce the insulin resistance and glycogenolysis process in the liver. Thiazolidinediones act on nuclear receptor peroxisome proliferator-activity receptor gamma (PPAR) a ubiquitously expressed receptor in adipose tissue. PPAR regulates the uptake and storage of lipid in peripheral tissue and stem cell differentiation into adipocytes.¹²³ The polypeptide hormone glucagon-like peptide-1 (GLP-1) and its analogues are used to enhance insulin secretion. Intrinsically, GLP-1 is secreted from the L-cell of intestine after food intake and stimulates insulin secretion from β -cells. In T2DM, the GLP-1 functions were suppressed. These drugs or combinations can target multiple pathological defects in T2DM and maintain the blood glucose level at an early stage. Although these drugs ameliorate insulin sensitivity or production, none of them prevent the insulin resistance and progression of β -cell dysfunctions. The dysfunction in β -cells in T2DM and T1DM requires insulin administration.¹²⁴

1.8 Insulin

Insulin, a peptide hormone produced by the β -cell of pancreas, maintains the blood glucose level. Insulin comprises 51 amino acids with two polypeptide chains called **A** and **B**.¹²⁵ The polypeptide chain A composed of 21 amino acids, while the **B** chain contains 30 amino acids. These two polypeptide chains are held together by two disulfide bridges at **A7-B7** and **A19-**

B19. The primary structure of insulin varies in animal species, but the position of the disulfide bond is conserved in all insulin variance in mammals.¹²⁶ The A chain adopts two antiparallel α -helices, while the B chain adopts a single α -helices with turn and β -strand conformations. The core of insulin is formed by a collection of hydrophobic amino acid residues. Although the biologically active insulin is monomeric, in the β -cell it exists as a hexamer, co-ordinated with Zn^{2+} .¹²⁷ Insulin secretes from β -cell of the pancreas in response to elevated blood glucose

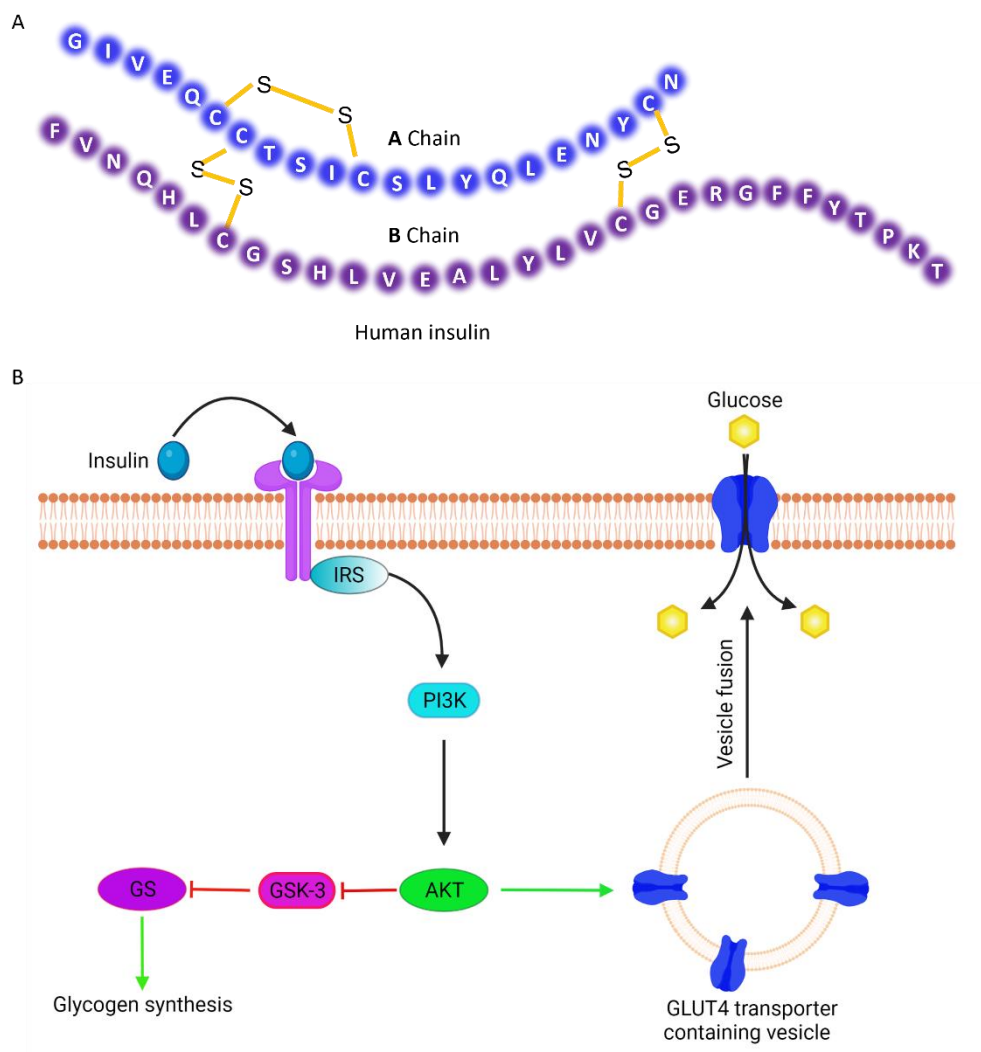


Figure 6. (A) Amino acid sequences of human insulin and disulfide bridge between A and B chain cysteine unit. (B) Insulin signalling pathway. Insulin binding promotes the fusion of GLUT4 glucose transporter containing vesicles to the membrane. The GLUT4 mediates the glucose uptake in various kinds of cells.

levels. Insulin receptors present in plasma membrane of liver, muscle, and adipose tissue binds with insulin at their α -subunit.¹²⁸ Insulin binding at α -subunit of insulin receptor promotes the phosphorylation of β -subunit and activates the insulin signalling pathways. Subsequently, the glucose transporter type 4 (GLUT4) containing vesicles are rapidly translocate and fuse with the cell membrane.¹²⁹ The GLUT4 receptors uptake the blood glucose and stored inside the cells as glycogen for further use. The dissociation of the insulin from insulin receptor recycles the GLUT4 transporter into cytosolic vesicle and terminates the glucose entry.

1.9 Animal Models in Diabetes Research

Several animal models have been established to investigate the mechanism underlying disease aetiology and to test potential interventions.¹³⁰ Insulin deficiency in animal models has been induced using a variety of methods, including chemical ablation, viral infection of beta cells, and spontaneous development of autoimmune diabetes. Streptozotocin (STZ) or Alloxan are used to chemically trigger beta cell death.¹³¹ STZ enters the pancreatic beta cell via the Glut-2 transporter and induces DNA alkylation, damage, and cell death. STZ at a single high dose of 100-200 mg/kg in mice and 35-65 mg/kg in rats causes rapid ablation of the beta cell and hyperglycemia.¹³² The chemical annihilation method is easy, inexpensive, and applicable to more animals. The chemical ablation method is appropriate for testing beta cell-independent glucose-lowering therapies (new insulin formulation, transplantation therapies). The downside of chemical usage is that these compounds are non-specifically harmful to other body organs. In addition to the chemical method, a spontaneous autoimmune type 1 model has been developed to better comprehend the therapeutic potential of the design formulation. The most common diabetic model is non-obese diabetes (NOD) and Bio breeding (BB) rat.¹³³

Along with the rodent model, other big animal models, such as rabbits, pigs, and monkeys, have been developed. Pancreatectomy, STZ, or their combination were exploited to induce

diabetes in large animal models. The type 2 diabetes animal models are primarily obese, reflecting the human condition.

1.10 Melanin

Melanin is a well-known naturally occurring conductive polymeric pigment widely distributed in living organisms.¹³⁴ It is responsible for structural coloration and protect from sunlight and radicals. Other functional properties of melanin included photosensitization, metal ion chelation, antibiotic, thermoregulation, and some involvement in nervous system. The chemical structure of melanin contains repeating units of 5,6-dihydroxyindole and 5,6-dihydroxyindole-2-carboxylic acid. In living organism, the melanin was synthesized by two-step enzymatic reaction. The first step involves the controlled oxidation of the side chain of the tyrosine followed by oxidative polymerization results in the formation of melanin. Synthetic melanin is prepared from dopamine. At alkaline condition, dopamine oxidized and simultaneously self-polymerized by oxygen into melanin.¹³⁵ Melanin owing to its polyphenolic nature is redox-active and show excellent free radical scavenging property.¹³⁴ The oligomeric aromatic backbone and hydration-dependent ionic conduction induce electrical conductivity.¹³⁶⁻¹³⁸ Thus, biocompatible, biodegradable, and electroactive melanin is a promising material option for preparing antioxidant biomaterial scaffolds in bioelectronics.¹³⁹⁻

141

1.11 Wound Healing

Wound healing is a complex biological process involving multiple biological pathways and chemical responses to retrieve tissue integrity and homeostasis.¹⁴² The repair process involves three distinct but overlapping phases of inflammation, tissue regeneration, and remodelling. After damage, blood coagulation cascades are activated to achieve haemostasis through platelet plugs and fibroin matrix formation. These fibrins plug matrix consist of polymerized

fibrinogen, fibronectin, vitronectin and thrombospondin embedded with platelets provides immediate coverage at damage site from infections. Followed by various cells undergoes phenotypic and genetic alternations leading to cell migrations, proliferation, and differentiation. Inflammatory neutrophile cells are recruited at wound sites to breakdown the degranulated platelets, damaged tissues, and bacteria.¹⁴³

The second stage of wound healing is new tissue formation, which starts after 2-10 days of damage. Keratinocyte cells are migrated from healthy site over the injured dermis layer. Sprouts of the new blood vessel capillaries along with the fibroblast and macrophage cells replace the clotted fibrin matrix with granulation tissues. Through granulation tissues, keratinocyte cells are migrated towards the wound site and proliferate, mature, restore the dermis layer of the skin. The vascular endothelial growth factor A (VEGFA) and fibroblast growth factor 2 (FGF2) play a major role in the new vessel formation process called angiogenesis process.¹⁴⁴ Fibroblast cells at the wound are differentiated into myofibroblasts by stimulation of macrophages and join the edges of wound.¹⁴⁵ The myofibroblast and fibroblast cells produce collagen extracellular matrix and form mature scar.¹⁴⁶ Various growth factors, hepatocyte growth factor (HGF), epidermal growth factor (EGF), fibroblast growth factor (FGF) transforming growth factor (TGF), and hormones act as cues for re-epithelialization at the damage site.

The final stage of healing is remodelling of newly generated tissues and extracellular matrix. This process starts from 2-3 weeks of the injury and can last till one year, depending on the damage sites. In this stage, all preactivated cascades after damage are slow down and further discontinued. Endothelial, macrophage, and myofibroblast cells present at wound site undergoes programable cell death (apoptosis) or leave the wound sites. Epithelial-mesenchymal interactions continuously regulate skin integrity and homeostasis.¹⁴⁷ The matrix

metalloproteinases secreted from the fibroblast, macrophages and endothelial cells remodelled the type III collagen to type I collagen matrix and provide the strength to regenerated skin.¹⁴⁸

1.12 Animal Models for Wound Healing

In wound healing studies, *in vitro*, and *in vivo* models are available to understand the tissue repair process.¹⁴⁹ However, the *in vivo* models remain the most predictive model for the realistic representation of wound environment, representing individual aspects of human physiology. Various preclinical models, such as mice, rats, rabbits, and pigs, can mimic acute and impaired related wounds. The most widely used species are rats and mice. Despite structural and physiological differences between rodent and human skin morphology, wound healing assessment will provide valuable transitional information.¹⁵⁰ Using the rodent family for the wound healing model, rats are a better choice than mice because of their thick keratinocyte layer compared to the latter and the possibility of a large sample size.

In comparison, rabbit and pig skin more closely matches human skin morphology and is a superior choice for wound healing assessments.¹⁵¹ Pig skin is more anatomically akin to human skin, with comparable levels of collagen, elastin, and growth factors. But they are more expensive to house and have chances to prompt infection. Wounds in the animal can be developed by excision or incision technique. Incisional wounds benefit surgical incision materials such as suture threads and mechanical properties through the evolution of tensile strength. Excisional wounds, on the other hand, reflect acute clinical injuries and represent the most commonly used animal model. Excisional wounds are created by surgically removing the whole skin layer, allowing us to explore the various phases of wound healing. The wound region can be imaged to determine the progress of wound closure over time. Animals can be sedated locally to get a biopsy punch or euthanized to collect regenerated skin patches for the histological investigation to assess the epithelial gap, granulation bed, and collagen

arrangement. Animal models mimicking the chronicity associated with non-healing wounds are used to replicate chronic disorders. The most frequently used chronic diseases are diabetes and nutritional-associated chronic conditions.

1.13 Cell Penetrating Peptides (CPPs)

Effective delivery of active ingredients into mammalian cells remains a major hurdle to realizing their therapeutic potential. The negatively charged cell membrane surface and hydrophobicity impede the delivery of hydrophilic drugs, proteins, nucleic acids, and nanosized materials in their effective concentration inside the cell. Several delivery vectors, liposomes, polymers, dendrimers, and exosomes are developed to enable efficient internalization into the cell.¹⁵²⁻¹⁵⁵ However, the problem associated with some delivery vectors is their toxicity and non-specific delivery to the cell. To overcome the toxicity, a biocompatible delivery vector cell penetrating peptides (CPPs) was introduced in the field of drug delivery.¹⁵⁶⁻¹⁶⁰ CPPs are diverse groups of polycationic peptides or protein domains with 5-30 amino acids sequence. CPPs were first introduced by Green and Loewenstein, and Frankel and Pabo in 1988.^{161,162} They observed that HIV's Transactivator of Transcription (TaT) protein can effectively internalize to cells and endorsed viral transactivation. Later, penetratin a 16-mer third helix transcription factor domain of *Drosophila Antennapedia* was discovered which can translocate through biological membrane.¹⁶³ In 1997 Vives et al. discovered that cationic lysine and arginine amino acid containing sequences from 49-57 of TaT is sufficient for cellular internalization.¹⁶⁴ Subsequently, several CPPs have been designed based on the charge and structural properties of the CPPs sequence.^{165,166} The cationic side chain present in CPPs interacts with negative and zwitterionic lipid membrane through hydrogen bonding and electrostatic interactions, which aid their internalization into the cell.¹⁶⁷⁻¹⁶⁹ Activity studies on structural conformation and charges showed minimum of six cationic charges are required for efficient cellular uptake. Other designed cationic peptides are the arginine and lysine based

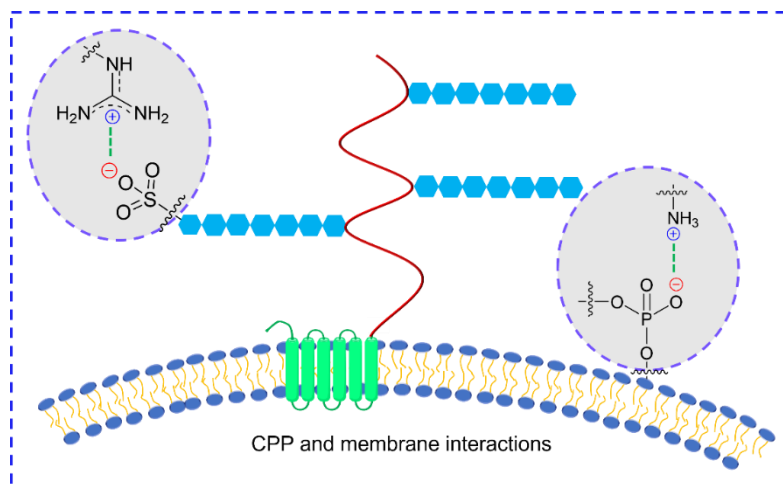


Figure 7. CPPs interactions with the membrane lipids and negatively charged sugar.

nuclear localization sequences like SV40 (PKKKRKV), NF- κ B (VQRKRQKLMP), TFIIE- β (SKKKKTKV).¹⁵⁸ Further, the CPPs were attached with the lipid to enhance the membrane binding and uptake.¹⁷⁰⁻¹⁷² Amphipathic peptides, where the hydrophobic domain was attached to the cationic or hydrophilic amino acids form a separate face of the α -helix for efficient grafting to the membrane.¹⁵⁸ The proline-rich amphipathic peptide of maize with 50% proline and arginine residues can effectively penetrate the membrane. Bactenecin-7 synthetically designed (PRR)_n and (PPR)_n SAP (VRLPPP)₃ are the best examples of amphipathic peptides.¹⁷³

CPP carriers are promising tools for effectively delivering several bioactive molecules into the cell. By utilizing the CPPs effective delivery of the peptide, proteins, antibiotics, siRNA, and drug-loaded nanoparticles was achieved. Morris et al. showed that CPPs effectively deliver the oligonucleotide into the cell with good transfection efficacy.¹⁷⁴ Schwarze et al. established the *in vivo* delivery protocol of 120 kDa β -galactosidase protein by fusion with HIV Tat peptide.¹⁷⁵ The well standardized chemical synthesis protocol provides the opportunity to design novel CPPs sequences with various target. Morris et al. designed a peptide sequence through a combination of different cellular target sequences, which effectively deliver large proteins

inside the cell.¹⁷⁶ The CPP and antibiotic conjugates showed the more effective targeting of drug resistance microbes than pristine antibiotic.¹⁷⁷ In drug delivery, CPPs hold the advantages of lower toxicity, uptake in various cell types, and non-dependency on cargo size.

1.14 Peptidomimetics

The proteolytic instability of peptides in biological media is one of the major concerns in peptide-based therapeutics and CPPs. To enhance the pharmacological properties of peptides, mimic of native analogue namely, peptidomimetics were developed.^{178,179} Peptidomimetics can be generated from its native peptide analogue through cyclization or coupling of unnatural amino acids. Several chemical modifications of native amino acids like amine alkylation, side chain substitution, and cyclization generates unnatural amino acids. Other classes of unnatural amino acids are β -amino acids, extended amino acids, and isosteric amino acids.

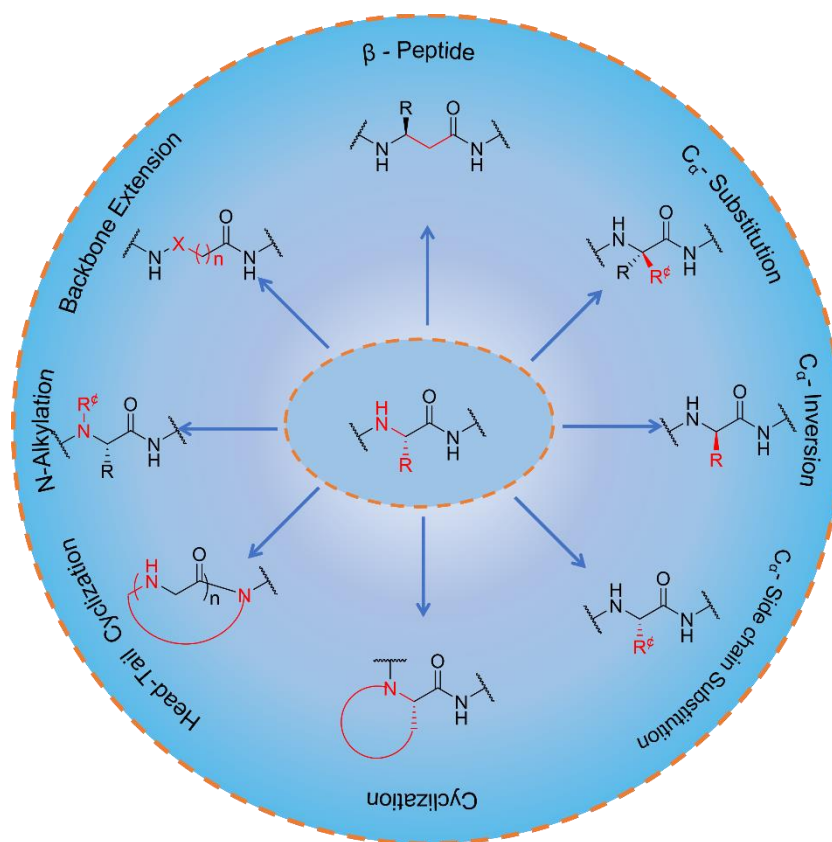


Figure 8. Structural and composition manipulation of native amino acids into peptidomimetics.

Isosteric replacement within the peptide backbone confers a new chemical structure, such replacement induces new secondary conformation, diverse electrostatic properties with improved pharmaco-kinetics properties. Isosteric replacement of amino group by isosteric atom like oxygen atom gives the depsipeptides with reduced hydrogen bonding sites. The variation in hydrogen bonding altered the secondary conformation and folding pattern on the peptides.¹⁸⁰ The lower resonance delocalization in ester compared to amide decreases rotational barrier for the cis-trans isomerization and induced better flexibility.¹⁸¹ Different analogues of the depsipeptides are found in fungi, bacteria, marine organism with various bioactivity like antimicrobial, antifungal, antitumor, immunosuppression, anti-inflammatory activity.¹⁸² The substitution of peptide bond with thiol groups gives isosteric peptidomimetics thiodepsipeptide. Inversion of the stereochemistry at α -carbon of the peptide generates D-peptide with improved protease stability. The replacement of the α -hydrogen by alkyl or others group or isoelectronic replacement of the α -carbon with the nitrogen generates azopeptides. The N substitution eliminates the chirality of α -carbon and changes its geometry from tetrahedral to trigonal which provides the β -turn conformation geometry of the peptide.¹⁸³ The electrophilicity of the carbonyl group also decreases due to resonance delocalization between the carbonyl and α -nitrogen and changes chemical and biological properties. Several backbones modified constitutional and configurational isomers were made by Seebach and Gellman group through incorporating extra carbon, nitrogen or other atom between carbonyl and amino group. The secondary and tertiary structure of these peptidomimetics depends on both the substitution pattern on the backbone and intermolecular hydrogen bonds.¹⁸⁴ Several backbone extended peptidomimetics like α or β or γ -aminooxy peptides, α -hydrazinopeptides and aza- β^3 -peptides are this class of peptides. The peptidomimetic analogues of the peptides has better pharmacokinetic stability compared to native peptide.

1.15 Cyclic Dipeptides

The head to tail cyclization of linear dipeptide generate 2,5-diketopiperazines, which is known as cyclic dipeptides (CDP), simplest cyclic peptide with rigid lactam core.^{185,186} CDPs are secondary metabolites conserved through the course of evolution, ubiquitously found in nature from bacteria to human.¹⁸⁷ These metabolites and synthetic derivatives show numerous biological activities like anticancer, antimalarials, antimicrobials, inhibitor, hormonal antagonist, blood-brain barrier (BBB) transporter and drug delivery agents.¹⁸⁸ Utilizing the rigid lactam scaffold overcome the limitations of native peptides such as proteolytic instability, poor bioavailability, and conformational flexibility. Our group developed cell penetrating peptidomimetics utilizing CDP core in the peptide backbone.¹⁸⁹ The designed peptidomimetics has very good protease stability. The CDP core participates in hydrogen bonding interaction with the phosphate group of lipid and facilitates cell penetration. Konar et al. engineered the A β 14-23 peptide by incorporating CDP units at predefined positions.¹⁹⁰ The designed Akd^{NMC} stabilized the A β -42 peptide and inhibits the toxic self-assembled amyloid fibril formation.

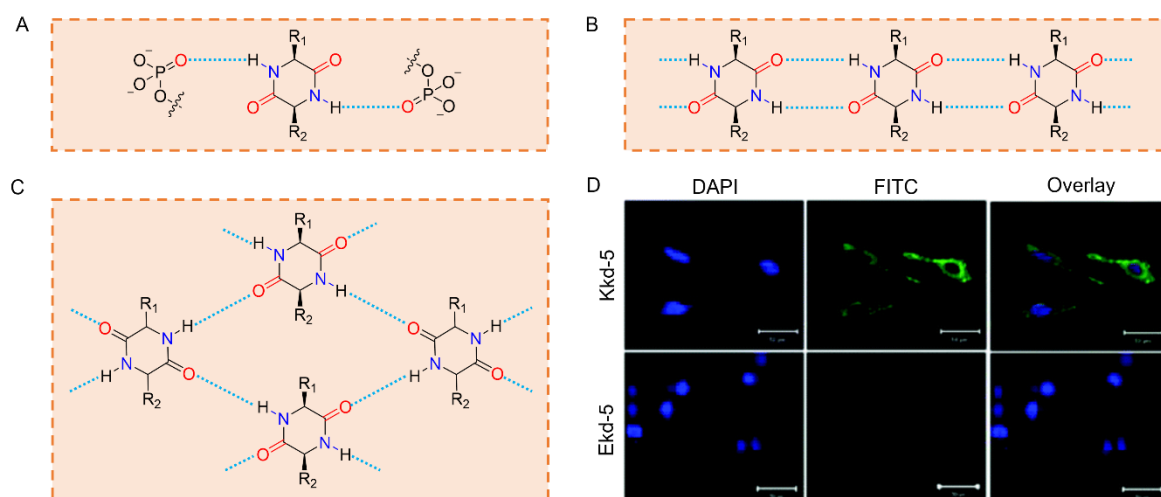


Figure 9. Schematic of hydrogen bonding propensity of CDP core. (A) The hydrogen bonding interaction between CDP amide proton with the phosphate group of lipids. (B) Hydrogen-bonded CDP molecular chain. (C) Molecular layer. (D) Cell membrane permeability of CDP-based peptidomimetics Kkd-5. Reproduced from reference 189.

The unique CDP scaffold provide multiple hydrogen bonding donor and acceptor sites and helps in directed self-assembly to govern various molecular architectures with high mechanical strength and stiffness.¹⁹¹⁻¹⁹⁴ In addition to the hydrogen bonding, amino acid side chain participates in other noncovalent interactions such as π - π interactions, van der Waal, electrostatic, and ionic interactions, which facilitate the self-assembly in 1D molecular chain or 2D layers.^{195,196} These CDP core also leads to self-assembled materials with potent activity in catalysis, sensing, and bioelectronic applications.^{197,198}

1.16 Objective

Motivated by the unparalleled biological functional activity of natural proteins and peptides, the biomaterial applications of fibrous SF, CPPs, and peptidomimetic systems have been studied to harness material fabrication for drug delivery and healthcare applications. The working chapters of the thesis were divided into two parts. The first three working chapters represent the control and responsive release of the drug or therapeutic from SF hydrogel for controlling glucose levels and wound healing in diabetes. However, several drug molecules could not penetrate the cell membrane to reach their target for therapeutic efficacy. Therefore, in the last two working chapters, we used the reductionist approach to design new cell penetrating peptide and peptidomimetic systems to deliver therapeutic drugs inside the cell efficiently. In the thesis **Chapter 2**, the gelation time of SF was tuned through mixing the glycols to fabricate injectable hydrogel with mesoporous structure. Biophysical studies have been performed to investigate the effective drug encapsulation and release behavior. The therapeutic efficacy of the insulin entrapped hydrogel was investigated in type I diabetes Wistar rat model, which shows controlled and sustained insulin delivery over 4 days. Chemically modified injectable stimuli responsive SF hydrogel was fabricated for on-demand insulin release in diabetes conditions in **Chapter 3**. In **Chapter 4**, the antioxidant SF composite hydrogel SFCH was fabricated to tackle the various pathological abnormality associated with

diabetes wounds. The berberine release study indicates controlled berberine release over time. *In vitro* studies have been performed to understand the potential of the hydrogel. The therapeutic efficacy of the hydrogel was evaluated in the diabetes type I Wistar rat model. These three chapters represent the controlled delivery of the therapeutic molecule. In **Chapter 5**, intrinsically disordered peptides from Ku-protein were designed and synthesized. The cell penetration efficacy, DNA condensation, and plasmid DNA transfection ability of peptides were investigated *in vitro* conditions. In **Chapter 6**, the peptidomimetic approach was applied to design an environment pH-sensitive cell penetrating peptidomimetics to selectively target the cancer cell by anticancer drug over normal cells. The delivery of the anticancer drug was investigated *in vitro* in cancer and normal cell line.

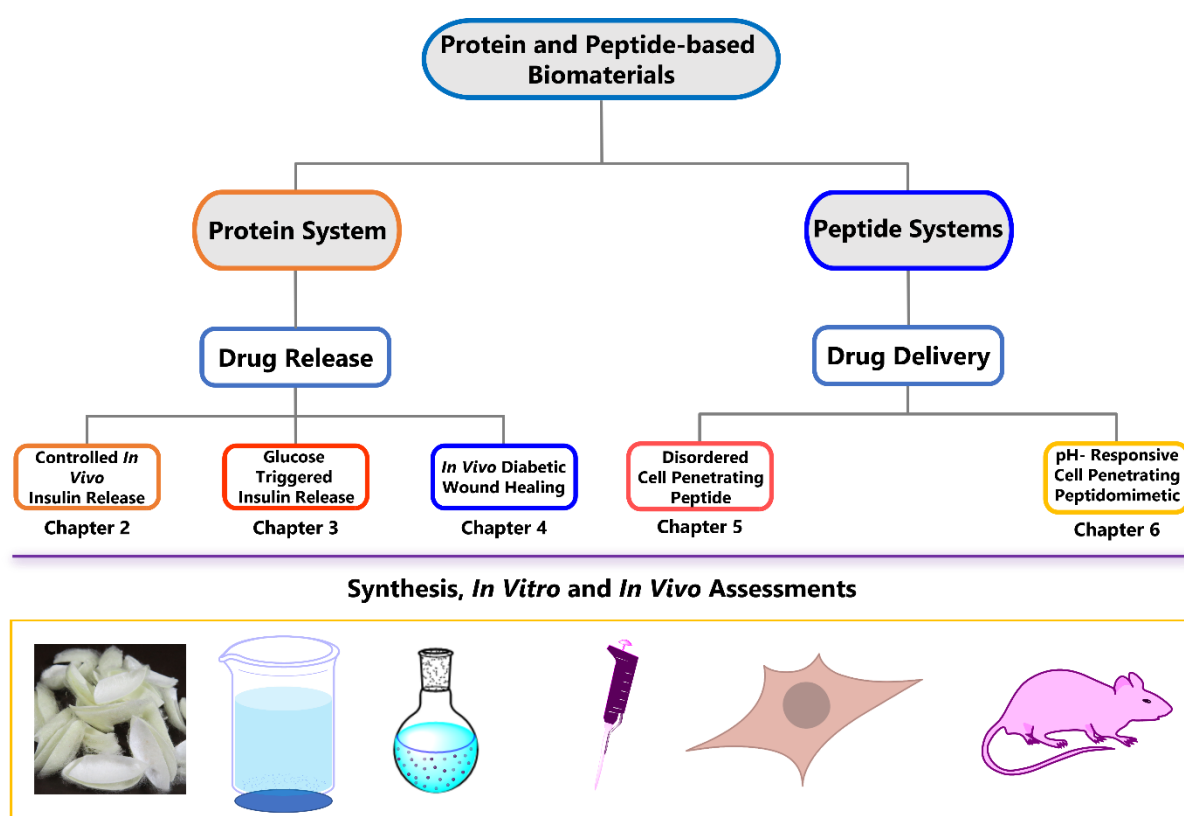


Figure 10. Outline of thesis chapters 1-6.

1.17 References

1. Langel, U.; Cravatt, B. F.; Graslund, A.; Heijne, N. G. H.; Zorko, M.; Land, T.; Niessen, S. *Introduction to peptides and proteins*. CRC Press, London, NY **2009**.
2. Nehete, J. Y.; Bhambar, R. S.; Narkhede, M. R.; Gawali, S. R. Natural proteins: Sources, isolation, characterization and applications. *Pharmacogn. Rev.* **2013**, 7, 107–116.
3. Kastin, A. J. *Handbook of biologically active peptides*, 2nd Ed. Academic Press, San Diego, CA, USA, **2013**.
4. Voet, D.; Voet, J. G.; Pratt, C. W. *Fundamentals of biochemistry: life at the molecular level*. 4th Ed. Wiley, Hoboken, NJ, USA **2013**.
5. Zuber, P. Non-ribosomal peptide synthesis. *Curr. Opin. Cell Biol.* **1991**, 3, 1046–1050.
6. Strieker, M.; Tanovic, A.; Marahiel, M. A. Nonribosomal peptide synthetases: Structures and dynamics. *Curr. Opin. Struct. Biol.* **2010**, 20, 234–240.
7. Evans, B. S. *Nonribosomal peptide and polyketide biosynthesis*, Springer, Saint Louis, MO, USA **2016**.
8. Marth, J. D. A unified vision of the building blocks of life. *Nat. Cell Biol.* **2008**, 10, 1015–1016.
9. Scheraga, H. A. Proteins and synthetic polypeptides. *Annu. Rev. Phys. Chem.* **1959**, 10, 191–218.
10. Berg, J. M.; Tymoczko, J. L.; Stryer, L. *Biochemistry*, 5th Ed. W. H. Freeman, NY, USA **2002**.
11. Shakhnovich, E. Protein folding thermodynamics and dynamics: Where physics, chemistry, and biology meet. *Chem. Rev.* **2006**, 106, 1559–1588.
12. Marsh, R. E.; Corey, R. B.; Pauling, L. An investigation of the structure of silk fibroin. *Biochim. Biophys. Acta* **1955**, 16, 1–33.
13. Knight, D.; Vollrath, F. Liquid crystalline spinning of spider silk. *Nature* **2001**, 410, 541–548.

14. Li, G.; Zhou, P.; Shao, Z.; Xie, X.; Chen, X.; Wang, H.; Chunyu, L.; Yu, T. The natural silk spinning process. *Eur. J. Biochem.* **2001**, *268*, 6600–6606.
 15. Soto, C. Protein misfolding and disease: Protein refolding and therapy. *FEBS Lett.* **2001**, *498*, 204–207.
 16. Soto, C. Unfolding the role of protein misfolding in neurodegenerative diseases. *Nat. Rev. Neurosci.* **2003**, *4*, 49–60.
 17. Selkoe, D. J. Cell biology of protein misfolding: The examples of Alzheimer's and Parkinson's diseases. *Nat. Cell Biol.* **2004**, *6*, 1054–1061.
 18. Chiti, F.; Dobson, C. M. Protein misfolding, functional amyloid, and human disease. *Annu. Rev. Biochem.* **2006**, *75*, 333–366.
 19. Hamley, I. W. Peptide fibrillization. *Angew. Chem. Int. Ed.* **2007**, *46*, 8128–8147.
 20. Datta, L. P.; Manchineella, S.; Govindaraju, T. Biomolecules-derive biomaterials. *Biomaterials* **2020**, *230*, 119633.
 21. Reches, M.; Gazit, E. Casting metal nanowires within discrete self-assembled peptide nanotubes. *Science* **2003**, *300*, 625–627.
 22. Lowik, D. W. P. M.; Leunissen, E. H. P.; Heuvel, M.; Hansen, M. B.; Hest, J. C. M. Stimulus responsive peptide based materials. *Chem. Soc. Rev.* **2010**, *39*, 3394–3412.
 23. Reches, M.; Gazit, E. Formation of closed-cage nanostructures by self-assembly of aromatic dipeptides. *Nano Lett.* **2004**, *4*, 581–585.
 24. Gazit, E. Self-assembled peptide nanostructures: the design of molecular building blocks and their technological utilization. *Chem. Soc. Rev.* **2007**, *36*, 1263–1269.
 25. Rica, R.; Matsui, H. Applications of peptide and protein-based materials in bionanotechnology. *Chem. Soc. Rev.* **2010**, *39*, 3499–3509.
-

26. Webber, M. J.; Kessler, J. A.; Stupp, S. I. Emerging peptide nanomedicine to regenerate tissues and organs. *J. Intern. Med.* **2010**, *267*, 71–88.
 27. Webber, M. J.; Tongers, J.; Renault, M-A.; Roncalli, J. G.; Losordo, D. W.; Stupp, S. I. Development of bioactive peptide amphiphiles for therapeutic cell delivery. *Acta Biomater.* **2010**, *6*, 3–11.
 28. Liu, L.; Yang, J.; Xie, J.; Luo, Z.; Jiang, J.; Yang, Y. Y.; Liu, S. The potent antimicrobial properties of cell penetrating peptide-conjugated silver nanoparticles with excellent selectivity for Gram-positive bacteria over erythrocytes. *Nanoscale* **2013**, *5*, 3834–3840.
 29. Rodriguez, A. L.; Parish, C. L.; Nisbet, D. R.; Williams, R. J. Tuning the amino acid sequence of minimalist peptides to present biological signals via charge neutralised self assembly. *Soft Matter* **2013**, *9*, 3915–3919.
 30. Giano, M. C.; Ibrahim, Z.; Medina, S. H.; Sarhane, K. A.; Christensen, J. M.; Yamada, Y.; Brandacher, G.; Schneider, J. P. Injectable bioadhesive hydrogels with innate antibacterial properties. *Nat. Commun.* **2014**, *5*, 4095.
 31. Gazit, E. Self-assembled peptide nanostructures: The design of molecular building blocks and their technological utilization. *Chem. Soc. Rev.* **2007**, *36*, 1263–1269.
 32. Pochan, D.; Scherman, O. Introduction: Molecular self-assembly. *Chem. Rev.* **2021**, *121*, 13699–13700.
 33. Pelesko, J. A. *Self assembly: The science of things that put themselves together*. CRC Press, NW, FL **2009**.
 34. Greef, T. F. A. D.; Smulders, M. M. J.; Wolfs, M.; Schenning, A. P. H. J.; Sijbesma, R. P.; Meijer, E. W. Supramolecular polymerization. *Chem. Rev.* **2009**, *109*, 5687–5754.
 35. Yang, L.; Tan, X.; Wang, Z.; Zhang, X. Supramolecular polymers: Historical development, preparation, characterization, and functions. *Chem. Rev.* **2015**, *115*, 7196–7239.
 36. Govindaraju, T.; Ariga, K. *Molecular architectonics and nanoarchitectonics*. Springer Singapore, Singapore, **2022**.
-

37. Krieg, E.; Bastings, M. M. C.; Besenius, P.; Rybtchinski, B. Supramolecular polymers in aqueous media. *Chem. Rev.* **2016**, *116*, 2414–2477.
38. Philp, D.; Stoddart, J. F. Self-assembly in natural and unnatural systems. *Angew. Chem. Int. Ed.* **1996**, *35*, 1154–1196.
39. Avinash, M. B.; Govindaraju, T. Nanoarchitectonics of biomolecular assemblies for functional applications. *Nanoscale* **2014**, *6*, 13348–13369.
40. Roy, B.; Govindaraju, T. Amino acids and peptides as functional components in arylenediimide-based molecular architectonics. *Bull. Chem. Soc. Jpn.* **2019**, *92*, 1883–190.
41. Vintiloiu, A.; Leroux, J. C. Organogels and their use in drug delivery—a review. *J. Control. Release* **2008**, *125*, 179–192.
42. Park, K. H.; Na, K.; Chung, H. M. Enhancement of the adhesion of fibroblasts by peptide containing an Arg-Gly-Asp sequence with poly(ethylene glycol) into a thermo-reversible hydrogel as a synthetic extracellular matrix. *Biotechnol. Lett.* **2005**, *27*, 227–231.
43. Avinash, M. B.; Govindaraju, T. Engineering molecular organization of naphthalenediimides: Large nanosheets with metallic conductivity and attoliter containers. *Adv. Funct. Mater.* **2011**, *20*, 3875–3882.
44. Schneider, J. P.; Pochan, D. J.; Ozbas, B.; Rajagopal, K.; Pakstis, L.; Kretsinger, J. Responsive hydrogels from the intramolecular folding and self-assembly of a designed peptide. *J. Am. Chem. Soc.* **2002**, *124*, 15030–15037.
45. Dou, X.-Q.; Fen, C.-L. Amino acids and peptide-based supramolecular hydrogels for three-dimensional cell culture. *Adv. Mater.* **2017**, *29*, 1604062.
46. Amit, M.; Yuran, S.; Gazit, E.; Reches, M.; Ashkenasy, N. Tailor-made functional peptide self-assembling nanostructures. *Adv. Mater.* **2018**, *30*, 1707083.
47. Sheehan, F.; Sementa, D.; Jain, A.; Kumar, M.; Tayarani-Najjaran, M.; Kroiss, D.; Ulijn, R. V. Peptide-based supramolecular systems chemistry. *Chem. Rev.* **2021**, *121*, 13869–13914.
48. Sinha, N. J.; Langenstein, M. G.; Pochan, D. J.; Kloxin, C. J.; Saven, J. G.; Peptide design and self-assembly into targeted nanostructure and functional materials. *Chem. Rev.* **2021**, *121*, 13915–13935.
-

49. Zhu, J.; Avakyan, N.; Kakkis, A.; Hoffnagle, A. M.; Han, K.; Li, Y.; Zhang, Z.; Choi, T. S.; Na, Y.; Yu, C.-J.; Tezcan, F. A. Protein assembly by design. *Chem. Rev.* **2021**, *121*, 13701–13796.
50. Howard, J. Mechanical signaling in networks of motor and cytoskeletal proteins. *Annu. Rev. Biophys.* **2009**, *38*, 217–234.
51. Janmey, P. A. Mechanical properties of cytoskeletal polymers. *Curr. Opin. Cell Biol.* **1991**, *3*, 4–11.
52. Nogales, E. Structural insights into microtubule function. *Annu. Rev. Biochem.* **2000**, *69*, 277–302.
53. Shoulders, M. D.; Raines, R. T. Collagen structure and stability. *Annu. Rev. Biochem.* **2009**, *78*, 929–958.
54. Wang, B.; Yang, W.; McKittrick, J.; Meyers, M. A. Keratin: Structure, mechanical properties, occurrence in biological organisms, and efforts at bioinspiration. *Prog. Mater. Sci.* **2016**, *76*, 229–318.
55. Gower, L. B. Biomimetic model systems for investigating the amorphous precursor pathway and its role in biomineralization. *Chem. Rev.* **2008**, *108*, 4551–4627.
56. Luo, Q.; Hou, C.; Bai, Y.; Wang, R.; Liu, J. Protein assembly: Versatile approaches to construct highly ordered nanostructures. *Chem. Rev.* **2016**, *116*, 13571–13632.
57. Xu, C.; Lu, P.; Gamal El-Din, T. M.; Pei, X. Y.; Johnson, M. C.; Uyeda, A.; Bick, M. J.; Xu, Q.; Jiang, D.; Bai, H.; et al. Computational design of transmembrane pores. *Nature* **2020**, *585*, 129–134.
58. Li, Q.; So, C. R.; Fegan, A.; Cody, V.; Sarikaya, M.; Vallera, D. A.; Wagner, C. R. Chemically self-assembled antibody nanorings (CSANs): Design and characterization of an anti-CD3 IgM biomimetic. *J. Am. Chem. Soc.* **2010**, *132*, 17247–17257.
59. Der, B. S.; Edwards, D. R.; Kuhlman, B. Catalysis by a de novo zinc-mediated protein interface: Implications for natural enzyme evolution and rational enzyme engineering. *Biochemistry* **2012**, *51*, 3933–3940.
60. Brodin, J. D.; Medina-Morales, A.; Ni, T.; Salgado, E. N.; Ambroggio, X. I.; Tezcan, F. A. Evolution of metal selectivity in templated protein interfaces. *J. Am. Chem. Soc.* **2010**, *132*, 8610–8617.
-

61. Buwalda, S. J.; Boere, K. W. M.; Dijkstra, P. J.; Feijen, J.; Vermonden, T.; Hennink, W. E. Hydrogels in a historical perspective: From simple networks to smart materials. *J. Controlled Release* **2014**, *190*, 254–273.
62. Wichterle, O.; Lim, D. Hydrophilic gels in biologic use. *Nature* **1960**, *185*, 117–118.
63. Zhang, Y.; Khademhosseini, A. Advances in engineering hydrogels. *Science* **2017**, *356*, 1–10.
64. Tibbitt, M. W.; Anseth, K. S. Hydrogels as extracellular matrix mimics for 3D cell culture. *Biotechnol. Bioeng.* **2009**, *103*, 655–663.
65. Nafea, E. H.; Poole-Warren, A. M. L. A.; Martens, P. J. Immunoisolating semi-permeable membranes for cell encapsulation: Focus on hydrogels. *J. Controlled Release* **2011**, *154*, 110–122.
66. Correa, S.; Grosskopf, A. K.; Hernandez, H. L.; Chan, D.; Yu, A. C.; Stapleton, L. M.; Appel, E. A. Translational applications of hydrogels. *Chem. Rev.* **2021**, *121*, 11385–11457.
67. Ward, M. A.; Georgiou, T. K. Thermoresponsive polymers for biomedical applications. *Polymers* **2011**, *3*, 1215–1242.
68. Srividya, B.; Cardoza, R. M.; Amin, P. Sustained ophthalmic delivery of ofloxacin from a pH triggered in situ gelling system. *J. Controlled Release* **2001**, *73*, 205–211.
69. Niece, K. L.; Czeisler, C.; Sahni, V.; Tysseling-Mattiace, V.; Pashuck, E. T.; Kessler, J. A.; Stupp, S. I. Modification of gelation kinetics in bioactive peptide amphiphiles. *Biomaterials* **2008**, *29*, 4501–4509.
70. Winne, J. M.; Leibler, L.; Du Prez, F. E. Dynamic covalent chemistry in polymer networks: A mechanistic perspective. *Polym. Chem.* **2019**, *10*, 6091–6108.
71. Appel, E. A.; Barrio, J. D.; Loh, X. J.; Scherman, O. A. Supramolecular polymeric hydrogels. *Chem. Soc. Rev.* **2012**, *41*, 6195–6214.
72. Guvendiren, M.; Lu, H. D.; Burdick, J. A. Shear-thinning hydrogels for biomedical applications. *Soft Matter* **2012**, *8*, 260–272.
73. Liu, J.; Scherman, O. A. Cucurbit[n]uril supramolecular hydrogel networks as tough and healable adhesives. *Adv. Funct. Mater.* **2018**, *28*, 1800848.
-

74. Stapleton, L. M.; Steele, A. N.; Wang, H.; Lopez Hernandez, H.; Yu, A. C.; Paulsen, M. J.; Smith, A. A. A.; Roth, G. A.; Thakore, A. D.; Lucian, H. J.; et al. Use of a supramolecular polymeric hydrogel as an effective post-operative pericardial adhesion barrier. *Nat. Biomed Eng.* **2019**, *3*, 611–620.
75. Deng, J.; Zhao, C. S.; Spatz, J. P.; Wei, Q. Nanopatterned adhesive, stretchable hydrogel to control ligand spacing and regulate cell spreading and migration. *ACS Nano* **2017**, *11*, 8282–8291.
76. Doring, A.; Birnbaum, W.; Kuckling, D. Responsive hydrogels – structurally and dimensionally optimized smart frameworks for applications in catalysis, micro-system technology and material science. *Chem. Soc. Rev.* **2013**, *42*, 7391.
77. Zhao, Y.; Song, S.; Ren, X.; Zhang, J.; Lin, Q.; Zhao, Y. Supramolecular adhesive hydrogels for tissue engineering applications. *Chem. Rev.* **2022**, *122*, 5604–5640.
78. Huang, G.; Li, F.; Zhao, X.; Ma, Y.; Li, Y.; Lin, M.; Jin, G.; Lu, T. J.; Genin, G. M.; Xu, F. Functional and biomimetic materials for engineering of the three-dimensional cell microenvironment. *Chem. Rev.* **2017**, *117*, 12764–12850.
79. Kharkar, P. M.; Kiick, K. L.; Kloxin, A. M. Designing degradable hydrogels for orthogonal control of cell microenvironments. *Chem. Soc. Rev.* **2013**, *42*, 7335.
80. Wang, H.; Shi, Y.; Wang, L.; Yang, Z. Recombinant proteins as cross-linkers for hydrogelations. *Chem. Soc. Rev.* **2013**, *42*, 891.
81. Esser-Kahn, A. P.; Iavarone, A. T.; Francis, M. B. Metallothionein-cross-linked hydrogels for the selective removal of heavy metals from water. *J. Am. Chem. Soc.* **2008**, *130*, 15820–15822.
82. Petka, W. A.; Harden, J. L.; McGrath, K. P.; Wirtz, D.; Tirrell, D. A. Reversible hydrogels from self-assembling artificial proteins. *Science* **1998**, *281*, 389–392.
83. Sui, Z.; King, W. J.; Murphy, W. L. Dynamic materials based on a protein conformational change. *Adv. Mater.* **2007**, *19*, 3377–3380.
84. Esser-Kahn, A. P.; Francis, M. B. Protein-cross-linked polymeric materials through site-selective bioconjugation. *Angew. Chem. Int. Ed.* **2008**, *47*, 3751–3754.
85. Mosiewicz, K. A.; Johnsson, K.; Lutolf, M. P. Phosphotransferase-catalyzed formation of bioactive hydrogels for tissue engineering. *J. Am. Chem. Soc.* **2010**, *132*, 5972–5974.
-

86. Lienemann, P. S.; Lutolf, M. P.; Ehrbar, M. Biomimetic hydrogels for controlled biomolecule delivery to augment bone regeneration. *Adv. Drug Delivery Rev.* **2012**, *64*, 1078–1089.
87. Wang, C.; Stewart, R. J.; Kopecek, J. Hybrid hydrogels assembled from synthetic polymers and coiled-coil protein domains. *Nature* **1999**, *397*, 417–420.
88. Wu, L. C.; Yang, J.; Kopecek, J. Hybrid hydrogels self-assembled from graft copolymers containing complementary β -sheets as hydroxyapatite nucleation scaffolds. *Biomaterials* **2011**, *32*, 5341–5353.
89. Foo, C. T. S. W. P.; Lee, J. S.; Mulyasmita, W.; Parisi-Amon, A.; Heilshorn, S. C. Two-component protein-engineered physical hydrogels for cell encapsulation. *Proc. Natl. Acad. Sci. U. S. A.* **2009**, *106*, 22067–22072.
90. Altman, G. H.; Diaz, F.; Jakuba, C.; Calabro, T.; Horan, R. L.; Chen, J.; Lu, H.; Richmond, J.; Kaplan, D. L. Silk-based biomaterials. *Biomaterials* **2003**, *24*, 401–416.
91. Kundu, S. C. *Silk Biomaterials for Tissue Engineering and Regenerative Medicine*, Woodhead Publishing, Cambridge, UK, **2014**.
92. Doblhofer, E.; Heidebrecht, A.; Scheibel, T. To spin or not to spin: Spider silk fibers and more. *Appl. Microbiol. Biotechnol.* **2015**, *99*, 9361–9380.
93. Zhou, C. Z.; Confalonieri, F.; Medina, N.; Zivanovic, Y.; Esnault, C.; Yang, T.; Jacquet, M.; Janin, J.; Duguet, M.; Perasso, R.; Li, Z. G. Fine organization of *Bombyx mori* fibroin heavy chain gene. *Nucleic Acids Res.* **2000**, *28*, 2413–2419.
94. Matsumoto, A.; Lindsay, A.; Abedian, B.; Kaplan, D. L. Silk fibroin solution properties related to assembly and structure. *Macromol. Biosci.* **2008**, *8*, 1006–1018.
95. Chen, F.; Porter, D.; Vollrath, F. Structure and physical properties of silkworm cocoons. *J. R. Soc. Interface* **2012**, *9*, 2299–2308.
96. Cheng, Y.; Koh, L. D.; Li, D.; Ji, B.; Han, M. Y.; Zhang, Y. W. On the strength of β -sheet crystallites of *Bombyx mori* silk fibroin. *J. R. Soc. Interface* **2014**, *11*, 2299–2308.
97. Naskar, D.; Sapru, S.; Ghosh, A. K.; Reis, R. L.; Dey, T.; Kundu, S. C. Nonmulberry silk proteins: Multipurpose ingredient in bio-functional assembly. *Biomed. Mater.* **2021**, *16*, 062002.
98. Kundu, B.; Rajkhowa, R.; Kundu, S. C.; Wang, X. Silk fibroin biomaterials for tissue regenerations. *Adv. Drug Deliv. Rev.* **2013**, *65*, 457–470.
-

99. Guo, C.; Li, C.; Vu, H. V.; Hanna, P.; Lechtig, A.; Qiu, Y.; Mu, X.; Ling, S.; Nazarian, A.; Lin, S. J.; Kaplan, D. L. Thermoplastic moulding of regenerated silk. *Nat. Mater.* **2020**, *19*, 102–108.
100. Omenetto, F. G.; Kaplan, D. L. New opportunities for an ancient material. *Science* **2010**, *329*, 528–531.
101. Kundu, B.; Kurland, N. E.; Bano, S.; Patra, C.; Engel, F. B.; Yadavalli, V. K.; Kundu, S. C. Silk proteins for biomedical applications: Bioengineering perspectives. *Progress in Polymer Science* **2014**, *39*, 251–267.
102. Mandal, B. B.; Kundu, S. C. Cell proliferation and migration in silk fibroin 3D scaffolds. *Biomaterials* **2009**, *30*, 2956–2965.
103. Kim, S. H.; Yeon, Y. K.; Lee, J. M.; Chao, J. R.; Lee, Y. J.; Seo, Y. B.; Sultan, Md. T.; Lee, O. J.; Lee, L. S.; Yoon, S.-I. et al. Precisely printable and biocompatible silk fibroin bioink for digital light processing 3D printing. *Nat. Commun.* **2018**, *9*, 1620.
104. Pal, R. K.; Farghaly, A. A.; Wang, C.; Collinson, M. M.; Kundu, S. C.; Yadavalli, V. K. Conducting polymer-silk biocomposites for flexible and biodegradable electrochemical sensors. *Biosensors and Bioelectronics* **2016**, *81*, 294–302.
105. Benfenati, V.; Stahl, K.; Gomis-Perez, C.; Toffanin, S.; Sagnella, A.; Torp, R.; Kaplan, D. L.; Ruani, G.; Omenetto, F. G.; Zamboni, R.; Muccini, M. Biofunctional silk/neuron interfaces. *Adv. Funct. Mater.* **2012**, *22*, 1871–1884.
106. Tien, L. W.; Wu, F.; Tang-Schomer, M. D.; Yoon, E.; Omenetto, F. G.; Kaplan, D. L. Silk as a multifunctional biomaterial substrate for reduced glial scarring around brain-penetrating electrodes. *Adv. Funct. Mater.* **2013**, *23*, 3185–3193.
107. Numata, K.; Kaplan, D. L. Silk-based delivery systems of bioactive molecules. *Adv. Drug Deliv. Rev.* **2010**, *62*, 1497–1508.
108. Marelli, B.; Brenckle, M. A.; Kaplan, D. L.; Omenetto, F. G. Silk fibroin as edible coating for perishable food preservation. *Sci. Rep.* **2015**, *6*, 25263.
109. Tansil, N. C.; Li, Y.; Teng, C. P.; Zhang, S.; Win, K. Y.; Chen, X.; Liu, X. Y.; Han, M. Y. Intrinsically colored and luminescent silk. *Adv. Mater.* **2011**, *23*, 1463–1466.
-

110. Tansil, N. C.; Koh, L. D.; Han, M. Y. Functional silk: Colored and luminescent. *Adv. Mater.* **2012**, *24*, 1388–1397.
111. Kapoor, S.; Kundu, S. C. Silk protein-based hydrogels: Promising advanced materials for biomedical applications. *Acta Biomaterialia* **2016**, *31*, 17–32.
112. Cui, Y.; Zhang, F.; Chen, G.; Yao, L. Zhang, N.; Liu, Z.; Li, Q.; Zhang, F.; Cui, Z.; Zhang, K. A stretchable and transparent electrode based on PEGylated silk fibroin for *in vivo* dual-modal neural-vascular activity probing. *Adv. Mater.* **2021**, *33*, 2100221.
113. Shi, C.; Hu, F.; Wu, R.; Xu, Z.; Shao, G.; Yu, R.; Liu, X. Y. New silk road: From mesoscopic reconstruction/ functionalization to flexible meso-electronics/ photonics based on cocoon silk materials. *Adv. Mater.* **2021**, 2005910.
114. Wang, Z.; Yang, Z.; Jiang, J.; Shi, Z.; Mao, Y.; Qin, N.; Tao, T. H. Silk microneedle patch capable of on-demand multidrug delivery to the brain for Glioblastoma treatment. *Adv. Mater.* **2022**, *34*, 2106606.
115. Zimmet, P.; Alberti, K. G.; Magliano, D. J.; Bennett, P. H. Diabetes mellitus on prevalence and mortality: Facts and fallacies. *Nat. Rev. Endocrinol.* **2016**, *12*, 616–622.
116. Milardi, D.; Gazit, E.; Radford, S. E.; Xu, Y.; Gallardo, R. U.; Caflisch, A.; Westermark, G. T.; Westermark, P.; Rosa, C. L.; Ramamoorthy, A. Proteostasis of islet amyloid polypeptide: A molecular perspective of risk factors and protective strategies for type II Diabetes. *Chem. Rev.* **2021**, *121*, 1845–1893.
117. Nerup, J.; Platz, P.; Andersen, O. O.; Christy, M.; Lyngsøe, J.; Poulsen, J. E.; Ryder, L. P.; Thomsen, M.; Nielsen, L. S.; Svejgaard, A. HL-A antigens and diabetes mellitus. *Lancet* **1974**, *304*, 864–866.
118. Ross, S. A.; Gulve, E. A.; Wang, M. Chemistry and biochemistry of type 2 Diabetes. *Chem. Rev.* **2004**, *104*, 1255–1282.
119. Schwartz, M. W.; Porte, D. J. Diabetes, obesity, and the brain. *Science* **2005**, *307*, 375–379.
120. www.diabetesatlas.org, IDF Diabetes Atlas, 2019.
121. Tuomi, T.; Santoro, N.; Caprio, S.; Cai, M.; Weng, J.; Groop, L. The many faces of diabetes: A disease with increasing heterogeneity. *Lancet* **2014**, *383*, 1084–1094.
-

122. Lebovitz, H. E. Type 2 diabetes mellitus—current therapies and the emergence of surgical options. *Nat. Rev. Endocrinol.* **2011**, *7*, 408–419.
123. Wang, S.; Dougherty, E. J.; Danner, R. L. PPAR γ signaling and emerging opportunities for improved therapeutics. *Pharmacol. Res.* **2016**, *111*, 76–85.
124. Hanefeld, M.; Fleischmann, H.; Siegmund, T.; Seufert, J. Rationale for timely insulin therapy in type 2 diabetes within the framework of individualised treatment: 2020 update. *Diabetes Ther.* **2020**, *11*, 1645–1666.
125. Brange, J.; Langkjoer, L. Insulin structure and stability. *Pharm. Biotechnol.* **1993**, *5*, 315–350.
126. Smith, G. D.; Pangborn, W. A.; Blessing, R. H. The structure of T6 bovine insulin. *Acta Crystallogr. Sect. D: Biol. Crystallogr.* **2005**, *61*, 1476–1482.
127. Zoete, V.; Meuwly, M.; Karplus, M. A Comparison of the dynamic behavior of monomeric and dimeric insulin shows structural rearrangements in the active monomer. *J. Mol. Biol.* **2004**, *342*, 913–929.
128. Saltiel, A. R.; Kahn, C. R. Insulin signalling and the regulation of glucose and lipid metabolism. *Nature* **2001**, *414*, 799–806.
129. Bryant, N. J.; Govers, R.; James, D. E. Regulated transport of the glucose transporter GLUT4. *Nat. Rev. Mol. Cell Biol.* **2002**, *3*, 267–277.
130. King, A. J. F. The use of animal models in diabetes research. *Br. J. Pharmacol.* **2012**, *166*, 877–894.
131. Wilson, G. L.; Patton, N. J.; McCord, J. M.; Mullins, D. W.; Mossman, B. T. Mechanisms of streptozotocin- and alloxan-induced damage in rat B cells. *Diabetologia* **1984**, *27*, 587–591.
132. Rakieten, N.; Rakieten, M. L.; Nadkarni, M. V. Studies on the diabetogenic action of streptozotocin (NSC-37917). *Cancer Chemother Rep* **1963**, *29*, 91–103.
133. Makino, S.; Knimoto, K.; Muraoka, Y.; Mizushima, Y.; Katagiri, K.; Tochino, Y. Breeding of a non-obese, diabetic strain of mice. *Exp. Anim.* **1980**, *29*, 1–13.
-

134. d'Ischia, M.; Wakamatsu, K.; Cicoira, F.; Mauro, E. D.; Garcia-Borrón, J. C.; Commo, S.; Galvan, I.; Ghanem, G.; Kenzo, K.; Meredith, P.; et al. Melanins and melanogenesis: From pigment cells to human health and technological applications. *Pigm. Cell Melanoma Res.* **2015**, *28*, 520–544.
135. Ju, K. Y.; Lee, Y.; Lee, S.; Park, S. B.; Lee, J. K. Bioinspired polymerization of dopamine to generate melanin-like nanoparticles having an excellent free-radical-scavenging property. *Biomacromolecules* **2011**, *12*, 625–632.
136. McGinnes, J.; Corry, P.; Proctor, P. Amorphous semiconductor switching in melanins. *Science* **1974**, *183*, 853–855.
137. Bothma, J. P.; Boor, J. -de.; Divakar, U.; Schwenn, P. E.; Meredith, P. Device-quality electrically conducting melanin thin films. *Adv. Mater.* **2008**, *20*, 3539–3542.
138. Bettinger, C. J.; Bruggeman, J. P.; Misra, A.; Borenstein, J. T.; Langer, R. Biocompatibility of biodegradable semiconducting melanin films for nerve tissue engineering. *Biomaterials* **2009**, *30*, 3050–3057.
139. Liu, Y.; Ai, K.; Lu, L. Polydopamine and its derivative materials: Synthesis and promising applications in energy, environmental, and biomedical fields. *Chem. Rev.* **2014**, *114*, 5057–5115.
140. Manchineella, S.; Thirvikraman, G.; Khanum, K. K.; Ramamurthy, P. C.; Basu, B.; Govindaraju, T. Pigmented silk nanofibrous composite for skeletal muscle tissue engineering. *Adv. Healthc. Mater.* **2016**, *5*, 1222–1232.
141. Nune, M.; Manchineella, S.; Govindaraju, T.; Narayan, K. S. Melanin incorporated electroactive and antioxidant silk fibroin nanofibrous scaffolds for nerve tissue engineering. *Mater. Sci. Eng. C* **2019**, *94*, 17–25.
142. Gurtner, G. C.; Werner, S.; Barrandon, Y.; Longaker, M. T. Wound repair and regeneration. *Nature* **2008**, *453*, 314–321.
143. Martin, P.; Leibovich, S. J. Inflammatory cells during wound repair: the good, the bad and the ugly. *Trends Cell Biol.* **2005**, *15*, 599–607.
144. Werner, S.; Grose, R. Regulation of wound healing by growth factors and cytokines. *Physiol. Rev.* **2003**, *83*, 835–870.
-

145. Opalenik, S. R.; Davidson, J. M. Fibroblast differentiation of bone marrow-derived cells during wound repair. *FASEB J.* **2005**, *19*, 1561–1563.
146. Werner, S.; Krieg, T.; Smola, H. Keratinocyte–fibroblast interactions in wound healing. *J. Invest. Dermatol.* **2007**, *127*, 998–1008.
147. Szabowski, A.; Maas-Szabowski, N.; Andrecht, S.; Kolbus, A.; Schorpp-Kistner, M.; Fusenig, N. E.; Szabowski, P. A. c-Jun and JunB antagonistically control cytokine-regulated mesenchymal–epidermal interaction in skin. *Cell* **2000**, *103*, 745–755.
148. Lovvorn, H. N.; Cheung, D. T.; Nimni, M. E.; Perelman, N.; Estes, J. M. Relative distribution and crosslinking of collagen distinguish fetal from adult sheep wound repair. *J. Pediatr. Surg.* **1999**, *34*, 218–223.
149. Masson-Meyers, D. S.; Andrade, T. A. M.; Caetano, G. F.; Guimaraes, F. R.; Leite, M. N.; Leite, S. N.; Frade, M. A. C. Experimental models and methods for cutaneous wound healing assessment. *Int. J. Exp. Path.* **2020**, *101*, 21–37.
150. Wong, V. W.; Sorkin, M.; Glotzbach, J. P.; Longaker, M. T.; Gurtner, G. C. Surgical approaches to create murine models of human wound healing. *J. Biomed. Biotechnol.* **2011**, *2011*, 969618.
151. Mustoe, T. A.; Pierce, G. F.; Morishima, C.; Deuel, T. F. Growth factor- induced acceleration of tissue repair through direct and inductive activities in a rabbit dermal ulcer model. *J. Clin. Invest.* **1991**, *87*, 694–703.
152. Kirtane, A. R.; Panyam, J. Polymer nanoparticles: Weighing up gene delivery. *Nat. Nanotechnol.* **2013**, *8*, 805–806.
153. Pattni, B. S.; Chupin, V. V.; Torchilin, V. P. New developments in liposomal drug delivery. *Chem. Rev.* **2015**, *115*, 10938–10966.
154. Yang, J.; Zhang, Q.; Chang, H.; Cheng, Y. Surface engineered dendrimers in gene delivery. *Chem. Rev.* **2015**, *115*, 5274–5300.
155. Moorthy, H.; Govindaraju, T. Dendrimer architectonics to treat cancer and neurodegenerative diseases with implications in theranostics and personalized medicine. *ACS Appl. Bio Mater.* **2021**, *4*, 1115–1139.
-

156. Copolovici, D. M.; Langel, K.; Eriste, E.; Langel, U. Cell-penetrating peptides: Design, synthesis, and applications. *ACS Nano* **2014**, *8*, 1972–1994.
157. Brooks, H., Lebleu, B.; Vives, E. Tat peptide-mediated cellular delivery: Back to basics. *Adv. Drug Del. Rev.* **2005**, *57*, 559–577.
158. Guidotti, G.; Brambilla, L.; Rossi, D. Cell-penetrating peptides: From basic research to clinics. *Trends Pharmacol. Sci.* **2017**, *38*, 406–424.
159. Peraro, L.; Kritzer, J. A. Emerging methods and design principles for cell-penetrant peptides. *Angew. Chem. Int. Ed.* **2018**, *57*, 11868–11881.
160. Schmidt, N.; Mishra, A.; Lai, G. H.; Wong, G. C. L. Arginine-rich cell-penetrating peptides. *FEBS Letters* **2010**, *584*, 806–1813.
161. Green, M.; Loewenstein, P. M. Autonomous functional domains of chemically synthesized human immunodeficiency virus tat trans-activator protein. *Cell* **1988**, *55*, 1179–1188.
162. Frankel, A. D.; Pabo, C. O. Cellular uptake of the tat protein from human immunodeficiency virus. *Cell.* **1988**, *55*, 1189–1193.
163. Derossi, D.; Joliot, A.H.; Chassaing, G.; Prochiantz, A. The third helix of the Antennapedia homeodomain translocates through biological membranes. *J. Biol. Chem.* **1994**, *269*, 10444–10450.
164. Vives, E.; Brodin, P.; Lebleu, B. A truncated HIV-1 Tat protein basic domain rapidly translocates through the plasma membrane and accumulates in the cell nucleus, *J. Biol. Chem.* **1997**, *272*, 16010–16017.
165. Schmidt, N.; Mishra, A.; Lai, G. H.; Wong, G. C. L. Arginine-rich cell-penetrating peptides. *FEBS Letters* **2010**, *584*, 806–1813.
166. Mishra, A.; Laia, G. H.; Schmidta, N. W.; Suna, V. Z.; Rodrigueza, A. R.; Tongd, R.; Tangd, L.; Chengd, J.; Deminga, T. J.; Kameia, D. T.; Wong, G. C. L. Translocation of HIV TAT peptide and analogues induced by multiplexed membrane and cytoskeletal interactions. *Proc. Natl. Acad. Sci.* **2011**, *108*, 16883–16888.
167. Madani, F.; Lindberg, S.; Langel, U.; Futaki, S.; Graslund, A. Mechanisms of cellular uptake of cell-penetrating peptides, *J. Biophys.* **2011**, 414729.
-

168. Kim, G. C.; Cheon, D. H.; Lee, Y. Challenge to overcome current limitations of cell-penetrating peptides. *BBA - Proteins and Proteomics* **2021**, *1869*, 140604.
169. Mishra, A.; Gordon, V. D.; Yang, L.; Coridan, R.; Wong, G. C. L. HIV TAT forms pores in membranes by inducing saddle-splay curvature: Potential role of bidentate hydrogen bonding. *Angew. Chem. Int. Ed.* **2008**, *47*, 2986–2989.
170. Avrahami, D.; Shai, Y. A new group of antifungal and antibacterial lipopeptides derived from non-membrane active peptides conjugated to palmitic acid. *J. Biol. Chem.* **2004**, *279*, 12277–12285.
171. Asai, T.; Tsuzuku, T.; Takahashi, S.; Okamoto, A.; Dewa, T.; Nango, M.; Hyodo, K.; Ishihara, H.; Kikuchi, H.; Oku, N. Cell-penetrating peptide-conjugated lipid nanoparticles for siRNA delivery. *Biochem. Biophys. Res. Commun.* **2014**, *444*, 599–604.
172. Biswas, A.; Chakraborty, K.; Dutta, C.; Mukherjee, S.; Gayen, P.; Jan, S.; Mallick, A. M.; Bhattacharyya, D.; Roy, R. S. Engineered histidine-enriched facial lipopeptides for enhanced intracellular delivery of functional siRNA to triple negative breast cancer cells. *ACS Appl. Mater. Interfaces* **2019**, *11*, 4719–4736.
173. Pujals, S.; Sabido, E.; Tarrag, T.; Giralt, E. All-d proline-rich cell-penetrating peptides: A preliminary *in vivo* internalization study. *Biochem. Soc. Trans.* **2007**, *35*, 794–796.
174. Morris, M.C.; Vidal, P.; Chaloin, L.; Heitz, F.; Divita, G. A new peptide vector for efficient delivery of oligonucleotides into mammalian cells. *Nucleic Acids Res.* **1997**, *25*, 2730–2736.
175. Schwarze, S. R., Ho, A., Vocero-Akbani, A.; Dowdy, S.F. *In vivo* protein transduction: Delivery of a biologically active protein into the mouse. *Science* **1999**, *285*, 1569–1572.
176. Morris, M. C.; Depollier, J.; Mery, J.; Heitz, F.; Divita, G. A peptide carrier for the delivery of biologically active proteins into mammalian cells. *Nat. Biotechnol.* **2001**, *19*, 1173–1176.
177. Zeiders, S. M.; Chmielewski, J. Antibiotic–cell-penetrating peptide conjugates targeting challenging drug-resistant and intracellular pathogenic bacteria. *Chem Biol Drug Des.* **2021**, *98*, 762–778.
178. Avan, I.; Hall, C. D.; Katritzky, A. R. Peptidomimetics via modifications of amino acids and peptide bonds. *Chem. Soc. Rev.* **2014**, *43*, 3575–3594.
-

179. Lenci, E.; Trabocchi, A. Peptidomimetic toolbox for drug discovery. *Chem. Soc. Rev.* **2020**, *49*, 3262–3277.
180. Scheike, J.A.; Baldauf, C.; Spengler, J.; Albericio, F.; Pisabarro, M. T.; Kocsch, B. Amide-to-ester substitution in coiled coils: The effect of removing hydrogen bonds on protein structure. *Angew. Chem. Int. Ed.* **2007**, *46*, 7766–7769.
181. Kang, Y. K.; Byun, B. J. Conformational preferences and cis-trans isomerization of L-lactic acid residue. *J. Phys. Chem. B* **2008**, *112*, 9126–9134.
182. Sarabia, F.; Chammaa, S.; Ruiz, A. S.; Ortiz, L. M.; Herrera, F. J. L. Chemistry and biology of cyclic depsipeptides of medicinal and biological interest. *Curr. Med. Chem.* **2004**, *11*, 1309.
183. Lee, H. J.; Song, J. W.; Choi, Y. S.; Park, H. M.; Lee, K. B. A Theoretical study of conformational properties of N-methyl azapeptide derivatives. *J. Am. Chem. Soc.* **2002**, *124*, 11881–11893.
184. Martinek, T. A.; Fulop, F. Peptidic foldamers: Ramping up diversity. *Chem. Soc. Rev.* **2012**, *41*, 687–702.
185. Balachandra, C.; Padhi, D.; Govindaraju, T. Cyclic dipeptide: A privileged molecular scaffold to derive structural diversity and functional utility. *ChemMedChem*, **2021**, *16*, 2558–2587.
186. Manchineella, S.; Govindaraju, T. Molecular self-assembly of cyclic dipeptide derivatives and their applications. *ChemPlusChem* **2017**, *82*, 88–106.
187. Bellezza, I.; Peirce, M. J.; Minelli, A. Cyclic dipeptides: From bugs to brain. *Trends Mol. Med.* **2014**, *20*, 551–558.
188. Borthwick, A. D. 2,5-Diketopiperazines: Synthesis, reactions, medicinal chemistry, and bioactive natural products. *Chem. Rev.* **2012**, *112*, 3641–3716.
189. Madhu, C.; Voshavar, C.; Rajasekhar, K.; Govindaraju, T. Cyclic dipeptide based cell-penetrating peptidomimetics for effective DNA delivery. *Org. Biomol. Chem.* **2017**, *15*, 3170–3174.
190. Konar, M.; Ghosh, D.; Samanta, S.; Govindaraju, T. Combating amyloid-induced cellular toxicity and stiffness by designer peptidomimetics. *RSC Chem. Biol.* **2022**, *3*, 220–226.
191. Benedetti, E.; Corradini, P.; Pedone, C. Crystal and molecular structure of trans-3,6-dimethyl-2,5-piperazinedione (L-alanyl-D-alanine 2,5-diketopiperazine). *J. Phys. Chem.* **1969**, *73*, 2891–2895.
-

192. Manchineella, S.; Murugan, N. A.; Govindaraju, T. Cyclic dipeptide-based ambidextrous supergelators: Minimalistic rational design, structure-gelation studies, and in situ hydrogelation. *Biomacromolecules* **2017**, *18*, 3581–3590.
193. Balachandra, C.; Govindaraju, T. Cyclic dipeptide-guided aggregation-induced emission of naphthalimide and its application for the detection of phenolic drugs. *J. Org. Chem.* **2020**, *85*, 1525–1536.
194. Shivaprasad, S.; Prathyusha, V.; Priyakumar, U. D.; Govindaraju, T. Solvent-induced helical assembly and reversible chiroptical switching of chiral cyclic-dipeptide-functionalized naphthalenediimides. *Chem. Eur. J.* **2013**, *19*, 16615–16624.
195. Govindaraju, T.; Pandeewar, M.; Jayaramulu, K.; Jaipuria, G.; Atreya, H. S. Spontaneous self-assembly of designed cyclic dipeptide (Phg-Phg) into two-dimensional nano- and mesosheets. *Supramol. Chem.* **2011**, *23*, 487–492.
196. Palmore, G. T. R.; Luo, T.-J. M.; McBride-Wieser, M. T.; Picciotto, E. A.; Reynoso-Paz, C. M. Engineering crystalline architecture with diketopiperazines: an investigation of the strength of hydrogen-bonded tapes based on the cyclic dipeptide of (S)-aspartic acid. *Chem. Mater.* **1999**, *11*, 3315–3328.
197. Chen, Y.; Yang, Y.; Orr, A. A.; Makam, P.; Redko, B.; Haimov, E.; Wang, Y.; Shimon, L. J. W.; Rencus-Lazar, S.; Ju, M. et al. Self-assembled peptide nano-superstructure towards enzyme mimicking hydrolysis. *Angew. Chem. Int. Ed.* **2021**, *60*, 17164–17170.
198. Manchineella, S.; Voshavar, C.; Govindaraju, T. Radical-scavenging antioxidant cyclic dipeptides and silk fibroin biomaterials. *Eur. J. Org. Chem.* **2017**, 4363–4369.

Chapter 2

Injectable Silk Fibroin-based Hydrogel for Sustained Delivery of Insulin in Diabetic Rats

Hypothesis: Diabetes is a chronic disease affecting over 400 million people worldwide. The conventional and last resort of treatment involves repeated subcutaneous insulin injections to maintain physiological glucose homeostasis. The continuous and multiple subcutaneous injections are associated with poor patient compliance and local amyloidosis of insulin, which can be overcome with controlled and sustained insulin delivery. In this context, we have hypothesized and formulated an injectable silk fibroin hydrogel (iSFH) system for sustained insulin delivery over a prolonged period under diabetic conditions.

Diabetes is a metabolic disorder and chronic medical condition that affects blood glucose regulation in the body.¹ Diabetic condition is typically characterized by the elevated physiological blood glucose levels, a major causative factor for severe long-term complications such as eye damage, cardiovascular diseases, chronic kidney dysfunction and neurodegenerative diseases.²⁻⁷ The disease condition arises from the failure of pancreatic β -cells to produce sufficient insulin (type I, T1DM), a peptide hormone that regulates glucose transporter activity and maintained the blood glucose homeostasis.⁸ On the other hand, liver hepatocytes, muscle and adipocyte cells become resistant to insulin (type II, T2DM), hampering the normal mechanism of glycogenesis.⁹ The bi-guanidine drugs are used as a first-line medication for T2DM as they potentially suppress hepatic glucose production and induce the phosphorylation of insulin-sensitive glucose transporter type 4 (GLUT4) enhancer factor to increase the glucose uptake.¹⁰ The sulfonylureas are second-line treatment options, known to decrease gluconeogenesis in liver and insulin clearance from the liver.¹¹ However, T1DM and the advanced stage of T2DM requires external administration (subcutaneous) of insulin once or multiple times a day.¹² The multiple subcutaneous insulin injections are associated with pain, local tissue necrosis, infection, nerve damage and locally concentrated insulin amyloidosis responsible for inability to achieve physiological glucose homeostasis.¹³

In recent times, researchers have focused on the development of self-regulated injectable hydrogel-based insulin delivery systems for continuous delivery of insulin.¹⁴⁻¹⁶ Attractive features of hydrogels such as porous cross-linked three-dimensional network structure, diverse stimuli-responsive chemical compositions and optimum mechano-physical properties have made these soft materials as potential candidates for innumerable biomaterial applications.¹⁷⁻¹⁹ The porous morphology allows encapsulation of various drug molecules within the hydrogel matrix. The encapsulate drugs are subsequently released depending on the diffusion coefficient of drugs and pore size of the gel-network.²⁰ Additionally, the injectable hydrogels have an

advantage of minimally invasive delivery without surgical implantation and infection risk.¹⁶ In this context, silk fibroin (SF) protein extracted from the cocoons of *Bombyx mori* is an excellent choice as a biomaterial owing to its biological origin, biocompatibility, biodegradability, and low immunogenic property. SF, the major structural protein component of cocoon can be processed into fibers, particles, films, sponges, hydrogels and electrospun mats depending on the intended biomaterial application.²¹⁻²⁷ In particular, silk hydrogels are excellent soft material platforms for drug delivery, tissue engineering, and regenerative medicine.²⁸ However, SF takes a relatively longer gelation time (4 days) in aqueous media due to slow conformational transition rate from the random coil to the β -sheet structure and not suitable for the iSFH preparation.²⁹ These drawbacks of SF have been overcome by fine-tuning the interaction between the β -sheet chains using various physical and chemical methods such as vortexing, sonication, pH and electric field or with the help of additives such as surfactant, acids, salts and polymers.³⁰⁻³⁶ The morphological architecture of SF hydrogel is tuneable and potent for materials and biological applications like controlled delivery of bone morphogenetic proteins in tissue engineering among other applications.^{37,38} However, alternation of material properties and maintaining sterile condition are difficult to achieve through reported methods.²⁹

The effective modulation of SF gelation at room temperature using additives ethylene glycol (EG) and triethylene glycol (TEG) to prepare an injectable hydrogel for insulin delivery in diabetic conditions is reported here. Glycols EG and TEG restrict the rotation of β -sheet emerging units in SF and facilitate the conformational transition from the random coil to the β -sheet structure. The additives and SF ratios in the formulation were standardized to ensure quick gelation with the retention of injectable properties. The prepared iSFH was mesoporous in nature and capable of encapsulating the human recombinant insulin without affecting its structural and functional integrity. The subcutaneous injection of iSFH encapsulated insulin (insulin-iSFH) in streptozotocin (STZ) induced T1DM Wistar diabetic

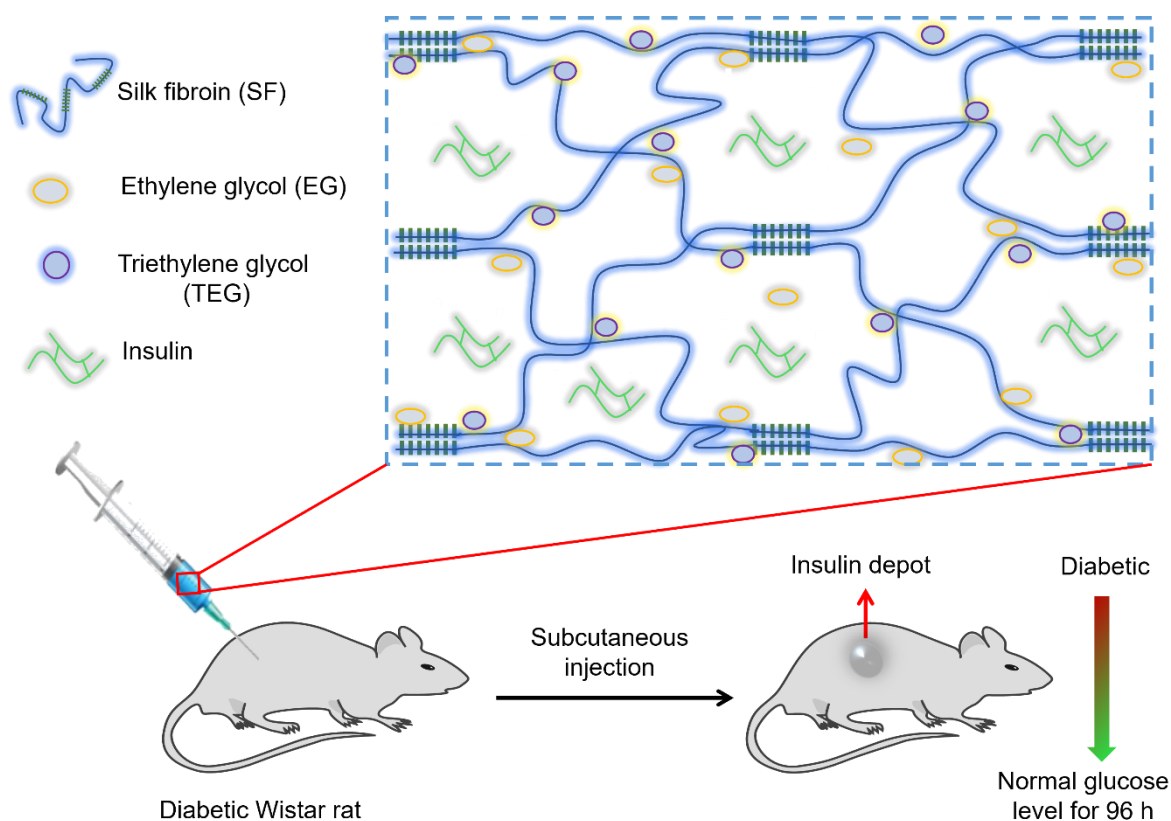


Figure 1. Schematic illustration of iSFH formation with the help of additives ethylene glycol and triethylene glycol (formulation: SF/EG/TEG = 60:20:20).

rats generated active insulin depot under the skin and slowly releases the entrapped insulin and maintained normal glucose level for 4 days under diabetic conditions (Figure 1).

2.1 Preparation and Characterization of iSFH

Injectable hydrogels have attracted much attention and interest as drug delivery tools due to their easy administration without invasive surgical implantation procedures and patient convenience.²¹ The SF undergoes self-assembly and forms hydrogel in 4 days at physiological conditions.³⁴ To prepare an iSFH formulation rapidly, EG and TEG were used as additives with SF protein. The sol to gel transformation was assessed by the vial inversion method at different

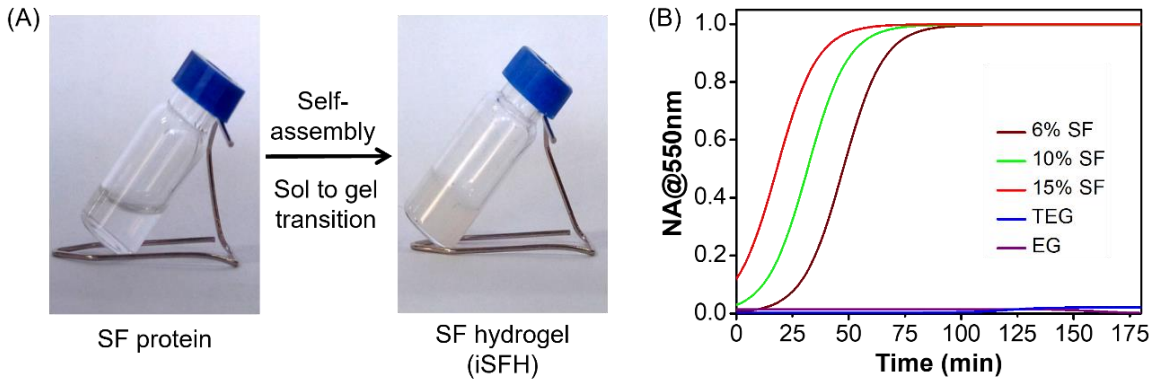


Figure 2. (A) Sol to gel transformation of SF in the presence of additives (EG and TEG) at room temperature. (B) Change in OD at 550 nm during the gelation process in the presence of individual additives (EG and TEG, 40%, v/v) and mixture of 20% EG and 20% TEG with different SF concentrations.

time intervals (Figure 2A). Besides, gelation time also monitored by measuring the optical density (OD) at 550 nm (Figure 2B). Transparent solutions of SF protein and additives individually showed weak absorption at 550 nm. Upon mixing, SF undergo self-assembly in presence of additives to form aggregates which increased the absorption intensity (550 nm)

Silk : EG : TEG ratio(V/V)	Gelation time
100 : 0 : 0	> 4 day
90 : 10 : 0	> 24 h
80 : 20 : 0	> 18 h
70 : 30 : 0	> 15 h
60 : 40 : 0	> 13 h
90 : 0 : 10	4 h 35 min
80 : 0 : 20	4 h 30 min
70 : 0 : 30	3 h 20 min
60 : 0 : 40	2 h 25 min
60 : 30 : 10	2 h 10 min
60 : 20 : 20	50 min
60 : 10 : 30	1 h 45 min

Table 1. Gelation time of 6% SF protein solution with different ratio of TEG and EG.

with time and reached maximum and this saturation is indicative of the complete gel formation (Figure 2B). Further, the concentration of SF and additives were tuned to optimize the gelation process to form iSFH (Table 1). The optimum ratio was found to be 6% SF with 20% (v/v) of each EG and TEG to develop iSFH in 50 min. In contrast, SF (6%) transformed into gel in the presence of individual additives (EG or TEG, 20%, v/v) over a period of 15 h and 4.5 h, respectively (Figure 2B). The glycols (combination of EG and TEG) increased the viscosity of the medium and broke the hydration layers of SF protein, which facilitated the effective collision between the β -sheet emerging units of SF proteins triggering rapid gelation.³⁹ Further, the effect of SF concentration was assessed to optimize the gelation process, and results showed that increasing concentrations of SF (6, 10, and 15%) decreased the gelation time at 50, 32, and 18 min, respectively (Figure 2B). Although higher SF concentration reduced the gelation time, the injectable properties of SFH were compromised due to the hardness of the hydrogel. Finally, the SF, EG, and TEG ratio was successfully optimized to 60:20:20, which effectively forms iSFH within 50 min for further applications.

Next, the morphology of freeze-dried iSFH was evaluated through field emission scanning microscope (FESEM), which displayed a mesoporous structure with elongated pores of 60-200 μm (variable size and shape) surrounded by laminar SF layer (Figure 3). A high magnification

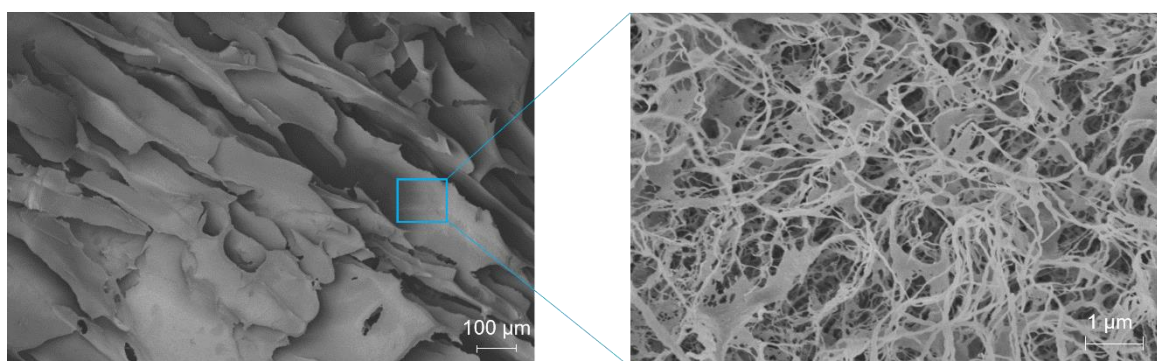


Figure 3. Field Emission scanning electron microscopy (FESEM) image of iSFH, the pores are elongated in shape and surrounded by a layer of SF.

image revealed extremely dense cross-linked fibrous assembly of SF in the laminar layers. The presence of this cross-linked layer is crucial to load the active drug molecules and its sustained release. This satisfied our design strategy and encouraged us to encapsulate drug molecule (insulin) to validate the therapeutic potency.

The secondary structure of SF in the matrix was studied by ATR-FTIR measurements (Figure 4A). The FTIR spectra of SF displayed the characteristic peaks at 1645 and 1512 cm^{-1} , corresponding to amide I and II peaks of random coiled structure. iSFH showed strong peak at 1620 cm^{-1} , which is a characteristic peak for β -sheet. Indicating conformational transformation of SF protein from the random coil to ordered β -sheet structure during the sol to gel transformation (Figure 4A).⁴⁰ In addition, the FTIR spectra of iSFH also showed two weak shoulder peaks at 1650 and 1696 cm^{-1} , which indicated the coexistence of random coil conformation along with β -sheet. The observed conformational transformation was further confirmed by the circular dichroism (CD) studies. SF solution showed a characteristic negative cotton effect at 197 nm, indicating less ordered random coil structure (Figure 4B). Interestingly, SF in

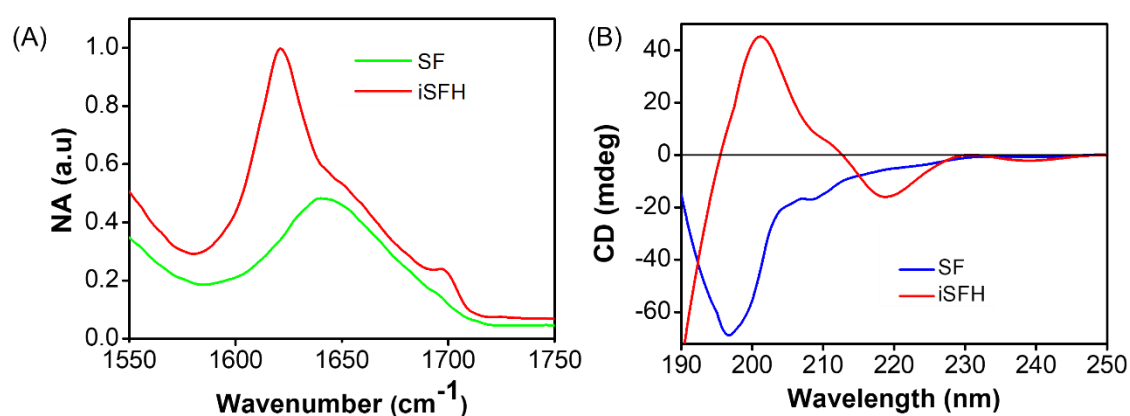


Figure 4. Characterization of the secondary structures of SF before and after gelation. (A) ATR-FTIR analysis of SF and a freeze-dried iSFH sample after washing with water. (B) CD spectra of the SF protein and iSFH. The CD spectra indicate the secondary conformation transformed from random coil to ordered β -sheet structure.

the gelation sample exhibited a characteristic negative cotton effect at 218 nm corresponding to β -sheet conformation while the negative cotton effect at 197 nm disappeared.³⁷ Thus, the conformational transformation of SF from random coil to β -sheet structure and the coexistence of minor random coil with the major β -sheet structure is the driving force for the rapid and injectable gelation property.

Next, the mechanical property of iSFH was investigated using dynamic frequency sweep measurements (Figure 5A). The energy stored in the iSFH (storage modulus, G') was ~ 70 kPa, which is higher than the dissipated energy ~ 12 kPa (loss modulus, G''), as shown in Figure 5A. The higher G' and G'' values indicate highly solid-like behavior inside the gel network. The high storage modulus allowed iSFH to encapsulate the drug molecules inside the pores and aid the controlled release from its matrix. Incorporation of insulin within iSFH matrix increased the storage modulus of the iSFH drastically to ~ 258 kPa. This signifies the cooperative interaction and alignment inside the hydrogel matrix, which enhanced the mechanical properties of iSFH without affecting the SF gelation behaviour. The excellent gelation kinetics and mechanical strength of iSFH reassured us to evaluate its injectable potential and

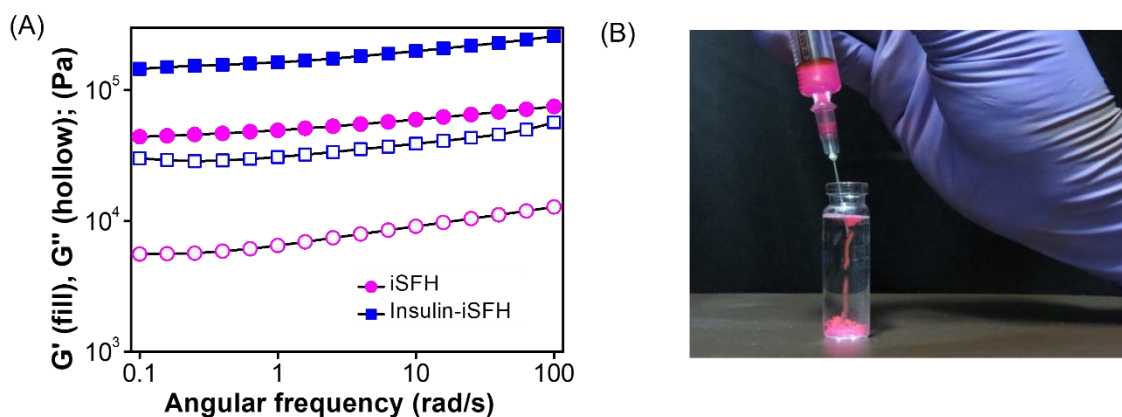


Figure 5. Mechanical properties of the iSFH. (A) Frequency sweep of iSFH and insulin-iSFH shows the storage modulus (G' , lines with solid symbols) and loss modulus (G'' , lines with hollow symbols). (B) Demonstration of the injectable property of 6% iSFH loaded with rhodamine B dye using a 23 G needle.

remarkably, iSFH was found to extrude easily through the 23 G needle (Figure 5B). The faster gelation, excellent mechanical strength, and injectable nature of iSFH make it an excellent drug carrier.

In addition, the swelling behavior influences the drug release from the hydrogel.⁴¹ The swelling ratio of iSFH was investigated in PBS buffer (10 mM, pH = 7.4) at 25 °C and found to reach the equilibrium in 4 h (Figure 6A). The maximum swelling ratio observed was ~41% which remained constant even after 12 h suggesting the possible slow release of the drugs after administration. The lesser swelling ratio and highly cross-linked structure signify its usefulness for the delivery of drug molecules. The interaction of additives and SF in the iSFH matrix was determined by monitoring its release from iSFH. The addition of water to iSFH showed ~23, 60 and 97% release of glycols at time intervals of 1, 6, and 24 h, respectively (Figure 6B). This indicates a weak van der Waals interaction between the glycols and SF protein in the iSFH matrix.⁴²

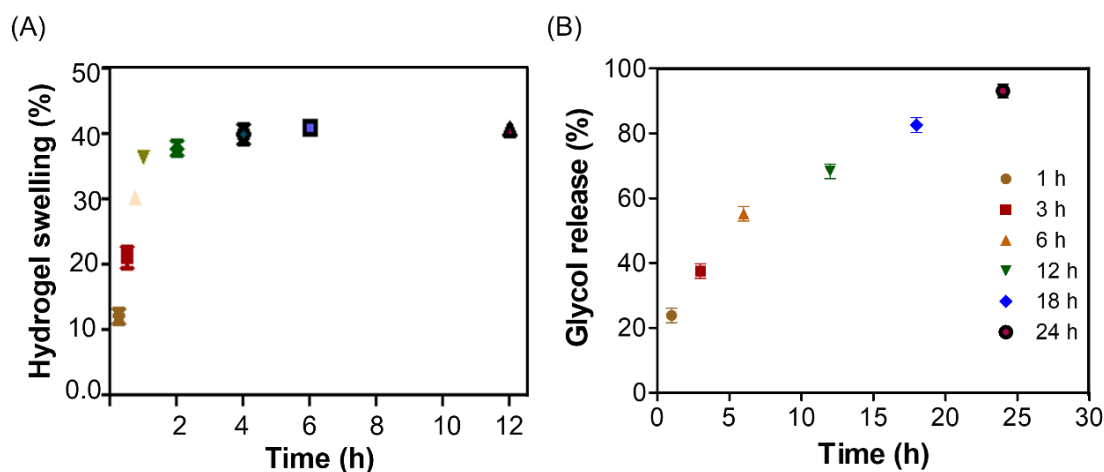


Figure 6. (A) Hydrogel swelling in PBS at 25 °C. The swelling becomes saturated in 4 h. (B) Release profile of the additive glycols from the iSFH with time.

2.2 Encapsulation and Sustained Release of Insulin

The potential of iSFH for the encapsulation and sustained release of insulin was investigated. The insulin was labelled with FITC dye using the previously reported protocols and characterized by MALDI-TOF mass spectrometry.^{43,44} The FITC labelled human recombinant insulin (FITC-insulin) was encapsulated into the iSFH matrix, and its release kinetics was monitored by the absorbance (Figure 7A) and fluorescence (Figure 7B) of FITC. Insulin was added during the SF gelation process to obtain insulin-iSFH. Upon addition of PBS (10 mM, pH = 7.4), insulin-iSFH swollen and slowly released the encapsulated insulin depending on its interaction with the iSFH matrix. As shown in Figure 7C, insulin was released gradually over

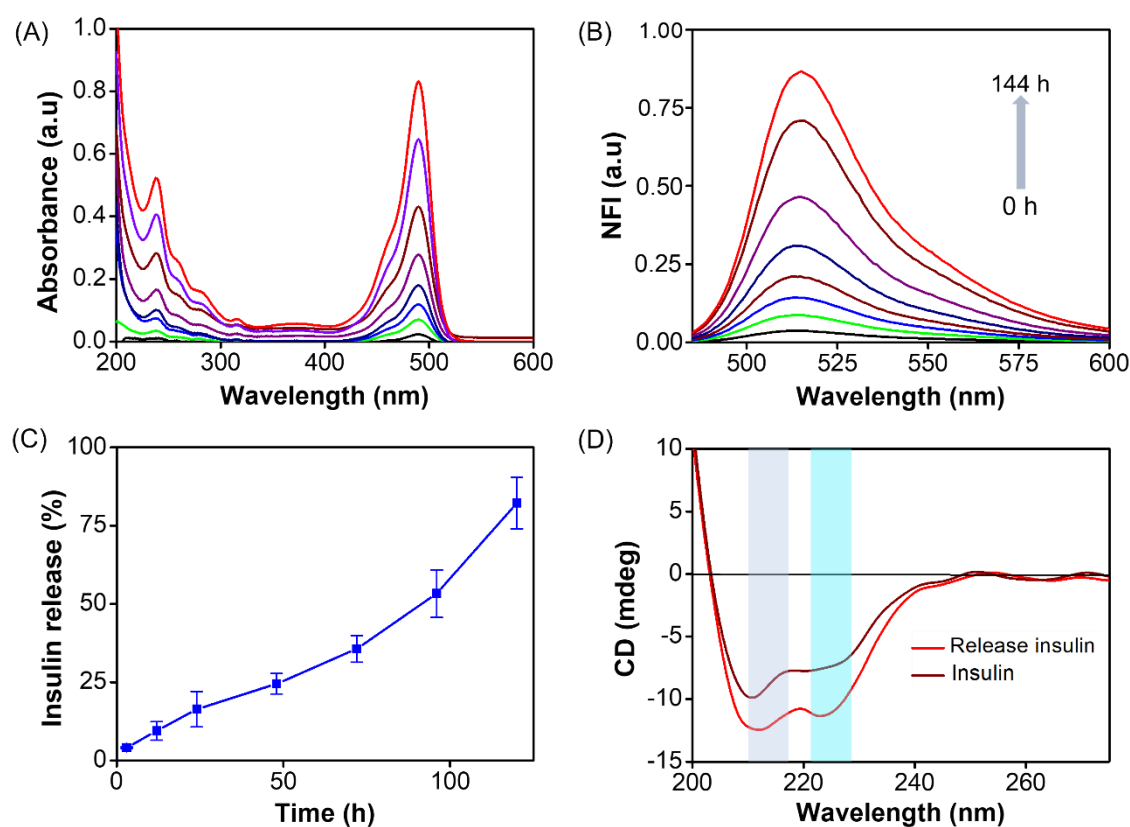


Figure 7. Release of FITC-insulin from iSFH at different time intervals. (A) The absorbance spectra of the released FITC-insulin. (B) The normalized fluorescence spectra of released FITC-insulin released from iSFH at different time intervals. (C) Release percentage of the insulin at different times. (D) Secondary structure of native insulin from iSFH hydrogel.

a period of 5 days from the iSFH matrix. This slow and sustained release of insulin from iSFH is in good agreement with the rheological and swelling properties of iSFH (Figure 5A). This study also signified the controlled release of insulin from the iSFH matrix over a prolonged period (up to 5 days) without the sudden or burst of high insulin release. Such controlled release profile is necessary for long-term insulin delivery under diabetic conditions to maintain the physiological glucose homeostasis. Further, the conformational and structural integrity of the insulin released from the insulin-iSFH matrix was ascertained by the CD measurements (Figure 7D). PBS (10 mM, pH = 7.4) was added to the insulin-iSFH at 37 °C, and CD measurement were performed for the insulin released at different time intervals. The insulin released from iSFH showed two negative cotton effect at 208 and 220 nm (Figure 7D), which are characteristic of α -helical secondary structure of insulin.¹⁵ This result suggests effective functional conformation of released insulin, besides its active storage inside the pores of iSFH. The insulin encapsulation and its slow-release kinetics have showcased the effectiveness of iSFH matrix for the prolonged insulin delivery with implications for diabetes treatment. The cytotoxicity of iSFH in L929 fibroblast cells and human red blood cells was investigated prior to evaluating the efficacy of insulin-iSFH in the animal model.

2.3 Cytotoxicity and Hemolysis Study

The viability of L929 fibroblast cells in the presence of different amounts of iSFH was evaluated according to ISO 10993-5-9-2009 protocol using 3-(4,5-dimethylthiazol-2-yl)-2,5-diphenyltetrazolium bromide (MTT) assay (Figure 8A).²⁵ To assess the cytotoxicity, L929 cells were cultured and treated with iSFH-DMEM extract in 48 well plate for 24, 48 and 72 h under cell growth media. The iSFH-DMEM extract treated cells showed > 93% cell viability (Figure 8A) after 72 h of incubation compared to the control cells (100%). This data indicates high viability of cells presence of iSFH and can be used for *in vivo* animal study. The hemolysis experiment was carried out to assess the cytotoxicity profile of iSFH towards the red blood

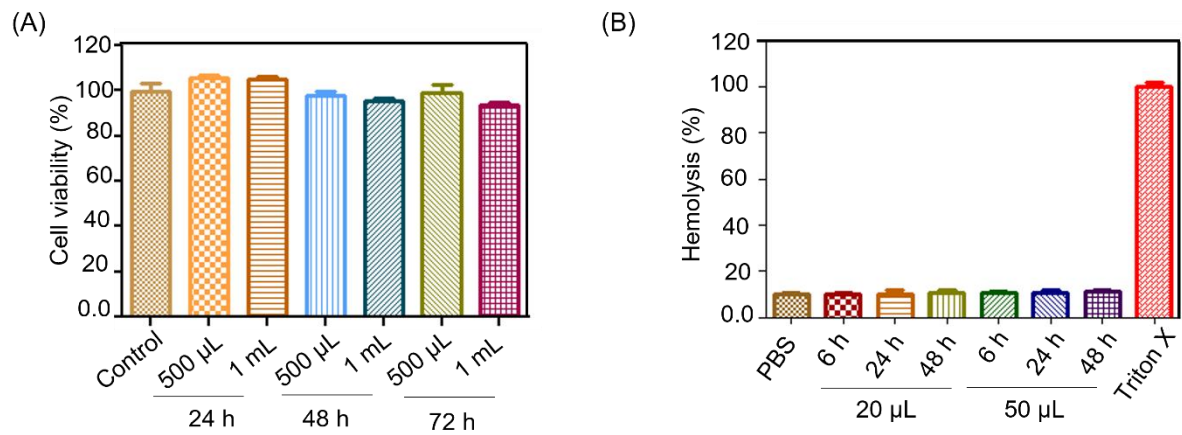


Figure 8. (A) *In vitro* cytotoxicity of iSFH in the mouse fibroblast cell line (L929) at different time of incubations (24, 48, and 72 h). (B) Toxicity profile of iSFH toward human red blood cells. The hemolysis data show that no detectable cell lysis was observed in the presence of iSFH.

cells (Figure 8B). Triton-X was used as a negative control in the experiment, which cause complete red blood cell lysis (100%). However, iSFH or PBS (10 mM, pH = 7.4) treated red blood cells did not show any significant lysis compared to Triton-X (Figure 8B).⁴⁵ These cytotoxicity results confirmed that iSFH is a suitable candidate for insulin delivery in animal model.

2.4 *In vitro* Insulin Functional Activity Assay

Inactivation of insulin function is a major concern. Hence the ability of iSFH to maintain the native structure and activity of insulin under *in vitro* conditions was assessed (Figure 9A). The glucose oxidase enzyme oxidizes glucose to gluconic acid and generates hydrogen peroxide (H_2O_2) in the presence of oxygen (Figure 9B).⁴⁶ Therefore, monitoring H_2O_2 levels by DCFDA correlates with the oxidation of glucose present in the solution. HEK 293T cells were cultured and treated for 24 h with insulin released from iSFH, and the cultured media were collected. The glucose concentration of collected media and fresh media was monitored by using glucose oxidase enzyme followed by DCFDA. As shown in Figure 9C, the glucose concentration of

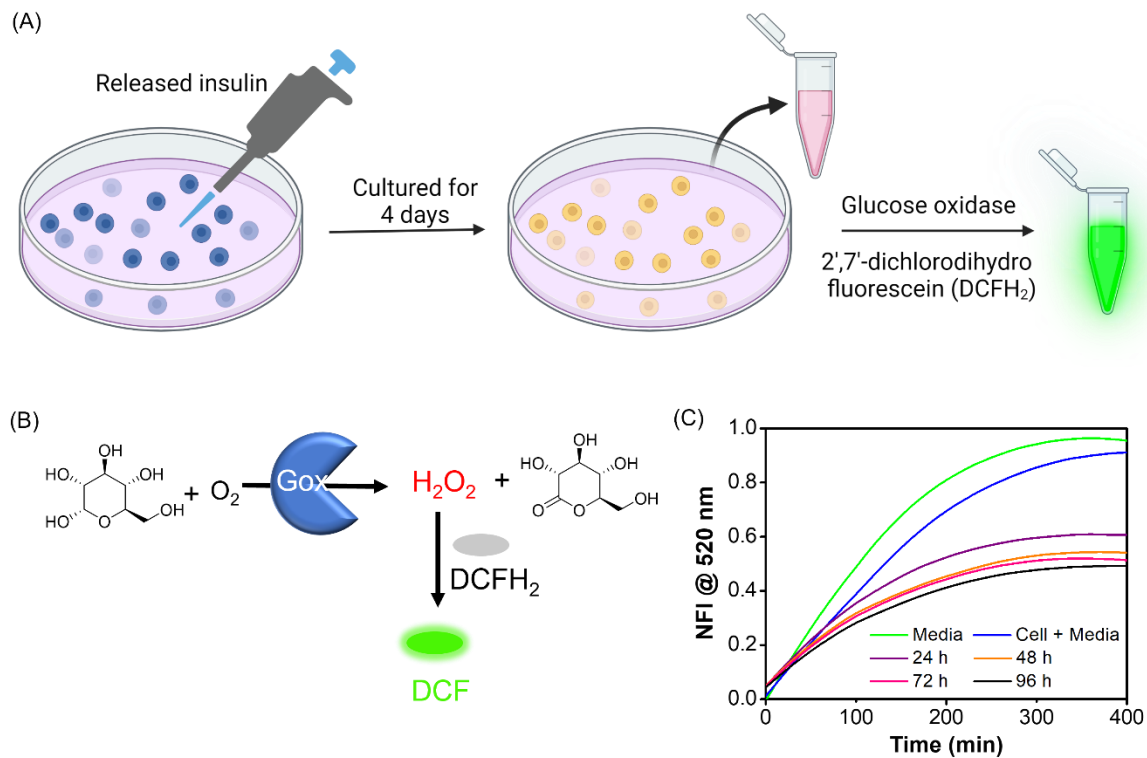


Figure 9. *In vitro* functional activity study of insulin released from insulin-iSFH in HEK 293 T cells. (A) Schematic experimental protocols. (B) Glucose oxidase enzyme's catalytic functional activity and oxidation of DCFH₂ to fluorescence DCF. (C) DCF fluorescence response of the cultured media in controls and insulin treatment after glucose oxidase treatment. All insulin treated samples showed less fluorescence response due to enhanced glucose uptake.

collected cell culture media in insulin-iSFH treated cells at 24 h was found to be lower than the control and untreated cells media. This indicates that high glucose uptake by HEK 293T cells in the presence of active released insulin from insulin-iSFH. These results confirmed that the functional activity of insulin encapsulated within the iSFH pore is preserved and encouraged us to evaluate the *in vivo* delivery and efficacy.

2.5 *In Vivo* Insulin Delivery in Diabetic Rat

The therapeutic efficacy of insulin-iSFH to regulate blood glucose levels under diabetic condition was evaluated in T1DM Wistar rats. The blood glucose level in normal healthy rats

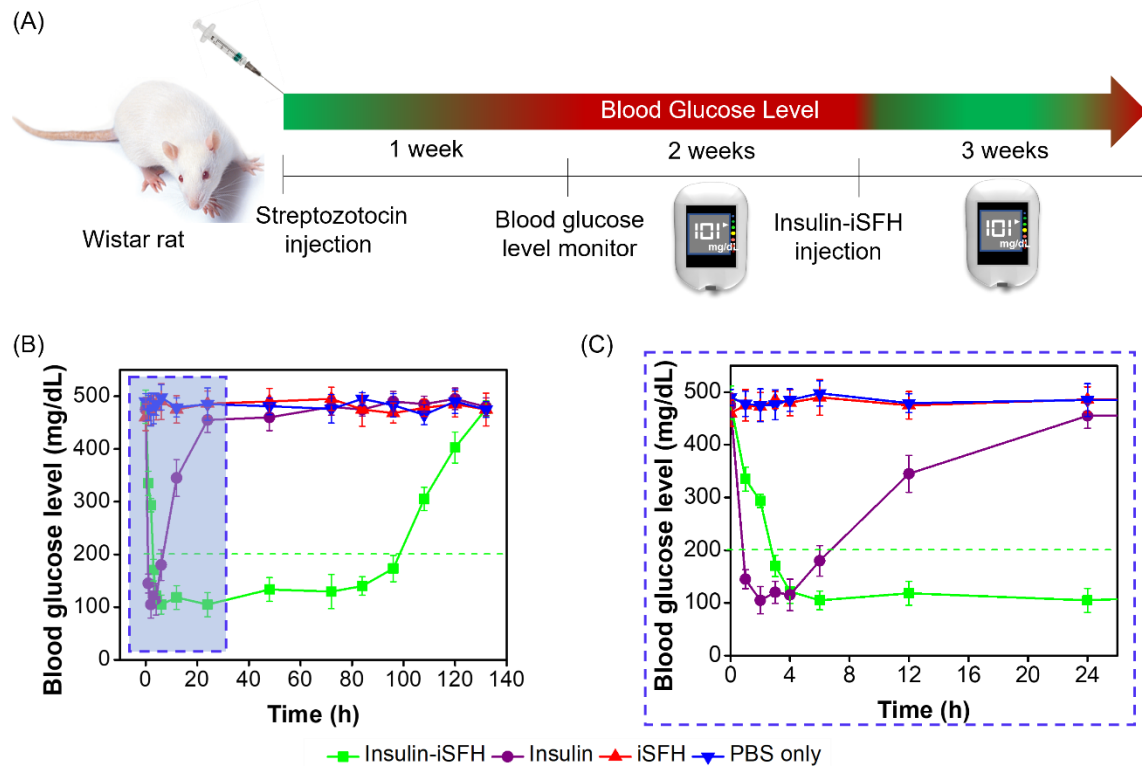


Figure 10. *In vivo* delivery and therapeutic efficacy of insulin-iSFH in the STZ injected Wistar rat model. (A) Creation of a diabetic rat model by injection with STZ, administration of insulin-iSFH, and monitoring the glucose levels at different time intervals (in days/weeks). (B) Blood glucose levels of Wistar rats after subcutaneous injection of free insulin, PBS, iSFH, and insulin-iSFH. Values represent mean \pm SD ($n = 5$ per group). (C) Initial change of blood glucose level after injection, data from (B).

was ~ 140 mg/dL, which elevated significantly and reached > 450 mg/dL after 7 days of intraperitoneal STZ treatment due to specific damage of insulin generating pancreas β -cells (Figure 10A).⁴⁷ Diabetic rats were randomly divided into individual groups and treated with PBS (10 mM), insulin (1 mg/mL), iSFH and insulin-iSFH (insulin dose 20 mg/kg). The blood glucose levels were monitored at different time interval (1, 6 and 12 h) using the ACCU CHEK Instant S glucometer. The blood glucose level of rats treated with PBS and iSFH did not show any significant changes compare to the control diabetic rats (480 mg/dL). The subcutaneous insulin injection reduced the high glucose level to its normal levels (140 mg/dL) for a short duration and expectedly the glucose level rose again after 6 h (Figure 10B).¹⁵ Remarkably,

treatment with insulin-iSFH reduced the glucose level from 480 mg/dL to 150 mg/dL within 3 h of injection without leading to hypoglycemia (Figure 10C), which is a frequently observed and major problem with subcutaneous insulin injection. Subsequently, the blood glucose level was maintained in a normoglycemia condition up to 4 days (Figure 10B). These studies have validated the potential of insulin-iSFH for *in vivo* delivery and controlled release of insulin for prolonged period to effectively manage glucose metabolism in diabetic Wistar rats.

2.6 Conclusion

Injectable SF protein hydrogel (iSFH) has been developed for controlled and sustained delivery of insulin under diabetic conditions. iSFH was standardized with SF (6%) in presence of two viscous additives, EG (20%) and TEG (20%) which transform into an injectable formulation at a faster rate (< 1 h). The viscous glycols restrict the mobility of SF protein backbones and aid the conformational transformation of random coil to ordered β -sheet structure while retaining minor quantity of random coil structure, which together results in the rapid gelation. FESEM analysis of iSFH revealed highly porous microstructures with different sizes surrounded by laminar aggregation of the SF layer. The iSFH microstructures have high mechanical strength and injectable using 23 G needle. The porous morphology of iSFH allowed the encapsulation of human recombinant insulin in its active form. *In vitro* release profiles of FITC-labeled insulin suggested that iSFH is a good delivery tool for sustained insulin delivery (~5 days) into the blood due to lower swelling ratio. Subcutaneous injection of insulin-iSFH in diabetic rats (T1DM Wistar rat) form active depot under the skin from which insulin leach out slowly and restores the physiological glucose homeostasis for a prolonged period of 4 days. Interestingly, the insulin-iSFH did not cause hypoglycemia through sudden burst of a high concentration of insulin into the blood. The excellent mechanical strength, cytocompatibility, encapsulation, storage, and sustained delivery of active insulin in the diabetic animal model

proved our design strategy of iSFH as effective insulin delivery tool and have potential implications for use in diabetic patients.

2.7 Experimental Methods

2.7.1 Materials

The mulberry silkworm *Bombyx mori* cocoons of CB gold variety were purchased from the Ramanagara silk cocoon market, Karnataka, India. Lithium bromide (purity >99%, MW: 86.84 g mol⁻¹), EG (purity > 99%, MW: 62.068 g mol⁻¹) and TEG (purity > 99%, MW: 150.174 g mol⁻¹) were purchased from Spectrochem India. Human recombinant insulin (MW: 5807.57 g mol⁻¹) was obtained from HiMedia (Cas No: 11061-68-0). MTT (3-(4,5-dimethylthiazol-2-yl)-2,5-diphenyltetrazolium bromide) dye (MW: 413.03 g mol⁻¹) was purchased from Merck. Dulbecco's modified eagle medium (DMEM) and fetal bovine serum (FBS) were obtained from ThermoFisher Scientific. L929 and HEK 293 cells were obtained from National Centre for Cell Science, Pune, India. The deionized water used for experiments (resistivity: 18.2 MΩ.cm at 25 °C) was obtained from the Barnstead GenPure water purifier system. High-performance liquid chromatography (Prep-Prominence UFPLC, Shimadzu LC-10A) was used to purify the FITC-labelled insulin, and the purity was monitored by the absorbance study at 215 nm and 495 nm. Matrix-assisted laser desorption ionization (MALDI) mass spectrometry (Autoflex max, Bruker) was used to characterize the integrity of FITC-labelled insulin. Absorbance and fluorescence measurements were performed using Agilent Cary series UV-Vis NIR Spectrophotometer, Agilent Cary Eclipse Fluorescence Spectrophotometer and SpectraMax i3x Microplate Reader (Molecular Devices). Zeiss Gemini SEM 500 was used to characterize the morphology of iSFH. Circular dichroism (CD) spectra of SF, iSFH, and insulin were measured using Jasco-815 Spectropolarimeter (Japan). ATR-FTIR spectra were recorded using

GladiATR, PerkinElmer. The mechanical properties were measured using Physica MCR 101 Rheometer (Anton Paar).

2.7.2 SF Extraction and Purification

SF was extracted from *Bombyx mori* cocoon according to the protocols reported earlier by our group and others.^{18,24} The silkworm was removed, and the cocoon was cut into an appropriate size, washed with water, and boiled for 1 h in 20 mM sodium carbonate solution. During this process, the residual sericin protein was removed. The SF was washed with plenty of water to completely remove the sericin protein and dried to obtain white fibroin fibers. It was then dissolved in 9.3 M lithium bromide as a denaturant at 60 °C for 4 h. The resulting solution was dialyzed using activated 14 kDa cellulose dialysis membrane in Milli-Q water with water changes (for six times) at a regular time interval. The solution was centrifuged to remove residual insoluble fibrous debris and stored in -20 °C or freeze-dried to get the SF powder. The final concentration of SF solution was close to 7% (w/v), which was further diluted with water to get different lower concentrations. A higher concentration of SF solution was prepared by solubilizing lyophilized solid powder in water.

2.7.3 iSFH Preparation

EG and TEG were added to induce a faster gelation of SF and mixed thoroughly at room temperature. For the gelation experiments, stock solutions of SF (6% W/V) in water and variable ratios of EG, TEG (10 - 40%) were mixed in a glass vial at room temperature. The gelation propensity and kinetics were checked by vial inversion procedure and through optical density measurements at 550 nm at 25 °C.

2.7.4 Optical Density (OD) Measurement

The gelation time for SF in water was determined by measuring the change in optical density (OD) at 550 nm due to self-assembling network formation.³⁹ For this, 6% SF solution in water

was mixed thoroughly with varied concentrations of EG and TEG and transferred into 24-well plates. The optical density was measured at 5 min intervals using a microplate reader. The gelation process resulted in the formation of cross-linked structures that can change the light diffraction from the solution, which results the change in optical density. The maximum optical density change was observed at the gelation point due to complete assembly of the SF.

2.7.5 Field Emission Scanning Electron Microscopy (FESEM)

The surface morphology and porosity of the SF hydrogel were analyzed by FESEM (Zeiss GeminiSEM 500) at 3 kV. The hydrogel was washed with water (Milli Q) several times to remove the EG and TEG additives, and the sample was dried through the freeze-drying process. Samples were mounted onto FESEM stubs using double-sided carbon tape, and gold sputtering was carried out on the sample prior to the imaging.

2.7.6 Circular Dichroism (CD) Study

The secondary structure of SF protein was studied by CD measurements. SF stock solutions (10 μL of 6% SF protein) were diluted with 200 μL of water (Milli-Q), and CD spectra were recorded from 300 to 190 nm using 1 mm quartz cuvette in Jasco-815 CD spectrometer (Jasco Co., Japan). For SF hydrogel, the SF solution (600 μL) was mixed with EG (200 μL) and TEG (200 μL). In addition, 20 μL aliquot was mixed with 180 μL of water and quickly transferred into a cuvette. CD spectra were recorded at different time intervals at room temperature.

2.7.7 EG and TEG Release Study

The hydrogel was prepared by mixing 150 μL of SF solution, EG (50 μL) and TEG (50 μL) in 1.5 mL tubes with a known weight. After gelation, the hydrogel was dried at 60 °C for 12 h to remove the residual water, and the weight of dried gel was measured (W_1). The tubes were kept in a glass beaker with water and slowly stirred. At different time intervals, the tubes were taken

out and dried at 60 °C to determine the weight of the dried gel (W_2). The percentage of glycol (EG and TEG) released was calculated as follows: $W_{rel} (\%) = (W_1 - W_2)/W_1 \times 100$

2.7.8 Hydrogel Swelling Study

The swelling property of the hydrogel samples was measured by gravimetric analysis. Dried samples of hydrogels were dipped into PBS, and the samples were removed at different time intervals. The surface water was removed using filter paper. The samples were weighed on an analytical balance. The swelling ratio was calculated from the following equation.

$$\text{Swelling ratio} = \frac{\text{Swollen weight of sample}}{\text{Dry weight of sample}} \times 100$$

2.7.9 Hydrogel Stability Measurement

The mechanical property of hydrogels was investigated using Physica MCR 101 Rheometer (Anton Paar) on a 25 mm parallel plate. Initially, the dynamic strain sweep was carried out to check the range of viscoelasticity. The dynamic frequency sweep was performed at 0.1% strain over a frequency range of 0.1 to 100 Hz at 25 °C. The storage modulus (G') and loss modulus were plotted against the angular frequency (ω).

2.7.10 Hydrogel Injectability

The injectability of hydrogel was investigated by extruding it from the syringe. The optimized SF solution (300 μ L, 6% SF) was mixed with EG (100 μ L) and TEG (100 μ L) and transferred into the syringe with 23 G needle. The hydrogel formulation (500 μ L) was extruded typically by applying pressure with syringe-piston, which confirmed that the entire sample was extruded easily through the 23 G needle.

2.7.11 Attenuated Total Reflectance Fourier-Transform Infrared Spectroscopy (ATR FT-IR)

The secondary structure of SF and iSFH was analyzed using FT-IR spectroscopy with attenuated total reflectance sampling technique. In case of SF, the freeze-dried protein sample was placed on a diamond crystal cell, and measurements were performed. For iSFH, the sample was prepared by freeze-drying after washing the glycols using water.⁴² The measurement was carried out in the wavenumber range 4000-400 cm^{-1} , and the data was plotted as absorbance against wavenumber (cm^{-1}).

2.7.12 FITC Labelling of Insulin

To monitor the drug release from iSFH, insulin was labelled with the fluorescein isothiocyanate (FITC) dye.^{43,44} Human recombinant insulin was dissolved in water, and FITC solution in DMSO was added dropwise under basic condition. The nucleophilic amino groups of insulin react with the isothiocyanate group of FITC. Due to the presence of several amino groups on insulin, different extents of labelling were observed. The mono FITC labelled insulin was purified by UFPLC and characterized by MALDI-TOF mass spectroscopy.

2.7.13 Insulin Encapsulation into iSFH

The porous gel network of iSFH was employed to encapsulate and control the release profile of recombinant human insulin. Insulin or FITC-insulin (50 μL , 1.0 mg) was added to a mixture of SF solution (300 μL), EG (100 μL) TEG (100 μL) and incubated at room temperature for gelation.³⁹ Interestingly, SF solution containing insulin efficiently formed hydrogel, which indicates effective encapsulation. FITC-insulin loaded iSFH (50 μL) was treated with 1 mL of PBS buffer (10 mM, pH = 7.4), and aliquots of 5 μL were removed at different time points. The absorbance and fluorescence spectra were recorded to assess and quantify the released insulin at different time points from the iSFH. Similarly, CD spectra were recorded to assess the native insulin structure released at different time points from the insulin-iSFH.

2.7.14 Cytotoxicity Assay

The cytocompatibility of the iSFH was assessed by measuring the cell viability in L929 fibroblast cell line following the ISO 10993-5-9-2009 protocol and using the MTT assay.²⁵ MTT dye (3-(4,5-dimethylthiazol-2-yl)-2,5-diphenyltetrazolium bromide) reacts with the mitochondrial reductase enzyme in live cells and converts to purple colored (*E,Z*)-5-(4,5-dimethylthiazol-2-yl)-1,3-dimethylformazan. For this assay, 1.5×10^4 cells were cultured in 24-well plate for 24 h using Dulbecco's modified eagle media (DMEM) with 10% fetal bovine serum (FBS) and 1% penicillin-streptomycin (PS). The iSFH was mixed with DMEM media and incubated at 37 °C for 72 h. Aliquot of the media was sterilized through a 0.22 μ m syringe filter to get iSFH-DMEM extract. The culture media of cells was exchanged with an equal volume of complete DMEM and iSFH treated media. The media was changed to complete DMEM at 24, 48, and 72 h of iSFH solution treatment. Cells were treated with 15% MTT solution (stock solution 5 mg/mL) in PBS and incubated for 4 h. The purple-colored formazan crystals were formed depending on the number of viable cells. These purple crystals were dissolved in 200 μ L of methanol: DMSO (1:1), and absorbance was recorded at 595 nm using a microplate reader.

2.7.15 Hemolysis Assay

The suitability of iSFH formulation for *in vivo* experiments was analyzed *via* hemolysis assay with human red blood cells. iSFH (500 μ L) was incubated with 500 μ L PBS solution (10 mM, pH = 7.4) for 72 h and sterilized through the 0.22 μ m syringe filter. The different aliquots of the solution were mixed with 100 μ L blood sample and incubated at 37 °C. The samples collected at different intervals were centrifuged to precipitate the red blood cells.⁴⁵ Triton-100 was used as a positive control, and 10 mM PBS was used as a negative control to check for hemolysis. Triton-100 completely lysed the red blood cells, and hemoglobin was distributed through the solution. The absorbance of the supernatant was recorded at 540 nm to detect lysed hemoglobin in the supernatant.

2.7.16 *In Vitro* Insulin Activity Assay

The preservation of native structure and activity of the encapsulated insulin inside the iSFH was analyzed through *in vitro* functional assay.¹⁴ HEK-293T cells were cultured in 24-well plates at 2×10^4 cell density per well with high glucose-containing media. After 24 h, the released insulin solutions (50 μ L) from insulin-iSFH were added to the cell culture. From this, an aliquot (50 μ L) of culture media was collected and treated with glucose oxidase solution (50 μ L of 1 mg/mL stock in 10 mM PBS to generate gluconic acid and hydrogen peroxide.⁴⁶ The hydrogen peroxide was detected using 2',7'-dichlorofluorescein diacetate (DCFDA, 50 μ M), which was converted into strongly fluorescence 2',7'-dichlorofluorescein in the presence of hydrogen peroxide.²⁵ The fluorescence of 2',7'-dichlorofluorescein was measured at 529 nm using the microplate reader.

2.7.17 *In Vivo* Insulin Delivery into Diabetic Rat

Wistar rats were obtained from JNCASR animal facility, which are maintained under 12 h light and dark cycles. Animal experiments were performed according to the guidelines of the Institutional Animal Ethics committee (IAEC), JNCASR. The protocol (TG 002) was approved by the IAEC and Committee for the Purpose of Control and Supervision of Experiments on Animals (CPCSEA). Experimental group sizes were made based on statistical power, feasibility, and ethical aspect. STZ (70 mg/kg dose) was injected subcutaneously into the Wistar rats once to induce type I diabetes (T1DM).⁴⁷ After STZ injections, blood was collected from rat tail, and glucose level in blood was monitored by using ACCU CHEK instant S glucometer (ISO 15197:2013 certified with 10/10 accuracy). After one week of treatment, rats were confirmed to be diabetic due to the STZ-induced damage of pancreatic beta cells. All the diabetic rats were divided into 4 groups, with each group containing 5 rats. Individual group was administered with insulin, iSFH, and insulin-iSFH (insulin dose, 20 mg/kg). The control

rats were treated with PBS to analyze the blood glucose levels in diabetic and normal conditions. Blood was collected from each rat tail, and glucose levels were monitored over time at regular intervals, initially at every 1 h (for first 6 h) and subsequently at 12 h intervals.

2.8 Appendix

- Animal ethical clearance



जवाहरलाल नेहरु उन्नत वैज्ञानिक अनुसंधान केन्द्र
(मान्यता प्राप्त विश्वविद्यालय)
JAWAHARLAL NEHRU CENTRE FOR ADVANCED SCIENTIFIC RESEARCH
(A Deemed University)
जक्कूर, बेंगलूर - 560 064, भारत / Jakkur, Bengaluru - 560 064. INDIA

CERTIFICATE

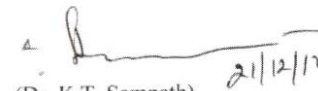
This is to certify that the project titled "Evaluation of drug entrapped hydrogel for wound healing and insulin entrapped hydrogel for insulin delivery in diabetes rat model. (TG 002)" submitted by Dr. Govindraju has been approved by the Institutional Animal Ethics Committee.

Name of Chairman / Member Secretary IAEC
Prof. Anuranjan Anand

Name of CPCSEA Nominee
Dr. K.T.Sampath

Signature with date (21.12.2017)


(Prof. Anuranjan Anand)


(Dr. K.T. Sampath) 21/12/17

2.9 References

1. Zimmet, P.; Alberti, K. G.; Magliano, D. J.; Bennett, P. H. Diabetes mellitus on prevalence and mortality: Facts and fallacies. *Nat. Rev. Endocrinol.* **2016**, *12*, 616–622.
 2. The effect of intensive treatment of diabetes on the development and progression of long-term complications in insulin-dependent diabetes mellitus. The diabetes control and complications trial research group. *N. Engl. J. Med.* **1993**, *329*, 977–986.
 3. Jeganathan, V. S. E.; Wang, J. J.; Wong, T. Y. Ocular associations of diabetes other than diabetic retinopathy. *Diabetes Care* **2008**, *31*, 1905–1912.
 4. Patti, G.; Cavallari, I.; Andreotti, F.; Calabro, P.; Cirillo, P.; Denas, G.; Galli, M.; Golia, E.; Maddaloni, E.; Marcucci, R. et al. Prevention of atherothrombotic events in patients with diabetes mellitus: From antithrombotic therapies to new-generation glucose-lowering drug. *Nat. Rev. Cardiol.* **2019**, *16*, 113–130.
 5. Alicic, R. Z.; Rooney, M. T.; Tuttle, K. R. Diabetic kidney disease challenges, progress, and possibilities. *Clin. J. Am. Soc. Nephrol.* **2017**, *12*, 2032–2045.
 6. Sims-Robinson, C.; Kim, B.; Rosko, A.; Feldman, E. L. How does diabetes accelerate Alzheimer disease pathology? *Nat. Rev. Neurol.* **2010**, *6*, 551–559.
 7. Rajasekhar, K.; Chakrabarti, M.; Govindaraju, T. Function and toxicity of amyloid beta and recent therapeutic interventions targeting amyloid beta in Alzheimer's disease. *Chem. Commun.* **2015**, *51*, 13434–13450.
 8. Owens, D. R.; Zinman, B.; Bolli, G. B. Insulins today and beyond. *Lancet* **2001**, *358*, 739–746.
 9. Pillai, O.; Panchagnula, R. Insulin therapies – past, present and future. *Drug Discov. Today* **2001**, *6*, 1056–1062.
 10. Veiseh, O.; Tang, B. C.; Whitehead, K. A.; Anderson, D. A.; Langer, R. Managing diabetes with nanomedicine: Challenges and opportunities. *Nat. Rev. Drug Discov.* **2015**, *14*, 45–47.
-

11. Coll, R. C.; Robertson, A. A. B.; Chae, J. J.; Higgins, S. C.; Munoz-Planillo, R.; Inerra, M. C.; Vetter, I.; Dungan, L. S.; Monks B. G.; Stutz, A. et al. A small-molecule inhibitor of the NLRP3 inflammasome for the treatment of inflammatory diseases. *Nat. Med.* **2015**, *3*, 248–255.
12. Raskin, P.; Allen, E.; Hollander, P.; Lewin, A.; Gabbay, R. A.; Hu, P.; Bode, B.; Garber, A. Initiating insulin therapy in type 2 Diabetes: A comparison of biphasic and basal insulin analogs. *Diabetes Care* **2005**, *28*, 260–265.
13. Orchard, T. J.; Nathan, D. M.; Zinman, B.; Cleary, P.; Brillon, D.; Backlund, J. Y. C.; Lachin, J. M.; The DCCT/EDIC Research Group. Association between seven years of intensive treatment of type 1 diabetes and long term mortality. *J. Am. Med. Assoc.* **2015**, *313*, 45–53.
14. Matsumoto, A.; Tanaka, M.; Matsumoto, H.; Ochi, K.; Moro-oka, Y.; Kuwata, H.; Yamada, H.; Shirakawa, I.; Miyazawa, T.; Ishii, H. et al. Synthetic "smart gel" provides glucose-responsive insulin delivery in diabetic mice. *Sci. Adv.* **2017**, *3*, eaaq072.
15. Zhao, F.; Wu, D.; Yao, D.; Guo, R.; Wang, W.; Dong, A.; Kong, D.; Zhang, J. An injectable particle-hydrogel hybrid system for glucose-regulatory insulin delivery. *Acta Biomater.* **2017**, *64*, 334–345.
16. Mo, R.; Jiang, T.; Di, J.; Tai, W.; Gu, Z. Emerging micro- and nanotechnology based synthetic approaches for insulin delivery. *Chem. Soc. Rev.* **2014**, *43*, 3595–3629.
17. Brooks, W. L. A.; Sumerlin, B. S. Synthesis and applications of boronic acid containing polymers: From materials to medicine. *Chem. Rev.* **2016**, *116*, 1375–1397.
18. Manchineella, S.; Murugan, N. A.; Govindaraju, T. Cyclic dipeptide-based ambidextrous supergelators: Minimalistic rational design, structure-gelation studies, and in situ hydrogelation. *Biomacromolecules* **2017**, *18*, 3581–3590.
19. Manchineella, S.; Govindaraju, T. Hydrogen bond directed self-assembly of cyclic dipeptide derivatives: Gelation and ordered hierarchical architectures. *RSC Adv.* **2012**, *2*, 5539–5542.

20. Huynh, D. P.; Nguyen, M. K.; Pi, B. S.; Kim, M. S.; Chae, S. Y.; Lee, K. C.; Kim, B. S.; Kim, S. W.; Lee, D. S. Functionalized injectable hydrogels for controlled insulin delivery. *Biomaterials* **2008**, *29*, 2527–2534.
21. Li, Y.; Rodrigues, J.; Tomas, H. Injectable and biodegradable hydrogels: Gelation, biodegradation, and biomedical applications. *Chem. Soc. Rev.* **2012**, *41*, 2193–2221.
22. Datta, L. P.; Manchineella, S.; Govindaraju, T. Biomolecules-derived biomaterials. *Biomaterials* **2020**, *230*, 119633.
23. Manchineella, S.; Govindaraju, T. Stimuli-responsive material inspired drug delivery systems and devices. In *stimuli-responsive drug delivery systems*, Singh, A.; Amiji, M. M. Eds.; RSC Publishing **2018**, 317–334.
24. Rockwood, D. N.; Preda, R. C.; Yucel, T.; Wang, X.; Lovett, M. L.; Kaplan, D. L. Materials fabrication from Bombyx mori silk fibroin. *Nat. Protoc.* **2011**, *6*, 1612–1631.
25. Manchineella, S.; Thirvikraman, G.; Khanum, K. K.; Ramamurthy, P. C.; Basu, B.; Govindaraju, T. Pigmented silk nanofibrous composite for skeletal muscle tissue engineering. *Adv. Healthc. Mater.* **2016**, *5*, 1222–1232.
26. Nune, M.; Manchineella, S.; Govindaraju, T.; Narayan, K. S. Melanin incorporated electroactive and antioxidant silk fibroin nanofibrous scaffolds for nerve tissue engineering. *Mater. Sci. Eng. C* **2019**, *94*, 17–25.
27. Manchineella, S.; Thirvikraman, G.; Basu, B.; Govindaraju, T. Surface-functionalized silk fibroin films as a platform to guide neuron-like differentiation of human mesenchymal stem cells. *ACS Appl. Mater. Interfaces* **2016**, *8*, 22849–22859.
28. Cheng, B.; Yan, Y.; Qi, J.; Deng, L.; Shao, Z. W.; Zhang, K. Q.; Li, B.; Sun, Z.; Li, X. Cooperative assembly of a peptide gelator and silk fibroin afford an injectable hydrogel for tissue engineering. *ACS Appl. Mater. Interfaces* **2018**, *10*, 12474–12484.
-

29. Kim, U. J.; Park, J.; Li, C.; Jin, H. J.; Valluzzi, R.; Kaplan, D. L. Structure and properties of silk hydrogels. *Biomacromolecules* **2004**, *5*, 786–792.
30. Yucel, T.; Cebe, P.; Kaplan, D. L. Vortex-induced injectable silk fibroin hydrogels. *Biophys. J.* **2009**, *97*, 2044–2050.
31. Wang, X.; Kluge, J. A.; Leisk, G. G.; Kaplan, D. L. Sonication-induced gelation of silk fibroin for cell encapsulation. *Biomaterials* **2008**, *29*, 1054–1064.
32. Leisk, G. G.; Lo, T. J.; Yucel, T.; Lu, Q.; Kaplan, D. L. Electrogelation for protein adhesives. *Adv. Mater.* **2010**, *22*, 711–715.
33. Wu, X.; Hou, J.; Li, M.; Wang, J.; Kaplan, D. L.; Lu, S. Sodium dodecyl sulfate-induced rapid gelation of silk fibroin. *Acta Biomater.* **2012**, *8*, 2185–2192.
34. Kim, U. J.; Park, J.; Li, C.; Jin, H. L.; Valluzzi, R.; Kaplan, D. L. Structure and properties of silk hydrogels. *Biomacromolecules* **2004**, *5*, 786–792.
35. Zhong, T.; Deng, C.; Gao, Y.; Chen, M.; Zuo, B. Studies of in situ-forming hydrogels by blending PLA-PEGPLA copolymer with silk fibroin solution. *J. Biomed. Mater. Res. A* **2012**, *100A*, 1983–1989.
36. Matsumoto, A.; Chen, J.; Collette, A. L.; Kim, U. J.; Altman, G. H.; Cebe, P.; Kaplan, D. L. Mechanisms of silk fibroin sol-gel transitions. *J. Phys. Chem. B* **2006**, *110*, 21630–21638.
37. Zhang, W.; Wang, X.; Wang, S.; Zhao, J.; Xu, L.; Zhu, C.; Zeng, D.; Chen, J.; Zhang, Z.; Kaplan, D. L. et al. The use of injectable sonication-induced silk hydrogel for VEGF165 and BMP-2 delivery for elevation of the maxillary sinus floor. *Biomaterials* **2011**, *32*, 9415–9424.
38. Diab, T.; Pritchard, E. M.; Brent, A.; Uhrig, B. A.; Boerckel, J. D.; Kaplan, D. L.; Guldberg, R. E. A silk hydrogel-based delivery system of bone morphogenetic protein for the treatment of large bone defects. *J. Mech. Behav. Biomed. Mater.* **2012**, *11*, 123–131.
39. Xiong, S.-Y.; Cheng, Y.-D.; Liu, Y.; Yan, S.-Q.; Zhang, Q.; Li, M.-Z. Effect of polyalcohol on the gelation time and gel structure of silk fibroin. *J. Fiber Bioeng. Inform.* **2011**, *3*, 236–243.
-

40. Hu, X.; Kaplan, D. L.; Cebe, P. Determining beta-sheet crystallinity in fibrous proteins by thermal analysis and infrared spectroscopy. *Macromolecules* **2006**, *39*, 6161–6170.
41. Liu, J.; Qi, C.; Tao, K.; Zhang, J.; Zhang, J.; Xu, L.; Jiang, X.; Zhang, Y.; Huang, L.; Li, Q. et al. Sericin/dextran injectable hydrogel as an optically trackable drug delivery system for malignant melanoma treatment. *ACS Appl. Mater. Interfaces* **2016**, *8*, 6411–6422.
42. Wang, X.; Partlow, B.; Liu, J.; Zheng, Z.; Su, B.; Wang, Y.; Kaplan, D. L. Injectable silk-polyethylene glycol hydrogels. *Acta Biomater.* **2015**, *12*, 51–61.
43. Jacob, D.; Taylor, M. J.; Tomlins, P.; Sahota, T. S. Synthesis and identification of FITC-Insulin conjugates produced using human insulin and insulin analogues for biomedical applications. *J. Fluoresc.* **2016**, *26*, 617–629.
44. Hentz, N. G.; Richardson, J. M.; Sportsman, J. R.; Daijo, J.; Sittampalam, G. S. Synthesis and characterization of insulin-fluorescein derivatives for bioanalytical applications. *Anal. Chem.* **1997**, *69*, 4994–5000.
45. Dobrovolskaia, M. A.; Clogston, J. D.; Neun, B. W.; Hall, J. B.; Patri, A. K.; McNeil, S. E. Method for analysis of nanoparticle hemolytic properties *in vitro*. *Nano Lett.* **2008**, *8*, 2180–2187.
46. Raba, J.; Mottola, H. A. Glucose oxidase as an analytical reagent. *Crit. Rev. Anal. Chem.* **1995**, *25*, 1–42.
47. Akbarzadeh, A.; Norouzian, D.; Mehrabi, M. R.; Jamshidi, S.; Farhangi, A.; Verdi, A. A.; Mofidian, S. M. A.; Rad, B. L. Induction of diabetes by streptozotocin in rats. *Indian J. Clin. Biochem.* **2007**, *22*, 60–64.

Chapter 3

Glucose Responsive Self-Regulated Injectable Silk Fibroin Hydrogel for Insulin Delivery

Hypothesis: In recent years, stimuli-responsive drug delivery systems have received significant attention owing to their environmental sensitivity and sustained release behavior. Current insulin treatment methods are self-administrational open-loop delivery systems. However, open-loop methods are associated with inaccurate doses, leading to acute and fatal hypoglycemia. Thus, glucose-responsive smart insulin delivery systems are promising in diabetes management. In this chapter, the design of glucose responsive SF system was hypothesized and developed

Stimuli-responsive drug delivery systems have received significant attention owing to their environmental sensitivity and sustained release behavior.^{1,2} Inherent sensing ability of stimuli-responsive systems convert the environmental stimulus into a signal to trigger the alteration of physical or chemical properties of the system. These exciting properties encourage the development of self-regulated intelligent molecular systems for various biological applications.³⁻⁶ In diabetes mellitus (DM), elevated blood glucose level compared to the basal physiological level lead to complications like cardiovascular diseases, renal dysfunction, blindness, and decreased overall quality of life.⁷⁻¹⁰ While several treatment options are available for the diabetes management, insulin therapy remains the last resort of treatment to control blood glucose level. Glycaemic control by insulin treatment effectively suppresses the evolution and escalating health complications.¹¹ Currently, insulin treatment methods are self-administrational open-loop delivery systems. However, open-loop methods are associated with inaccurate doses, leading to acute and fatal hypoglycemia. Therefore, glucose-responsive smart insulin delivery systems are promising in diabetes management.^{12,13} In recent times, several attempts have been made on the design of self-regulated closed-loop delivery systems to deliver more precise amounts of drugs in response to the environment glucose level.^{14,15} Closed-loop systems are integrated delivery modules of glucose-sensing feedback control elements and insulin storage systems, also called the artificial pancreas. There have been continuous research efforts focusing on the development of such closed-looped artificial pancreas systems.¹⁶⁻¹⁹ The glucose sensing elements in closed-loop electronic devices continuously monitor the glucose level, and the integrated infusion pump releases insulin in response to elevated glucose level.²⁰ However, high cost of the devices, complex periodic calibration against standards, discomfort in wearing, and biofouling have limited their applications.^{21,22} Therefore, glucose-responsive chemical approaches encompassing low-cost, bio-compatible, and bio-degradable materials are alternative options.²³⁻²⁶ These materials respond to the environmental glucose alternations and

undergo various structural reorganizations like swelling, shrinkage, dissociation, and degradation to facilitate the tuneable release of encapsulated insulin. The glucose-sensing ability of glucose oxidase (GOx), sugar-binding lectin, and concanavalin A are utilized to bestow the storage system with prerequisite sensitivity.²⁷⁻²⁹

Phenylboronic acid (PBA) and its derivatives are primarily exploited as glucose sensing molecular systems for high glucose sensitivity. The boronic acid group of PBA reversibly binds with the *cis*-diol of glucose and induces hydrophilicity to the network. The chemical conversion leads to matrix swelling or degradation, which aid the sustainable insulin release.³⁰⁻³² The GOx was frequently integrated with boronic ester-containing delivery systems to catalyze glucose oxidation into gluconic acid and H₂O₂.³³⁻³⁶ The generated gluconic acid alter the environment pH, and H₂O₂ reacts with boronic ester matrix. These environmental changes triggered structural rearrangements include matrix degradation, swelling, shrinkage, pore generation, and material dissolution. Therefore, phenylboronic acid and GOx combined systems can be employed to construct glucose-mediated responsive delivery systems. The glucose-sensing elements and drug storage modules are integrated into the same formulation.³⁷ The entrapped glucose-sensing elements can easily leak out after dissociating the drug storage module, limiting the formulations for multi-round sensitivity of glucose fluctuations. The preservation of the functional activity of the drug (insulin) during storage and administration remains a challenge for developing a long-acting closed-loop delivery system.³⁸ Therefore, suitable materials that stabilize glucose-sensing elements and insulin in functional form inside the matrix are highly desirable.

Herein, the fabrication of glucose and H₂O₂ responsive silk fibroin (SF) protein hydrogel (SFBH) was described to deliver a precise dose of insulin for prolonged time. The natural SF protein was utilized as matrix for drug loading owing to its excellent biocompatibility, biodegradability, low immune response, and accessibility. Amino acids side chain of SF were

covalently modified with glucose-responsive phenylboronic acid. Side chain modification directs boronic ester formation between boronic acid and serine residues, brings proximity between the hydrogen bonding sites, and induces rapid gelation. SFBH possesses good mechanical strength and porous morphology suitable for effective drug encapsulation. Hydrogel retains the active conformation of encapsulated glucose-sensing element GOx inside its pore and regulates the enzyme activity in response to the environment glucose level. Hydrogel matrix swells depending on environment glucose concentration and degrades by the generated H₂O₂ via elimination of the boronic ester. The stepwise GOx activity entails hydrogel holds the encapsulated GOx for extended periods, which reiterate its suitability to employ as continuous and live diffusive systems. *In situ* release profile reveals glucose-dependent encapsulated insulin release kinetics from hydrogel matrix at various environmental glucose levels. SFBH exhibited promising pulsatile insulin release kinetics on fluctuation of glucose level. Therefore, the designed glucose-responsive cytocompatible hydrogel acts as a closed-loop artificial pancreas and can be applied for controlled insulin delivery over an extended time.

3.1 Synthesis and Characterization of Phenylboronic Acid Modified SF

SF is a fibrous protein consisting of 5509 amino acids. The major crystalline hydrophobic domains of SF are interspersed with short amorphous hydrophilic domains consisting of functionalizable serine, threonine, aspartic acid, glutamic acid and lysine amino acids. The side chain conjugations of SF with glucose-responsive phenylboronic acid was performed by amide bond formation using N-hydroxy succinimide activated 4-carboxy phenylboronic acid (Figure 1). Modified SF (SFB) readily forms hydrogel (SFBH) in 4 to 6 h at low protein concentration (0.8%). However, the pristine SF at 1-2% concentration forms hydrogel over weeks to months.³⁹

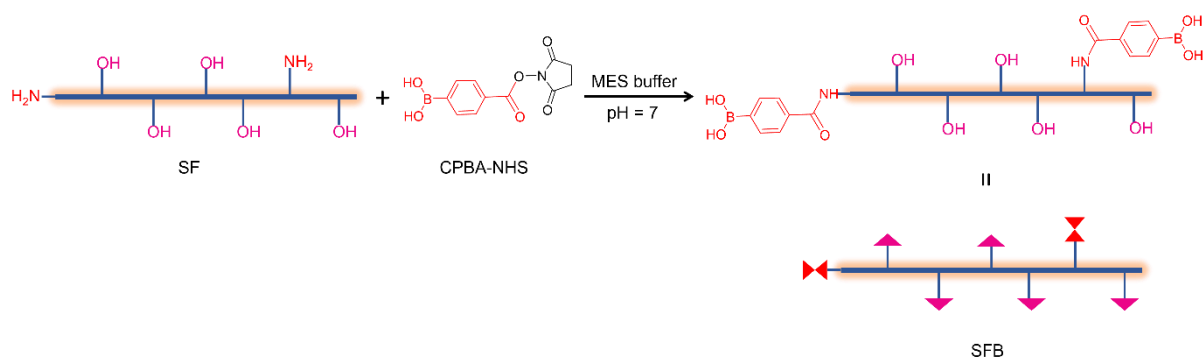


Figure 1. Schematic of SF side-chain functionalization with N-hydroxy succinimide activated 4-carboxy phenylboronic acid

The rapid gelation of SFB is attributed to high affinity of phenylboronic acid with alcohol. The boronic acid modification leads to the formation of boronic ester between the boronic acid and serine residues of SF (Figure 2A). Boronic ester formation amalgamates the β -sheet forming sequences of two different SF chains or terminals of the single protein, accelerating the protein crosslinking and rapid gelation (Figure 2B). The GOx enzyme was subsequently encapsulated inside the hydrogel for glucose-responsive drug release. Integration of the insulin and GOx into the SFB does not alter the gelation process and results in a homogeneous hydrogel (SFBH). GOx facilitates the glucose responsive H_2O_2 generation and dissociation of the boronic ester of hydrogel matrix and release of encapsulated insulin.

Infrared spectroscopy was performed to validate the boronic acid functionalization of SF and its conformational transition during the gelation process. Lyophilized SF has characteristic absorbance peak at 1642 and 1510 cm^{-1} attributed to amide I and amide II stretching in random coil structure (Figure 3A). The SFBH absorbs at 1621 cm^{-1} , indicating the adaptation of β -sheet secondary conformations during the gelation process.^{40,41} However, significant absorbance at 1650 cm^{-1} suggests the coexistence of random coil conformations

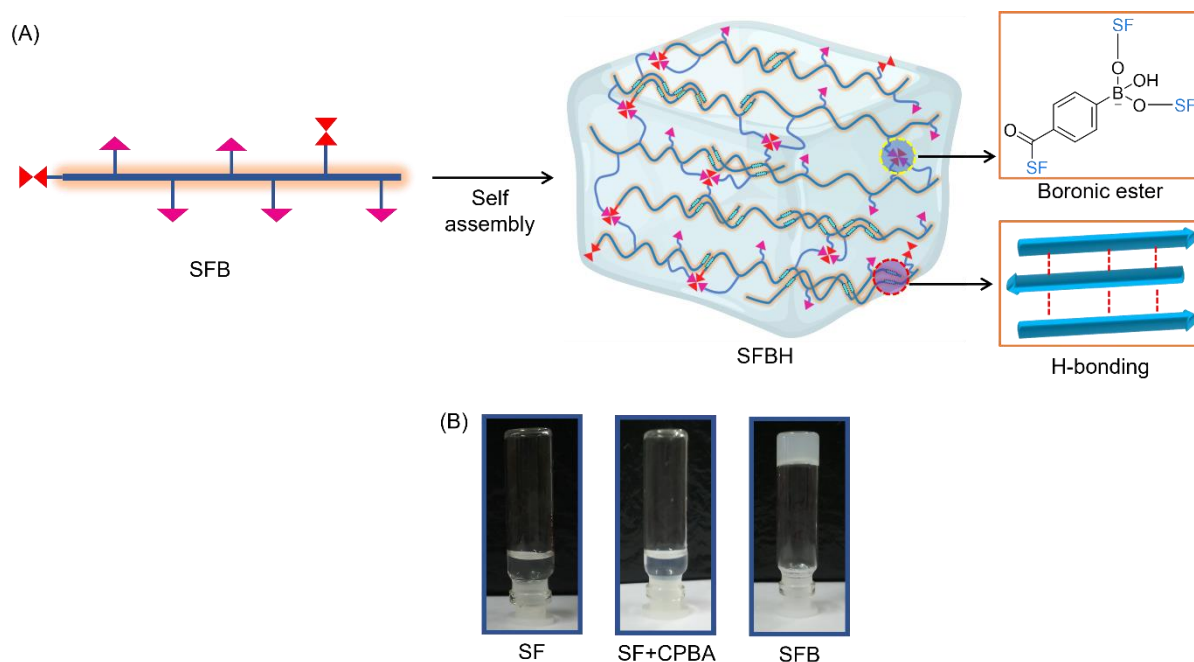


Figure 2. Hydrogel formation (A) SFB assembly through β -sheet formation of protein backbone supported by boronic ester formation between the serine residue side chain and boronic acid. (B) Optical images of inverted vials of SF, physical mixture of SF with CPBA-NHS and SFB after 24 h incubation. SFB form hydrogel, whereas other solution does not form hydrogel.

and β -sheet (Figure 3A). The presence of significance random coil structure might be the effect of side-chain modification, which blocks the transformation of several β -sheet forming units into ordered β -sheet conformations. Further, B-O bond stretching at 1333 cm^{-1} , O-B-O out of plane bending peaks at 770 , 693 , 637 , and 600 cm^{-1} , and in-plane broad stretching of O-B-O bonds indicates the functionalization of SF with boronic acid.^{42,43} The carbonyl stretching of succinic anhydride at 1725 cm^{-1} was absent in SFBH, which confirms the covalent modification of SF by activated PBA. The hydroxyl group stretching of boronic acid at 3380 cm^{-1} was diminished in SFBH due to boronic ester formation (Figure 3B). The β -sheet conformation in SFBH indicates the PBA functionalization retains majority of the H-bonding sites in SF. Thus, covalent modification will not hamper the protein mechanical strength.

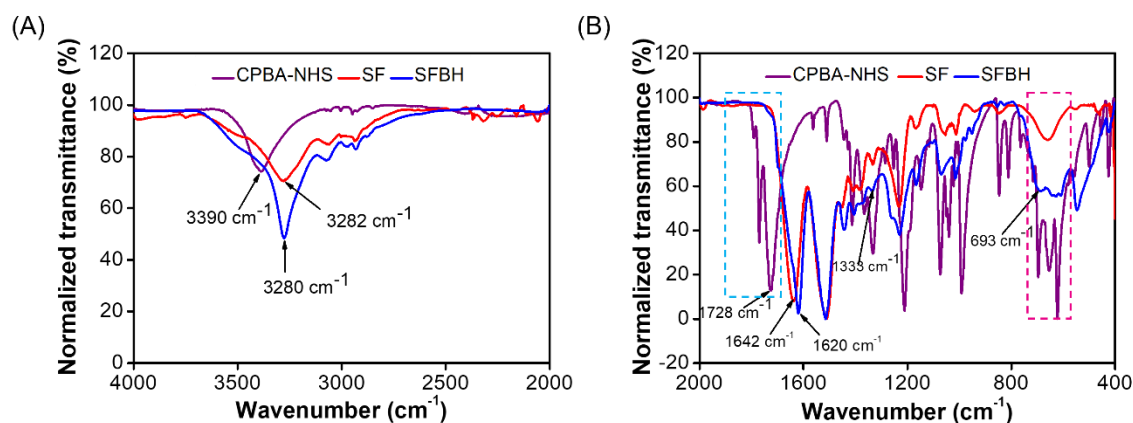


Figure 3. FTIR spectra of CPBA-NHS, SF, and SFBH. (A) FTIR spectral region from 4000 to 2000 cm^{-1} showing N-H and O-H stretching. The O-H stretching of boronic acid was absent in SFBH due to boronic ester formation. (B) FTIR spectra from 2000 to 400 cm^{-1} . The peak at 1333 cm^{-1} and broad peak from 700 to 550 cm^{-1} suggest the boronic acid functionalization in SF. The peak at 1620 cm^{-1} indicates the presence of β -sheet structures in SFBH.

The hydrogel morphology was visualized by field emission scanning electron microscopy (FESEM). FESEM Images show highly porous morphology of hydrogel matrix suitable for substantial amounts of drug encapsulation (Figure 4A). All the pores are surrounded by crosslinked SF aggregate layers. Higher magnification of layers revealed the presence of highly crosslinked SF nanofiber without any significant minor pores in the layers (Figure 4A). The energy dispersive X-ray analysis (EDX) of the scaffold revealed the homogeneous distribution of boron in the hydrogel matrix (Figure 4B). The incorporation of insulin and GOx exhibit similar mesoporous hydrogel scaffolds. Interestingly, significant amounts of closed pores were observed inside the hydrogel matrix, which will be effective for multi-round responsiveness of glucose alternations. The porous and close-packed morphology of the hydrogel indicates significant drug loading capacity inside the hydrogel matrix and sustained release kinetics.

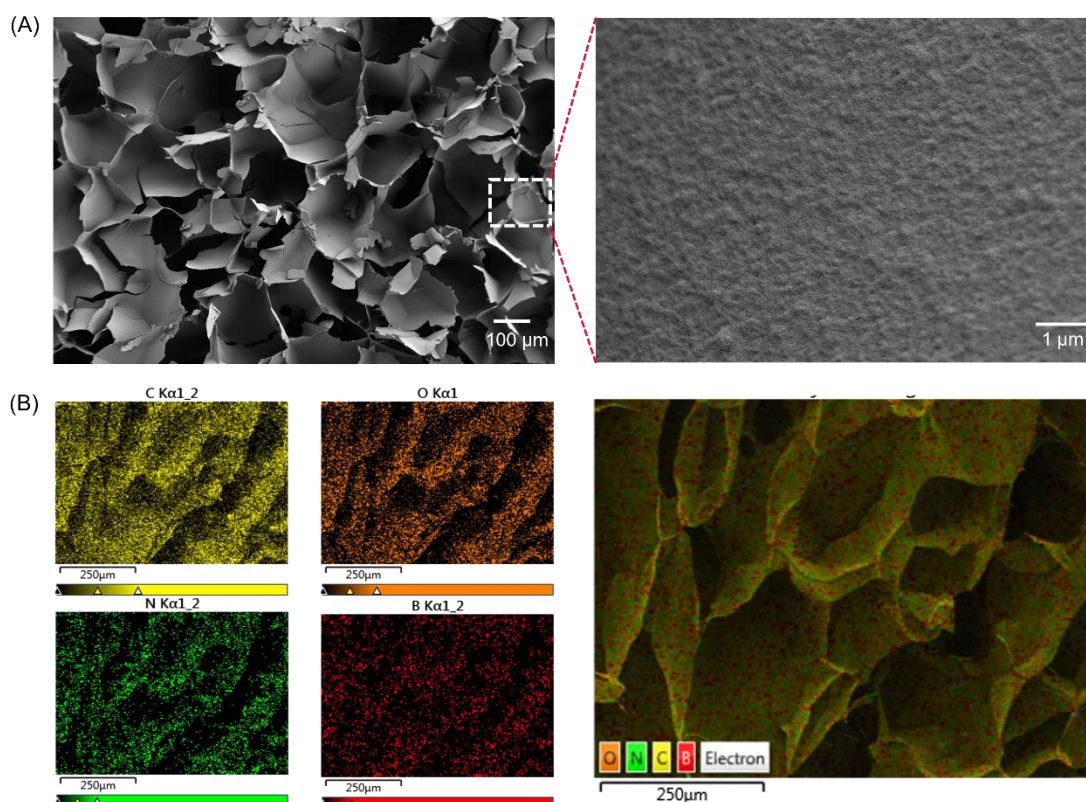


Figure 4. Morphological analysis of SFBH. (A) FESEM image of dried cross-sections of SFBH. Hydrogel has highly porous morphology, and pores are enclosed by aggregation layer of SF aggregates. Higher magnified images of SF aggregation layers show that the layers are made of highly closed-packed SF fibers. (B) EDX elemental analysis of SFBH cross-section. The boron is uniformly distributed throughout the hydrogel matrix.

3.2 Rheological Analysis

The mechanical properties of the hydrogel were analyzed by performing rheological experiments. The dynamic amplitude sweep was measured from oscillation strain of 0.01 to 100% to determine the stability of the hydrogel. Hydrogel maintains a linear range of the storage modulus (G') up to 1.22% shear strain. The increment of shear strain from 1.22% breaks the hydrogel matrix (Figure 5A). Frequency sweep was performed from 0.1 to 100 rad/s at a constant strain of 0.1% to discern the stiffness and viscoelastic properties. Hydrogel has G' of 5.1 kPa, indicating good

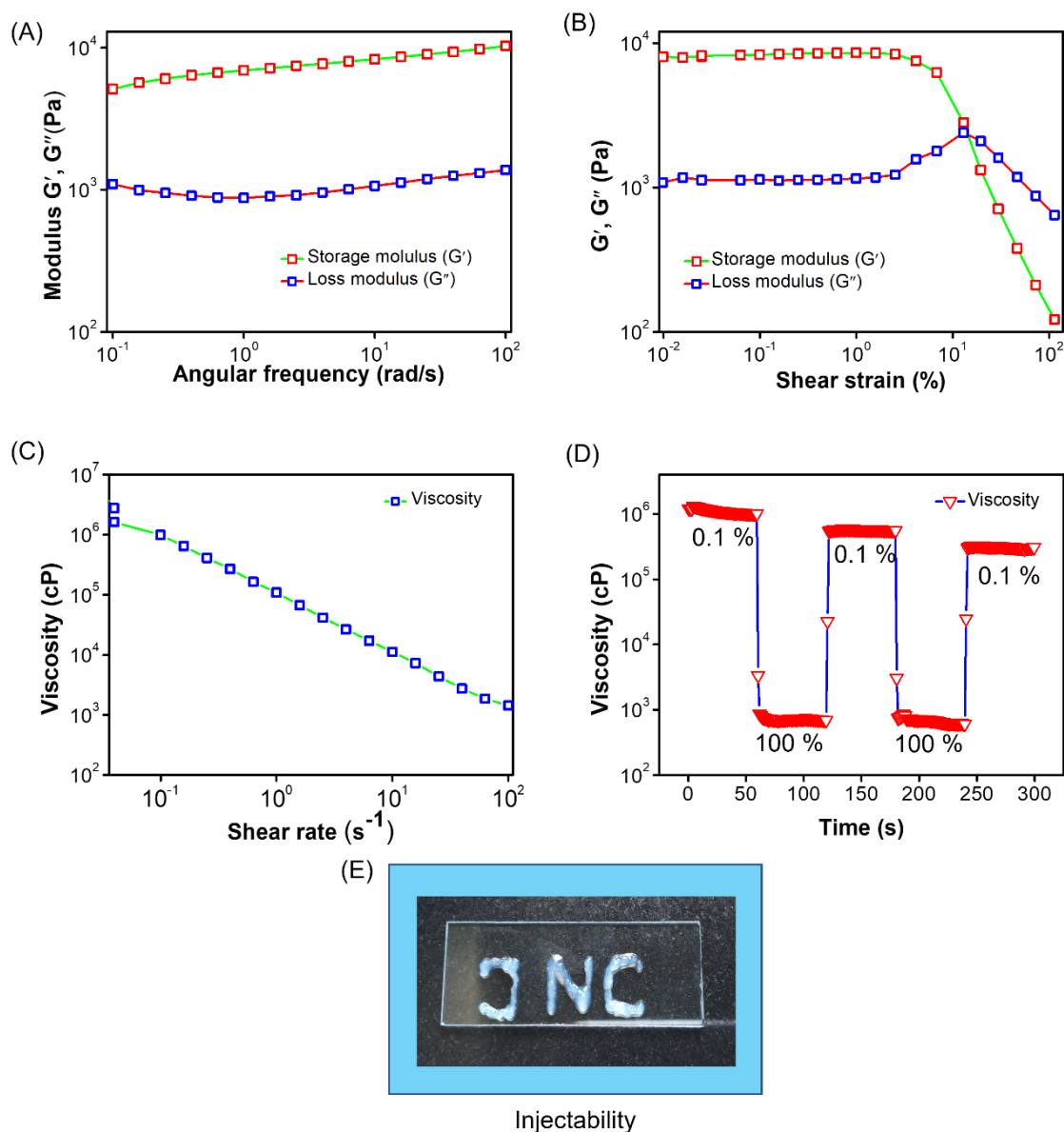


Figure 5. Mechanical properties of SFBH. (A) Frequency sweep from 0.1 to 100 rad/s. The storage modulus of SFBH was higher than the loss modulus. (B) Amplitude sweeps of the hydrogel from shear strain of 0.01-100%. Hydrogel maintained steady storage modulus up to 2.57% of shear strain further increment of the strain breaks the hydrogel matrix. (C) Viscosity at different shear rates of 0.1 to $100 s^{-1}$. Viscosity was declined with rise in shear rate due to the shear-thinning ability of the hydrogel. (D) Viscosity changes with time in alternative shear rates of 0.1% and 100%. The thixotropic hydrogel almost recovered the viscosity to its initial state after strain removal. (E) Injectability of the hydrogel through 25 G needle. SFBH is easily injectable through the needle, indicating the injectable behavior.

mechanical properties attributed to β -sheet structure of SF (Figure 5B). The viscosity of the hydrogel was measured with variable shear rate of 0.015 to 100 s^{-1} . Viscosity was gradually decreased with the increased shear rate due to shear thinning properties of the hydrogel (Figure 5C). Viscosity was measured with alternate low (1 s^{-1}) and high (100 s^{-1}) shear rates to understand the reversibility of the hydrogel to regain the initial gel like structure. Hydrogel viscosity was completely declined at 100 s^{-1} shear rate. It retrieves the viscosity alike to the initial state after shear removal, indicating the injectable behavior (Figure 5D). The hydrogel was injected through 25G needle, and very smooth flow of hydrogel from the needle was observed (Figure 5E). Therefore, this hydrogel can be utilized for delivery of encapsulated drugs without any surgical implantation.^{44, 45}

3.3 Glucose Responsive Studies

The GOx enzymatic activity inside the hydrogel was evaluated to ascertain the utility of the hydrogel system. GOx enzyme oxidizes the β -D-glucose in the presence of oxygen into glucono-1,5-lactone and H_2O_2 . The generated glucono-1,5-lactone hydrolyzed into gluconic acid through non-enzymatic pathways and reduces the pH of the medium (Figure 6A). Thus, pH change of the medium was monitored to determine GOx activity inside the hydrogel matrix with various glucose concentrations. The GOx encapsulated hydrogel was treated with PBS, 1 mg/mL, and 5 mg/mL of glucose solution. The pH of only PBS treated hydrogel sample was not altered with time due to the absence of glucose in the medium (Figure 6B). However, pH of glucose-treated hydrogel gradually decreased with time, and pH change was depending on glucose concentration of the medium. In 1 mg/mL glucose treated samples, pH the solution reached 6.5 and attained saturation. Whereas the hyperglycemic glucose concentration of 5 mg/mL reduced the pH of the solution to \sim 4. These observations confirmed that the hydrogel system preserved the functional activity of the encapsulated GOx inside the pore of hydrogel.⁴⁶ Further, the GOx functional activity inside the hydrogel system was

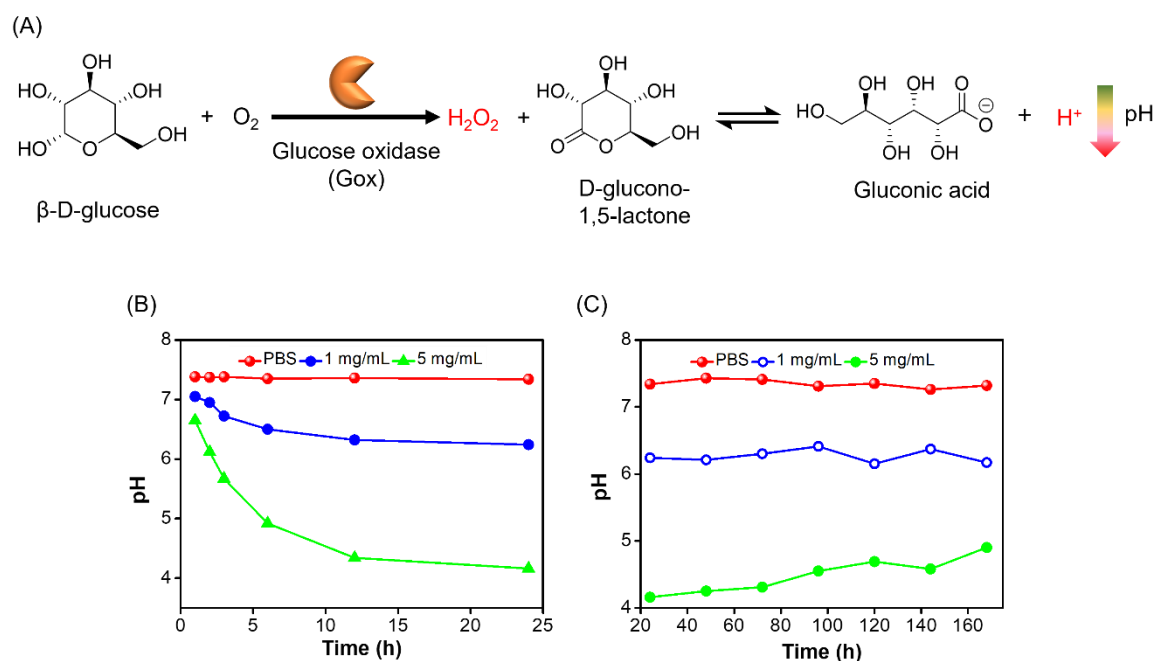


Figure 6. Glucose responsiveness of GOx. (A) Schematic representation of GOx activity on $\beta\text{-D}$ glucose. The glucose converted to D-glucono-1,5-lactone and H_2O_2 . D-glucono-1,5-lactone hydrolyzed through nonenzymatic pathway and declined the medium pH. (B) pH change of the aliquot solution with time in different glucose concentrations. The GOx catalytic activity inside the hydrogel depends on environment glucose levels. (C) Stepwise GOx functional activity over one week inside the hydrogel.

monitored by removal of treated glucose solution with fresh solution in 24 h intervals to understand the enzyme presence and matrix stability after multiple glucose fluctuations. The hydrogel holds the GOx and maintained the steady decline of pH over 7 days (Figure 6C). The catalytic activity slowly declined over a period of 7 days due to the release of GOx from the hydrogel matrix. The prolonged enzymatic activity of hydrogel matrix is indication of slow degradation of the hydrogel matrix and slow diffusion of large GOx from hydrogel pores. Overall, the designed glucose responsive hydrogel SFBH preserves the sensing element GOx for an extended period and effective in prolong insulin delivery.

The glucose responsive nature of SFBH was further determined through the swelling ratio with different glucose concentrations. SFBH xerogel was incubated in PBS, 1 mg/mL, 3

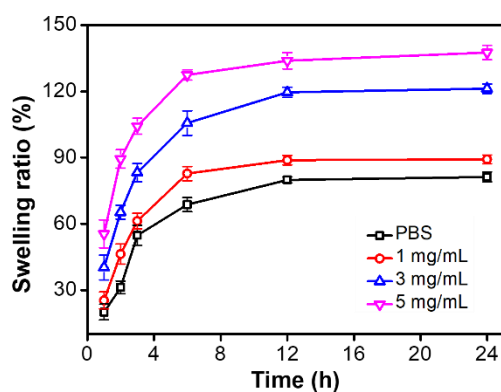


Figure 7. The swelling ratio of SFBH xerogel at different glucose concentrations. The swelling ratio was enhanced with increase in glucose concentrations. A significant change in the swelling ratio was observed between the normoglycemic and hyperglycemic glucose concentrations.

mg/mL, and 5 mg/mL of glucose solution and incubated at 37 °C. All hydrogel samples absorb water from the buffer and swell with time, and equilibrium was established at 12 h of incubation (Figure 7). The SFBH exhibited swelling ratio of 80% in PBS and 134% in the presence of 5 mg/mL of glucose. The swelling ratio of glucose-treated hydrogels is higher compared to the PBS-treated hydrogel, owing to its strong binding affinity with the boronic acid group of the SFBH through five-membered ring formation. Glucose binding release SF serine groups from boronate ester, results in increased hydrogel volume and enhanced swelling.

Next, the environment glucose concentration-dependent insulin release profile from hydrogel matrix was investigated. FITC-insulin was used as a model drug to investigate the insulin release from the hydrogel.⁴⁷ The FITC-insulin added SFBH was found to form hydrogel at identical environmental conditions suggesting effective encapsulation of FITC-insulin inside the pore of hydrogel. The hydrogel was treated with PBS and varying clinically relevant glucose concentrations of 1 mg/mL (normoglycemic condition) and 5 mg/mL glucose (hyperglycemia condition). At 24 h time the insulin release in PBS, 1 mg/mL

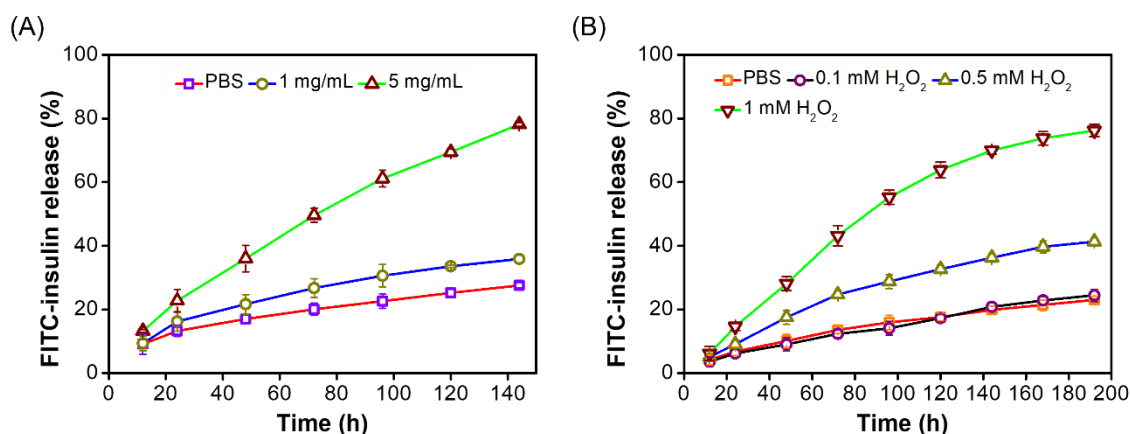


Figure 8. Stimuli responsive insulin release. (A) Glucose responsive FITC-insulin release from SFBH in different glucose concentrations. SFBH releases basal levels of insulin at normoglycemic conditions, but insulin release was significantly enhanced in hyperglycemic glucose levels. (B) H₂O₂ concentration dependent FITC-insulin release kinetics of SFBH. Slow insulin release was observed at 0.1 mM concentration of H₂O₂. Whereas insulin release was maximum at 1 mM H₂O₂ concentration. Which is comparable to the total insulin release at 5 mg/mL glucose concentration.

and 5 mg/mL solutions were 16%, 16.5% and 23% (Figure 8A). Although the FITC-insulin release was comparably high at hyperglycemia, however, not superior because of the osmotic release phase. On PBS treatment hydrogel releases a basal level of insulin. The basal insulin release under normoglycemic conditions is also required in insulin-based therapy to manage certain changes in blood glucose fluctuations.⁴⁸ The insulin release rate was not significant at 1 mg/mL glucose concentration and it similar to the PBS treatment. The release rate was significantly enhanced in response to hyperglycemic glucose level (5 mg/mL). The cumulative insulin release was continuously increased in hyperglycemic conditions, and 78% of the encapsulated insulin releases over six days. The overall insulin release in PBS and 1 mg/mL glucose treated SFBH was 27% and 35%, significantly lower than the hyperglycemic glucose level. This suggests the presence of closed packed SF aggregation layers play major crucial role in controlled release of insulin from hydrogel pores. Higher glucose concentration promotes the total cumulative release of encapsulated insulin. The insulin release rate was

correlated with the glucose-responsive swelling ratio (Figure 7) and GOx triggered pH change inside the hydrogel (Figure 6B). These improved insulin release kinetics of hydrogel in response to glucose concentrations have the potential to deliver more insulin to normalize the enhance blood glucose level.

To determine the role of *in situ* generated H₂O₂ towards the insulin release from the hydrogel, FITC-insulin encapsulated SFBH was treated with PBS, 0.1, 0.5, and 1 mM of H₂O₂ in PBS buffer. As shown in Figure 8B, the insulin release rate was significantly increased in 1 mM H₂O₂ treatment, and 76% of the insulin release was observed over 8 days. GOx catalytic oxidation produces gluconic acid and decreases the pH of the medium. The combined effect of pH and H₂O₂ enhances the total insulin release up to 79% in 7 days. Thus, H₂O₂ produced by catalytic oxidation of the glucose leads to slow degradation of the hydrogel matrix and generates pores in the highly packed crosslinked hydrogel layers. Relatively low molecular weight insulin molecules diffuse from these pores effectively compared to large molecular weight GOx. Thus, H₂O₂-induced degradation of the hydrogel matrix plays key decisive role in the responsive and controlled release of encapsulated insulin.

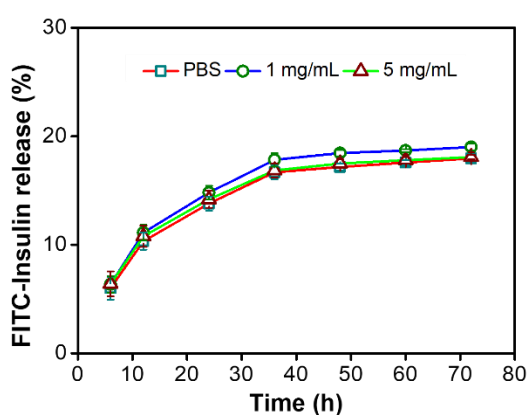


Figure 9. Insulin release from pristine SF hydrogel. The insulin release kinetics was similar in different glucose concentrations.

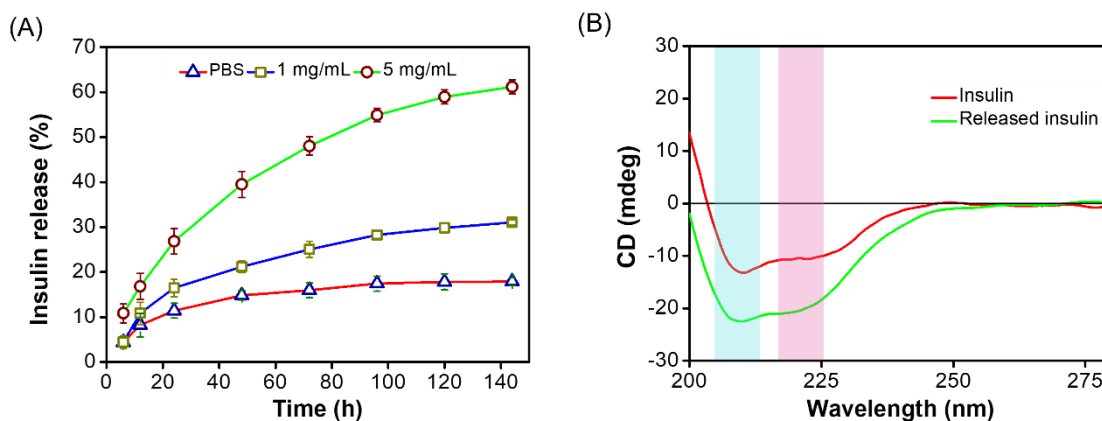


Figure 10. Glucose-dependent insulin release. (A) Insulin release profile at different concentrations of glucose. SFBH shows faster insulin release kinetics at hyperglycemic glucose level of 5 mg/mL than the normal glucose level due to the glucose-responsive ability of the hydrogel. (B) CD spectra of the insulin solution and released insulin from the SFBH matrix. The secondary conformation of released insulin showed identical cotton effect alike insulin.

The insulin release profile of the pristine SF hydrogel (SFH) encapsulated with glucose-sensing element GOx, and insulin was investigated. The SF (2.5% solution) forms hydrogel after one week and showed the glucose concentration dependent GOx activity comparable to the SFBH. However, the insulin release rate in PBS, 1 mg/mL, and 5 mg/mL glucose concentrations remains constant (Figure 9). Thus, the covalent modification of the SF side chain with pendant PBA in SFB imparts glucose responsive behavior and hydrogel release the encapsulated insulin on integration of glucose sensing element GOx. The pristine SFH lacks glucose-responsive functional groups and does not show glucose-responsive drug release. Altogether, these results ascertained that insulin release kinetics was glucose responsive in SFBH.

The insulin release from the hydrogel was further analyzed by Bradford assay. The unmodified insulin release rate was faster compared to the FITC-insulin. At 24 h of incubation, 27% of the insulin release was observed under hyperglycemic conditions, which increases to 60% in 4 days (Figure 10A). The secondary structure of the released insulin from the hydrogel matrix

was ascertained by CD spectroscopy analysis. The released insulin showed negative cotton effect at 222 and 209 nm which are identical to the native insulin (Figure 10B). Thus, SFBH effectively preserved the functional secondary conformation of encapsulated insulin inside its pores.

The insulin secretion from the pancreatic β -cells follow the pulsatile release pattern in both animals and humans.^{49,50} The changes in membrane potential of β -cells coupled with the variation of glucose concentration in blood stimulate or downregulate insulin secretion. The enhanced blood glucose levels facilitate the glucose transport to the electrically excitable β -cells by GLUT1 and GLUT3 glucose transporter. The glucokinase present in β -cells phosphorylate the glucose into glucose phosphate. Through metabolic cycle, glucose phosphate

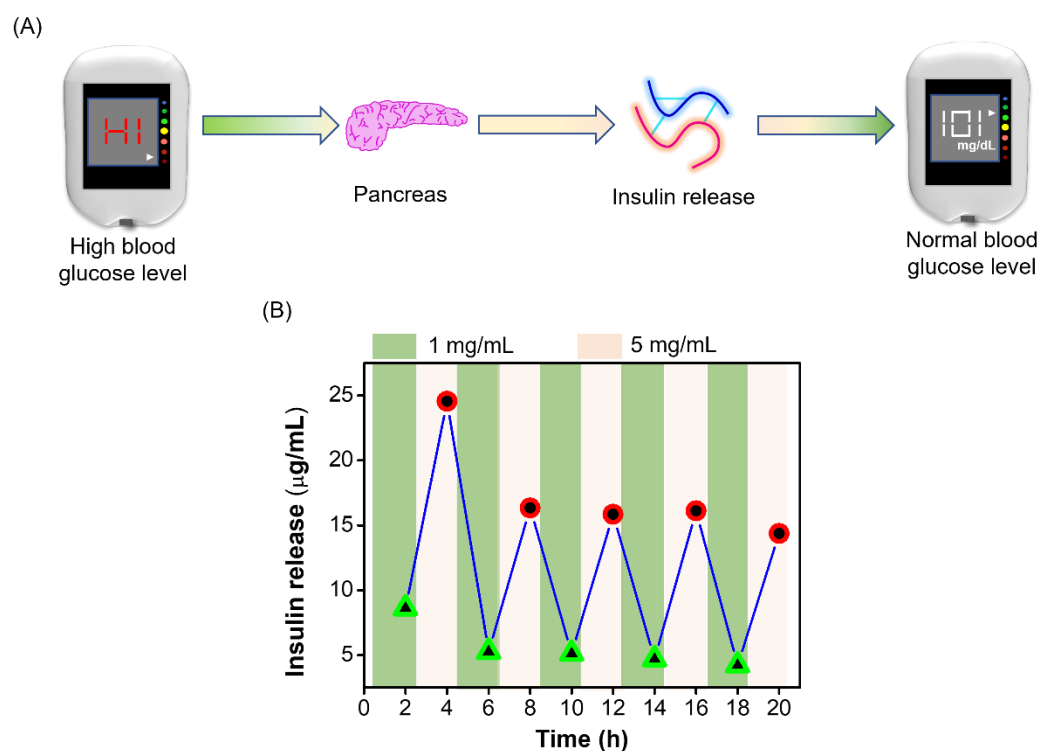


Figure 11. Pulsatile insulin release. (A) schematic of insulin release behavior of pancreas on the fluctuation of glucose concentration inside the body after food uptake. The enhanced glucose concentration after food uptake stimulates the β -cells of the pancreas and promotes insulin secretion. (B) Released insulin on altering the glucose level from 1 mg/mL to 5 mg/mL. SFBH maintains pulsatile insulin release kinetics in multiple cycles of glucose alternation.

produces ATP and excites the membrane K^+ channel. This generates high Ca^{2+} concentration impulse inside the β -cells and triggers the exocytosis release of the insulin granules. The lower glucose concentration inhibits the insulin secretion from β -cells. Mimicking the pulsatile mechanism of the β -cells in synthetic materials holds clinical importance (Figure 11A). A major advantage of periodic release compared to the continuous hormone release minimizes the risk of hypoglycemia and provides the long-term release behavior of the encapsulated insulin. Therefore, we have investigated the insulin release profile on alternation of the glucose concentration from 5 mg/mL to 1 mg/mL to understand the pulsive release ability of the hydrogel. The insulin release was significantly decreased on reduction of glucose concentration to 1 mg/mL compared to 5 mg/mL, and this pattern was observed in multiple cycles (Figure 11B). Thus, SFBH acts as an artificial pancreas to deliver more insulin in hyperglycemia compared to the normoglycemic conditions.

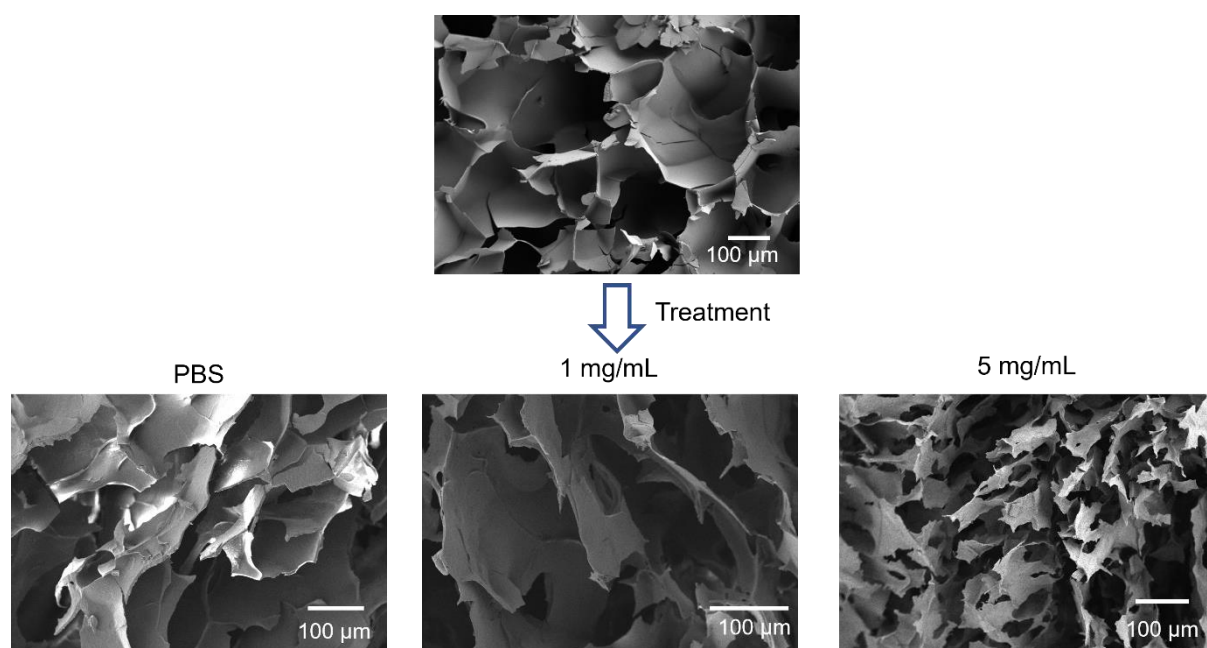


Figure 12. Morphological analysis of hydrogel after 7 days of treatment. The aggregation layers of the SF were almost intact after PBS treatment. Few pores were observed in the matrix layer of the hydrogel in 1 mg/mL glucose treatment. Matrix layers become completely fragile after 5 mg/mL glucose treatment.

The structural morphology and mechanical strength of SFBH after various treatments were analyzed through FESEM and rheological studies. PBS treatment over 7 days did not alter the structural morphology of matrix layers, suggesting good hydrogel stability. Considerable pores were observed in matrix layers upon 1 mg/mL glucose treatment. The hydrogel becomes completely fragile, and various pores are observed in hydrogel layers on 5 mg/mL glucose treatment (Figure 12), indicating the degradation of the matrix by H_2O_2 . Further, the mechanical strength of hydrogel after glucose treatment was investigated through frequency sweep measurement at 0.1% constant strain. The mechanical strength of the hydrogel was decreased from 5.1 kPa to 1.48 kPa after seven days of treatment with 1 mg/mL of glucose (Figure 13). In hyperglycemic conditions, the storage modulus reached 0.3 kPa, due to the major collapse of the hydrogel matrix by the H_2O_2 degradation.

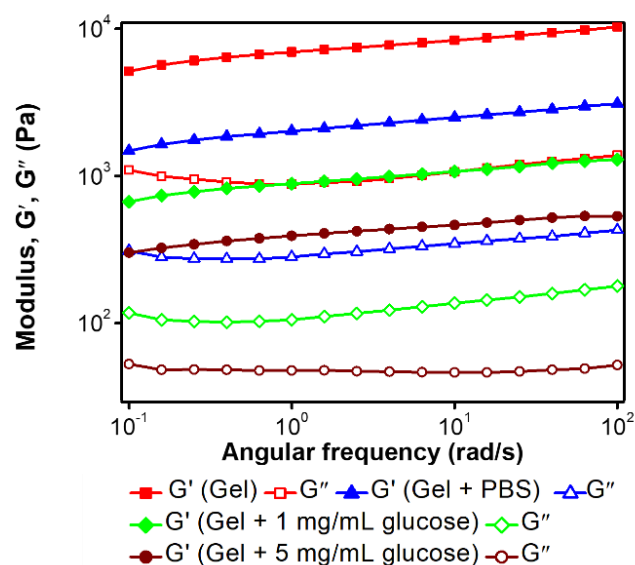


Figure 13. Rheological analysis of SFBH after 7 days of treatment with PBS, 1 mg/mL, and 5 mg/mL of glucose concentration. The storage modulus declined after one week of treatments. Reduction of storage modulus was maximum for the 5 mg/mL of the glucose treatment.

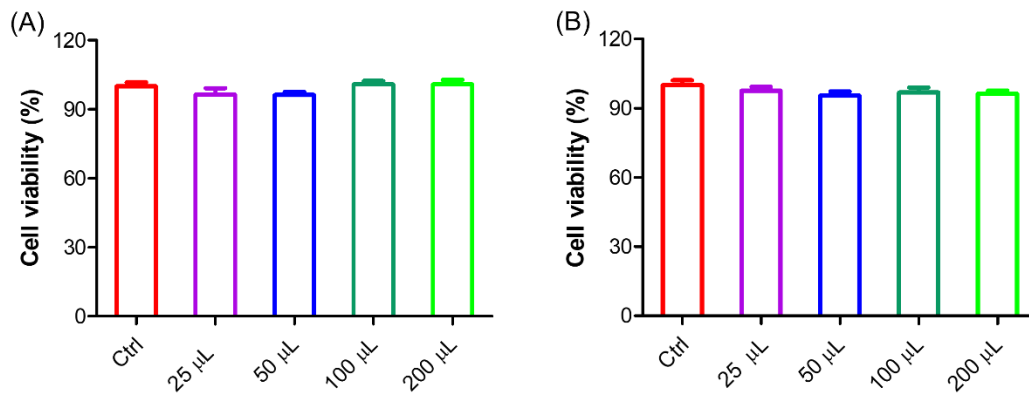


Figure 14. *In vitro* cell viability of the L929 fibroblast cells. (A) cell viability after treatment of the different amounts of only SFBH solution. (B) cell viability after treatment with GOx encapsulated SFBH. Cell viability remains more than 94%, which indicate relatively non-toxic nature of the hydrogel.

3.4 Cytocompatibility and Hemolysis

For the applicability of any delivery tools in living system, it is essential to address the biocompatibility. To evaluate the cytocompatibility of SFBH, viability of L929 fibroblast cells in the presence of different amounts of hydrogel solution was carried out using MTT assay. Cells were cultured in 48 well plates, treated with varying amounts of the hydrogel extract, and cultured for 24, 48, and 72 h. No significant change in the cell viability was observed even

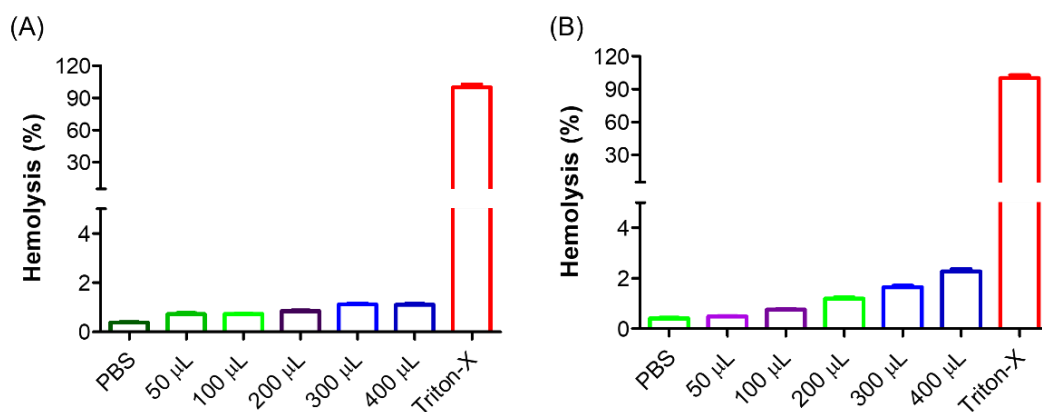


Figure 15. Hemolysis propensity of SFBH. (A) The percentage of human red blood cells hemolysis with different amounts of SFBH solution. (B) Hemolysis percentage in the presence of GOx encapsulated SFBH.

after 72 h of incubation with hydrogel extract and in all cases, cell viability remains > 94% (Figure 14A, Figure 14B). Therefore, the hydrogel system is cytocompatible and can be used for *in vivo* insulin delivery applications. For application of SFBH in animal models, the hemolysis assay was performed with human red blood cells. Triton-X-100 was used as positive control for the experiment, which is known to lyse the red blood cells, and PBS was used as negative control. The hemolysis percentage shows only 1.11% lysis of the red blood cells even at 200 μ L of hydrogel solution (Figure 15A). Although a slight increment of hemolysis (2.27%) was observed in SFBH encapsulated with the GOx enzyme (Figure 15B), it is considered within the acceptable limit for applications. The hemolysis results showed SFBH has low hemolytic proclivity and can be utilized for further insulin delivery and blood glucose level monitoring.

3.5 Conclusion

Glucose-responsive injectable SF hydrogel (SFBH) was fabricated through covalent modifications of reactive amino acid residues of SF with phenylboronic acid. The doped pendant phenylboronic acid reacts with abundant serine side chain to form boronic ester between two protein units and accelerates the crosslinking through β -sheet formation. The modified SF has the propensity to form hydrogel at low protein concentration (0.8%). The SFBH showed good mechanical strength and injectable through 25-gauge needle. Encapsulated GOx displays environmental glucose responsive functional activity inside the hydrogel. Hydrogel releases basal levels of insulin at normoglycemia conditions, but release was significantly enhanced in response to hyperglycemia. The *in vitro* studies confirm the cytocompatibility and low hemolytic behavior. Therefore, self-regulated glucose-sensing elements containing SFBH act as the artificial pancreas to deliver the encapsulated insulin to environmental demands. Further studies on biocompatibility, *in vivo* evaluation of insulin release pharmacokinetics and glucose level control in animal models are required, which will be pursued in near future. Overall, the cytocompatible, stimuli response and cost effective

SFBH may potentially be useful in the controlled release of insulin for the effective treatment and management of diabetes.

3.6 Experimental Methods

3.6.1 SF Extraction and Purification

Extraction of the SF from the cocoon was performed following the previously reported protocol by our group and others. Briefly, cocoons are separated from silkworm and boiled for 1 h in 20 mM sodium carbonate solution to remove the additive sericin protein. The fibroin fibre was washed and dried at room temperature to get dried protein. The protein fibre was mixed with 9.3 M of LiBr and kept at 60 °C for 4 h to denature the fibre and transform it into solution. The resulting solution was dialyzed against distilled water for 3 days with water exchange in 12 h intervals to remove the salt. Dialysed solution was centrifuged to remove the debris and give the 6% (w/v) protein solution. Extracted protein was stored at -20 °C until further use.

3.6.2 CPBA-NHS Preparation

Activated N-hydroxy succinimide ester of the carboxy phenylboronic acid was prepared by following the previously reported protocols. Briefly, carboxy phenylboronic acid (1g, 6.02 mmol) was dissolved in 20 mL of dimethylformamide (DMF) under ice-cold conditions and 2.5 mL of N,N-diisopropylethylamine (1.95 g, 2.5 mL, 15.05 mmol) was added. N-ethyl-N'-(3-dimethylaminopropyl) carbodiimide hydrochloride (1.7 g, 9.03 mmol) was then added to the solution and stirred for 30 min. N-hydroxy succinimide (1.04 g, 9.03 mmol) was added to the solution, and the reaction mixture was stirred for 24 h. DMF was evaporated under vacuum, redissolved in dichloromethane (DCM), and washed with 0.1 N HCl solution (3×100 mL). The product was collected in DCM layer. Column was performed in Methanol/DCM solvent system, product was eluted at 5:95 Methanol/DCM and gives crystalline solid at 71% yield. ¹H-NMR (400 MHz, DMSO-*d*₆) δ 2.90 (m, 4H), 8.00 (m, 4H), 8.44 (s, 2H). ¹³C-NMR (100

MHz, DMSO-*d*6) δ_{ppm} 25.3, 125.5, 128.6, 134.7, 161.9, 170.2. HRMS (ESI-MS): found 262.0298, calculated for $\text{C}_{11}\text{H}_9\text{BNO}_6$ $[\text{M}-\text{H}]^-$ $m/z = 262.0528$.

3.6.3 Boronic Acid Modification of SF

4 mL of 6% SF was added dropwise in 6 mL of 0.1 M of MES buffer at 4 °C with constant stirring. CPBA-NHS (40mg in 1 mL DMSO) was drop wisely added to the fibroin solution. The pH of the solution was adjusted to pH 7 by using 1 M of sodium bicarbonate. The reaction was stirred for 6 h at room temperature. Unreacted CPBA-NHS was removed through dialysis once in 2% DMSO/water followed by water in 6 h intervals. The dialyzed solution was centrifuged at 4 °C to remove debris present in the solution. Phenylboronic acid modified SF solution (SFB) was kept at 37 °C for gelation. Gelation was monitored by vial inversion procedure. The solution was mixed with 100 μL of GOx (10 mg/mL) solution to make glucose responsive drug release system.

3.6.4 Attenuated Total Reflectance-Fourier Transform Infrared Spectroscopy

Ligation of SF with phenylboronic acid was checked by the FTIR spectroscopy studies. Hydrogel was dried through freeze-drying process and placed on a diamond crystal cell and measurement was carried out in wavenumber range of 4000-400 cm^{-1} . The spectra of SF and CPBA-NHS were also performed similarly, data were plotted as transmittance vs wavenumber (cm^{-1}).

3.6.5 Morphological Analysis

The structural morphology of the SFBH was visualized using field emission scanning electron microscopy (Zeiss Gemini SEM 500). Hydrogel samples were frozen slowly at -80 °C freeze to form the ice crystal and further froze using liquid nitrogen and dried using lyophilizer. The hydrogel cross section was made by using the surgical blade and mounted into the carbon tape. Elemental analysis was performed to confirm boron doping.

3.6.6 Glucose Responsiveness of Hydrogel

The glucose responsiveness properties of the hydrogel were checked through the pH change of the medium after glucose treatment. The hydrogel was treated with phosphate buffer saline (PBS, pH = 7.4), 1 mg/mL, 5 mg/mL glucose solution in PBS. Every 24 h, the aliquots were removed, and the fresh glucose solution was added to the hydrogel. The pH of the aliquots was measured to check the gluconic acid release from the catalytic consumption of the glucose by encapsulated GOx.

3.6.7 Swelling Ratio

SFBH was dried by vacuum to get the xerogel. The xerogel was dipped into the PBS, 1 mg/mL, 3 mg/mL, 5 mg/mL of glucose solutions. At different time intervals, the hydrogels were taken out and surface-bound water was removed by wiping through the tissue paper and weight of the hydrogel was measured. The swelling ratio was calculated by using the following equation

$$\text{Swelling ratio} = \frac{W_s - W_d}{W_d}$$

Where W_s is the swollen mass of the xerogel and W_d is the initial weight of the dried xerogel.

3.6.8 Rheological Analysis

The rheological behavior of the hydrogels was performed on Physica MCR 101 Rheometer with a 25 mm parallel plate at 25 °C. Frequency sweep and strain sweep were performed to check the mechanical strength and viscoelasticity. Frequency sweep was tested in a constant strain of 0.1% over 0.1 to 100 Hz frequency range. Amplitude sweep was performed from 0.1% to 100% strain at a constant frequency of 6.28 rad/s. Viscosity of the hydrogel was measured with change of the shear rate from 0.1 to 100 s⁻¹. Further, viscosity of the hydrogel system was monitored by applying alternative small oscillation force ($\gamma = 1\%$ strain) and large one ($\gamma = 100\%$ strain).

3.6.9 FITC-Insulin Release Profile

The encapsulation and release profile of encapsulated drug (insulin) from hydrogel system was further carried out. FITC-insulin (100 μ L, 1 mg) and GOx (100 μ L, 1 mg) were mixed with the 800 μ L of SFB solution and kept at 37 °C to form the hydrogel in 5 mL glass vials. The hydrogel was treated with 2mL of PBS, 1 mg/mL, and 5 mg/mL of glucose solution in PBS and incubated at 37 °C incubators with constant shaking. The aliquot was removed at different time intervals and replaced with fresh glucose solutions. The absorbance of the aliquots was measured in Cary series spectrometer and plotted with times.

3.6.10 H₂O₂ Responsive Release

SFB solution was mixed with 100 μ L of FITC-insulin and incubated at 37 °C for gelation in 5 mL glass vials. The hydrogel was treated with PBS, 1 mM, 5 mM, 10 mM of H₂O₂, and 10 mM of H₂O₂ in acetate buffer pH 5, incubated at 37°C with constant shaking. At different time intervals, aliquots were removed, and gels were filled with fresh buffer solutions. The absorbance of the released insulin was measured in Cary series spectrometer and cumulative release was plotted against time.

3.6.11 Insulin Release Study

Further human recombinant insulin was encapsulated, and glucose responsive release was performed. Insulin (100 μ L, 1 mg) and GOx (100 μ L, 1 mg) were mixed with the 800 μ L of SFB solution and kept at 37 °C to form the hydrogel in 5 mL glass vials. The hydrogel was treated with PBS, 1 mg/mL, and 5 mg/mL of glucose solution in PBS and incubated at 37 °C incubators with constant shaking. The aliquot was removed at different time intervals and replaced with fresh buffer and glucose solutions. The amount of insulin released was quantified by the Bradford assay. Only PBS-treated samples were subtracted during quantification of each

sample. CD spectroscopy was performed to check the structural conformation of the released insulin from the hydrogel matrix.

3.6.12 Glucose Responsive Morphology Change and Mechanical Strength

The morphology of the hydrogel after glucose treatments was analyzed by the FESEM. Hydrogels after 7 days of treatments were frozen and lyophilized to get dried hydrogel scaffold, cut by the surgical blade, and mounted into the carbon tap. The images were captured after gold sputting. The mechanical strength of the treated hydrogels was checked by rheological experiments. Frequency sweep was performed from 0.1 to 100 Hz frequency range at 0.1% constant strain to check the storage modulus and loss modulus of the hydrogel.

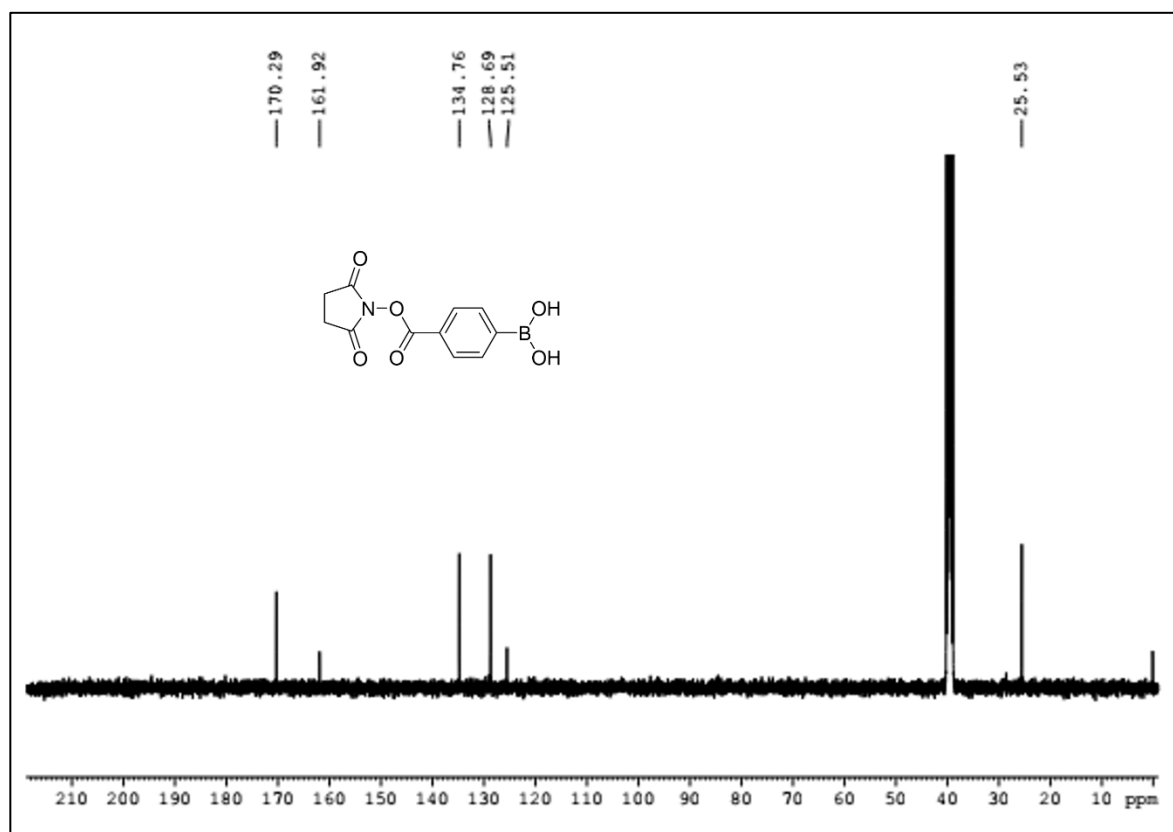
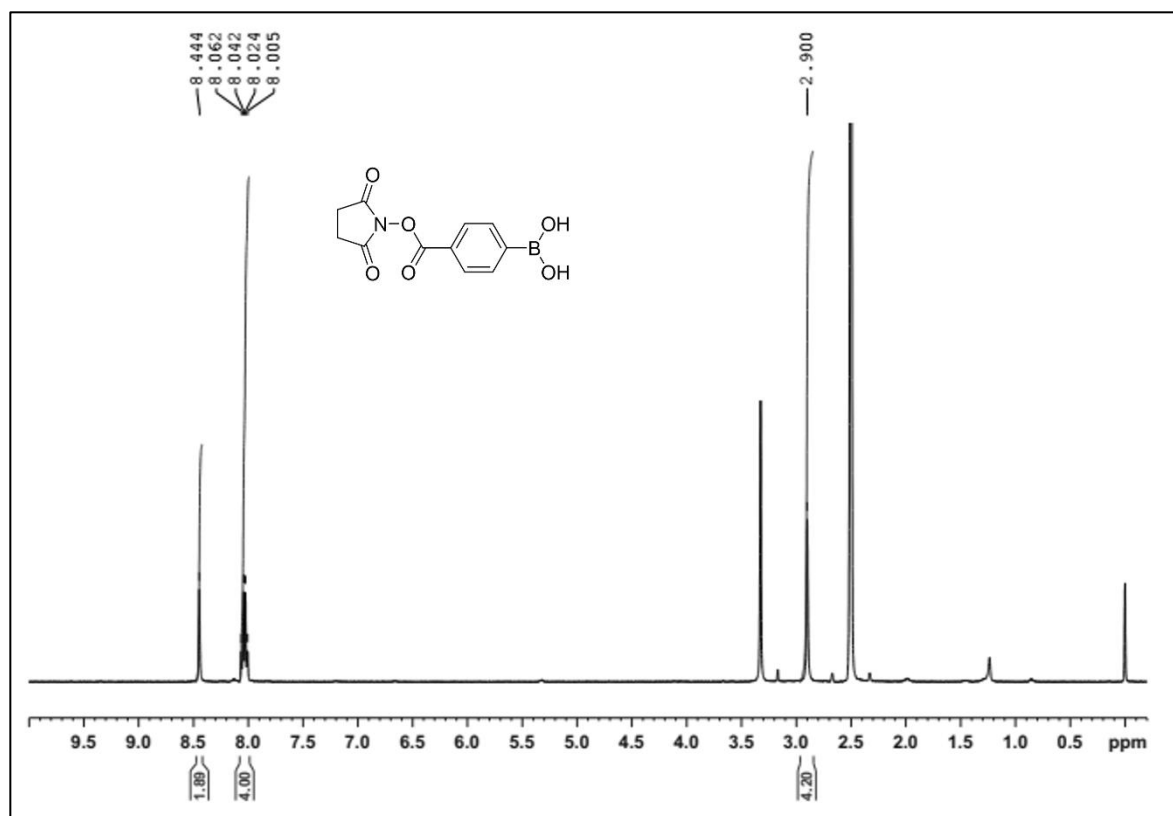
3.6.13 Cytotoxicity and Hemolytic Assay

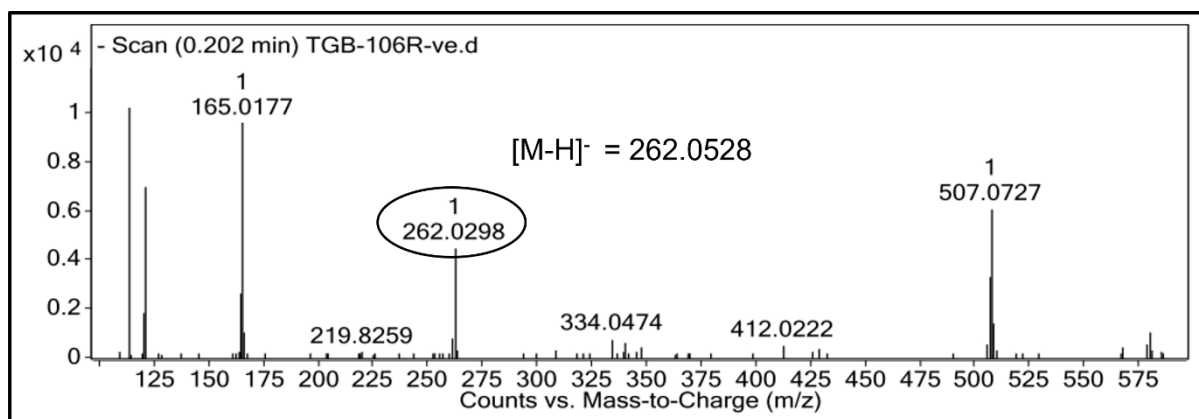
In vitro biocompatibility of hydrogel system was performed using MTT assay in L929 cell. Cells were cultured in Dulbecco's modified Eagle's medium (DMEM) supplemented with 10% FBS and 1% penicillin-streptomycin at 37 °C in 5% CO₂. 1.5×10^4 cells were plated in 48 well plates and cultured for 24 h. Hydrogel (1 mL) was mixed with 1 mL of glucose-free DMEM media and vortex for 30 min to form a homogeneous extract. 25, 50, 100, and 200 μ L of the hydrogel extract was added to the wells and further cultured for 24, 48, and 72 h. In control cells, the same amounts of media were added. After predetermined time points, wells were treated with 15 μ L of MTT dye solution (5 mg/mL in PBS) and further cultured for 3 h to form formazan crystals. Crystals were dissolved in 200 μ L of 1:1 methanol/DMSO and absorbance was recorded at 570 nm with background absorbance at 690 nm. The percentage of the viable cells was plotted using GraphPad Prism software.

3.7 Appendix

- ¹H and ¹³C NMR analysis of CPBA-NHS

- HRMS analysis of CPBA-NHS





3.8 References

1. Wu, Q.; Wang, L.; Yu, H.; Wang, J.; Chen, Z. Organization of glucose-responsive systems and their properties. *Chem. Rev.* **2011**, *111*, 7855–7875.
2. Manchineella, S.; Govindaraju, T. Stimuli-responsive material inspired drug delivery systems and devices. In *stimuli-responsive drug delivery systems*, Singh, A.; Amiji, M. M. Eds.; RSC Publishing, **2018**, 317–334.
3. Kamaly, N.; Yameen, B.; Wu, J.; Farokhzad, O. C. Degradable controlled-release polymers and polymeric nanoparticles: Mechanisms of controlling drug release. *Chem. Rev.* **2016**, *116*, 2602–2663.
4. Karimi, M.; Ghasemi, A.; Zangabad, P. S.; Rahighi, R.; Basri, S. M. M.; Mirshekari, H.; Amiri, M.; Pishabad, Z. S.; Aslani, A.; Bozorgomid, M. et al. Smart micro/nanoparticles in stimulus-responsive drug/gene delivery systems. *Chem. Soc. Rev.* **2016**, *45*, 1457–1501.
5. Doring, A.; Birnbaum, W.; Kuckling, D. Responsive hydrogels – structurally and dimensionally optimized smart frameworks for applications in catalysis, micro-system technology and material science. *Chem. Soc. Rev.* **2013**, *42*, 7391–7420.
6. Yan, X.; Wang, F.; Zheng, B.; Huang, F. Stimuli-responsive supramolecular polymeric materials. *Chem. Soc. Rev.* **2012**, *41*, 6042–6065.
7. Zimmet, P.; Alberti, K. G.; Magliano, D. J.; Bennett, P. H. Diabetes mellitus statistics on prevalence and mortality: Facts and fallacies. *Nat. Rev. Endocrinol.* **2016**, *12*, 616–622.

8. Alicic, R. Z.; Rooney, M. T.; Tuttle, K. R. Diabetic kidney disease challenges, progress, and possibilities. *Clin. J. Am. Soc. Nephrol.* **2017**, *12*, 2032–2045.
 9. Patti, G.; Cavallari, I.; Andreotti, F.; Calabro, P.; Cirillo, P.; Denas, G.; Galli, M.; Golia, E.; Maddaloni, E.; Marcucci, et al. Prevention of atherothrombotic events in patients with diabetes mellitus: from antithrombotic therapies to new-generation glucose-lowering drugs. *Nat. Rev. Cardiol.* **2019**, *16*, 113–130.
 10. Jeganathan, V. S. E.; Wang, J. J.; Wong, T. Y. Ocular associations of diabetes other than diabetic retinopathy. *Diabetes Care* **2008**, *31*, 1905–1912.
 11. Wang, J.; Yu, J.; Zhang, Y.; Zhang, X.; Kahkoska, A. R.; Chen, G.; Wang, Z.; Sun, W.; Cai, L.; Chen, Z. et al. Charge-switchable polymeric complex for glucose-responsive insulin delivery in mice and pigs. *Sci. Adv.* **2019**; *5*, eaaw4357.
 12. Chen, W.; Tian, R.; Xu, C.; Yung, B. C.; Wang, G.; Liu, Y.; Ni, Q.; Zhang, F.; Zhou, Z.; Wang, J. et al. Microneedle-array patches loaded with dual mineralized protein/peptide particles for type 2 diabetes therapy. *Nat. Commun.* **2017**, *8*, 1777.
 13. Ohkubo, Y.; Kishikawa, H.; Araki, E.; Miyata, T.; Isami, S.; Motoyoshi, S.; Kojima, Y.; Furuyoshi, N.; Shichiri, M. Intensive insulin therapy prevents the progression of diabetic microvascular complications in Japanese patients with non-insulin-dependent diabetes mellitus: A randomized prospective 6-year study. *Diabetes Res. Clin. Pract.* **1995**, *28*, 103–117.
 14. Kumareswaran, K.; Evans, M. L.; Hovorka, R. Closed-loop insulin delivery: Towards improved diabetes care. *Discov. Med.* **2012**, *13*, 159–170.
 15. Qiu, Y.; Park, K. Environment-sensitive hydrogels for drug delivery. *Adv. Drug Deliv. Rev.* **2001**, *53*, 321–339.
 16. Yu, J. C.; Zhang, Y.; Ye, Y.; DiSanto, R.; Sun, W.; Ranson, D.; Ligler, F. S.; Buse, J. B.; Gu, Z. Microneedle-array patches loaded with hypoxia-sensitive vesicles provide fast glucose-responsive insulin delivery. *Proc. Natl. Acad. Sci. U.S.A.* **2015**, *112*, 8260–8265.
-

17. Veiseh, O.; Tang, B. C.; Whitehead, K. A.; Anderson, D. G.; Langer, R. Managing diabetes with nanomedicine: Challenges and opportunities. *Nat. Rev. Drug Discov.* **2015**, *14*, 45–57.
 18. Chen, X.; Luo, J.; Wu, W.; Tan, H.; Xu, F.; Li, J. The influence of arrangement sequence on the glucose-responsive controlled release profiles of insulin-incorporated LbL films. *Acta Biomater.* **2012**, *8*, 4380–4388.
 19. Luo, J.; Cao, S.; Chen, X.; Liu, S.; Tan, H.; Wu, W.; Li, J. Super long-term glycemic control in diabetic rats by glucose-sensitive LbL films constructed of supramolecular insulin assembly. *Biomaterials* **2012**, *33*, 8733–8742.
 20. Dolgin, E. Medical devices: Managed by machine. *Nature* **2012**, *485*, S6–S8.
 21. Vashist, S. K. Non-invasive glucose monitoring technology in diabetes management: A review. *Anal. Chim. Acta* **2012**, *750*, 16–27.
 22. Wickramasinghe, Y.; Yang, Y.; Spencer, S. A. Current problems and potential techniques in in vivo glucose monitoring. *J. Fluoresc.* **2004**, *14*, 513–520.
 23. Ravaine, V.; Ancla, C.; Catargi, B. Chemically controlled closed-loop insulin delivery. *J. Control. Release* **2008**, *132*, 2–11.
 24. Mo, R.; Jiang, T.; Di, J.; Tai, W.; Gu, Z. Emerging micro-and nanotechnology based synthetic approaches for insulin delivery. *Chem. Soc. Rev.* **2014**, *43*, 3595–3629.
 25. Aronoff, S.; Chen, T.; Cheveldayoff, M. Complexation of D-glucose with borate. *Carbohydr. Res.* **1975**, *40*, 299–309.
 26. Kataoka, K.; Miyazaki, H.; Bunya, M.; Okano, T.; Sakurai, Y. Totally synthetic polymer gels responding to external glucose concentration: Their preparation and application to on-off regulation of insulin release. *J. Am. Chem. Soc.* **1998**, *120*, 12694–12695.
 27. Brownlee, M.; Cerami, A. A glucose-controlled insulin-delivery system: Semisynthetic insulin bound to lectin. *Science* **1979**, *206*, 1190–1191.
-

28. Kim, S. W.; Pali, C. M.; Kimico, M.; Seminoff, L. A.; Holmberg, D. L.; Gleeson, J. M.; Wilson, D. E.; Mack, E. J. Self-regulated glycosylated insulin delivery. *J. Control. Release* **1990**, *11*, 193–201.
29. Xiao, Y.; Sun, H.; Du, J. Sugar-breathing glycopolymerosomes for regulating glucose level. *J. Am. Chem. Soc.* **2017**, *139*, 7640–7647.
30. Kataoka, K.; Miyazaki, H.; Bunya, M.; Okano, T.; Sakurai, Y. Totally synthetic polymer gels responding to external glucose concentration: Their preparation and application to on-off regulation of insulin release. *J. Am. Chem. Soc.* **1998**, *120*, 12694.
31. Chen, S.; Matsumoto, H.; Moro-oka, Y.; Tanaka, M.; Miyahara, Y.; Suganami, T.; Matsumoto, A. Smart microneedle fabricated with silk fibroin combined semiinterpenetrating network hydrogel for glucose-responsive insulin delivery. *ACS Biomater. Sci. Eng.* **2019**, *5*, 5781–5789.
32. Matsumoto, A.; Ishii, T.; Nishida, J.; Matsumoto, H.; Kataoka, K.; Miyahara, Y. A synthetic approach toward a self-regulated insulin delivery system. *Angew. Chem. Int. Ed. Engl.* **2012**, *51*, 2124–2128.
33. Hu, X.; Yu, J.; Qian, C.; Lu, Y.; Kahkoska, A. R.; Xie, Z.; Jing, X. Buse, J. B.; Gu, Z. H₂O₂-responsive vesicles integrated with transcutaneous patches for glucose-mediated insulin delivery. *ACS Nano* **2017**, *11*, 613–620.
34. Gordijo, C. R.; Shuhendler, A. J.; Wu, X. Y. Glucose-responsive bioinorganic nanohybrid membrane for self-regulated insulin release. *Adv. Funct. Mater.* **2010**, *20*, 1404–1412.
35. Gu, Z.; Aimetti, A. A.; Wang, Q.; Dang, T. T.; Zhang, Y.; Veisoh, O.; Cheng, H.; Langer, R. S.; Anderson D. G. Injectable nano-network for glucose-mediated insulin delivery. *ACS Nano* **2013**, *7*, 4194–4201.
36. Zhang, M.; Song, C.-C.; Du, F.-S.; Li, Z.-C. Supersensitive oxidation-responsive biodegradable PEG hydrogels for glucose triggered insulin delivery. *ACS Appl. Mater. Interfaces* **2017**, *9*, 25905–25914.
-

37. Tai, W.; Mo, R.; Di, J.; Subramanian, V.; Gu, X.; Buse, J. B.; Gu, Z. Bio-inspired synthetic nanovesicles for glucose-responsive release of insulin. *Biomacromolecules* **2014**, *15*, 3495–3502.
38. Wallqvist, A.; Covell, D. G.; Thirumalai, D. Hydrophobic interactions in aqueous urea solutions with implications for the mechanism of protein denaturation. *J. Am. Chem. Soc.* **1998**, *120*, 427–428.
39. Kim, U.-J.; Park, J.; Li, C.; Jin, H.-J.; Valluzzi, R.; Kaplan, D. L. Structure and properties of silk hydrogels. *Biomacromolecules* **2004**, *5*, 786–792.
40. Seo, J.; Hoffmann, W.; Warnke, S.; Huang, X.; Gewinner, S.; Schöllkopf, W.; Bowers, M. T.; Helden, G. V.; Pagel, K. An infrared spectroscopy approach to follow β -sheet formation in peptide amyloid assemblies. *Nat. Chem.* **2017**, *9*, 39–44.
41. Kong, J.; Yu, S. Fourier transform infrared spectroscopic analysis of protein secondary structures. *Acta Biochimica et Biophysica Sinica* **2007**, *39*, 549–559.
42. Faniran, J. A.; Shurve, H. F. Infrared spectra of phenylboronic acid (normal and deuterated) and diphenyl phenylboronate. *Can. J. Chem.* **1968**, *46*, 2089.
43. Cheng, C.; Zhang, X.; Wang, Y.; Sun, L.; Chaoping, L. Phenylboronic acid-containing block copolymers: Synthesis, self-assembly, and application for intracellular delivery of proteins. *New J. Chem.* **2012**, *36*, 1413–1421.
44. Li, Y.; Rodrigues, J.; Tomas, H. Injectable and biodegradable hydrogels: gelation, biodegradation and biomedical applications. *Chem. Soc. Rev.* **2012**, *41*, 2193–2221.
45. Correa, S.; Grosskopf, A. K.; Hernandez, H. L.; Chan, D.; Yu, A. C.; Stapleton, L. M.; Appel, E. A. Translational applications of hydrogels. *Chem. Rev.* **2021**, *121*, 11385–11457.
46. Lu, S.; Wang, X.; Lu, Q.; Hu, X.; Uppal, N.; Omenetto, F. G.; Kaplan, D. L. Stabilization of enzymes in silk films. *Biomacromolecules* **2009**, *10*, 1032–1042.
47. Maity, B.; Samanta, S.; Sarkar, S.; Alam, S.; Govindaraju, T. Injectable silk fibroin-based hydrogel for sustained insulin delivery in diabetic rats. *ACS Appl. Bio Mater.* **2020**, *3*, 3544–3552.
-

48. Tai, W.; Mo, R.; Di, J.; Subramanian, V.; Gu, X.; Buse, J. B.; Gu, Z. Bio-inspired synthetic nanovesicles for glucose-responsive release of insulin. *Biomacromolecules* **2014**, *15*, 3495–3502.
49. Hellman, B. Pulsatility of insulin release – a clinically important phenomenon. *Ups. J. Med. Sci.* **2009**, *114*, 193–205.
50. Rorsman, P.; Braun, M. Regulation of insulin secretion in human pancreatic islets. *Annu. Rev. Physiol.* **2013**, *75*, 155–179.

Chapter 4

Antioxidant Silk Fibroin Composite Hydrogel for Rapid Healing of Diabetic Wound

Hypothesis: Wound healing is a complex biological process that requires activation and synchronization of multiple pathways and chemical responses to recover tissue integrity. In diabetic patients, increased production of reactive oxygen species, attack of pathogenic microorganisms, and high glucose levels delay the normal healing process. Therefore, a composite hydrogel formulation of SF protein with antioxidant-electroactive melanin and anti-inflammatory-antibacterial berberine has been anticipated to combat pathological abnormalities associated with diabetic wound healing.

Diabetes is a major metabolic disorder that seriously affects the overall health condition of an individual with an added economic burden. The prevalence of diabetes is growing rapidly because of changes in lifestyle and diet. International Diabetes Federation (IDF) 2019 global report revealed that more than 463 million people are suffering from diabetes worldwide and are expected to reach 578 million by 2030.¹ Under diabetic conditions, human body becomes incapable of producing or using the metabolic hormone insulin, which maintains glucose homeostasis.² Imbalance in glucose levels causes health complications like blindness, kidney failure, heart attack, and delayed wound healing.³⁻⁷ While wound care management is well established, the effective treatment of the diabetic wound remains challenging due to prevalent oxidative stress, inadequate angiogenesis, and exacerbated inflammation.⁸⁻¹² Wound healing is a complex multi-stage process that includes coordination of cell signaling, growth factors, extracellular matrix deposition, and cell recruitment.¹³ After tissue damage, coagulation cascades are activated to achieve hemostasis by clotting the platelet plugs and fibrin matrix, which prevent blood and body fluid loss. The inflammatory neutrophil cells at the wound site degrade the degranulated platelets, damaged tissues, and bacteria present at the wound site. Subsequently, keratinocytes are migrated to the damaged dermis, and the angiogenesis process is initiated with the help of vascular endothelial growth factor A (VEGF) and fibroblast growth factor (bFGF). The blood vessel capillaries with the spout of fibroblast cells and macrophages replace the fibrin matrix and generate support for keratinocyte migration. In the process, keratinocytes slowly mature and regain the epithelial barrier function.^{14,15} The fibroblast cells in stimulation with the macrophages transform into myofibroblast cells, which bring the wound edges together.¹⁶ In the remodeling stage, all preactivated processes initiated after tissue damage are deactivated. Activated immune cells (macrophages, myofibroblast cells) present at the wound site either emerge into blood circulation or undergoes apoptosis. The interaction between the epithelial and mesenchymal cells regulates skin integrity and homeostasis.¹⁷

However, hyperglycemia in diabetic patients leads to several cellular impairments, including poor glucose metabolism, enhanced microvascular endothelial injury, reduced oxygen delivery, flawed neural growth, and activated immune system.¹⁸⁻²⁰ As a result, hyperglycemia conditions cause cell hypoxia, tissue ischemia, increased production of reactive oxygen species (ROS), and weakening of defensive mechanisms against pathogenic microorganisms at the wound site.²¹ These multiple factors adversely affect and delay the cell migration, proliferation, and remodeling of the extracellular matrix at the wound site.

In the last few decades range of pharmaceutical formulations, including foam dressings, hydrogels, hydro fibers, nanoparticles, and electrospun scaffolds, have been used for diabetic wound healing.²²⁻²⁴ Among them, hydrogels are preferred for topical applications due to their softness, absorption ability of wound exudates, and maintaining the hydrated environment at the wound site. Hydrogel scaffolds protect the wound from pathogenic microorganisms and deliver drugs, growth factors, cytokines, and antibiotics in a controlled manner.²⁵ Notably, hydrogels are structurally analogous to the extracellular matrix and serve as three-dimensional support for complete tissue regeneration and new vascular network formation.^{26,27} Besides, soft, flexible nature of hydrogels provides greater comforts and can be easily applied and removed from the wound site without causing discomfort and additional damage. Keeping this in mind, researchers have developed a variety of hydrogels using several natural and synthetic materials.²⁶

SF protein extracted from silkworm cocoons (*Bombyx mori*) has been widely used for tissue engineering and regenerative applications.²⁷⁻³¹ The surface adhesion, proliferation, and differentiation of various cell types, including fibroblast, epithelial, endothelial, keratinocytes, osteoblast, and glial cells, were enhanced on the SF scaffold. The tunable mechanical strength and excellent biocompatibility of SF have found utility for the development of wound dressing materials.³² Numerous studies have reported SF hydrogel efficacy to control the delivery of

growth factors and drugs.³³⁻³⁶ SF is found to enhance the NF- κ B signaling pathway through the expression of cyclin D1, VEGF, fibronectin, and vimentin, which modulates the cellular activities like adhesion, proliferation, inflammation, and scavenging of ROS.³⁶⁻⁴⁰ Therefore, SF-based materials are sought-after in fabricating wound repair formulations. Recently, our group developed a pigmented and conducting nanofibrous composite scaffold by doping SF matrix with melanin for skeletal muscle tissue engineering.²⁹ Broad absorption range of melanin in UV-visible light and near-infrared (NIR) imparts intrinsic photoacoustic signals suitable for imaging and photothermal therapy.⁴¹ Melanin with large numbers of catechol, amine, and imine groups serve as an effective antioxidant to detoxify several types of radicals and ROS.⁴² The inherent antioxidant and conducting property of SF doped with melanin improved the proliferation of myoblast cells and induced their differentiation into myotubes while reducing the ROS level.

Bacterial infection at the wound site is one of the significant problems in wound recovery.⁴³ Moreover, bacteria and microbes have developed resistance to conventional antibiotics. In this context, utilizing natural products as antibiotics at the wound site is considered an effective strategy to control bacterial infections.^{44,45} Berberine, an isoquinoline natural product widely used in Chinese herbal medicine and India for its antibacterial, antioxidant, anti-inflammatory, immuno-enhancer, and hypoglycemic properties.⁴⁶ The versatile properties of berberine are anticipated to enhance wound closure in diabetic patients. The natural occurrence of berberine has a low tendency to suffer antibiotic resistance and retain an excellent inhibitory effect against pathogens. The hydrophobic and cationic nature of berberine permits cell membrane permeability and stable intercalation with microorganism DNA. Binding suppresses DNA and protein synthesis selectively in microorganism cells.

Herein, a hybrid hydrogel (SFCH) formulation of natural constituent hypolipidemic SF, antioxidant melanin, and anti-inflammatory berberine has been reported to stimulate the

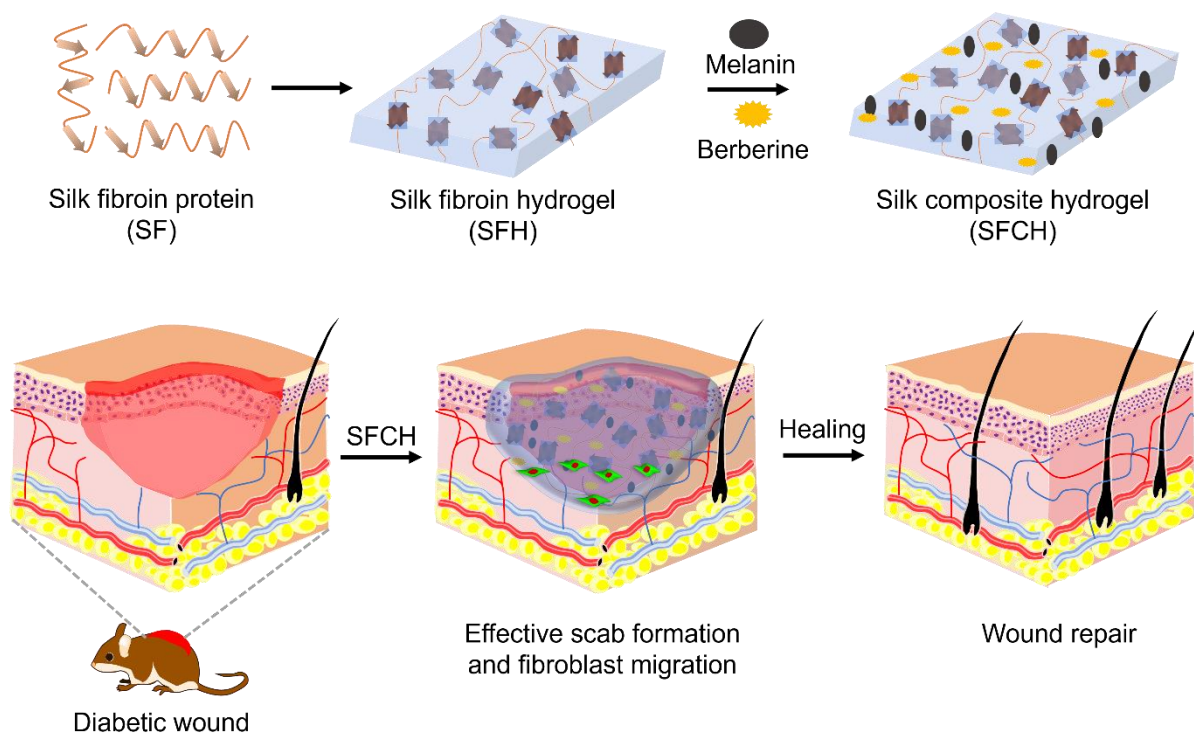


Figure 1. Schematic illustration of silk fibroin and silk fibroin-melanin (antioxidant)-berberine (drug) composite hydrogels (SFH and SFCH, respectively) and effective wound healing process upon treatment with drug-load antioxidant SFCH in diabetic rat.

wound healing process in diabetes. Melanin and berberine addition into the SF did not affect the hydrogel mechanical stiffness. SFCH hydrogel exhibited excellent antioxidant properties and effectively reduced oxidative stress. Berberine release kinetics indicates the hydrogel slowly releases the encapsulated berberine over a prolonged time. Encapsulated berberine molecules protect the wound site against pathogenic infection. The hybrid hydrogel formulation is biocompatible and supports excellent cell migration under *in vitro* conditions. The hydrogel efficacy in wound repair was evaluated in streptozotocin (STZ)-induced diabetic Wistar rats, which showed effective wound closer on applying the hydrogel at the wound site (Figure 1). The SFCH hydrogel treatment effectively controls the macrophage presence during the healing process, promotes angiogenesis, and enhances collagen deposition. This study reveals that the biocompatible SFCH with natural constituents is a potential healing formulation for diabetic wounds.

4.1 Hydrogel Preparation

The biocompatible, biodegradable, antioxidant, and drug loaded SFCH was formulated by the synergistic combination of 4% SF protein, 0.01% antioxidant melanin, and 0.1% therapeutic berberine (Figure 1). The naturally occurring SF protein tends to aggregate and form a hydrogel in physiological conditions. The crystalline β -sheet domain in the protein sequence imparts high mechanical strength and long-term stability to the hydrogel. Hydrogel was prepared by the physical mixing of SF protein, melanin, and berberine solutions. The incorporation of melanin and a mixture of melanin and berberine were found not to disrupt the gelation ability of SF. The gelation process was monitored by the vial inversion method for all the solutions (Figure 2).

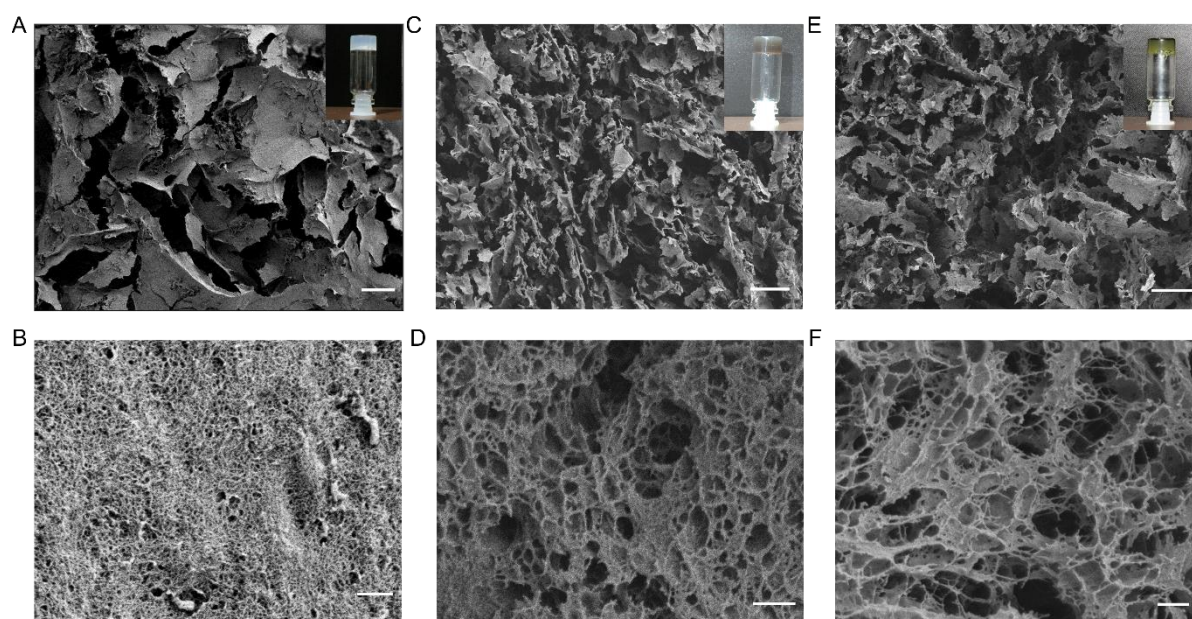


Figure 2. FESEM images of SFH (A), SFMH (C), and SFCH (E) and the insets show the photographs of inverted vials containing corresponding hydrogels. Scale bar 100 μm . SFH shows loose microstructure with low porosity. SFMH show higher porosity in the hydrogel matrix. SFCH exhibit highly porous morphology revealing its suitability as a three-dimensional matrix for cellular growth. (B, D, F) High magnification FESEM images of SFH, SFMH, and SFCH correspond to (A, B, C). Scale bar: 400 nm. The macroscopic porous structures consist of cross-linked nanofiber.

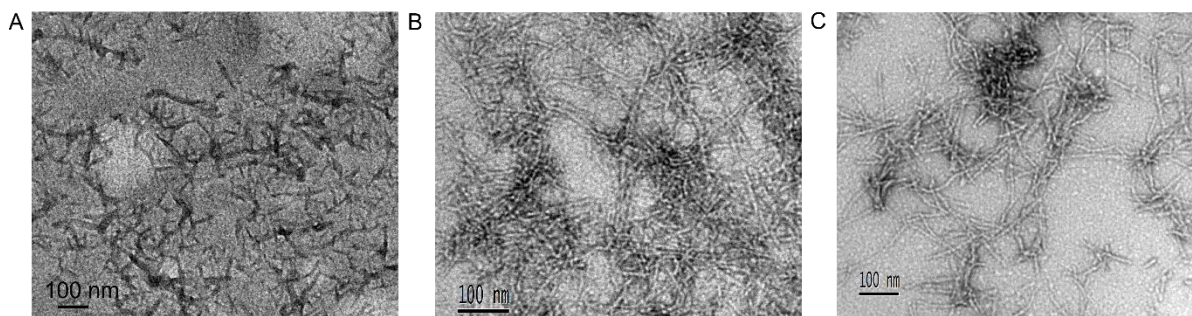


Figure 3. TEM images of the nanofibers of the hydrogel scaffold.

4.2 Morphological Analysis

The structural morphology of hydrogels was analyzed by field emission scanning electron microscopy (FESEM) to gain insights into the architectural characteristics of hydrogel matrix and its suitability as soft biomaterials to use with soft tissues. The silk fibroin hydrogel (SFH) showed loose nonuniform porous microstructure (Figure 2A, 2B) of fibrous cross-linked aggregates with 10-20 nm width (Figure 3). The incorporation of melanin into SF solution did not alter the cross-linking between the hydrophobic domains of SF protein. However, pore density in hydrogel matrix was increased significantly compared to that of SFH (Figure 2C, 2D). The increase in cross-linking relies on multiple hydrogen bonding sites of polymeric melanin. Notably, adding berberine into SF and melanin to obtain SFCH hydrogel did not alter the porous morphology and fiber width (Figure 2E). Besides, berberine incorporation introduced highly porous morphology suitable for cellular infiltration and accelerated cellular growth inside the hydrogel matrix (Figure 2F).⁴⁷ The highly porous morphology observed with SFCH compared to SFH emphasized the suitability of the former for infiltration and proliferation of cells inside the hydrogel matrix compared to the latter.⁴⁸

4.3 Conformation Analysis

The secondary conformation changes in SF after gelation was assessed by the powder X-ray diffraction (PXRD) analysis of the xerogels. SF, after processing from cocoon adopts the amorphous structure. All hydrogel samples showed crystalline morphology with diffraction

peaks (2θ) at 8.62° , 20.72° , and 24.2° (Figure 4A). The weak diffraction peak at $2\theta = 20.72^\circ$ indicates a crystalline silk II structure with higher mechanical strength. The weak diffraction peak at 19.7° in SFCH revealed the presence of crystalline silk I and silk II conformations. The driving force for the observed cross-linking during the gelation of SF protein was studied by FTIR spectroscopy analysis. The structural conformation of a protein can be determined by monitoring the amide region of the FTIR spectrum (Figure 4B). SF protein extracted from the cocoon showed absorption bands at 1649 cm^{-1} and 1517 cm^{-1} , corresponding to amide I (C=O stretch) and amide II (N-H deformation), respectively, indicative of random coil structure (Figure 4B). The strong absorption band observed for SFH at 1621 cm^{-1} (amide I) revealed β -sheet conformation of SF in the hydrogel matrix.⁴⁹ In addition, the shoulder peak at 1648 cm^{-1} suggests the co-existence of β -sheet and random coil structure in the hydrogel. SFMH showed absorption peaks at 1621 cm^{-1} and 1521 cm^{-1} corresponding to amide I and amide II bands, which suggest melanin incorporation did not affect the gelation process of SF

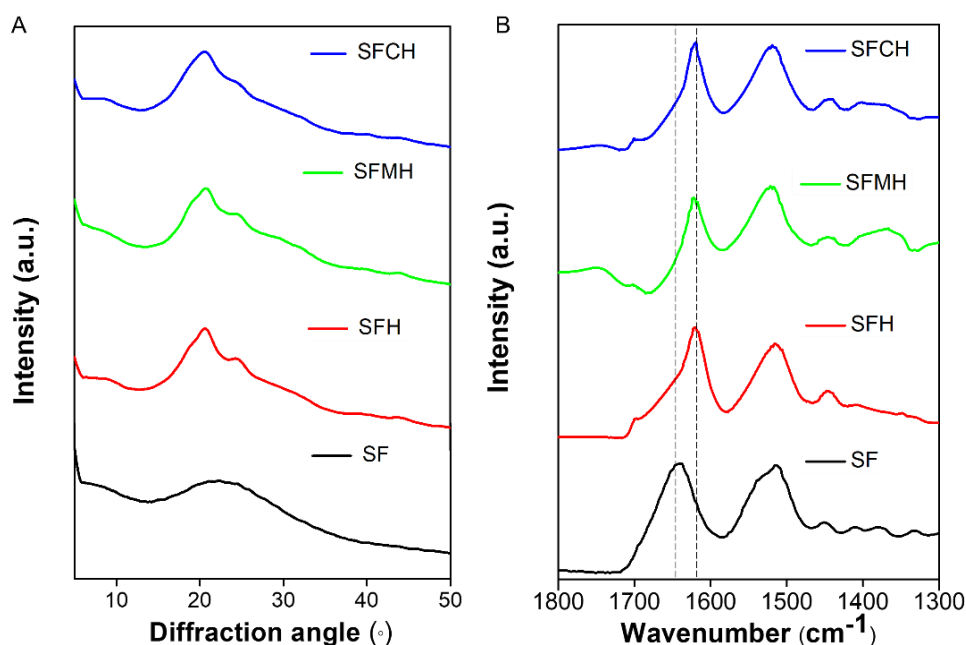


Figure 4. (A) PXRD of SF protein and xerogels. (B) FTIR spectra of SF protein, SFH, SFMH, and SFCH. The amide peaks at 1650 cm^{-1} in SF and 1620 cm^{-1} in SFH, SFCH indicates the conformational transition from random coil to the order β -sheet structure.

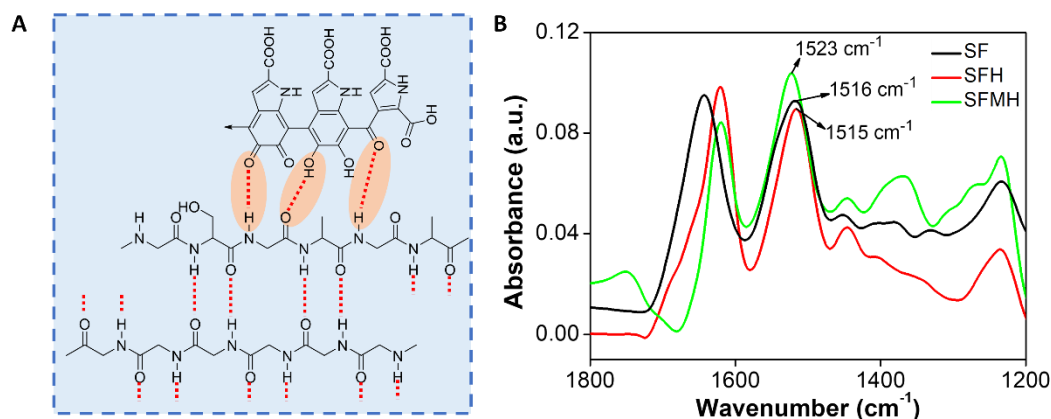


Figure 5. (A) The possible hydrogen bonding pattern between melanin and SF. (B) The FTIR spectra of SF, SFH and SFMH indicates the hydrogen bonding between SF and melanin.

protein. However, the slight shift in the amide II band suggests the interactions between the amide N-H of SF with carbonyl groups of melanin (Figure 5A, 5B). Addition of berberine did not alter the amide peak position confirming the absence of its influence on conformational transition from random coil to ordered β -sheet structure of SF protein. Overall, the IR data revealed structural rearrangement of SF protein involving the conformational change from random coil to β -sheet leading to fibrillar network to support the gelation process.

4.4 Mechanical Properties

Next, the mechanical properties of SFH and SFCH were investigated. The ideal wound dressing hydrogel must exhibit optimal mechanical properties to maintain its structural integrity during the healing process.⁵⁰ The frequency sweep measurement revealed a linear storage modulus range and loss modulus in experimental frequencies from 0.01 to 100 Hz due to its higher stiffness property. Both SFH and SFCH exhibited higher storage modulus (G') than the loss modulus (G''), indicating higher cross-linking density and solid-like behavior within the hydrogel matrix (Figure 6A). The mechanical properties of the hydrogels correlate with the cross-linked porous architecture observed in microscopy data. The loose structure of the SFH exhibit lower mechanical strength. Melanin incorporation to discern the stiffness and viscoelasticity of hydrogels. As shown in Figure 6A, the SFCH increased the

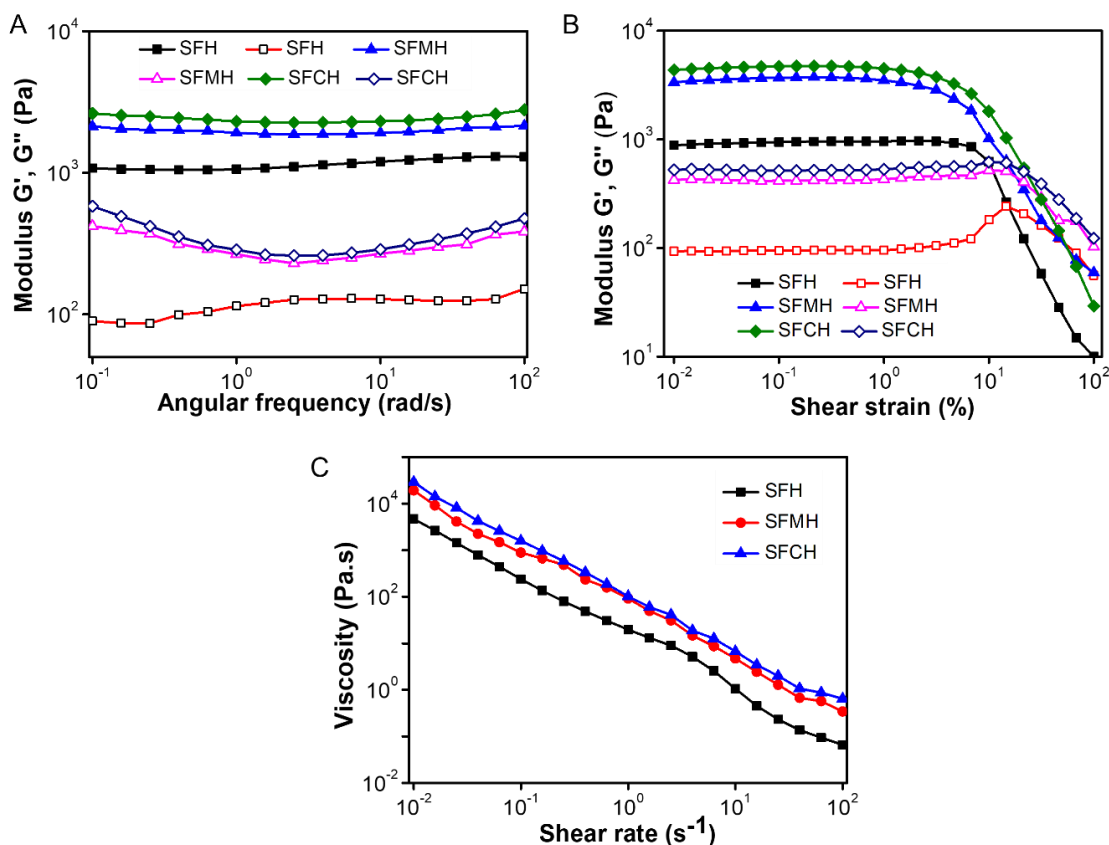


Figure 6. Rheological frequency sweep of SFH, SFMH, and SFCH. The storage modulus (G') indicated with solid symbols and loss modulus (G'') with hollow symbols. (d) Shear strain measurement of SFH and SFCH performed from 0.1% to 100% strains.

cross-linking through hydrogen bonding interactions, which resulted in enhanced mechanical strength of SFCH. The mechanical strength (stiffness) of hydrogel matrix has a crucial role in cell adhesion and proliferation to aid the faster wound healing process. The comparable stiffness of the SFCH matrix with extracellular matrix (ECM) enhances the cell adherent property. The comparable stiffness of hydrogel with tissue is an essential parameter for tissue engineering and wound healing applications. The stiffness of the human tissue varies from Pa to GPa, while the stiffness of the human dermis tissue is in the range of a few tens of kPa.⁵¹ The storage modulus of SFCH matrix was 4.5 kPa, comparable to the stiffness of human dermis tissue (Figure 6B). The similar mechanical properties endorse the suitability of SFCH as a wound dressing formulation to support cell adhesion, proliferation, and new tissue formation.

The flow property of the hydrogels was studied by steady-shear measurement, which is a relevant property to ascertain the suitability of the materials for application at the wound site. The viscosity of SFH and SFCH was reduced rapidly upon increasing the shear rate from 0.01 to 100 S⁻¹ due to their shear-thinning properties (Figure 6C). The shear strain measurement showed the linear range of viscoelasticity up to 10% of shear strain for both SFH and SFCH, where hydrogels maintained solid-like behavior. The shear strain property of the SFCH is comparable to the strain experienced by tissue. Overall, the mechanical properties of SFCH matrix are within the range to maintain the dynamic physiological environment and suitable as a wound dressing formulation.

4.5 Swelling Ratio

For a potential wound dressing material, the wound exudate absorption ability is a crucial parameter.⁵² The water absorption propensity of SFH, SFMH, and SFCH from the PBS solution (pH = 7.4) was assessed. The water absorption ability of the dried SFCH xerogel scaffold was 87% which is similar to the native SFH (Figure 7). This indicates that hydrophobic berberine loading has no significant effect on the water absorption efficacy of SFCH. Thus, SFCH is capable of wound exudate absorption and provides a humid environment for tissue regeneration.

4.6 Antioxidant Assay

The reactive oxygen species (ROS) are produced at the inflammatory stage of the wound healing process from the respiratory burst of phagocytic cells and enzymatic cycles of the fibroblast cells at the wound site.⁵³ ROS acts as a defensive agent for the invaded pathogens crucial mediator for cellular signaling and neo-angiogenesis. However, a significant increment of ROS level significantly damages the tissue and slows the wound healing process.⁵⁴ The antioxidant property of SFCH and individual components were evaluated using the DPPH radical inhibition assay over a period of 72 h. The pink colored DPPH radicals in a

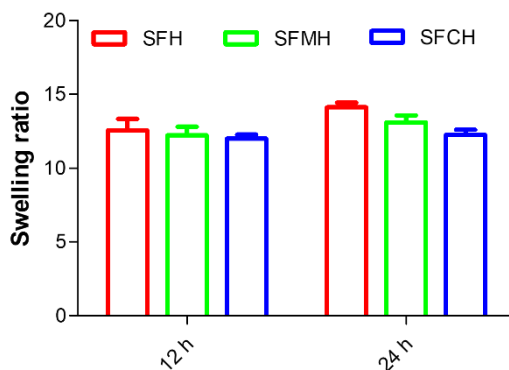


Figure 7. Swelling ratio of the SFH, SFMH and SFCH xerogels at 12 and 24 h.

mixture of ethanol/water take electrons from antioxidants and quenched to colorless form. Due to the high electron density of the natural antioxidant pigment melanin, it instantly inhibited DPPH radicals in a concentration-dependent manner. The antioxidant efficacy of melanin solution at 50 $\mu\text{g/mL}$ was 80%, comparable to natural antioxidant ascorbic acid (Figure 8B). Although the melanin solution alone showed rapid radical scavenging, the SFCH showed persisted time-dependent activity, and saturation was reached in 24 h (Figure 8D). The rapid inhibition of radicals by melanin is attributed to its instant availability in the solution state, whereas ROS has to diffuse into the SFCH matrix to react with melanin. Therefore, the equilibrium was reached over a prolonged time in the case of SFCH compared to the melanin solution. The time-dependent and sustained antioxidant activity of SFCH is a desired property to be used in dynamically regulated living systems. The ROS scavenging efficacy of SFCH was comparable to the SFMH system, which confirmed that the observed scavenging property of SFCH is mostly attributed to melanin and possibly some contribution from berberine. The consistent antioxidant activity of SFCH is anticipated to alleviate oxidative stress during the wound healing process.

4.7 Drug Release Profile

Berberine has been used in Chinese medicine topically as antibacterial and antioxidant agent. Due to the presence of hydrophobic aromatic core and cationic charge, berberine exhibit a low

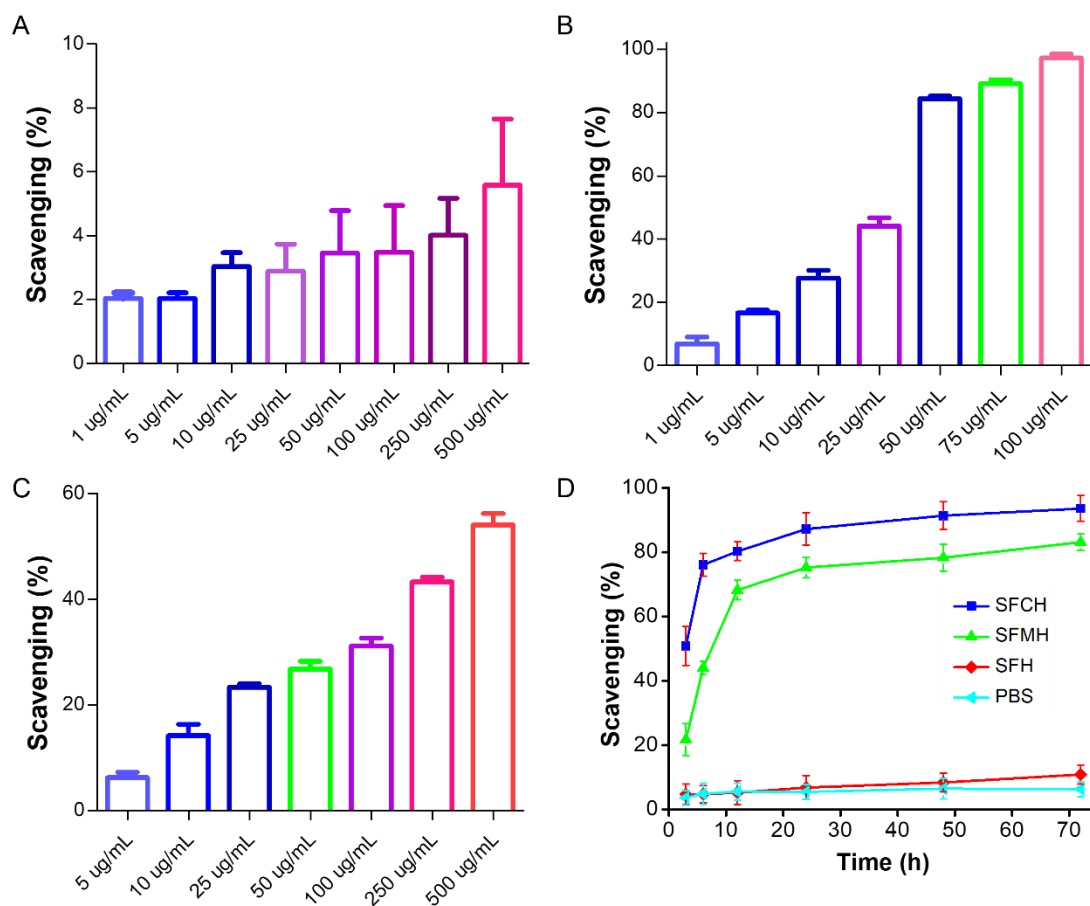


Figure 8. Antioxidant properties of SFH, SFMH, SFCH, and PBS solution (DPPH assay). The radical (DPPH) scavenging affinity of SF (A), melanin (B), berberine (C), and SFCH (D).

tendency towards bacterial resistance.⁵⁵The cumulative release of encapsulated berberine from SFCH and berberine encapsulated SFH (SFBH) was estimated under physiologically relevant conditions (37 °C, PBS, pH = 7.4). The release rate of berberine from the hydrogel matrix at different time points are shown in Figure 9A. At initial 24 h, 40% of berberine was released due to surface binding and high concentration gradient, which enhanced the drug diffusion rate. Thereafter, a steady linear release kinetic was followed until 7 days, where diffusion is the primary driving force for berberine release. The drug release profiles also showed a higher berberine release rate from SFCH than berberine containing SFBH. This variation in berberine release from the hydrogel matrixes is correlated with the pore size observed in the FESEM analysis (Figure 2C) and cross-linking density of the matrix. Melanin addition into the hydrogel

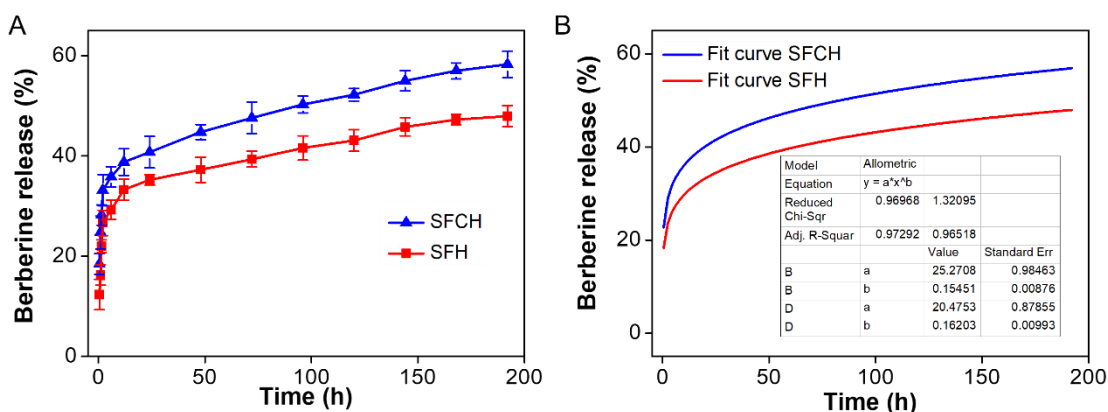


Figure 9. The release profile for berberine from SFH and SFCH up to 8 days.

matrix introduces a highly porous structure with more surface areas than SFBH. The high surface area of SFMH/SFCH correlates to more berberine-loading and release. To understand the mechanism of drug release from SFBH and SFCH matrix, the time-dependent berberine release data were fitted to a semi-empirical power-law model following the Ritger-Peppas equation, widely followed in diffusion-controlled release systems. The different release kinetics for SFH and SFCH were obtained from the n values of the logarithm equation. For a swellable hydrogel matrix, the release behavior will be purely Fickian when $n \leq 0.45$ and anomalous transport for $0.45 < n < 0.85$. The fitting curve (Figure 9B) showed n values of 0.16 (SFBH) and 0.15 (SFCH), indicating the release of berberine is dominated by the diffusion rate and least extent to its swelling ratio. The higher k value of SFCH (25.27) compared to SFBH (20.47) is attributed to its highly cross-linked structure, which enhanced the berberine diffusion rate from the hydrogel matrix. However, total berberine release of 60% was observed after 8 days. The strong interaction between the β -sheet crystals of SF aggregates and aromatic berberine molecules has a significant role in its slow release.

4.8 Antibacterial Activity

Infection at the wound site delay the healing process. Thus, an efficient dressing must inhibit the bacterial growth responsible for severe infection. The SFCH hydrogel consists of berberine with inherent antibacterial and anti-inflammatory effects. The commonly observed pathogenic

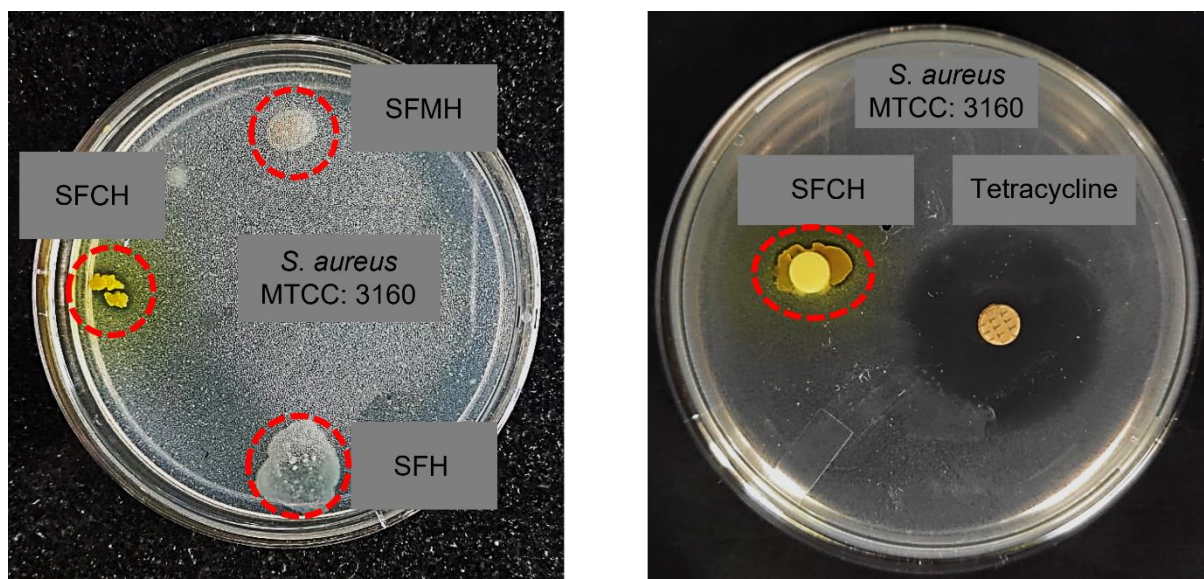


Figure 10. Antibacterial activity of SFH, SFMH and SFCH hydrogel against *Staphylococcus aureus* at 12 h.

bacteria responsible for the infections are *Staphylococcus aureus* and *Escherichia coli*. The antibacterial propensity of the hydrogel against *Staphylococcus aureus* was determined by zone inhibition assay. No inhibition zone was observed for SFH and SFMH against pathogenic bacteria (Figure 10). The SFCH effectively inhibited the growth of pathogenic *Staphylococcus aureus*, and an apparent inhibition zone was observed after 12 h contact interval (Figure 10). Thus, berberine-loaded SFCH possesses antibacterial properties and efficiently protects the wound from pathogenic bacteria during the healing process.

4.9 Cytotoxicity Studies

Biocompatibility is one of the major criteria for *in cellulo* and *in vivo* application of a biomaterial. Thus, the viability of SFCH to NIH3T3 fibroblast cells was accessed using the MTT assay. The fibroblast cells incubated with hydrogel solution in cell growth medium showed good viability regardless of the incubation times from 24 h to 72 h. As shown in Figure 11A, SFCH showed >95% cell viability after 72 h incubation compared to control cells (NIH3T3 cultured in complete medium, 100% viability). Thus, the hydrogel system did not alter the metabolic activity and confluency. Therefore, the antioxidant SFCH formulation is

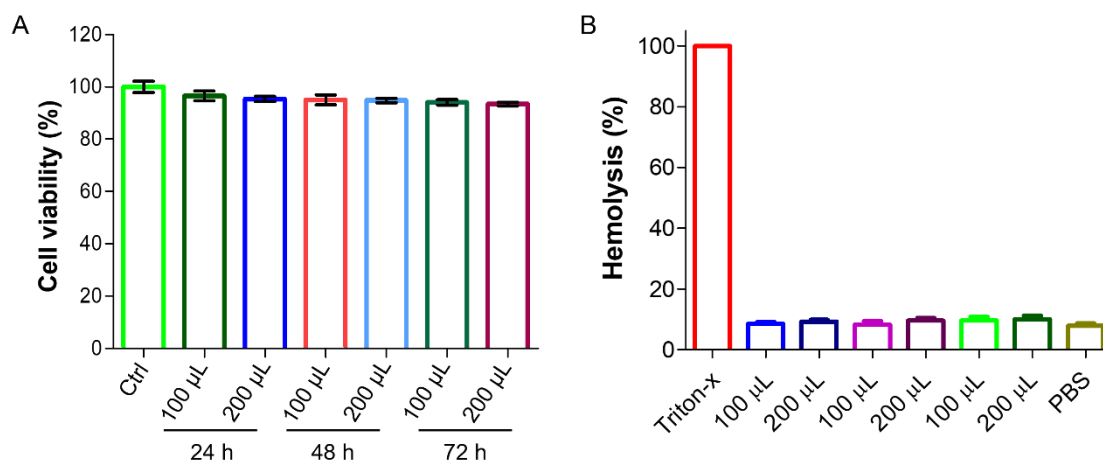


Figure 11. Biocompatibility of SFCH. (A) The cell viability of NIH3T3 cell lines in the presence of SFCH solution in different time intervals. (B) The hemolytic behaviour of Triton-X-100, SFH, SFMH, SFCH and PBS.

biocompatible and viable to be used for tissue regeneration ability in live wound sites. The hemolysis of human red blood cells (RBC) was performed to understand the acute toxicity nature of SFCH. The SFCH solution incubated with RBC did not show significant hemolysis (Figure 11B), comparable to PBS buffer. In contrast, the triton-100 used in the control experiment showed complete lysis of the RBC membrane and solubilization of hemoglobin. These biocompatibility and viability attributes have validated the potential of SFCH for *in vivo* applications.

4.10 Cell Rescue Studies from Oxidative Stress

An optimum level of ROS at the wound sites contributed to the cell signaling pathway. However, the overproduction of ROS at the diabetic wound site causes oxidative stress to the surrounding tissue and delays the cell migration and rearrangement essential for tissue regeneration and repair. The ROS content inside the cells was detected using the 2',7'-dichlorofluorescein diacetate (DCFDA). The non-fluorescence DCFDA internalize inside the cell and hydrolyze into 2',7'-dichlorodihydrofluorescein (H2-DCF), and oxidized by the cellular ROS into highly fluorescent 2',7'-dichlorofluorescein (DCF). NIH3T3 cells on treatment with

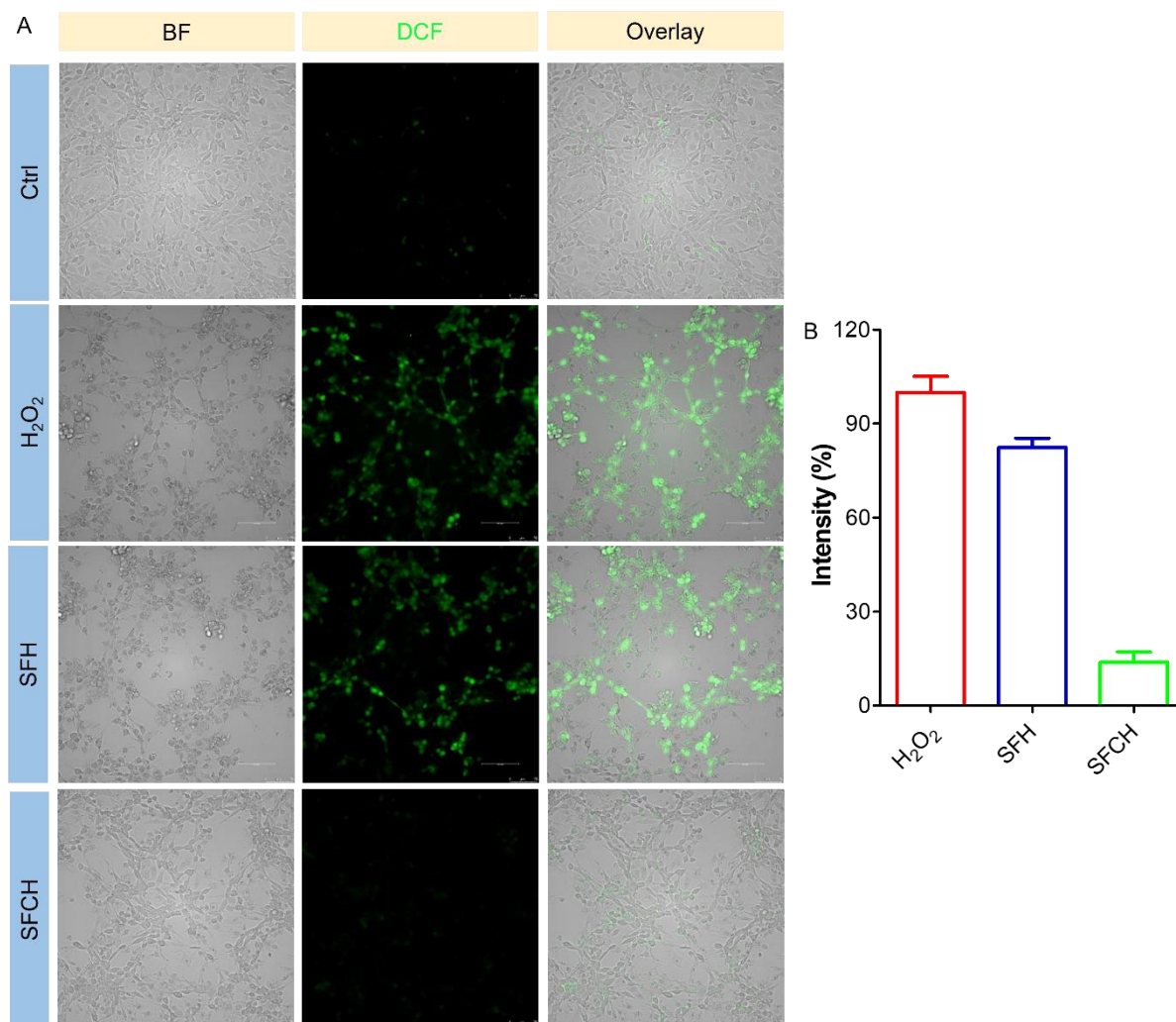


Figure 12. The intracellular ROS level visualization by DCFDA. (A) Microscopy images of NIH3T3 cells treated with H₂O₂ and combination of H₂O₂ and hydrogel solution (B) Quantification data of DCF fluorescence.

H₂O₂ showed high DCF fluorescence, remarkably decreasing to the normal state upon treatment with SFCH (Figure 12A). Further, NIH3T3 cell rescue from H₂O₂-induced oxidative stress was performed to assess the protective effect of SFCH by MTT cell viability assay. The oxidative microenvironment by H₂O₂ (200 μM) induces oxidative stress and decreases the cell viability to 33% (Figure 13). However, treating cells with SFCH solution significantly increased the viability in a concentration-dependent manner. The cell viability increased to 55%, 60%, 70% and 82% upon treatment with 50, 100, 150 and 200 μL of SFCH solution.

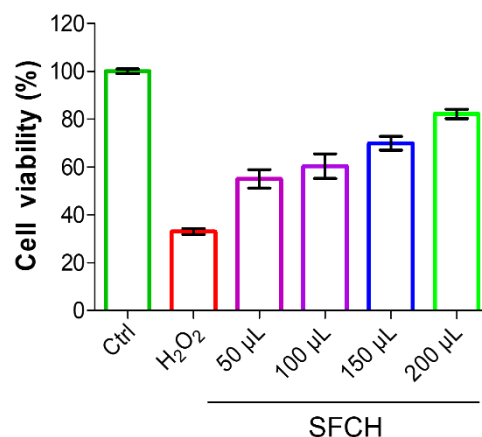


Figure 13. NIH 3T3 cell rescue from H₂O₂ (200 µM) induced oxidative stress. The viability of the NIH 3T3 cells increased in the presence of SFCH solution.

These studies have confirmed that SFCH effectively quenches ROS and reduces oxidative damage to cells.

4.11 *In Vitro* Cell Migration

The crucial stage in quick wound healing is the new tissue generation process at the wound sites. The effectiveness of this process was evaluated by the migration and proliferation of new tissue layers, sprouts of capillaries bound with the macrophages, and fibroblast cells start fibroblast cells over the injured dermis layers. New blood vessel begins to form through the new tissue layers and serve as support for further keratinocytes migration. Initially, keratinocytes proliferate effectively and become mature to restore the epithelial barrier function. Therefore, the ability of hydrogel toward migration and proliferation behavior of NIH3T3 fibroblast cells was assessed. The migration of NIH3T3 cells was significantly increased after the addition of SFCH solution compared to untreated control NIH3T3 cells (Figure 14). The SFCH completely healed the scratch length in 24 h, very few cells were migrated from the bulk cell site in the control scratch, and effective healing was not observed (Figure 15). This confirmed the acceleration of the healing behavior of SFCH through the enhancement of the different growth factors from fibroblast cells. The enhanced migration of

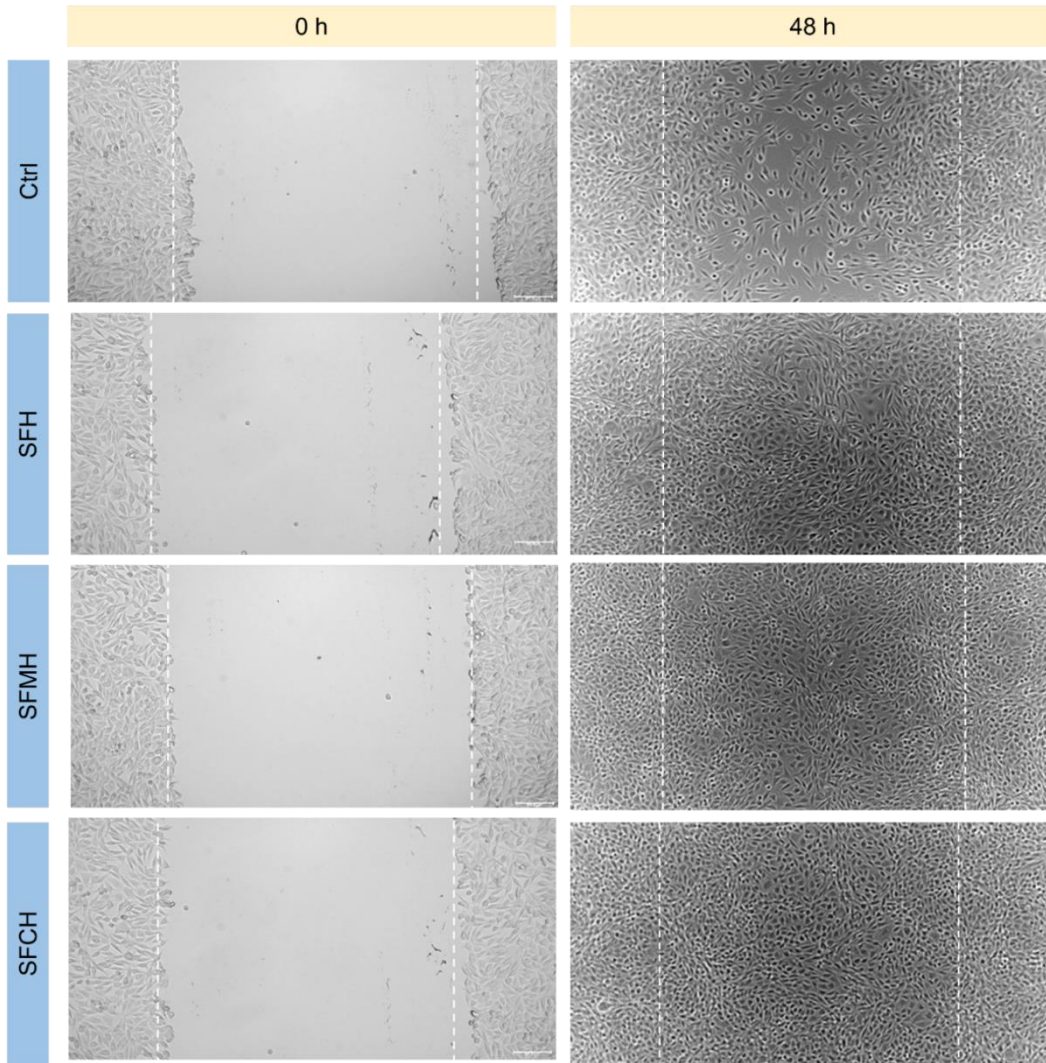


Figure 14. Scratch test assay of the NIH3T3 cells in the presence of SFH, SFMH and SFCH solutions at 48 h. Effective migration of the cells toward the scratch sites in the presence of hydrogel solutions.

NIH3T3 cells indicates the pertinency of SFCH *in vivo* tissue re-epithelialization.

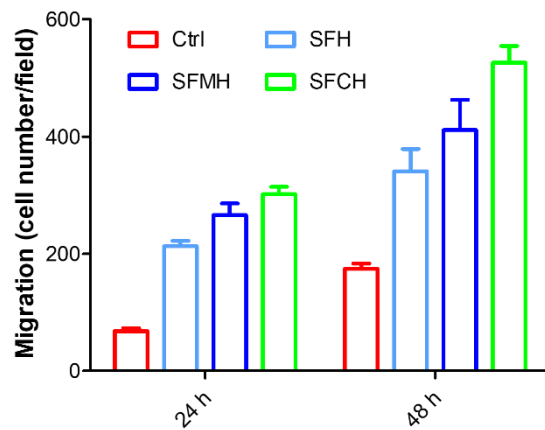


Figure 15. Quantification of cells migrated into the centre of scratch site in 24 h and 48 h.

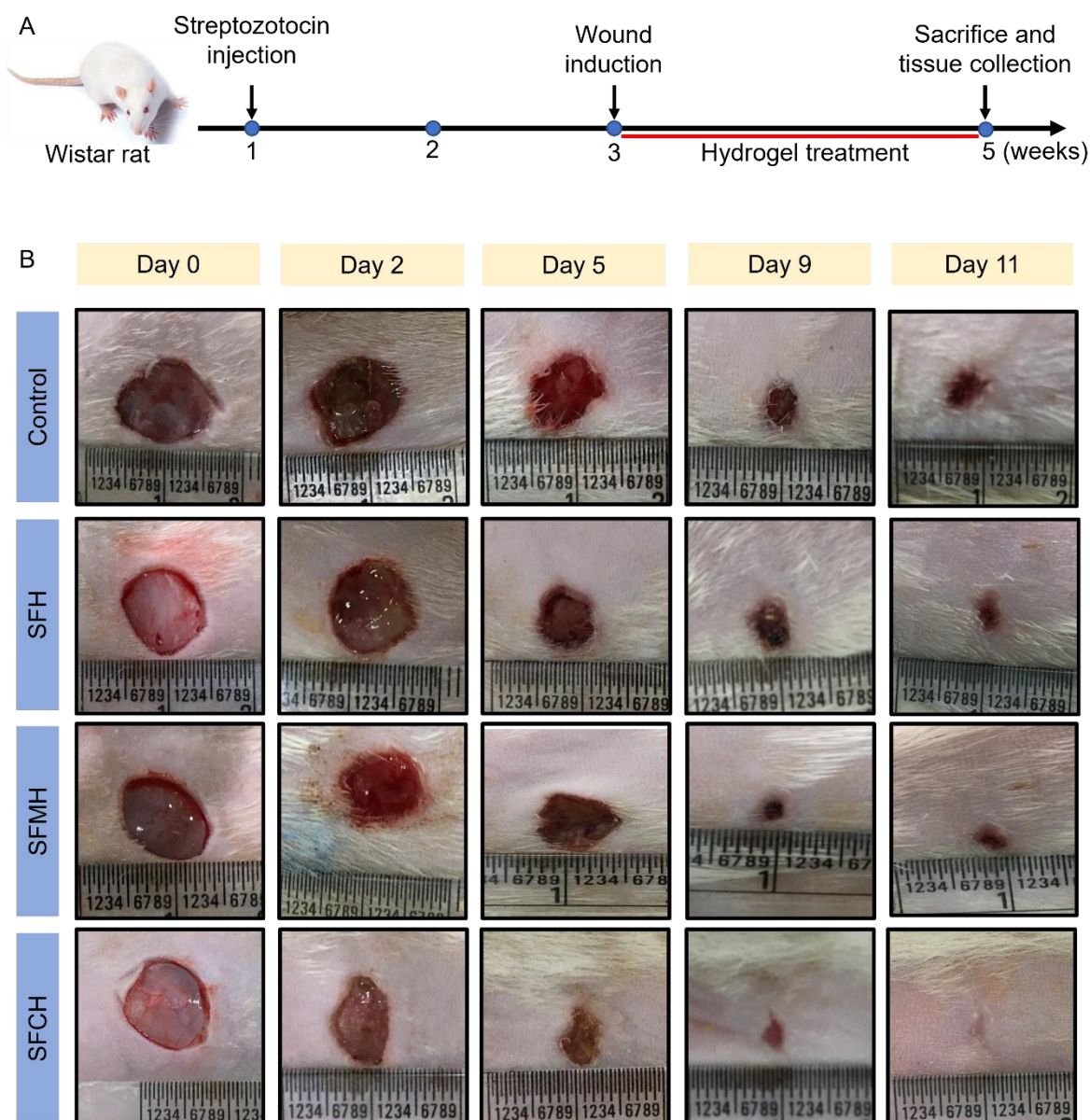
4.12 *In Vivo* Wound Healing

Figure 16. *In vivo* therapeutic wound healing activity of SFCH. (A) Scheme shows the plan for animal experiments. Wistar rats were administered with single dose of STZ to induce diabetes. Full exertion wound was created on the back shoulder, treated with hydrogels, and further monitored until complete wound healing. (B) Gross observation of wound healing in diabetic type 1 Wistar rats treated with SFH, SFMH, and SFCH at 0, 3, 5, 9, and 11 days. Scab formation and quick wound healing were observed in rats treated with SFCH.

The wound tissue regenerative ability of SFCH was evaluated in STZ induced diabetic type I Wistar rat model. High doses of STZ selectively destroy the pancreatic β -cells and prevent

insulin production, which typically generates a type I diabetic model (Figure 16A). After a week of STZ injection, the blood glucose level of rats was elevated from 80-120 mg/dL to 450-500 mg/dL, confirming the destruction of β -cells and impaired insulin production. A full-thickness excision wound was created on diabetic rats, SFH, SFMH, and SFCH were applied to the wound area. The untreated diabetic rats and SFH treated rats were considered as controls. Scab formation, dryness, and wound closer behavior in treated rats were monitored. The gross observation photos of the wounds on initial and days 2, 5, 9, and 11 after being treated with different hydrogel formulations and control groups are shown in Figure 16B. The macroscopic observations of wound closure images indicates, the hydrogel-treated wounds showed better wound healing at all time points of observations compared to non-treated wounds. In 3 days, the SFCH treated wounds displayed less leaching of pathological fluid and good scab formation compared to the control diabetic group and SFH treated group (Figure 16B). The complete dryness of the wound area and scab formation were observed in SFCH treated group on day 6. Whereas the complete dryness and scab formation were observed on day 9 for the control group. SFCH treated wound showed complete wound contraction and re-epithelialization in 11 days. The control, SFH, and SFMH treated groups showed complete wound closure on days 18, 16, and 15, respectively. These results revealed that the percentage of the wound closed in SFCH treated groups is highest at every

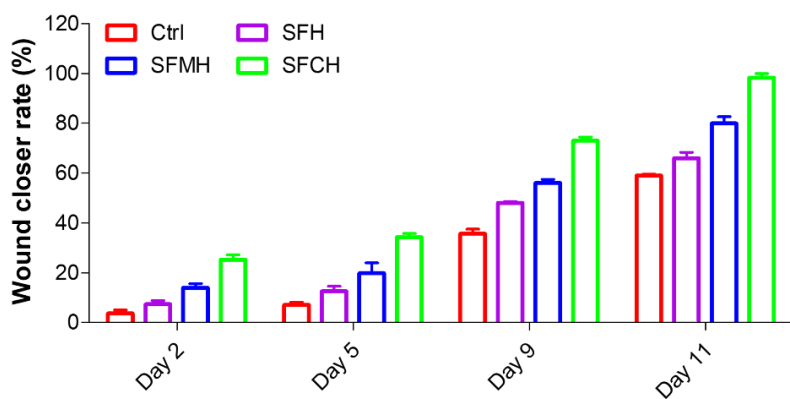


Figure 17. Quantification of wound closure rate in rats treated with SFH, SFMH, and SFCH at different time points.

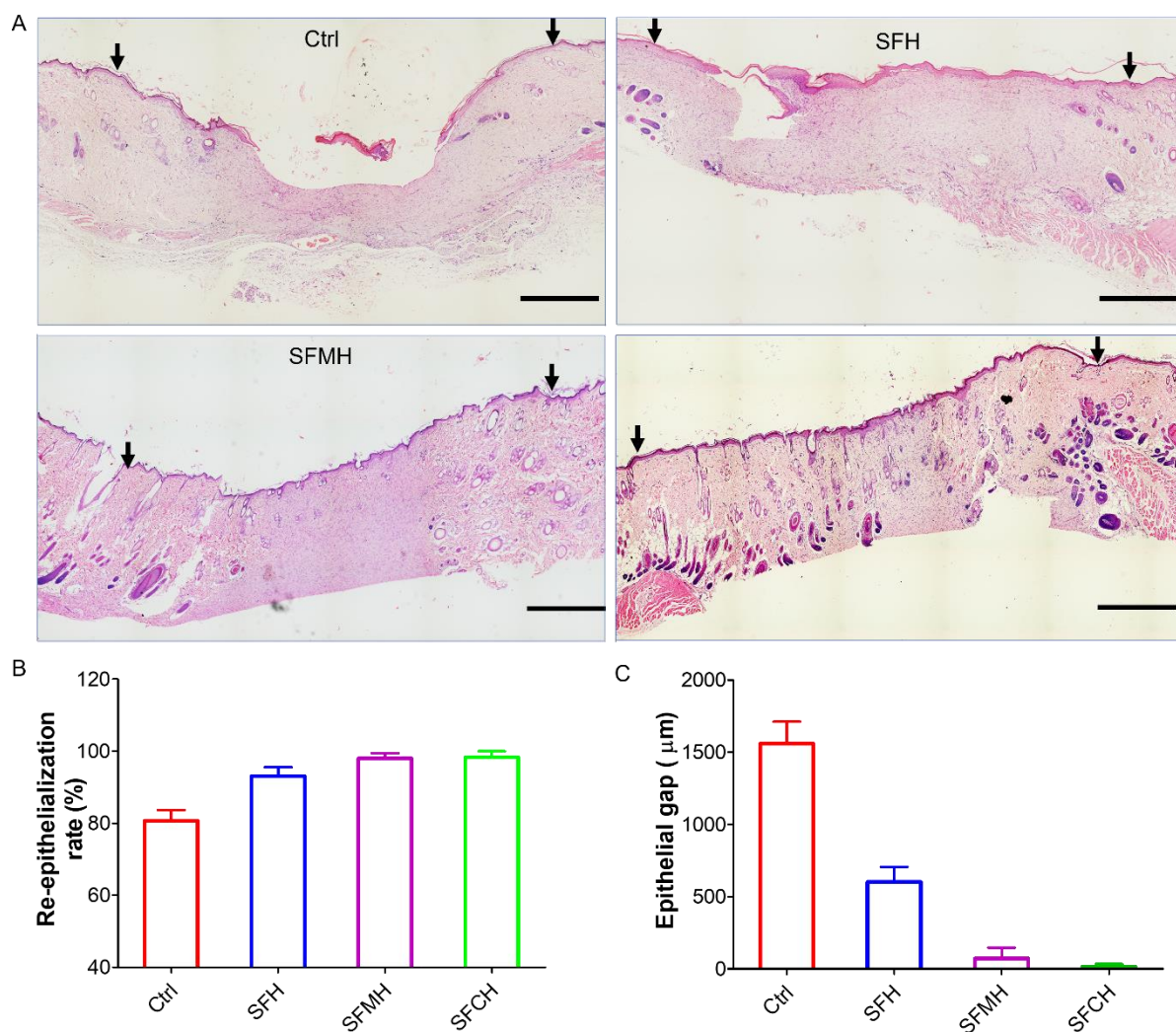


Figure 18. (A) Hematoxylin and eosin (H &E) staining of the wound tissue samples after 14 days of post-operation. All hydrogel-treated samples exhibited good re-epithelialization and healing of the wound site. The SFCH treated wound showed complete re-epithelialization of wound tissue and appearance of the skin glands and blood vessels. Black arrows indicated the edges of the initial wound sites (scale bar 1 mm). (B, C) Quantification of the re-epithelialization rate and epithelial gaps from H&E staining.

measurement time point compared to other treated and untreated groups (Figure 17). Incorporation of melanin and berberine in SF hydrogel (SFCH) effectively enhanced the re-epithelialization at the wound site and accelerate the closure process at a significant rate. Thus, the biocompatible and antioxidant SFCH system consisting of natural components is an effective dressing formulation to treat wounds under diabetic conditions.

Next, hematoxylin and eosin (H & E) staining was performed on the wound skin tissue samples collected after 14 days to analyze the regeneration of the epithelial barrier at the wound site. In the control sample, the epithelial barrier of the skin was not healed completely, as 30% of the wound site remained open (Figure 18A). In SFH-treated wounds, the encloser rate of the epithelial barrier was increased, albeit remains unhealed (Figure 18B). The sample from the wound site treated with the SFMH showed complete healing of the epithelial barrier at 14 days of treatment with a better proliferation of the dermis layer. Notably, the sample from SFCH treated wound site showed complete healing of the epithelial layer and the presence of sebaceous glands and blood vessels. This revealed that the high moisture content of hydrogel (SCFH) supplemented with antioxidant and therapeutic effects of melanin and berberine, respectively, provided a conducive environment for epidermal regeneration. The good re-

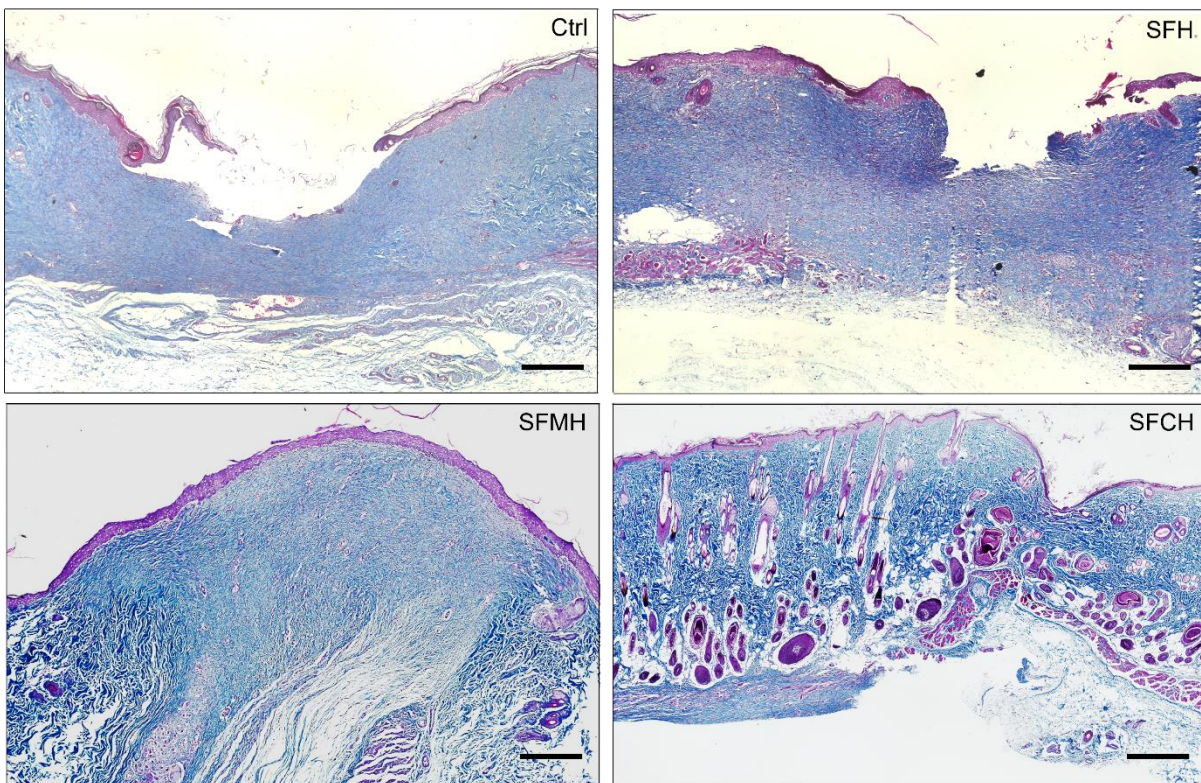


Figure 19. Masson's trichrome staining of the wound tissue cross sections after 2 weeks of treatment with hydrogels. Effective collagen deposition and maturation is observed in SFCH treated skin section (scale bar 500 μ m).

epithelialization of the skin layer upon SCFH treatment correlates with the enhanced cell migration observed in the *in vitro* (scratch test assay) study. The ability of SFCH to modulate excess ROS and oxidative stress and the therapeutic effect of berberine have accelerated the wound closer. The controlled release of berberine from SFCH to wound sites

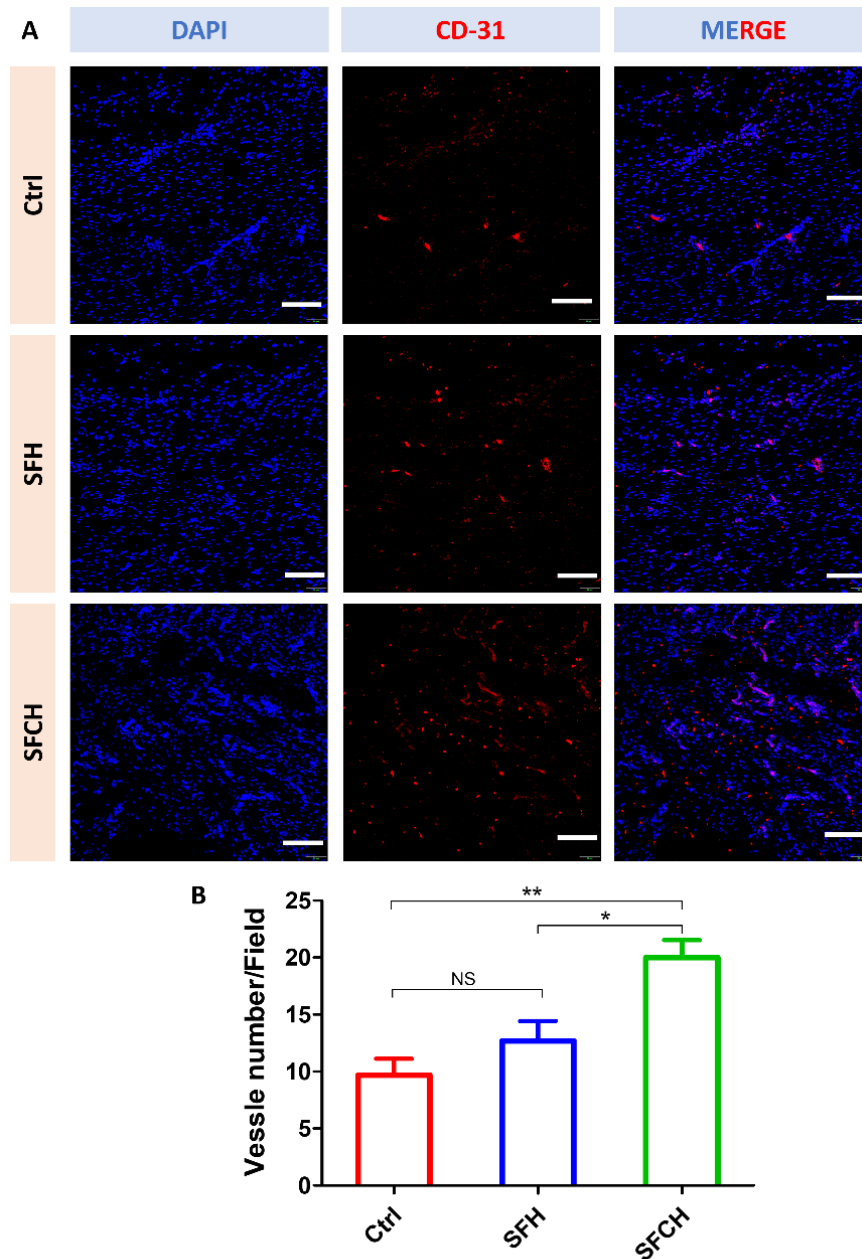


Figure 20. CD31 immunofluorescence staining. (A) Staining of skin section after 14 days. Nucleus was counterstained with DAPI. Scale bar 100 μ m. (B) Quantifications of vessel number present. N =3 for each group. * p <0.05, analyzed by one-way ANOVA.

has decreased the prolonged inflammation on the diabetic wound site. The antioxidant and anti-inflammatory effects of SFCH have been presumed to play an influential role in stimulating the healing process.

Collagen deposition and maturation are crucial processes in the remodeling stage of wound healing. Masson's trichrome stain was performed to identify the collagen deposition, maturation, and granular tissue formation at the wound site. Deposition of the collagen on all hydrogel-treated wounds was observed (Figure 19). However, the wound treated with SFCH showed the highest collagen deposition reflected by the deep blue staining and most orderly collagen rearrangement like normal skin samples and the presence of granular tissues compared to control and SFH treated wounds. Therefore, SFCH is an effective wound healing dressing formulation to manage oxidative stress and promote re-epithelialization and collagen deposition.

Immunofluorescence staining of CD31 glycoprotein at 21 days post-operation wound site was performed to investigate the angiogenesis responses with new tissue generation. Very few CD31 positive staining was found in the control group, while the SFCH treated wound showed large expression of CD31 positive cells (Figure 20A). The vascular density in control, SFH, and SFCH treated samples was 9.66, 12.66, and 20 vessels/field (Figure 20B). The control wound showed less vascular density at the healed site. The SFCH treated wound showed 2-fold increment of the vessels present at regenerated site. Angiogenesis enhances the oxygen and nutrients supply to cells, which augments cell activities in the proliferation phase of wound healing. Thus, the SFCH hydrogel dressing activates the angiogenesis process, stimulates blood circulation, and promotes the maturation of granulation tissues. Diabetic chronic wounds are associated with prolonged inflammation phase and enriched with macrophage cells. The F4/80 immunofluorescence staining was performed to determine the presence of macrophages in the wound site (Figure 21A). The macrophage number

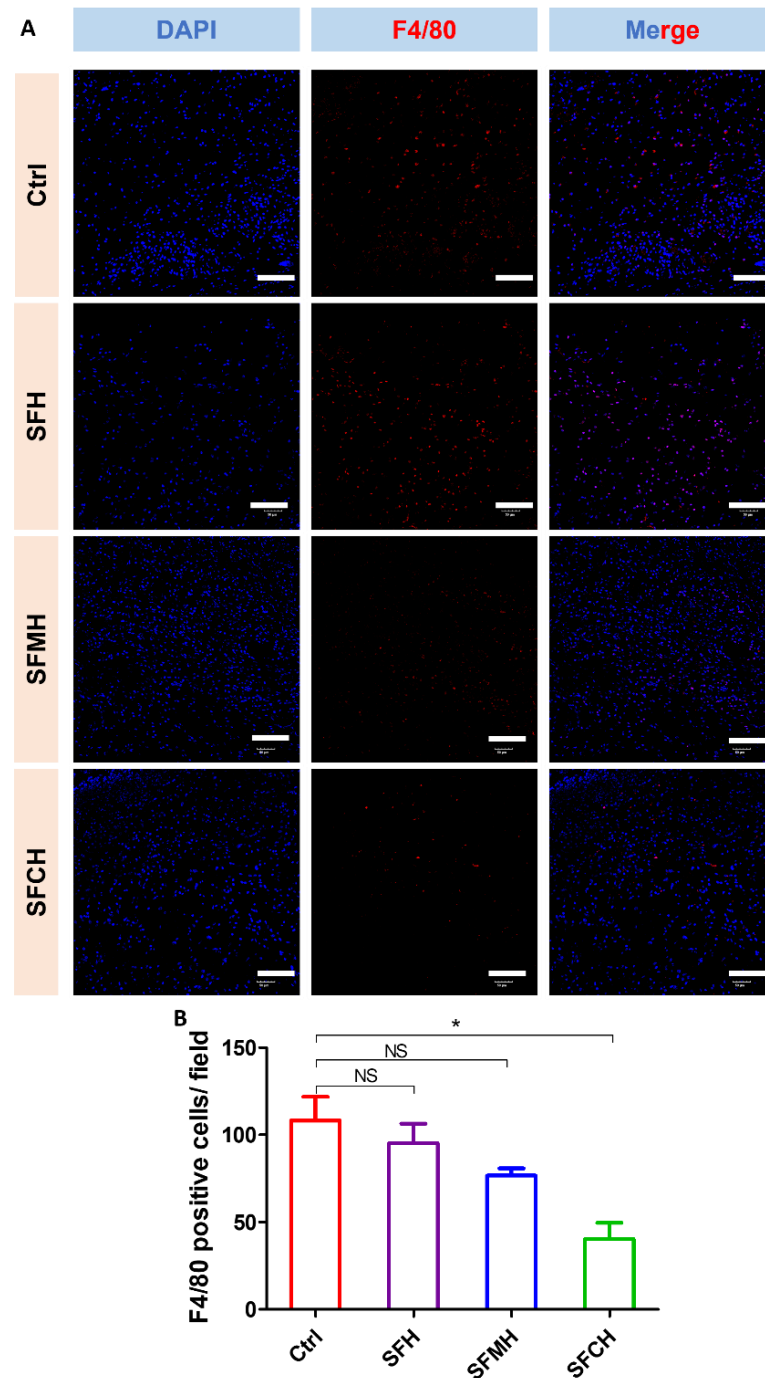


Figure 21. (A) Immunofluorescence staining of F4/80 macrophages in 5 days post-operation wounds. SFCH treatment significantly reduces the macrophage presence at wound site and transform to the proliferation phase of wound healing. Scale bar 100 μ m (B) Quantification of the macrophage number. N=3 for each group. * p < 0.05, analyzed by one-way ANOVA.

in control groups at 5 days post-operation wounds was significantly higher, and they decreased significantly on SFCH treatment (Figure 21B). This indicates the control wound is in

proinflammatory phase, while SFCH-treated tissues are in advanced phase of the wound healing process.

4.13 Conclusion

We have developed a composite hydrogel (SFCH) to accelerate wound healing in diabetic conditions. The SFCH dressing comprises natural ingredients silk fibroin (SF) protein, antioxidant melanin, and bioactive drug berberine. SFCH scaffold is highly mesoporous with suitable pore size for cellular infiltration and proliferation. Antioxidant biopolymer melanin present in the hydrogel was found to scavenge excessive ROS for a prolonged time in the wound bed. The SF matrix in SFCH effectively promotes cellular growth and enhances the migration of fibroblast cells, which helps tissue re-epithelialize in the wound site. The nontoxic SFCH dressing supported the wound scab formation in quick time and significantly increased the regenerative capacity by promoting cell migration. Furthermore, SFCH treatment enhanced the re-epithelialization of damaged skin barriers, deposition, maturation of collagen, and generation of new skin glands and blood vessels. Therefore, berberine-loaded, biocompatible, and antioxidant SFCH can be used to facilitate diabetic wound repair.

4.14 Experimental Methods

4.14.1 Materials

The CB gold variety cocoons of mulberry silkworm (*Bombyx mori*) were purchased from the Ramanagara silk cocoon market, Karnataka, India. Lithium bromide (MW: 86.84 g/mol) was purchased from Spectrochem India. Melanin, berberine chloride dihydrate (MW: 371.81 g/mol) and 3-(4,5 dimethylthiazol-2-yl)-2,5-diphenyltetrazolium bromide (MTT) dye (MW: 413.03 g/mol) were purchased from Merck. Fetal bovine serum (FBS) and Dulbecco's modified eagle medium (DMEM) were obtained from Invitrogen. NIH3T3 cells were purchased from the National Centre for Cell Science, Pune, India. Water used in the experiments (resistivity: 18.2 M Ω cm at 25 °C) was obtained from the Barnstead GenPure water purifier system.

Absorbance and fluorescence measurements were performed on Agilent Cary series UV-vis NIR spectrophotometer and Agilent Cary Eclipse fluorescence spectrophotometer or SpectraMax i3x Microplate reader (Molecular Devices). Zeiss Gemini SEM 500, and JEOL, JEM 3010 were used for morphology characterization. Attenuated total reflectance-Fourier transform infrared spectroscopy (ATR-FTIR) spectra were recorded using GladiATR spectrometer (PerkinElmer). Rheological experiments were measured using Physica MCR 101 rheometer (Anton Paar).

4.14.2 SF Protein Extraction

Silk cocoons are made of fiber protein (SF: silk fibroin) and an adhesive protein called sericin. Fibroin was extracted from the silk cocoon following the previously described method with slight modification.^{28, 33} In brief, silk moth from the cocoons was removed by making a slit using a surgical blade on one side of the cocoon. Obtained cocoon was further cut into small pieces and cleaned with water. The cocoon pieces were boiled in 20 mM sodium carbonate solution for 30 min with constant stirring to remove the residual sericin proteins. The obtained white fiber was washed thoroughly with water and kept overnight for air drying. Dried SF fibers were dissolved in 9.3 M lithium bromide solution at 65-70 °C for 2 h and the solution was dialyzed in 13.4 kDa cellulose membrane against deionized water for 3 days. Water was exchanged every 12 h interval with fresh water. The obtained solution was centrifuged at 10000 g/min for 15 min at 4 °C to remove insoluble fiber debris. The resultant aqueous fibroin solution (~7%, w/v) was stored at -20 °C until further use.

4.14.3 Preparation of SFCH Formulation

SFCH formulation was prepared using three components viz., SF, melanin, and berberine. Sterile aqueous SF solution (500 µL, 4% W/V) was mixed with 0.005% of melanin (2.5 µL of 10 mg/mL melanin in DMSO) and 0.1% of berberine (25 µL of 20 mg/mL berberine in DMSO/water) through pipetting the solution. The resulting solution was kept at 37 °C to form

the hydrogel and the gelation was monitored through vial inversion method at different time points.

4.14.4 Morphological Analysis

Field emission scanning electron microscopy (Zeiss Gemini SEM 500) measurements were performed to understand the structural morphology of SFCH. SFCH was snap freeze in liquid nitrogen and lyophilized for 24 h. The lyophilized SFCH was kept in a desiccator for 24 h at room temperature under a vacuum to remove moisture. FESEM imaging was performed after fixing the lyophilized hydrogel on the carbon tape followed by gold sputting. Transmission electronic microscopy (TEM) was performed to determine the fiber length in SFCH scaffold. SFCH was mixed with the deionized water, vortex to remove the fibers from the SFCH scaffold and kept to settling the debris. The water part was drop cast on copper grid, stained with uranyl acetate, and images were captured on JEOL, JEM 3010 operated at 300 kV.

4.14.5 Fourier Transform Infrared Spectroscopy (FTIR)

The conformational transition of the SF protein during the gelation process was assessed by recording the FTIR spectra of the hydrogels. Hydrogel was prepared in a glass vial, cooled at -80 °C, and further frozen in liquid nitrogen, lyophilized to obtain a solid gel scaffold. The spectra of the solid gel scaffolds were recorded using an attenuated total reflectance-Fourier transformed infrared spectrometer (ATR-FTIR). The spectra were plotted as absorbance versus wavenumber.

4.14.6 Powder X-ray Diffraction (PXRD)

XRD patterns of the hydrogel samples were recorded with a Rigaku-99 (Miniflex) diffractometer using Cu K α radiation ($\lambda = 1.5406 \text{ \AA}$). Hydrogels were frozen in liquid nitrogen and dried in lyophilizer followed by vacuum drying at room temperature. XRD patterns were recorded from diffraction angle (2θ) 5° to 50° at a scan speed 3°/min.

4.14.7 Rheological Analysis

The mechanical strength of hydrogels was investigated using Physica MCR 101 Rheometer (Anton Paar) on a 25 mm parallel plate. The frequency sweep and shear strain measurements were performed to check the stability of the hydrogel. The dynamic strain sweep was performed to check the viscoelasticity range. The dynamic amplitude sweep was performed from 0.1% to 100% strain at a constant frequency of 10 rad/s. The frequency sweep was carried out in a constant strain of 0.3% over 0.1 to 100 Hz frequency range. The storage modulus (G') and loss modulus (G'') of hydrogels were plotted against the angular frequency (ω) and shear strain.

4.14.8 Swelling Ratio

SF hydrogel (SFH), SFMH, and SFCH were freeze-dried using lyophilizer, immersed in the phosphate buffer solution (PBS, pH = 7.4) at 37 °C. Hydrogel scaffold was taken out at different time interval and wiped with filter paper to remove the excess buffer solution. The wet weight of the hydrogel scaffold was measured. The swelling ratio of the hydrogel was calculated using following equation

$$\text{Swelling ratio} = \frac{W_s - W_d}{W_d}$$

Where W_s is the swollen material mass and W_d is the initial weight of the dried hydrogel.

4.14.9 Antioxidant Property of Hydrogels

The antioxidant efficacy of silk hydrogels was evaluated by 2,2-diphenyl-1-picrylhydrazyl (DPPH) radical scavenging assay. For these experiments, 25, 50, and 75 mg of the SFH, SFMH, and SFCH were mixed with 1 mL of 100 μ M DPPH solution in 95:5 ethanol/water. The samples were incubated at 37 °C and absorbance of the solutions was measured at 516 nm using a microplate reader. Percentage of radical scavenging activity was calculated from the following equation

$$\text{Scavenging activity (\%)} = \left[1 - \frac{(A_s - A_b)}{A_c} \right] \times 100$$

Where A_s = sample absorbance at 516 nm, A_b = absorbance of the blank sample at 516 nm, and A_c = absorbance of the control DPPH solution.

Radical scavenging activity of the hydrogels at different incubation times was plotted as function of percentage of radical scavenging. The radical scavenging property of the SFCH was compared with the ascorbic acid and free melanin and free berberine, and SFMH.

4.14.10 Drug Release Study

The release rate of encapsulated berberine from the hydrogel matrix was examined in PBS (pH =7.4) buffer solution. 100 mg of SFCH containing 0.1 mg of berberine was added into 1 mL of PBS buffer and incubated at 37 °C. The aliquots of the solution were taken out at pre-determined time points and absorbance was recorded. Release studies were performed in triplicates. The release behavior of berberine from the hydrogel matrix was determined by fitting the empirical relationship given by the Ritger–Peppas.

$$\frac{M_t}{M} = kt^n$$

Where M_t/M is the percentage of fraction of drug release at a defined time t ; k is the kinetic constant, and n is the diffusion exponent. The n values highly depend on the geometry of the matrix and release mechanism. The kinetic constant k measures the drug release rate. The exponential factor n values were determined from the following logarithm equation.

$$\log (M_t/M) = \log k + n \log t$$

4.14.11 Antibacterial Activity

The antimicrobial activity of hydrogels was tested against *Staphylococcus aureus* (MTCC 3160) standard bacterial strains obtained from IMTECH, Chandigarh, India, using spot-on lawn assay. The microbial culture plates were filled with 10 mL of nutrient agar (NA) and allowed to solidify. For each test organism, 20 μ L of pure culture of bacteria (OD= 0.1 at 600 nm) from culture broth were taken and poured into 15 mL sterilized glass tube containing media. The media was thoroughly shaken and poured into labeled nutrient agar plates and

allowed to solidify further. 5 μL of Tetracycline (100 $\mu\text{g}/\mu\text{L}$) was used as a positive control. SFH, SFMH, and SFCH hydrogels weight of 100 mg were placed on the agar plate. The organisms were kept in BOD incubator at 37 $^{\circ}\text{C}$ for growth for 12 h and inhibition was visualized.

4.14.12 Cell Viability Studies of SFCH

Toxicity of SFCH was assessed using mouse embryo fibroblast cell line (NIH3T3) through MTT assay using the established protocols. In brief, NIH3T3 cells were obtained from NCCS Pune, India, and maintained in Dulbecco Modified Eagle Medium (DMEM) cell growth media supplemented with 10% fetal bovine serum (FBS) and 1% penicillin-streptomycin. Cells were counted using a hemocytometer and 1×10^4 cells were seeded per well in 48 well plates and allowed to attach to the surface in a humidified CO_2 incubator (5% CO_2) at 37 $^{\circ}\text{C}$. After 24 h, cells were treated with SFCH solution and equal amount of cell culture media (control group) and further incubated for 24, 48, and 72 h. 20 μL of MTT solution (5 mg/mL in PBS) was added in each well after changing the media and incubated for 4 h. Dimethyl sulfoxide (DMSO) and methanol (50:50) were added to each well (100 μL / well) and incubated at 37 $^{\circ}\text{C}$ to dissolve the formazan crystals and absorbance was recorded in a microplate reader at 570 nm. Cell viability was measured using the following equation

$$\text{Cell Viability (\%)} = \frac{A_T}{A_C} \times 100$$

Where A_T is average absorbance of treatment wells and A_C is average absorbance of cell culture media treated wells. Control cells were considered as 100% viability.

4.14.13 Scratch Test Assay

The ability of hydrogels to support the re-epithelialization was evaluated in real-time by assessing the cell migration and expansion of cells toward scratch site in scratch test assay. The fibroblast NIH 3T3 cells were cultured in 48 well plates until complete confluency is attained. The scratch wound was created by using a sterile 20-200 μL pipette and scratch cell fragments

were washed with PBS. The cells were treated with SFH and SFCH and further cultured for 24 and 48 h. The cells were washed and fixed with 4% paraformaldehyde and the nucleus was stained with DAPI to visualize the cell nucleus for cell number quantification. The images were captured using Leica DMI8 microscope.

4.14.14 Cell Rescue from Oxidative Stress

To evaluate the antioxidant property of hydrogels, NIH 3T3 cell rescue study from hydrogen peroxide (H₂O₂) induced oxidative stress was performed. NIH 3T3 cells are plated in 96 well plates at 1×10^4 cells/well and cultured for 24 h. Cell culture media was removed and 200 μ M of H₂O₂ was added into the wells with different amounts of SFCH solution prepared in DMEM media. The cells were cultured for further 24 h and media was replaced with complete DMEM media. The viability of these cells was assessed by MTT assay. In addition, the ROS generated in the cells was quantified by 2',7'-dichlorofluorescein diacetate (DCFDA) assay. NIH 3T3 cells were cultured in 48 well plates at 2×10^4 cells/well for 24 h. Cells were treated with 20 μ M of DCFDA for 45 min followed by treatment with 200 μ M of H₂O₂ for 1 h in low serum containing media. Cells were washed with PBS (pH = 7.4) and imaged under Leica DMI8 microscope.

4.14.15 Animal Model and Hydrogels Treatments

Albino Wistar rats were maintained under 12 h light and dark cycles in the JNCASR animal facility. All animal experiments were performed according to the guidelines of the Institutional Animal Ethics Committee (IAEC), JNCASR. Experiment protocol (TG 002) was approved by the IAEC and Committee for Control and Supervision of Experiments on Animals (CPCSEA). Experimental group sizes were created based on statistical power, and feasibility. Rats weighing 200 ± 50 g were given a single intraperitoneal streptozotocin (STZ, 70 mg/kg doses) injection. After one week, the blood glucose level was monitored by collecting blood from the rat tail vein using ACCU-CHEK instant S glucose meter. STZ-treated rats with blood glucose levels higher than 300 mg/dL were considered as diabetic and used for the study. Before 8 -

12 h of surgery, rats were administered with an intraperitoneal buprenorphine (0.05 mg/kg) injection. Further, rats were anesthetized using ketamine (50 mg/kg/rat). An outline of 10 mm in diameter, was drawn by a surgical marker pen on the clean shaved shoulder. A full thickness wound was created using a scalpel blade. Rats were kept under continuous observation to make sure the applied hydrogel is not wiped out. Besides, position of wound was along the back of the neck, away from their mouth reach. The animals were divided into four groups (n=5 rats/group), and each was kept in separate wire cages. Hydrogels were applied on the wound sites and covered with sterile cotton gauze. In control groups only cotton gauze was used.

4.14.16 Wound Healing Analysis

Wound images were captured using a CCD camera from the day wounds were created (Day 0) until the wounds healed in each experimental group. During image capturing a ruler was kept beside the wounds for area calculation and size comparison under various conditions. Wound area was calculated using ImageJ software and wound closer rate were plotted at different time periods for evaluating healing efficacy.

4.14.17 Immunofluorescence Studies

For histological analysis, rats were euthanized 14 days after injury. Skin tissue samples were excised and fixed with 10% neutral buffer formalin. Tissues were dehydrated by using sucrose gradient from 10% to 30% (in PBS at 4 °C), embedded with OCT, and sectioned to 16 µm. Tissues were stained with hematoxylin-eosin (H &E) or Masson trichrome, and images were captured by Olympus confocal microscope. For the immunofluorescence study of CD31, antigen retrieval was performed in 10 mM acetate buffer (pH 6.0) for 20 min at 90 °C. Tissue sections were washed, blocked with 3% goat serum in 1% bovine serum albumin (BSA) for 1 h, treated with primary antibody CD31 (ABclonal, 1:100 dilution in 1% BSA) overnight, washed, and incubated with Alexa fluorophore 568 conjugated secondary antibody (1:400 dilution) for 1 h. DAPI was used to counterstain the nucleus. After 5 days of post-operation,

rats (n =3) were euthanized, and tissues were collected to determine the macrophage number by F4/80. Antibody staining was performed by using previously mentioned protocols. Images were captured by using Olympus confocal microscope. Blood vessel and macrophage numbers were counted using the Image J software.

4.14.18 Statistical Analysis

The mean \pm standard deviation was used to describe the data, and Graphpad Prism software was employed for data analysis. The significance level was accessed using One-way ANOVA. The significant difference was determined using Tukey's Multiple Comparison Test.

4.15 Appendix

- **Animal ethical form**



जवाहरलाल नेहरु उन्नत वैज्ञानिक अनुसंधान केन्द्र
(मान्यता प्राप्त विश्वविद्यालय)
JAWAHARLAL NEHRU CENTRE FOR ADVANCED SCIENTIFIC RESEARCH
(A Deemed University)
जक्कूर, बेंगलूर - 560 064, भारत / Jakkur, Bengaluru - 560 064, INDIA


CERTIFICATE

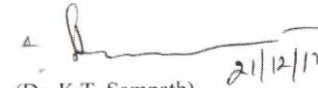
This is to certify that the project titled "Evaluation of drug entrapped hydrogel for wound healing and insulin entrapped hydrogel for insulin delivery in diabetes rat model. (TG 002)" submitted by Dr. Govindraju has been approved by the Institutional Animal Ethics Committee.

Name of Chairman / Member Secretary IAEC
Prof. Anuranjan Anand

Name of CPCSEA Nominee
Dr. K.T.Sampath

Signature with date (21.12.2017)


(Prof. Anuranjan Anand)


(Dr. K.T. Sampath) 21/12/17

4.16 References

1. Saeedi, P.; Petersohn, I.; Salpea, P.; Malanda, B.; Karuranga, S.; Unwin, N.; Colagiuri, S.; Guariguata, L.; Motala, A. A.; Ogurtsova, K. et al. On behalf of the IDF Diabetes Atlas Committee. Global and regional diabetes prevalence estimates for 2019 and projections for 2030 and 2045: Results from the International Diabetes Federation Diabetes Atlas, 9th edition. *Diabetes Res. Clin. Pract.* **2019**, *157*, 107843.
2. Zimmet, P.; Alberti, K. G.; Magliano, D. J.; Bennett, P. H. Diabetes mellitus on prevalence and mortality: Facts and fallacies. *Nat. Rev. Endocrinol.* **2016**, *12*, 616–622.
3. The effect of intensive treatment of diabetes on the development and progression of long-term complications in insulin-dependent diabetes mellitus. The diabetes control and complications trial research group. *N. Engl. J. Med.* **1993**, *329*, 977–986.
4. Jeganathan, V. S. E.; Wang, J. J.; Wong, T. Y. Ocular associations of diabetes other than diabetic retinopathy. *Diabetes Care* **2008**, *31*, 1905–1912.
5. Patti, G.; Cavallari, I.; Andreotti, F.; Calabro, P.; Cirillo, P.; Denas, G.; Galli, M.; Golia, E.; Maddaloni, E.; Marcucci, R. et al. Prevention of atherothrombotic events in patients with diabetes mellitus: Antithrombotic therapies to new-generation glucose lowering drugs. *Nat. Rev. Cardiol.* **2019**, *16*, 113–130.
6. Alicic, R. Z.; Rooney, M. T.; Tuttle, K. R. Diabetic kidney disease challenges, progress, and possibilities. *Clin. J. Am. Soc. Nephrol.* **2017**, *12*, 2032–2045.
7. Sims-Robinson, C.; Kim, B.; Rosko, A.; Feldman, E. L. How does diabetes accelerate Alzheimer disease pathology? *Nat. Rev. Neurol.* **2010**, *6*, 551–559.
8. Ghomi, E. R.; Khalili, S.; Khorasani, S. N.; Neisiany, R.E.; Ramakrishna, S. Wound dressings: Current advances and future directions. *J. Appl. Polym. Sci.* **2019**, *136*, 47738.

9. Boateng, J. S.; Matthews, K. H.; Stevens, H. N. E.; Eccleston, G. M. Wound healing dressing and drug delivery system: A review. *J. Pharm. Sci.* **2008**, *97*, 2892–2923.
10. Falanga, V. Wound healing and its impairment in the diabetic foot. *Lancet* **2005**, *366*, 1736–1743.
11. Martin, A.; Komada, M. R.; Sane, D. C. Abnormal angiogenesis in diabetes mellitus. *Med. Res. Rev.* **2003**, *23*, 117–145.
12. Schafer, M.; Werner, S. Oxidative stress in normal and impaired wound repair. *Pharmacol. Res.* **2008**, *58*, 165–171.
13. Singer, A. J.; Clark, R. A. Cutaneous wound healing. *N. Engl. J. Med.* **1999**, *341*, 738–746.
14. Gurtner, G. C.; Werner, S.; Barrandon, Y.; Longaker, M. T. Wound repair and regeneration. *Nature* **2008**, *453*, 314–321.
15. Eming, S. A.; Martin, P.; Tomic-Canic, M. Wound repair and regeneration: Mechanism, signaling, and translation. *Sci Transl Med.* **2014**, *3*, 265.
16. Werner, S.; Krieg, T.; Smola, H. Keratinocyte–fibroblast interactions in wound healing. *J. Invest. Dermatol.* **2007**, *127*, 998–1008.
17. Szabowski, A.; Mass-Szabowski, N.; Andrecht, S.; Kolbus, A.; Schropp-Kistner, M.; Fusenig, N. E.; Angel, P. Jun and JunB antagonistically control cytokine-regulated mesenchymal–epidermal interaction in skin. *Cell* **2000**, *103*, 745–755.
18. James, T. J.; Hughes, M. A.; Cherry, G. W.; Taylor, R. P. Evidence of oxidative stress in chronic venous ulcers. *Wound Repair Regen.* **2003**, *11*, 172–176.
19. Schafer, M.; Werner, S. Oxidative stress in normal and impaired wound repair. *Pharmacol Res.* **2008**, *58*, 165–171.

20. Hirose, A.; Tanikawa, T.; Mori, H.; Okada, Y.; Tanaka, Y. Advanced glycation end products increase endothelial permeability through the RAGE/Rho signaling pathway. *FEBS Lett.* **2010**, *584*, 61–66.
21. Li, J.; Chen, J.; Kirsner, R. Pathophysiology of acute wound healing. *Clin. Dermatol.* **2007**, *25*, 9–18.
22. Sharifi, S.; Hajipour, M. J.; Gould, L.; Mahmoudi, M. Nanomedicine in healing chronic wounds: Opportunities and challenges. *Mol. Pharm.* **2021**, *18*, 550–575.
23. Memic, A.; Abudula, T.; Mohammed, H. S.; Navare, K. J.; Colombani, T.; Bencherif, S. A. Latest progress in electrospun nanofibers for wound healing applications. *ACS Appl. Bio Mater.* **2019**, *2*, 952–969.
24. Jones, A.; Vaughan, D. Hydrogel dressings in the management of a variety of wound types: A review. *J. Orthop. Nurs.* **2005**, *9*, S1–S11.
25. Madsen, J.; Armes, S. P.; Bertal, K.; Lomas, H.; MacNeil, S.; Lewis, A. L. Biocompatible wound dressings based on chemically degradable triblock copolymer hydrogels. *Biomacromolecules* **2008**, *9*, 2265–2275.
26. Xiao, Y.; Reis, L. A.; Feric, N.; Knee, E. J.; Gu, J.; Cao, S.; Laschinger, C.; Londono, C.; Antolovich, J.; McGuigan, A. P. et al. Diabetic wound regeneration using peptide-modified hydrogels to target re-epithelialization. *Proc. Natl. Acad. Sci.* **2016**, *113*, E5792–E5801.
27. Datta, L. P.; Manchineella, S.; Govindaraju, T. Biomolecules-derived biomaterials. *Biomaterials* **2020**, *230*, 119633.
28. Manchineella, S.; Thirvikraman, G.; Khanum, K. K.; Ramamurthy, P. C.; Basu, B.; Govindaraju, T. Pigmented silk nanofibrous composite for skeletal muscle tissue engineering. *Adv. Healthc. Mater.* **2016**, *5*, 1222–1232.

29. Manchineella, S.; Thirivikraman, G.; Basu, B.; Govindaraju, T. Surface-functionalized silk fibroin films as a platform to guide neuron-like differentiation of human mesenchymal stem cells. *ACS Appl. Mater. Interfaces* **2016**, *8*, 22849–22859.
30. Nune, M.; Manchineella, S.; Govindaraju, T.; Narayan, K. S. Melanin incorporated electroactive and antioxidant silk fibroin nanofibrous scaffolds for nerve tissue engineering. *Mater. Sci. Eng. C* **2019**, *94*, 17–25.
31. Cheng, B.; Yan, Y.; Qi, J.; Deng, L.; Shao, Z.-W.; Zhang, K.-Q.; Li, B.; Sun, Z.; Li, X. Cooperative assembly of a peptide gelator and silk fibroin afford an injectable hydrogel for tissue engineering. *ACS Appl. Mater. Interfaces* **2018**, *10*, 12474–12484.
32. Chouhan, D.; Mandal, B. B. Silk biomaterials in wound healing and skin regeneration therapeutics: From bench to bedside. *Acta Biomater.* **2020**, *103*, 24–51.
33. Zhang, W.; Wang, X.; Wang, S.; Zhao, J.; Xu, L.; Zhu, C.; Zeng, D.; Chen, J.; Zhang, Z.; Kaplan, D. L. et al. The use of injectable sonication-induced silk hydrogel for VEGF165 and BMP-2 delivery for elevation of the maxillary sinus floor. *Biomaterials* **2011**, *32*, 9415–9424.
34. Maity, B.; Samanta, S.; Sarkar, S.; Alam, S.; Govindaraju, T. Injectable silk fibroin-based hydrogel for sustained insulin delivery in diabetic rats. *ACS Appl. Bio Mater.* **2020**, *3*, 3544–3552.
35. Wu, H.; Liu, S.; Xiao, L.; Dong, X.; Lu, Q.; Kaplan, D. L. Injectable and pH-responsive silk nanofiber hydrogels for sustained anticancer drug delivery. *ACS Appl. Mater. Interfaces* **2016**, *8*, 17118–17126.
36. Rezaei, F.; Damoogh, S.; Reis, R. L.; Kundu, S. C.; Mottaghitlab, F.; Farokhi, F. Dual drug delivery system based on pH-sensitive silk fibroin/alginate nanoparticles entrapped in PNIPAM hydrogel for treating severe infected burn wound. *Biofabrication* **2020**, *13*, 015005.
-

37. Park, Y. R.; Sultan, Md. T.; Park, H. J.; Lee, J. M.; Ju, H. W.; Lee, O. J.; Lee, D. J.; Kaplan, D. L.; Par, C. H. NF- κ B signaling is key in the wound healing processes of silk fibroin. *Acta Biomater.* **2018**, *67*, 183–195.
38. Hayden, M. S.; West, A. P.; Ghosh, S. SnapShot: NF- κ B signaling pathways, *Cell* **2006**, *127*, 1286–1287.
39. Qin, S.; Qin, L.; Zhang, C.; Liu, L.; Sun, W.; Li, N.; Wu, R.; Wang, X. p120-Catenin modulating nuclear factor- κ B activation is partially RhoA/ ROCK dependent in scratch injury. *Wound Repair Regener.* **2015**, *23*, 231–240.
40. Wang, L.; Wu, X.; Shi, T.; Lu, L. Epidermal growth factor (EGF)-induced corneal epithelial wound healing through nuclear factor κ B subtype-regulated CCCTC binding factor (CTCF) activation. *J. Biol. Chem.* **2013**, *288*, 24363–24371.
41. Liu, Y.; Ai, K.; Ji, X.; Askhatova, D.; Du, R.; Lu, L.; Shi, J. Comprehensive insights into the multi-antioxidative mechanisms of melanin nanoparticles and their application to protect brain from injury in ischemic stroke. *J. Am. Chem. Soc.* **2017**, *139*, 856–862.
42. Liu, Y.; Ai, K.; Lu, L. Polydopamine and its derivative materials: Synthesis and promising applications in energy, environmental, and biomedical fields. *Chem. Rev.* **2014**, *114*, 5057–5115.
43. Yamada, M.; Ishihara, K.; Ogawa, T.; Sakurai, K. The inhibition of infection by wound pathogens on scaffold in tissue-forming process using N-acetyl cysteine. *Biomaterials* **2011**, *32*, 8474–8485.
44. Das, M.; Goswami, U.; Kandimalla, R.; Kalita, S.; Ghosh, S. S.; Chattopadhyay, A. Iron-copper bimetallic nanocomposite reinforced dressing materials for infection control and healing of diabetic wound. *ACS Appl. Bio Mater.* **2019**, *2*, 5434–5445.
45. Wang, X.; Qiu, S.; Yao, X.; Tang, T.; Dai, K.; Zhu, Z. Berberine inhibits staphylococcus epidermidis adhesion and biofilm formation on the surface of titanium alloy. *Inc. J. Orthop. Res.* **2009**, *27*, 1487–1492.
-

46. Rajasekhar, K.; Samanta, S.; Bagoband, V.; Murugan, A.; Govindaraju, T. Antioxidant berberine-derivative inhibits multifaceted amyloid toxicity. *iScience* **2020**, *23*, 101005.
47. Annabi, N.; Mithieux, S. M.; Boughton, E. A.; Ruys, A. J.; Weiss, A. S.; Dehghani, F. Synthesis of highly porous cross-linked elastin hydrogels and their interaction with fibroblasts in vitro. *Biomaterials* **2009**, *30*, 4550–4557.
48. Vasconcelos, A.; Gomes, A. C.; Cavaco-Paulo, A. Novel silk fibroin/elastin wound dressings. *Acta Biomater*, **2012**, *8*, 3049–3060.
49. Hu, X.; Kaplan, D.; Cebe, P. Determining beta-sheet crystallinity in fibrous proteins by thermal analysis and infrared spectroscopy. *Macromolecules* **2006**, *39*, 6161–6170.
50. Discher, D. E.; Janmey, P.; Wang, Y. Tissue cells feel and respond to the stiffness of their substrate. *Science* **2005**, *310*, 1139–1143.
51. Pailler-Mattei, C.; Bec, S.; Zahouani, H. In vivo measurements of the elastic mechanical properties of human skin by indentation tests. *Med. Eng. Phys.* **2008**, *30*, 599–606.
52. Webb, K.; Hlady, V.; Tresco, P. A. Relative importance of surface wettability and charged functional groups on NIH 3T3 fibroblast attachment, spreading, and cytoskeletal organization. *J. Biomed. Mater. Res.* **1998**, *41*, 422–430.
53. Wlaschek, W.; Kochanek, K. S. Oxidative stress in chronic venous leg ulcers. *Wound Repair Regen* **2005**, *13*, 452–461.
54. Steiling, H.; Munz, B.; Werner, S.; Brauchle, M. Different types of ROS-scavenging enzymes are expressed during cutaneous wound repair. *Exp Cell Res* **1999**, *247*, 484–494.
55. Huh, A. J.; Kwon, Y. J. Nanoantibiotics: A new paradigm for treating infectious diseases using nanomaterials in the antibiotics resistant era. *J. Controlled Release* **2011**, *156*, 128–145.

Chapter 5

Cell Penetrating Peptides Derived from Intrinsically Disordered Ku- Protein for DNA Delivery

Hypothesis: The cellular uptake of active ingredients to accomplish their intended functions within the cellular milieu is a major challenge in biomedical sciences. Cell penetrating peptides (CPPs) are viable and attractive carriers to facilitate the effective delivery of active ingredients into cells. Herein, the design of CPPs derived from the disordered tail extension of DNA binding Ku-proteins was conceived.

Effective delivery of active ingredients into cells remains a major hurdle in realizing their potential activity. The negatively charged lipid bi-layer membrane act as semi-permeable filter allowing the passage of hydrophobic hormones, water, and small uncharged molecules.¹ Glucose, ions, and other hydrophilic nutrients are transported through protein channels or transporters present in membrane.² Consequently, the effective delivery of hydrophilic molecules, protein, DNA, and other large molecules remains a challenge.³ The negative charge of DNA and enzymatic stability are the major concern for gene therapy in treating inherited disorders, viral infection, and cancer among others.^{4,5} Several delivery vectors such as polymers,^{6,7} liposomes,⁸ dendrimers,⁹ exosomes,¹⁰ and CPPs¹¹⁻¹³ have been developed for efficient DNA delivery. These vectors were designed to interact with DNA, screen the negative charges, provide protection from enzymatic degradation, and facilitates their safe delivery inside the cell. Although viral vectors are efficient in DNA delivery, they suffer from immunotoxicity and genotoxicity. Non-viral vectors such as cationic polymers and liposomes induce toxicity to the cells.¹⁴ In this context, cell-penetrating peptides (CPPs) have established themselves as efficient tools to deliver active ingredients through the biological membrane.^{15,16} After the discovery of the protein transduction domain in the transactivator of transcription protein in 1988, several natural and synthetic peptides evolved as CPPs.^{17,18} These CPPs are diverse polycationic peptides or protein domains with 5-40 amino acid sequences.¹⁹ The well-established chemical synthesis and easy structural modulation of CPPs provide enormous advantages compared with other delivery vehicles. The natural occurrence of amino acids provides the biocompatibility of CPPs and makes them superior delivery agents.²⁰ The intracellular delivery of various therapeutic cargoes by CPPs was extensively studied in the biomedical field.^{21,22} Majority of CPPs contains positively charged arginine and lysine residues known to interact with negatively charged lipids or carbohydrates present in membrane through electrostatic interaction and facilitate the cellular entry. Peptide interaction with membrane

increases local concentration in the vicinity and enhance the uptake profile. Cationic CPPs in the native state exist in random coil structure but transform to order secondary structures upon interactions with cell membrane.²³ Structural folding onto membrane helps in cellular translocation of some CPPs. However, the peptide folding associated with enhanced self-association on membrane layer induces potent membrane lytic behavior limiting the applicability as delivery vehicle.

In this context, we have chosen the intrinsically disorder proteins (IDPs), a class of proteins lacking well-defined three dimensional conformations to identify a new class of potent CPPs.^{24,25} Nevertheless, IDPs have vital regulatory roles in macromolecular recognition, signalling, and compartmentalization through protein-protein and protein-nucleic acid interactions.^{26,27} IDPs exhibit unique characteristic properties of low sequence complexity, poor hydrophobicity, high net charges, and repeated amino acid sequences.²⁸⁻³¹ Many experimental and computational studies have revealed that nucleoid-associated protein (Hu protein) and non-homologous DNA end-joining Ku-protein have IDP sequences at the N-terminal, which regulates the DNA binding affinity.³²⁻³⁴ The IDP sequences in heparin-binding extracellular protein hemagglutinin aid the mycobacterium pathogenesis through interaction with host epithelial cells containing negatively charged heparan sulfate proteoglycans.³⁵ The functional activities of these IDPs inspired us to design a set of intrinsically disordered peptides containing AAKKA and PAKKA repeat sequences as potential CPPs (Figure 1). The presence of the proline residues provides structural length confining properties which helps in structural compaction. Peptides were synthesized, and membrane permeability efficacy was evaluated in normal and cancer cell lines. One of the designed peptides Ku-P4 has shown good cell membrane penetration and cytocompatibility. Further DNA binding studies indicates Ku-P4 forms cationic DNA polyplex, which show effective cell penetration and transfection efficiency.

5.1 Design and Synthesis of IDP-based CPPs

The disorder regions of IDPs play a crucial role in protein-nucleic acid interactions. These disordered regions (70%) are abundant in the tail domains of IDPs and perform essential regulatory functions through protein-DNA interactions. Lysine-rich cationic C-terminal of Ku-protein has shown crucial regulatory role in DNA compaction and chromatin organization.^{13,14} Specifically, the C-terminal of Ku-protein acts as affinity tuner and facilitates sequence-specific interaction with DNA. Molecular recognition by IDPs involves conformational selection, flexibility modulation, competitive binding, and tethering. These tail regions contribute to fast protein diffusion, exceeding the theoretical rate limit. The flexible disorder region consisting of proline, alanine, and lysine is known as PAK-tail of DNA binding protein,

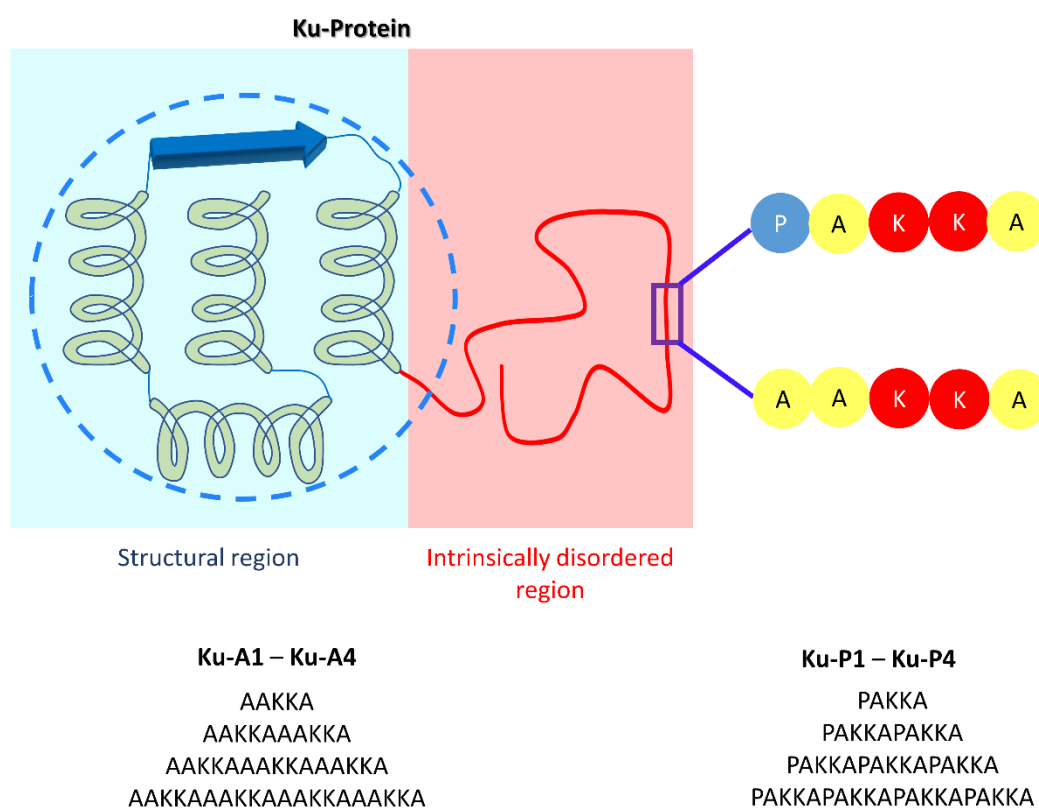


Figure 1. Schematic of Ku-protein structural conformations. N-terminal of Ku-protein maintains proper folded structure and C-terminal is intrinsically disorder region. C-terminal contains repeats of AAKKA and PAKKA sequences. Selected peptide sequences from the C-terminal disordered tail region to study their potential role as CPPs.

which is commonly observed among the three evolutionary IDP types, constrained disorder, non-conserved disorder and intrinsically disorder. The conserved disordered region with repeat of a few amino acids is a result of rapid evolution in these sequences. The PAK tails are widespread in bacterial proteomes but not common in human proteomes except the histone proteins. In eukaryotic proteomes, PAK tails are found in histone proteins and possess functional similarity with bacterial histone-like proteins and nucleoid-associated proteins.¹⁶ The electrostatic interaction between negatively charged phospholipid and lysine residues of PAK-tail effect the membrane rearrangements to allow its delivery into cell.

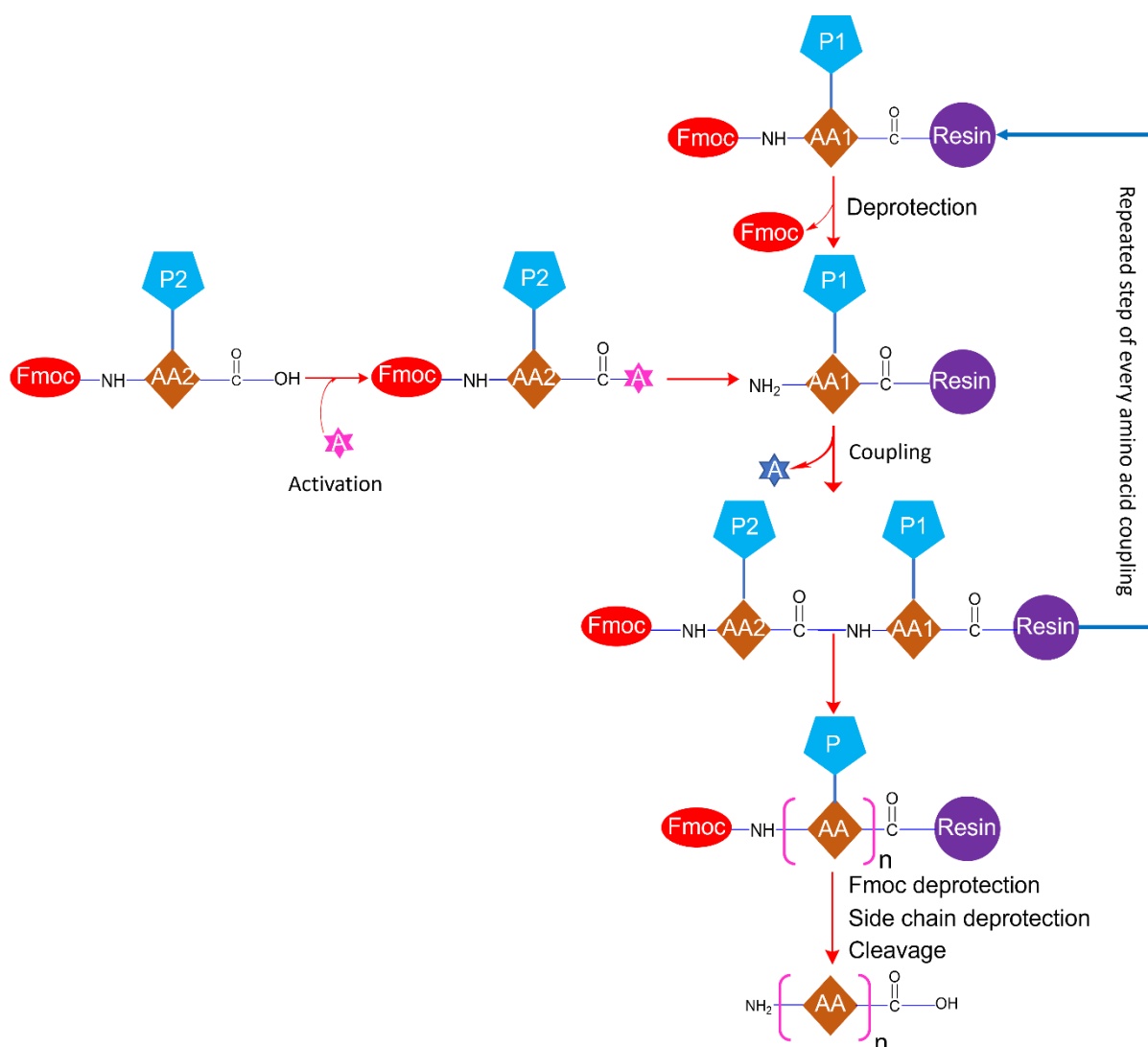


Figure 2. Schematic illustration of the solid phase peptide synthesis (SPPS) protocol used for the synthesis of designed peptides shown in Figure 1.

Intriguing properties of PAK tails have motivated us to evaluate their membrane permeability, DNA binding, and cellular delivery. The size and the charge density of peptides are decisive factors for DNA delivery and transfection efficacy. Thus, two series of peptides derived from the Ku-protein C-terminal with PAKKA and AAKKA repeats were chosen to identify a potential CPP candidate with superior membrane penetration ability, plasmid DNA compaction, and delivery. The peptides were synthesized using standard Fmoc solid-phase peptide synthesis (SPPS) protocols (Figure 2). Peptides were labelled with 5,6-carboxyfluorescein (CF) at the N-terminal to evaluate cell membrane penetration proficiency. Purification of peptides was performed by RP-HPLC, and integrity was ascertained by HRMS or MALDI analysis.

5.2 Secondary Structure Analysis

The secondary structure of the peptides was assessed by circular dichroism (CD) spectroscopy in phosphate buffer saline (PBS, 10 mM, pH 7.4). Ku-A4 and Ku-P4 in PBS showed broad negative cotton effect beginning from 216 nm and persisting to 190 nm, along with positive cotton effect between 230 nm to 216 nm, indicating the random coil conformation in PBS

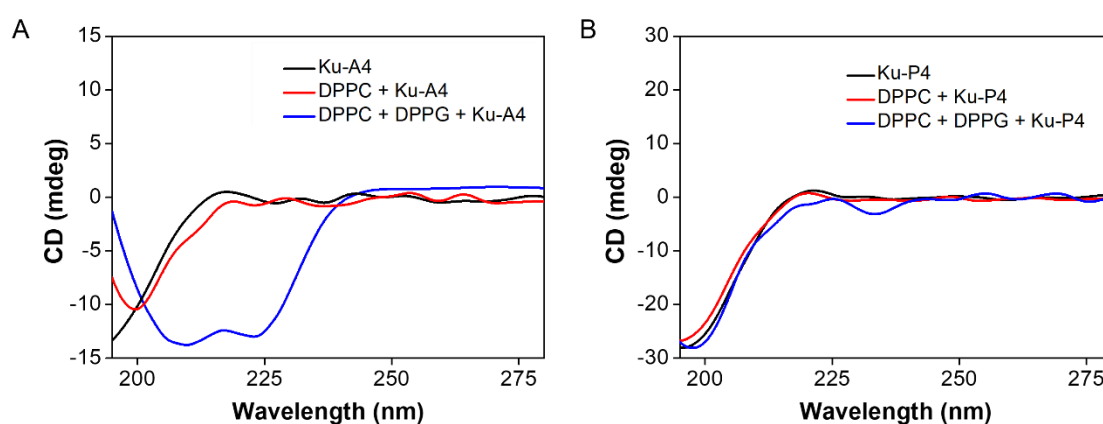


Figure 3. Secondary conformations of Ku-peptides. (A) CD spectra of Ku-A4 in PBS, zwitterionic, anionic model lipid membrane. Ku-A4 adopts helical conformation in presence of anionic lipid membrane. (B) CD spectra of Ku-P4 demonstrated Ku-P4 retains its secondary conformation in presence of model lipid membrane.

(Figure 3A, 3B).^{36,37} Further, CD spectroscopy was performed in zwitterionic and anionic model lipid membrane in PBS. Ku-P4 peptide displayed no characteristic change of CD signal in both zwitterionic and anionic lipid membranes. The peptide Ku-P4 remained mostly in disordered random coil conformation in the model lipid membrane. The bulky and hydrophobic proline residue induces the higher hydration of its own backbone and adjacent amino acid sequences, impedes the hydration of the peptide backbone, and restricts the conformational transition. Thus, proline residues altered the rigidity, backbone flexibility and augmented the conformational heterogeneity in the peptide backbone. However, significant conformational transition was observed in peptide Ku-A4 in anionic lipid membrane. The characteristic cotton effect of random coils conformations was diminished, and dominant-negative cotton effect at 222 nm and 210 nm was observed in anionic lipid membrane. Thus, peptide Ku-A4 transformed into ordered helical conformation. The alanine residues do not play significant role in preserving the intrinsically disorder conformations.³⁸ Whereas the proline unit inhibits peptide folding in membrane proximity.

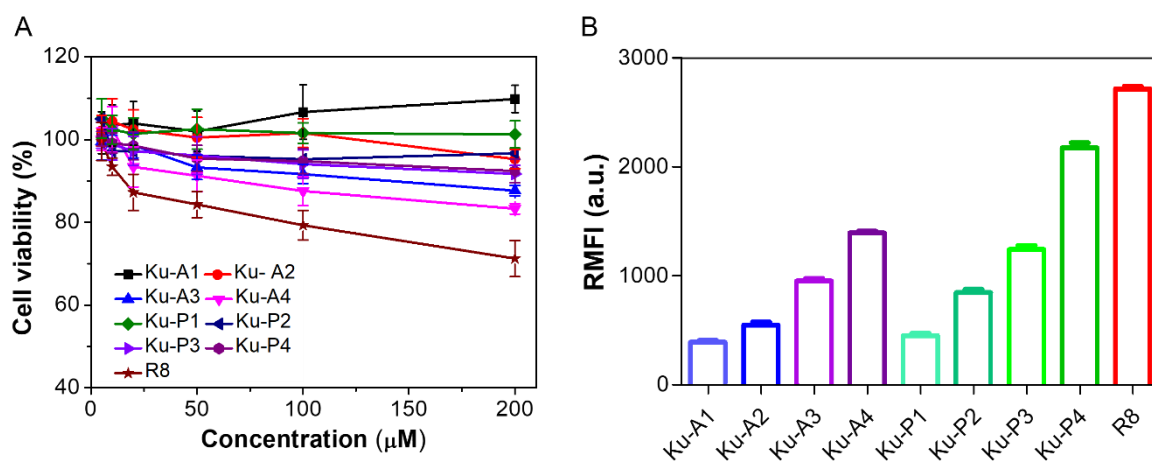


Figure 4. (A) Viability of L929 cells in the presence of 1-200 μM of Ku-peptides at 24 h incubation. The cell viability remains more than 90% even at 200 μM concentration of all PAKKA series peptides. Relatively the cell viability was declined in Ku-A3 and Ku-A4 peptides. While stearyl-R8 showed gradual decrease in the cell viability with increasing concentration. (B) FACS analysis of 10 μM of carboxyfluorescein (CF) labeled peptide after 3 h incubation. Peptides Ku-A4 and Ku-P4 showed good cell membrane penetration comparable to the R8 peptide.

5.3 Cytocompatibility Assessment

The biocompatibility of Ku-peptides was evaluated to assess their applicability in L929 cells. All PAKKA based Ku-peptides exhibited excellent cell viability due to their non-toxic nature, and cell viability remains more than 90% in the concentration range of 10 μ M to 200 μ M. However, the longer AAKKA peptides Ku-A3, Ku-A4 showed slight toxicity at higher concentrations. Cell viability declined to 87% and 80% for Ku-A3 and Ku-A4 at 200 μ M of peptide. The drop of the cell viability by Ku-A3 and Ku-A4 peptides is in agreement with their structural folding in negatively charged lipid membrane observed in CD analysis. The commercially available arginine-rich R8 peptide has shown considerable toxicity with reduced cell viability of 70% at 200 μ M concentration (Figure 4A).³⁹ Cell viability study has confirmed excellent cytocompatibility of Ku-P4 and its possible utility in cellular experiments.

5.4 Cellular Uptake

The cell penetration efficacy of Ku-peptides in L929 cells was evaluated by FACS analysis. For these experiments, a non-toxic concentration of 10 μ M was chosen to investigate the cell-based intercellular uptake studies of all Ku-peptides. The uptake profile showed superior cell penetration ability of Ku-A4 and Ku-P4 compared to other Ku-peptides in the series. Among the two, the uptake of Ku-P4 was higher than the peptide Ku-A4 and comparable to control CF-R8 (Figure 4C). The higher cell membrane permeability of Ku-P4 and Ku-A4 is due to more lysine residues in peptide backbone and the peptide length. The superior membrane penetration of Ku-P4 might be attributed to hydrophobic proline residues and its rigidity, and conformational stabilization.

The fluorescence microscopy was performed to visualize the internalization pattern of CF labelled peptides. Both Ku-A4 and Ku-P4 efficiently entered the cell compared to other peptides in the series. The peptide Ku-A4 and Ku-P4 were largely distributed in entire cell

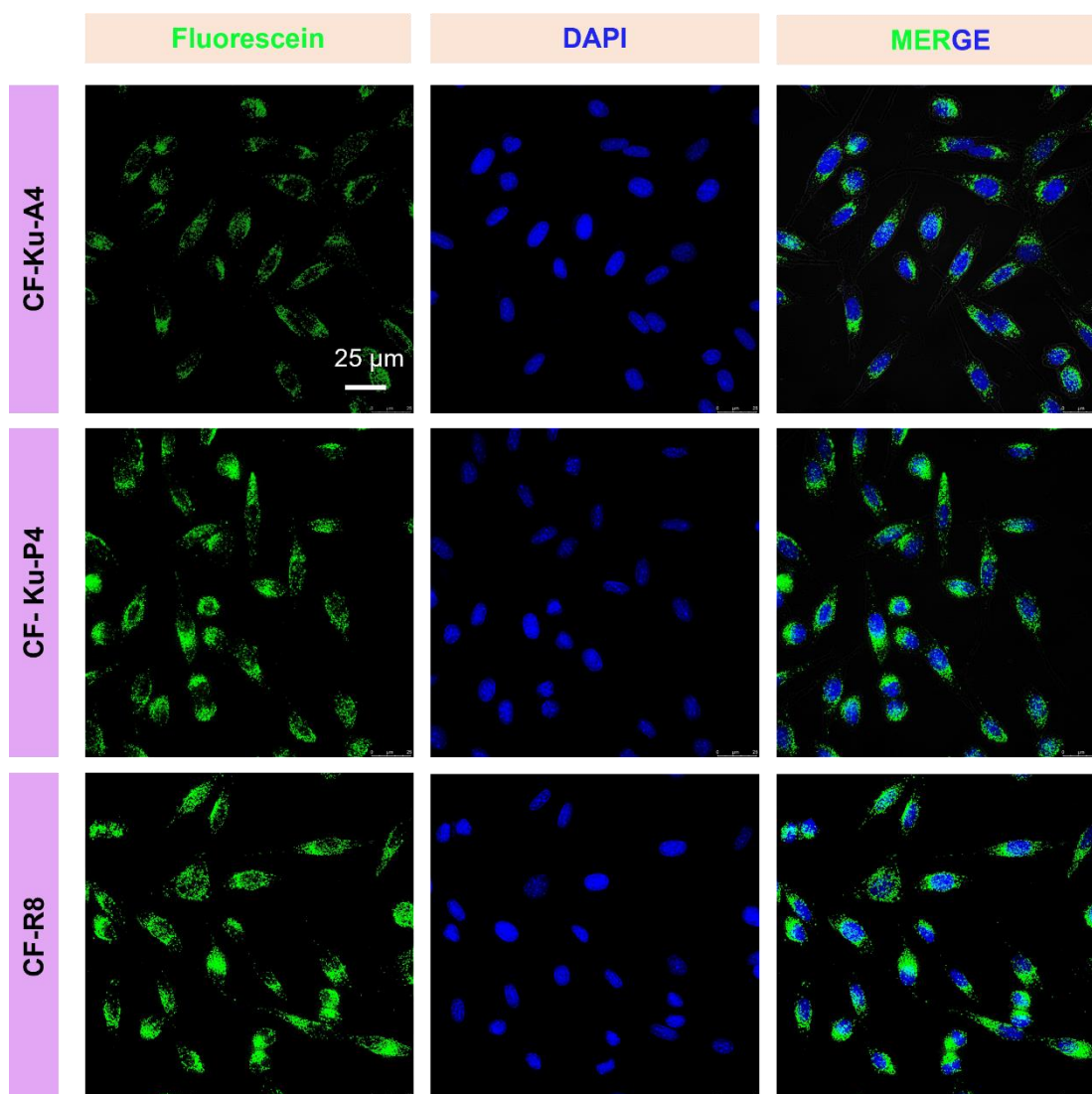


Figure 5. Fluorescence microscope images show the internalization pattern of peptides Ku-A4, Ku-P4, and CF-R8 in L929 cells (10 μ M). Ku-A4 and Ku-P4 effectively penetrated the cell membrane and distributed into the cytoplasm (scale bar: 25 μ m).

cytosols and nucleus of L929 cells (Figure 5). However, the other Ku-peptide derivatives does not effectively penetrate the cell membrane (Figure 6). Thus, more lysine residues present in peptide backbone of Ku-P4 and Ku-A4 has influential role in peptide uptake.

5.5 DNA Binding Studies

The promising cellular uptake of Ku-P4 and Ku-A4 motivated us to investigate their ability to deliver plasmid DNA into the cell. The DNA binding efficacy of Ku-peptides

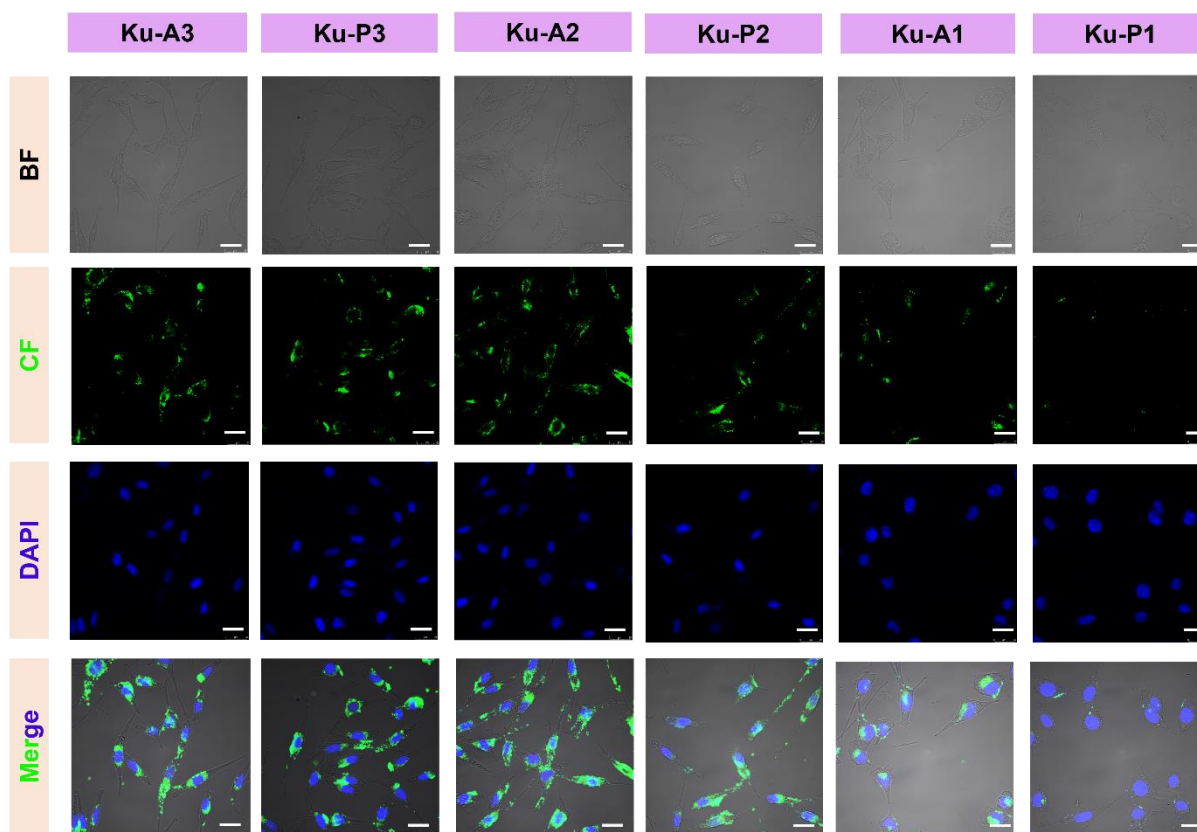


Figure 6. Fluorescence microscope images show the internalization pattern of Ku-A1, Ku-A2, Ku-A3, Ku-P1, Ku-P2, and Ku-P3 peptides in L929 cells. The uptake was significantly reduced with the length of the peptide sequence (scale bar: 25 μm).

were investigated by the DNA bound dye displacement assay.^{40,41} The Ku-peptides have positively charged lysine residues in their sequence which has the ability to interact with the negatively charged phosphate backbone of DNA through electrostatic and hydrogen bonding interactions. Ethidium bromide (EtBr), a DNA intercalating dye has significantly high fluorescence in DNA bound state compared to the free state due to stable intercalation between the hydrophobic DNA base pairs, which restricts it in planer conformation. In DNA bound state EtBr has strong emission at 607 nm, which was titrated by sequential addition of Ku-peptide. Upon stepwise addition of 1 μM Ku-peptides, the EtBr fluorescence was decline due to displacement from DNA. The significant quenching of the EtBr fluorescence was observed

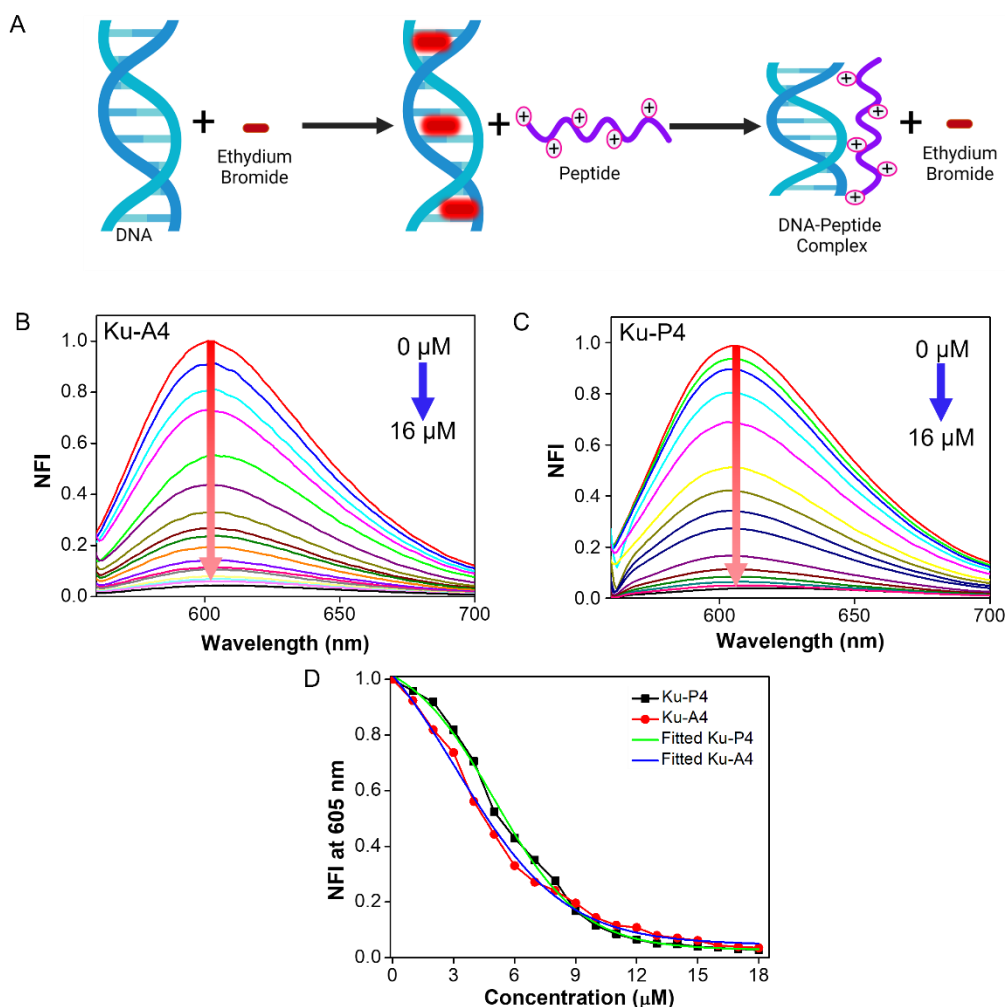


Figure 7. Dye displacement assay. (A) Schematic of EtBr binding with DNA and its displacement on peptide binding. (B, C) Normalized EtBr fluorescence upon titration with the successive addition of peptide Ku-A4 and Ku-P4. (D) Fitting curve of dye displacement with peptide concentration.

with minimal concentration variations for Ku-A4 and Ku-P4 (Figure 7B, 7C). Complete EtBr displacement was observed at 15 μM of Ku-A4 and Ku-P4 peptide. However, complete fluorescence quenching of the EtBr for Ku-A3 and Ku-P3 was observed at 150 μM and 200 μM , respectively (Figure 7D). However, the peptides Ku-A1, Ku-A2, Ku-P1 and Ku-P2 did not show any significant DNA binding ability. The EtBr displacement was attributed to the strong interaction between the peptide and DNA phosphate backbone. Peptide binding transform the DNA conformations into compact structure and reduces the distance between

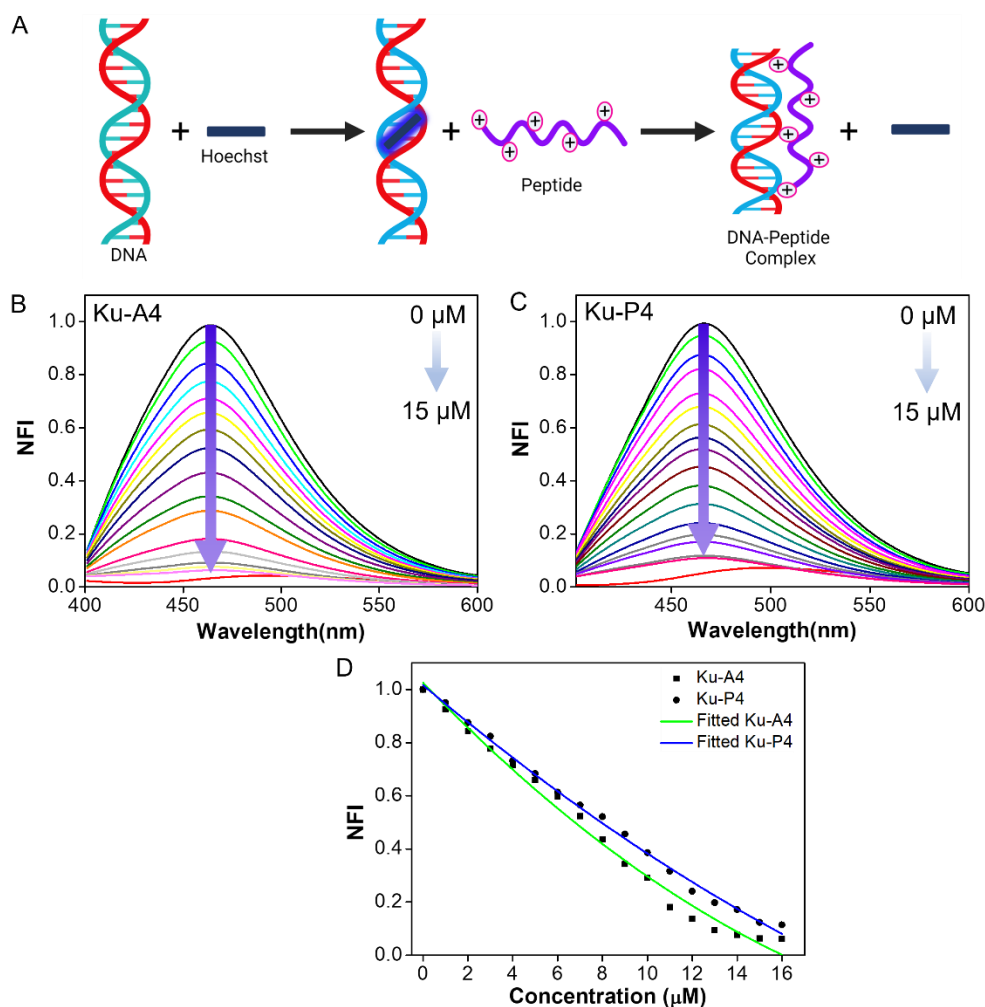


Figure 8. Hoechst dye displacement assay. (A) Schematic of minor groove binding site of Hoechst and its displacement upon peptide binding. (B, C) Normalized Hoechst dye displacement in presence of Ku-A4 and Ku-P4. (D) Fitting curve of normalized Hoechst displacement with concentrations.

base pairs. The intercalator dye EtBr not able to fit inside the base pairs and displaced from DNA.

The DNA binding ligands can interact with DNA in its minor grooves and major grooves. Proteins are reported to bind major grooves of DNA, and peptides prefer the minor grooves as an ideal site for binding. Thus, we have studied the groove binding ability through the Hoechst dye displacement assay.²⁷ Hoechst, the bis-benzimide dye known to interact at minor grooves of DNA and upon binding exhibit enhanced fluorescence at 460 nm. The Hoechst bound

ctDNA was titrated with sequential addition of peptides, and the fluorescence at 460 nm was monitored. The binding of peptide interferes with the Hoechst binding at DNA minor groove sites, which result in the reduction of fluorescence at 460 nm. Peptide Ku-A4 and Ku-P4 completely displaced the Hoechst at 10 μM and 12 μM concentrations, respectively, due to their interaction with DNA through lysine units (Figure 8B, 8C). Hoechst displacement from the DNA grooves confirmed the binding of peptide in the minor groove or transform the DNA into a compact structure. Thus, the dye displacement studies imply the strong binding affinity of Ku-A4 and Ku-P4 peptides to DNA and condensation into compact structures.

The peptide-DNA complexation was visualized through agarose gel electrophoretic mobility shift assay. Circular plasmid DNA (pDNA, 4.7 kb, 100 ng) was treated with the varying

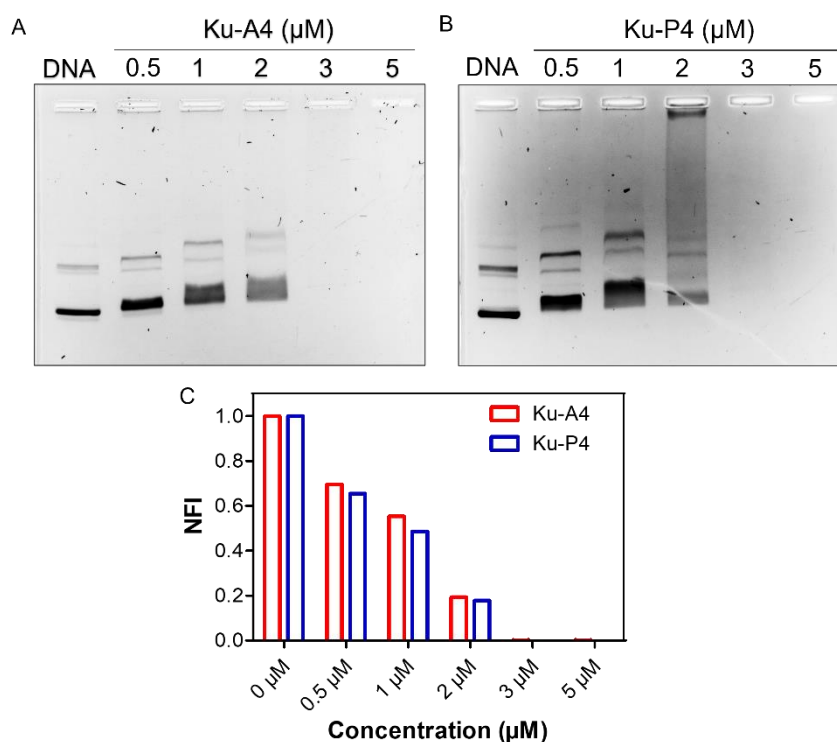


Figure 9. (A, B) Agarose gel electropherogram of plasmid DNA (200 ng) and polyplex formed with the Ku-A4 and Ku-P4. 0.5 to 5 μM of peptides. DNA bands were gradually decreased and completely disappeared at 3 μM indicating complete condensation of DNA in the presence of peptide. (C) Quantification of DNA band intensity with peptide concentrations.

concentrations of peptides and incubated at 4 °C for 3 h. These samples were loaded in 1% agarose gel in 10 mM TBE buffer, and electrophoresis was performed at 140 V for 1 h. The DNA band was visualized using DNA binding dye EtBr. Plasmid DNA typically showed three bands in agarose gel electrophoresis corresponding to its supercoiled, open circular, and linear form. Upon binding with the peptide, the DNA movements toward positively charged electrode was retarded and DNA was localized to gel well (Figure 9A, 9B). With increasing peptide concentrations, the DNA band intensity decreases and completely disappears due to condensation of DNA. Both Ku-A4 and Ku-P4 have shown complete condensation of DNA at 3 μ M of peptide (Figure 9A, 9B). The dragging of the DNA bands after the addition of peptide is an indication of the electrostatic interactions between the peptide (lysine units) and DNA phosphate backbone.⁴² Thus, Ku-A4, Ku-P4 peptides have strong binding interaction with DNA and are promising DNA condensing agents.

DNA conformational transition upon peptide binding was ascertained by CD spectroscopy. The double-stranded ctDNA exhibit negative cotton effect at 245 nm corresponding to backbone helicity, and a positive cotton effect at 275 nm arises from the nucleobase π - π stacking in B-conformation. Upon increasing the peptide concentration, the ellipticity at 275 nm gradually decreased along with the concomitant redshift of the signal due to the interaction of peptides with ctDNA (Figure 10A, 10B).^{43,44} The negative cotton effect at 245 nm also moderately decreased with increasing concentration of peptides, indicating the distortion of the helicity upon peptide binding. These results correlated with displacement assay data with the minor groove binding Hoechst dye. Nevertheless, the ctDNA CD cotton effect pattern signifies the B-conformation was preserved with compact form after peptide interaction. Although the agarose gel retardation studies showed the condensation of DNA at 3 μ M of Ku-peptides, the complete compaction of DNA require 25 μ M of peptides. This indicates

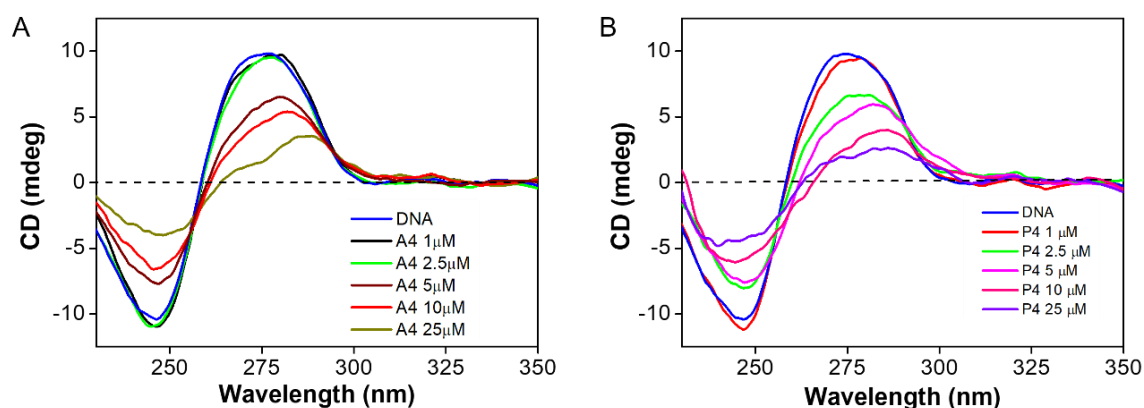


Figure 10. CD spectra of the ctDNA with increasing Ku-A4 (A) and Ku-P4 (B) concentration. The band intensity of the DNA gradually changes with peptide concentration due to DNA compaction. Complete compaction was observed at 25 μM peptides.

the complete condensation of ctDNA at 25 μM concentration of peptide transform it into compact aggregates or condensates.

The size and charge of the polyplex formed by Ku-peptides were characterized by combination of dynamic light scattering (DLS) and ζ -potential measurements. pDNA (50 $\mu\text{g}/\text{mL}$) in Tris-HCl buffer (10 mM, pH 7.4) were treated with different concentrations of Ku-A4 and Ku-P4, incubated at 4 $^{\circ}\text{C}$ for 3 h. The only pDNA has size of 180 nm (Figure 11B) due to its unorganized random structure. In the presence of 5 μM of peptide, DNA conformation becomes organized to condensed polyplex architectures, and hydrodynamic radius reduces to 70 nm (Figure 11B, 11C). The polyplex sizes were further increased to 140 nm with concentration of peptides due to further deposition of peptides in the condensate. Polyplex size distribution was quite similar for both the Ku-peptides. The ζ -potential measurement indicates the charge reversal of negatively charged DNA upon binding with positively charged peptide. The DNA has a potential of -50.33 mV, which became $+10.56$ mV at 5 μM of Ku-A4 and further increased to $+16.4$ at 25 μM peptides due to increment in phosphate (DNA) to amine (peptide) charge ratio (Figure 11D). The Ku-A4 peptide also showed ζ -potential of $+13.20$ at

5 μM of peptide concentration which further increased to +21.1 at 25 μM of peptide concentration (Figure 11E). The DLS studies indicate Ku-peptides transformed unorganized random DNA structures into compact condensed particles. The polyplex positive ζ -potential will enhance cellular uptake through the negatively charged cell membrane.

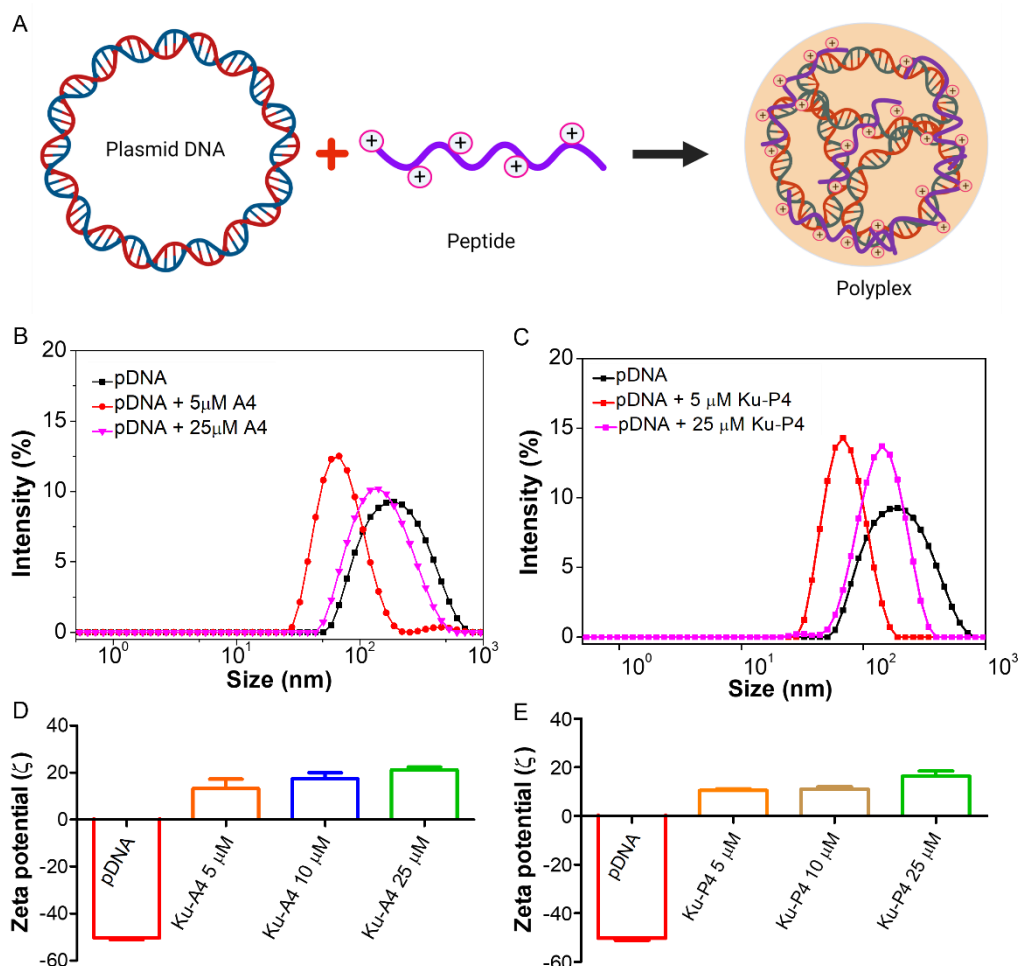


Figure 11. (A) Schematic of the peptide binding and condense particle formation of DNA with peptides. (B, C) The hydrodynamic size of the free plasmid DNA and at different concentrations of Ku-A4 and Ku-P4. Interactions between peptides and DNA decrease the size of DNA. The hydrodynamic radius further increases with higher peptide concentration indicating the further attachment of the peptides and formation of polyplex. (D, E) ζ -potential of the DNA and polyplex formed after condensation of the DNA. Condensation transformed the negative charged DNA into the positively charged polyplex.

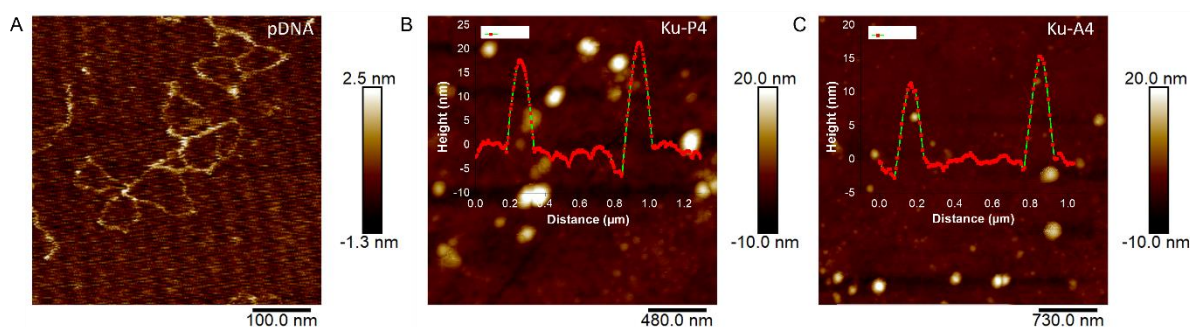


Figure 12. AFM images of the pDNA (A) and polyplexes with 25 μM of Ku-P4 (B) and Ku-A4 (C). The AFM images show nanoparticle nature of polyplexes.

The nature of DNA condensates was further investigated by atomic force microscopy (AFM). Free plasmid DNA displayed a thread-like morphology due to its unstructured loose structure (Figure 12A). While the DNA condensates are nanoparticles in nature with diameter of 110–160 nm (Figure 12B, 12C). The result confirmed DNA structural transformation upon binding with the Ku-peptides. There was no free DNA structure observed in the presence of Ku-A4 and Ku-P4. Thus, all biophysical studies correlate the DNA compaction ability of Ku-A4 and Ku-P4. Altogether, the nanoparticle polyplex with high surface positive charges might enable efficient cellular uptake and successful DNA delivery.

The stability of the polyplex in biological media has an important role in their DNA transfection efficiency. The biological media containing proteins and ions can interact with peptides and destabilize the polyplex, resulting in degradation of DNA by nuclease enzymes. Therefore, the polyplex stability in different concentrations of sodium chloride (NaCl) solution was assessed in agarose gel retardation assay. pDNA (150 ng) was condensed with 25 μM of the Ku-peptides to form the polyplexes and the polyplexes were further treated with different concentrations of (NaCl) solution (Figure 13A, 13B). The sample was incubated further for 6 h and loaded in agarose gel well, and gel electrophoresis was performed at 140 v for 1 h. The

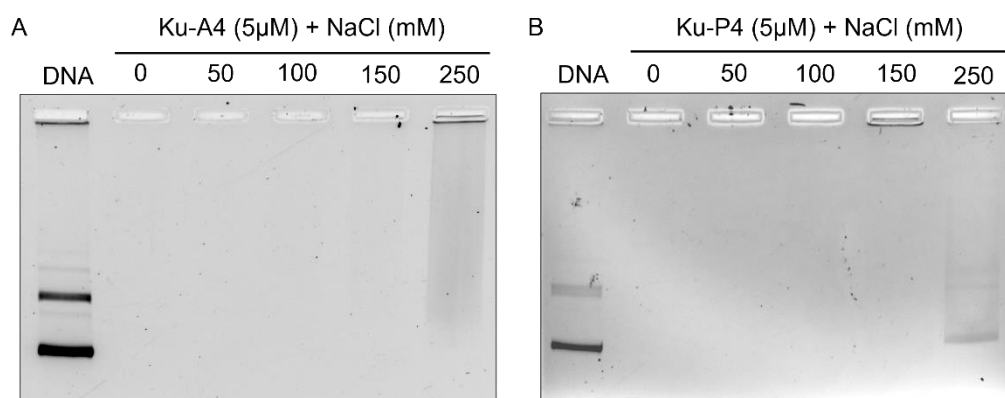


Figure 13. Electropherogram of polyplex of 5 μ M of Ku -A4 (A) and Ku-P4 (B) in presence of NaCl concentration from 0 mM to 250 mM. Polyplexes are stable at 150 mM salt concentration. Indicates the robustness of polyplex to maintain the DNA stability. Polyplex disassembles at 250 mM of NaCl. The dynamic nature of polyplex system will release the DNA inside the cell.

polyplexes are stable up to 150 mM of NaCl, and no DNA release was observed. The excellent salt tolerance of polyplex is indication of strong DNA binding with peptides and minimization of premature DNA release in biological buffers. However, the polyplex becomes unstable at 250 mM of NaCl and slowly starts to release the pDNA. This reversible binding of peptide and pDNA is essential for the de-condensation after polyplex delivery inside the cell by different cellular proteins or other ligands.

5.6 Plasmid DNA Transfection

The stable DNA polyplex formation with positive ζ -potential encourages us to check the DNA delivery efficacy of Ku-A4 and Ku-P4 peptides as DNA transfection agents. The transfection was carried out in HEK 293T cells, commonly used for transfection studies. The plasmid DNA pEGFP-C2 (4.7 kb) and peptide polyplex was prepared in optiMEM media and treated into low serum containing cells. The expression of the green fluorescent protein (GFP) inside the cell was visualized by the green fluorescence emission. The pDNA alone due to its negative charges was unable to penetrate the cell membrane, and no GFP transfection was observed. In the

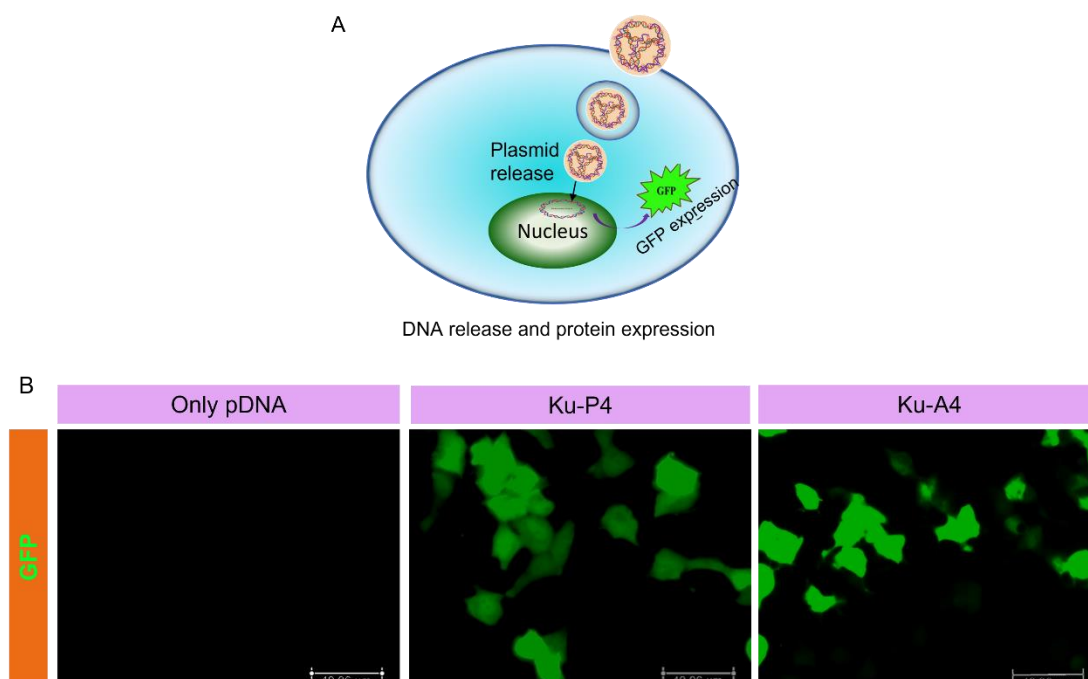


Figure 14. Schematic of polyplex delivery and DNA transfection. (B) Fluorescence microscopy images of pEGFP-C2 plasmid DNA transfected HEK-293 T cell using the peptide Ku-A4 and Ku-P4 after 48 h. The GFP fluorescence into the cell discloses delivery of the plasmid DNA inside the cell by using Ku-peptides and further expression of the protein inside the cell.

presence of pDNA/Ku-peptide polyplex, the GFP expression was observed inside the cell after 48 h of incubation time (Figure 14). This indicates that the Ku-peptides can deliver the DNA (Figure 14) into the cells for effective transfection. Although, the transfection efficiency of the Ku-peptides was relatively low compared to the commercially available lipofectamine 3000, the low toxicity profile of these peptides might be helpful for further modification to generate superior transfection agents.

5.7 Conclusion

In summary, we developed a novel cell-penetrating peptide derived from the intrinsically disordered region of Ku-protein. The Ku-peptides are non-toxic and have good cell membrane permeability. Various studies showed excellent DNA binding and stabilization into compact nanoparticles. These DNA-peptide polyplexes with positive ζ -potential showed effective

plasmid DNA delivery through the negatively charged cell membrane and good transfection. Thus, designed Ku-peptides could be applied as a delivery shuttle for plasmid DNA transfection and drug delivery.

5.8 Experimental Methods

5.8.1 Peptide Synthesis

Ku-peptides were synthesized using standard 9-fluorenylmethyloxycarbonyl (Fmoc) solid phase peptide synthesis (SSPS) protocol on rink amide resin. Amino acid coupling and Fmoc de-protection efficacy were monitored by the Kaiser test. After completion of peptide sequences, peptide and side chain of the amino acids were cleaved by using the cocktail solution containing trifluoroacetic acid (TFA): triisopropyl silane (TIPS): DCM (95:2.5:2.5) for 3 h at room temperature. Solutions were collected and triturated with the cold ether to obtain a white precipitation. The peptides were purified by RP-HPLC in the C18 column using acetonitrile/water mobile phase and characterized by MALDI- TOF, and HRMS (Q-TOF). The purity of the peptides was analysed through an HPLC chromatogram.

5.8.2 CD Spectroscopy Studies

The CD spectra of Ku-peptides were acquired in 10 mM of PBS (pH = 7.4) using Jasco J-810 spectropolarimeter. 100 μ M of peptide was incubated for 24 h prior to scanning, and spectra were recorded from 350 nm to 190 nm in 1 mm quartz cuvette with a bandwidth of 1 nm. All spectra were collected thrice, and blank spectra were subtracted from each spectrum. The artificial lipid membrane was prepared using dipalmitoylphosphatidylcholine (DPPC), dipalmitoylphosphoglycerol (DPPG) and cholesterol. The zwitterionic membrane was prepared using DPPC: Cholesterol ratio 70:30, and negatively lipid membrane was prepared using the DPPC: DPPG: Cholesterol of ratio 70: 20: 10. Lipids were solubilized in mixture of chloroform and methanol (2:1) to make 2 mM stock solution, and solvents were evaporated

completely using nitrogen gas followed by vacuum to make lipid films. The lipid film was hydrated in PBS buffer and vortex vigorously for 30 min to get lipid emulsion. The emulsion was dipped into liquid nitrogen for 5 minutes, leading to instant cooling. The solution was further dipped into a 60 °C water bath for 5 min, and freeze-thaw cycles were repeated 7 times. The lipid vesicles were stored at 4 °C and further used for the experiment. Peptide was mixed with the lipid at 1:50 ratio and incubated at 37 °C for 6 h and CD experiments were carried out.

5.8.3 Cytotoxicity Studies

The cytotoxic effect of Ku-peptides on L929 cells was evaluated using colorimetric MTT assay. L929 cells were cultured in Dulbecco Modified Eagle Media (DMEM) supplemented with 10% Fetal bovine serum (FBS) and 1% penicillin-streptomycin (PS). Cells were seeded at cell density of 1×10^4 in a 96-well plate and cultured for 24 h. Cells were treated with 20 – 200 μ M of peptides solution and incubated for 24 h. 10 μ L of 0.5% MTT solution was added and further incubated for 4 h. The supernatant was removed carefully without disturbing the formazan crystals. The formazan crystals were dissolved in 100 μ L of 1:1 dimethyl sulfoxide and methanol. The absorbance of the formazan dye was measured in SpectroMax i3x microplate reader at 570 nm wavelength, followed by background correction at 690 nm.

5.8.4 Cellular Uptake Studies

The intracellular localization of Ku-peptides in L929 cells was quantified using fluorescence-activated cell sorting (FACS) analysis. L929 cells were seeded at a density of 50×10^4 in a 12-well plate, cultured for 24 h, and treated with 10 μ M of fluorophore-labelled peptides for 6 h. Cell wells are washed with PBS (10mM, pH = 7.4) and detached from wells using 0.25% trypsin. The cell pellet was washed with PBS three times, and cellular uptake was analyzed. For fluorescence analysis by microscopy, L929 cells were plated in confocal disk at density of 2×10^4 and cultured for 24 h. Fluorophore labelled peptide solution (10 μ M) was treated and

incubated for 6 h. Unbound peptides were removed by washing with 10 mM of PBS solution and fixed with 4% paraformaldehyde, cell nucleus was stained with DAPI. Images were captured using Leica DMI8 fluorescence microscope.

5.8.5 DNA Binding Studies

Fluorescence spectral measurements were conducted using Agilent Cary Eclipse fluorescence spectrophotometer. Briefly, 4 μM of intercalator dye ethidium bromide (EtBr) was incubated with 100 μM ctDNA for 6 h and titrated with increased peptide concentration. The EtBr fluorescence was recorded on excitation at 526 nm and emission from 555 to 700 nm. The fluorescence measurement was continued until the EtBr fluorescence got saturated.

5.8.6 Agarose Gel Electrophoresis Mobility Shift Assay

200 ng of green fluorescence protein plasmid DNA was incubated at room temperature with different concentrations of peptides for 45 min in Tris.HCl buffer (10 mM, pH = 7.4) to form the condensed particle. The solutions were mixed with 2 μL of loading dye (20% glycerol, 25 mM EDTA, and 0.05% bromophenol blue and xylene cyanol) and transferred into wells. Electrophoresis was performed in TBE buffer at 140 v for 1 h. For polyplex stability studies, 2 μL of various NaCl concentrations were mixed with the polyplex solutions, incubated at 37 $^{\circ}\text{C}$ for 3 h, and loaded into the gel well.

5.8.7 DNA Conformational Analysis

The CD spectra of ct-DNA with presence of the peptides were performed for the conformation changes during the condensation. To a 100 μM ct-DNA in tris buffer 0 to 50 μM peptide solution was added and incubated for 45 min at room temperature. The spectrum was collected from 350 nm to 200 nm in a 1 cm quartz cuvette using Jasco-810 spectropolarimeter.

5.8.8 DLS Studies

To a 200 ng eGFP plasmid DNA was mixed with 0 to 25 μM of peptide solution and incubated at room temperature for 45 min. The sample was transferred into the fluorescence quartz cuvette of pathlength 1 cm, and measurement was performed in Malvern Zetasizer nano-ZS.

5.8.9 AFM Analysis

The nature of the condensed particle formed was further characterized through AFM analysis. Briefly, 10 mM NiCl_2 was drop cast on a freshly cleaved mica sheet, kept for 10 min and wiped out with filter paper. 40 μL of eGFP plasmid DNA (1 ng/ μL in Tris.HCl buffer) was transferred into the activated mica sheet and further incubated for 20 min. The aliquot was removed with filter paper, washed trice with 100 μL of filtered Milli Q water, and kept at 37 $^\circ\text{C}$ for drying. The polyplex samples were dropped cast without activation of the mica surface. Imaging was performed in a Bruker Bioscope Resolve microscope at scanning rate of 1 Hz using a 3 nm probe. Images were further processed with NanoScope analysis software.

5.8.10 eGFP Plasmid DNA Isolation and Purification

Enhanced plasmid DNA pEGFP-C2 (4.7 kb) was isolated from E. Coli DH5 α and purified using the Qiagen miniprep plasmid isolation kit. The concentration of pEGFP was determined using nanoDrop in SpectraMax i3x microplate reader. The purity was checked from the absorbance ratio at 260 nm and 280 nm.

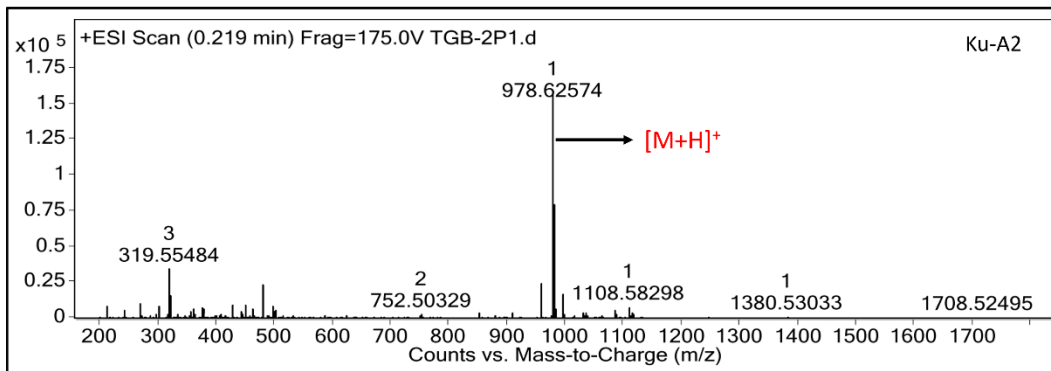
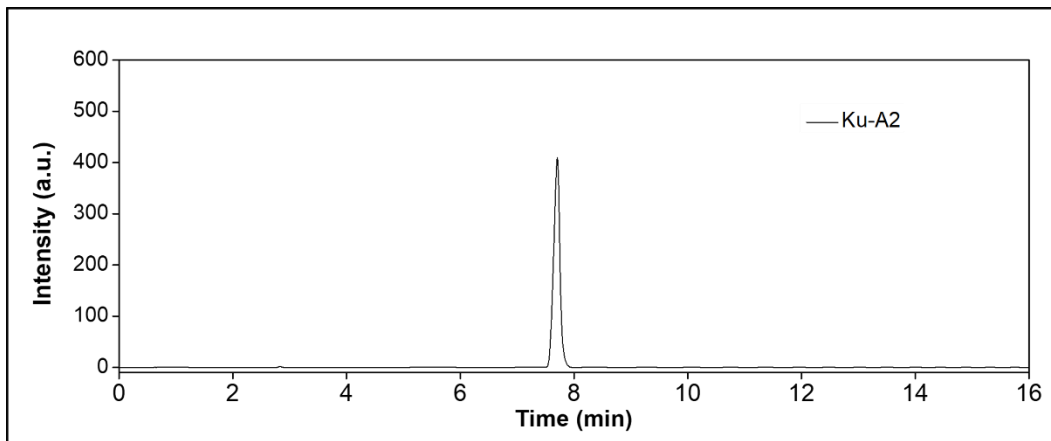
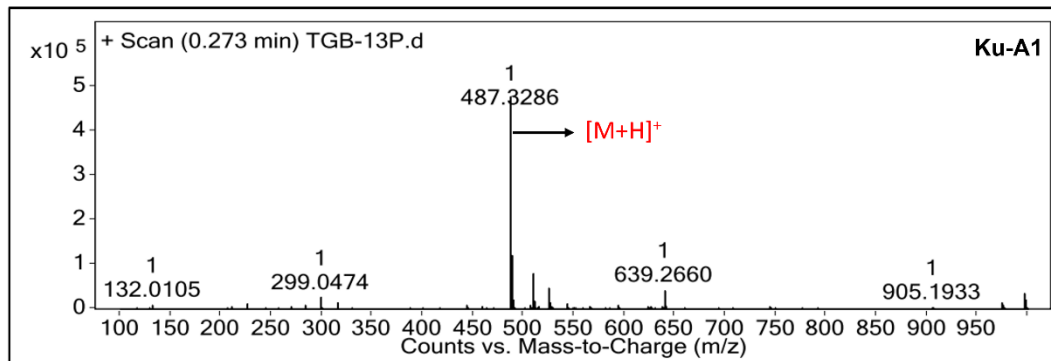
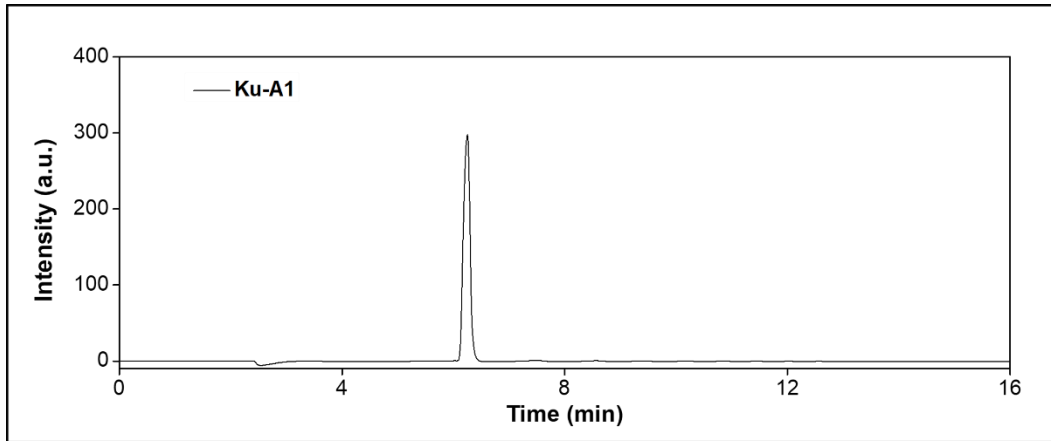
5.8.11 eGFP Plasmid DNA Transfection

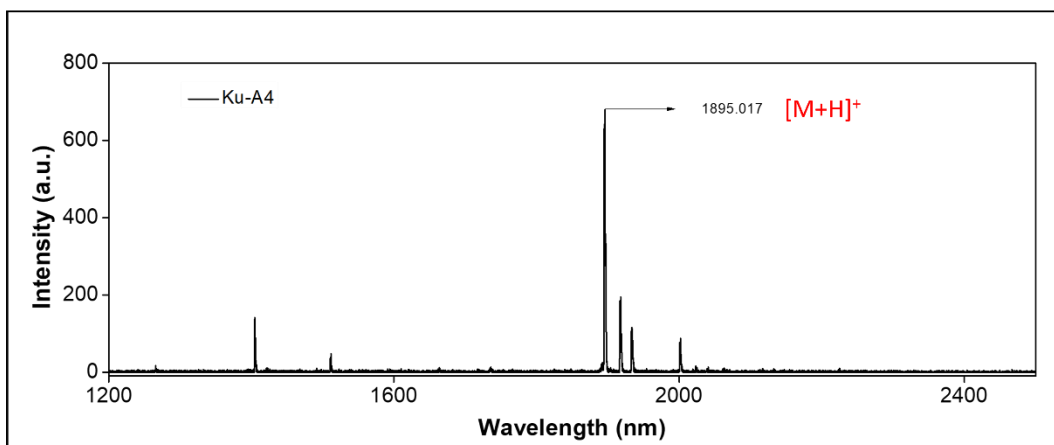
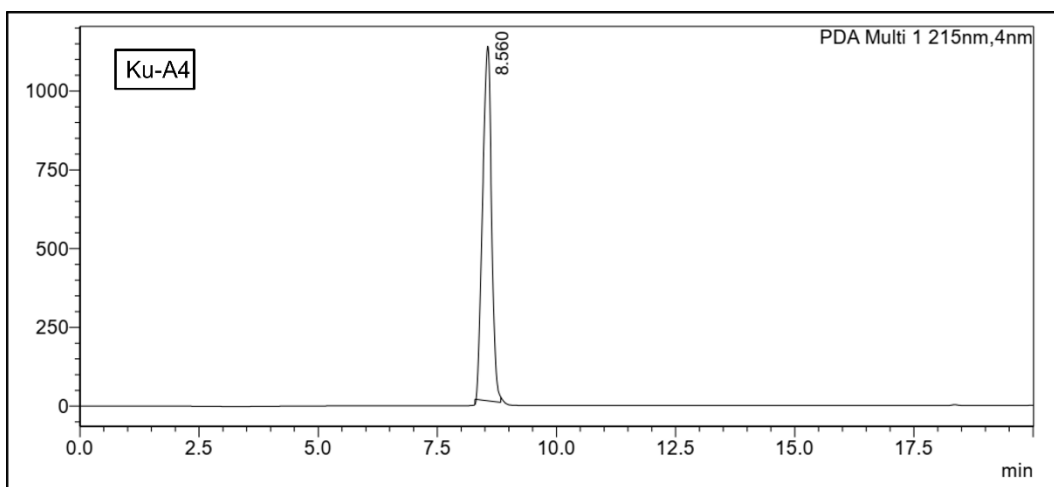
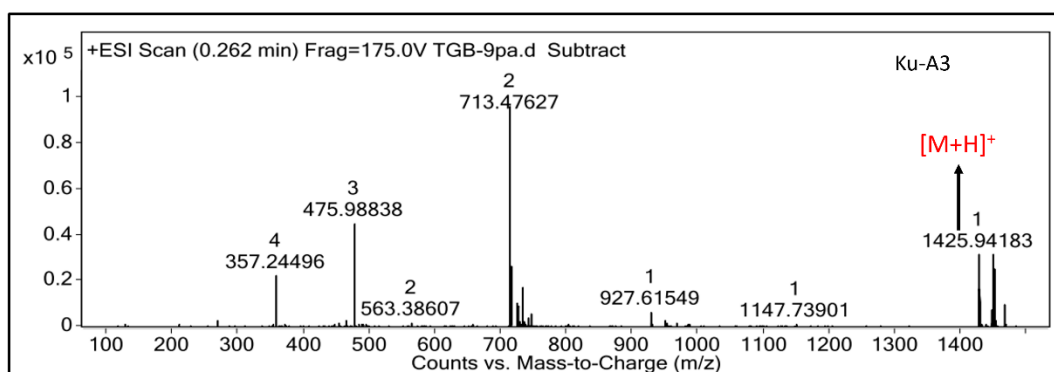
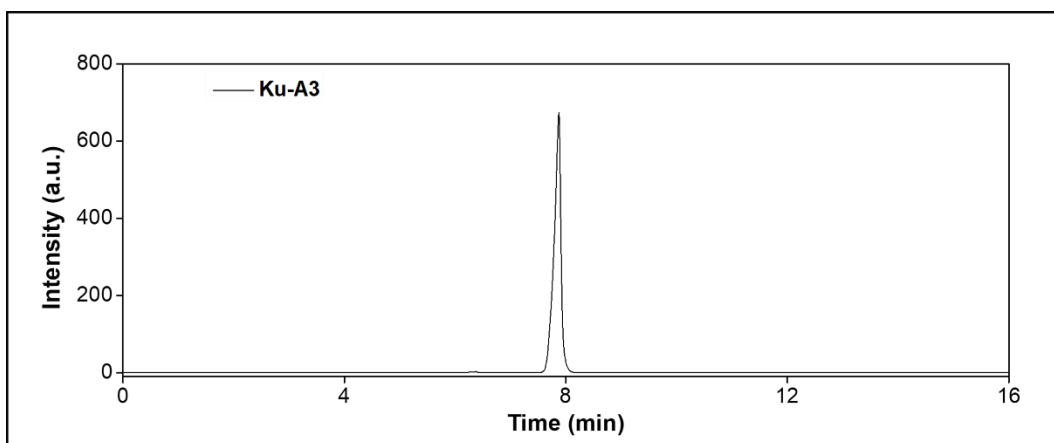
The eGFP plasmid DNA transfection experiment was performed to check the DNA delivery efficacy of the peptides in HEK293T cells. In a solution of 200 ng of eGFP plasmid in optiMEM, 50 μM peptide solution was added dropwise and mixed properly through gentle vertexing. The mixture was kept at room temperature for 45 min to form the condensed polyplex structure. The polyplex sample was transferred to 70% confluent 48-cell wells containing 2% FBS without antibiotics. After 12 h of incubation, the cultured media was

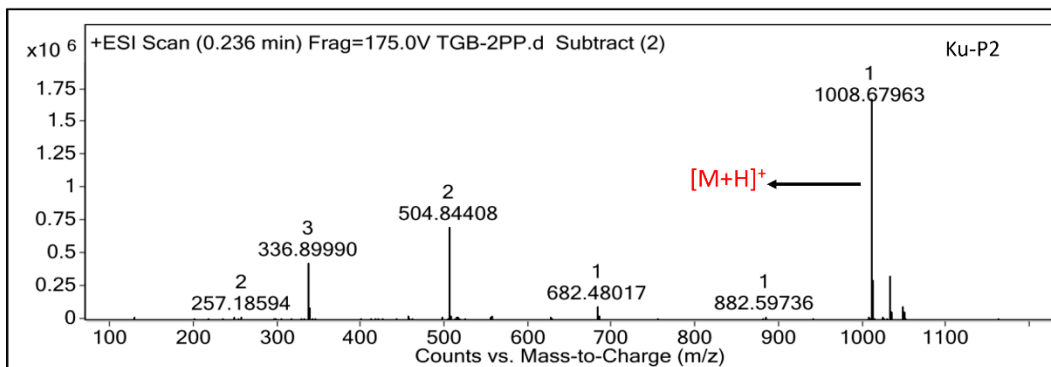
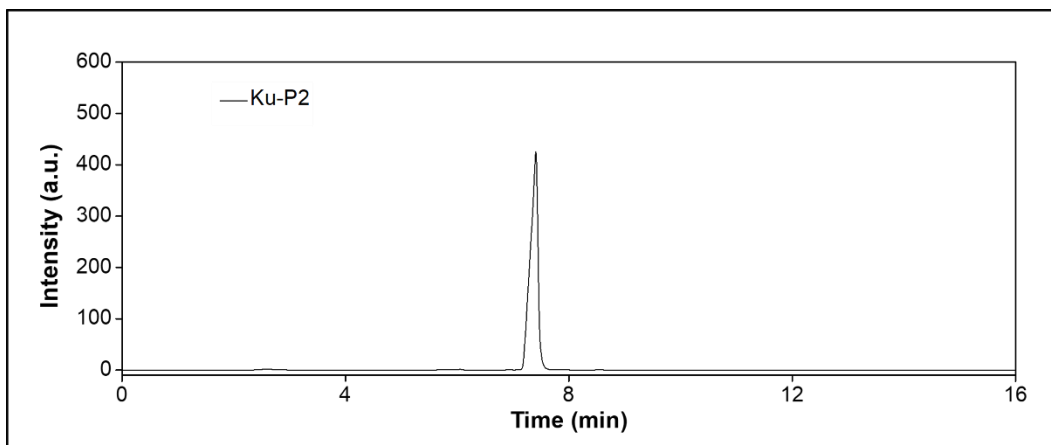
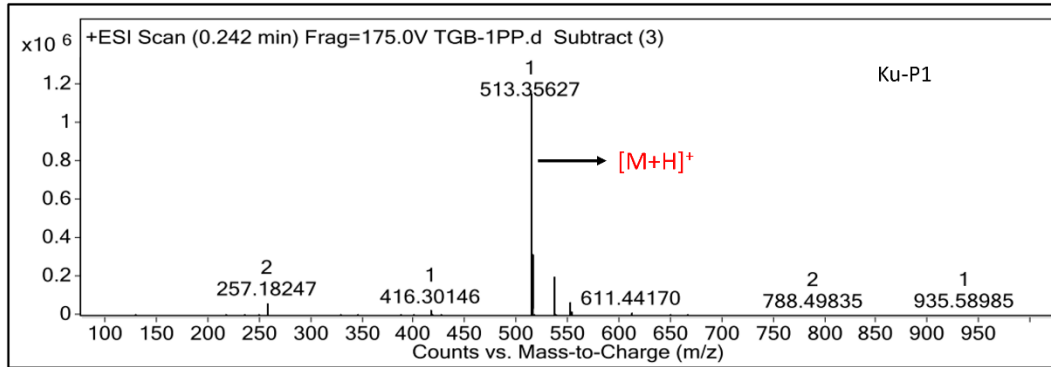
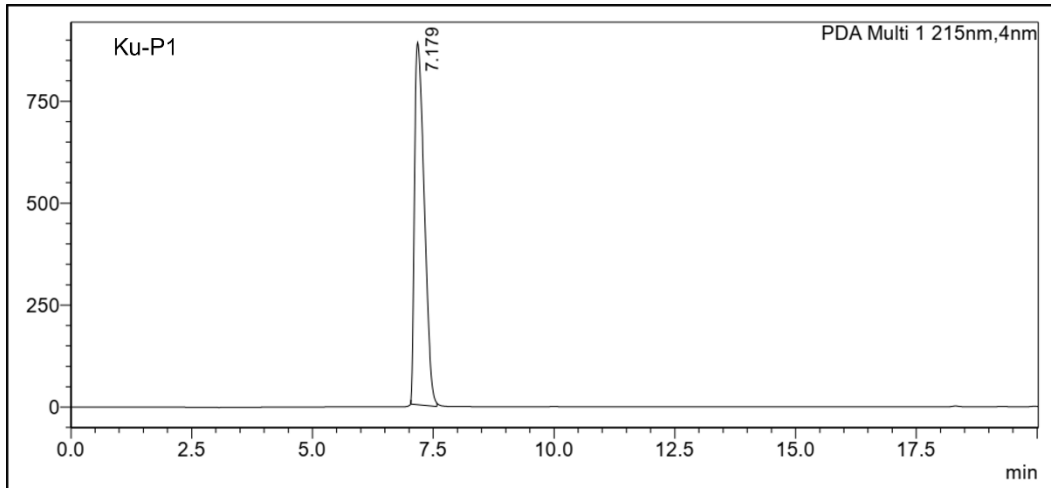
replaced with fresh media and further cultured for 72 h, and green fluorescence protein expression was imaged under Leica Dim8 fluorescence microscope.

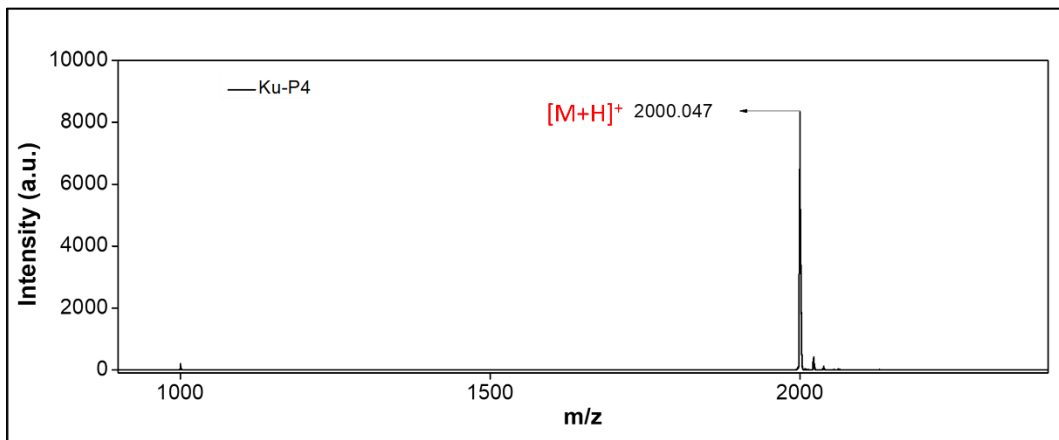
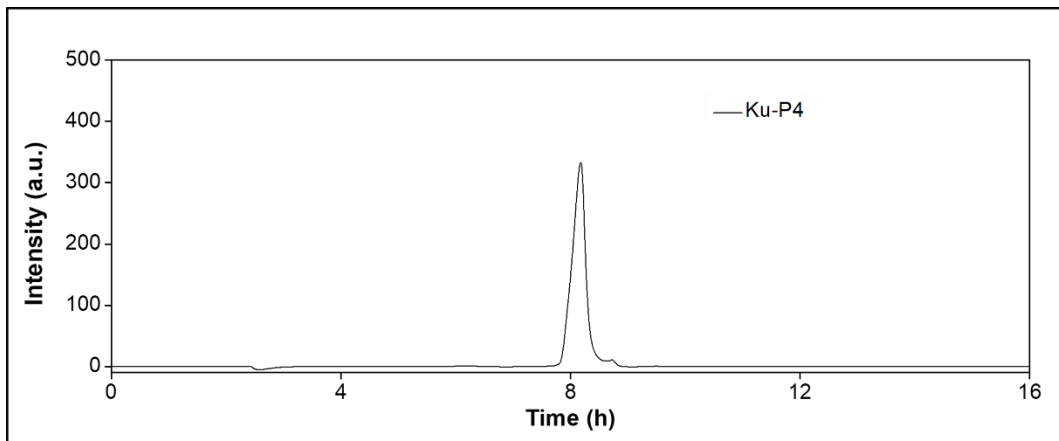
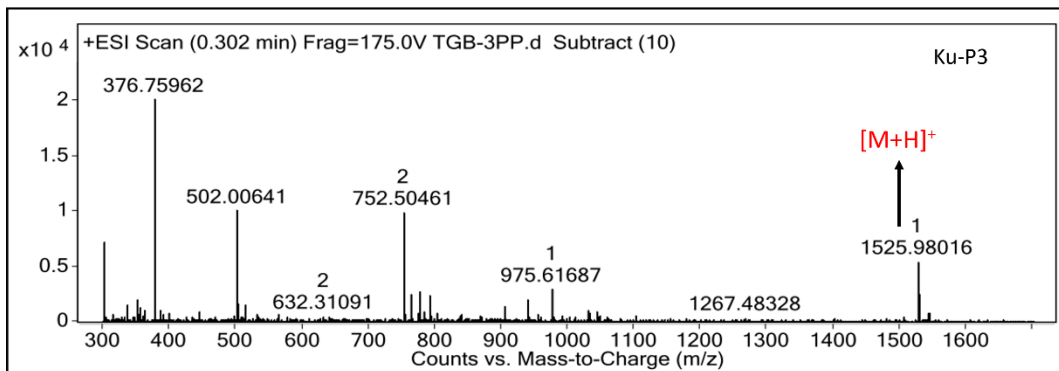
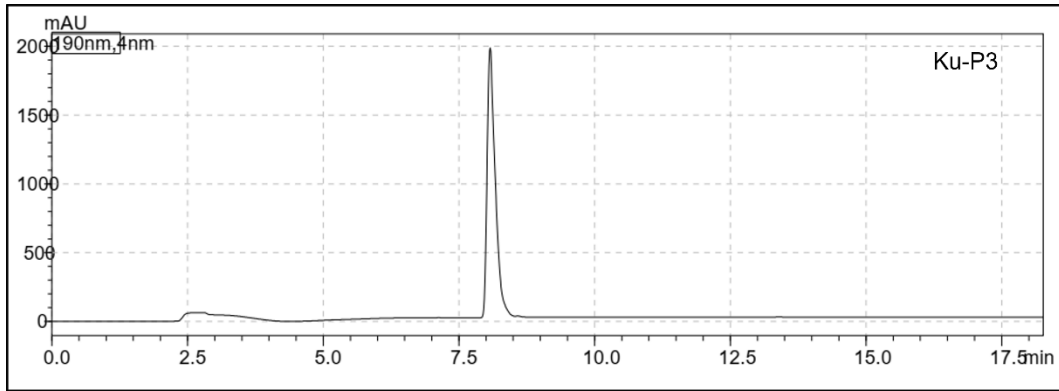
5.9 Appendix

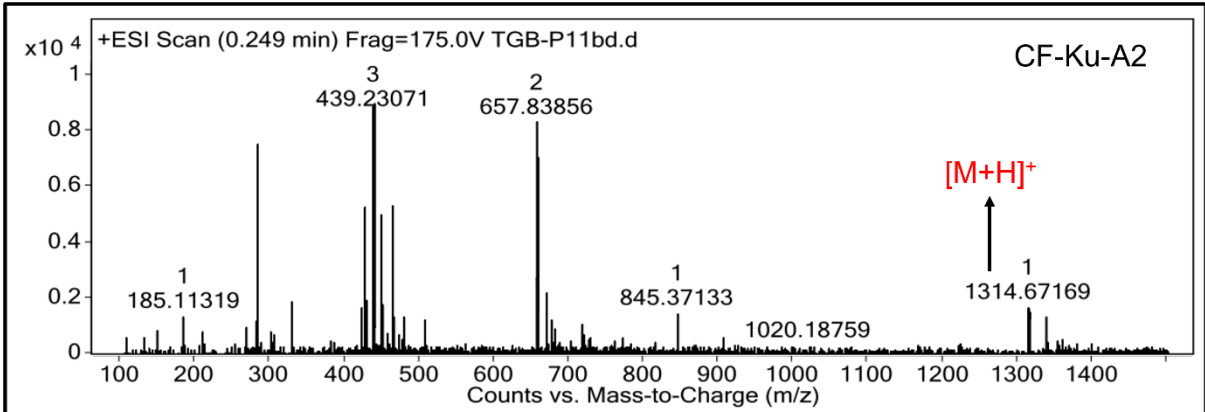
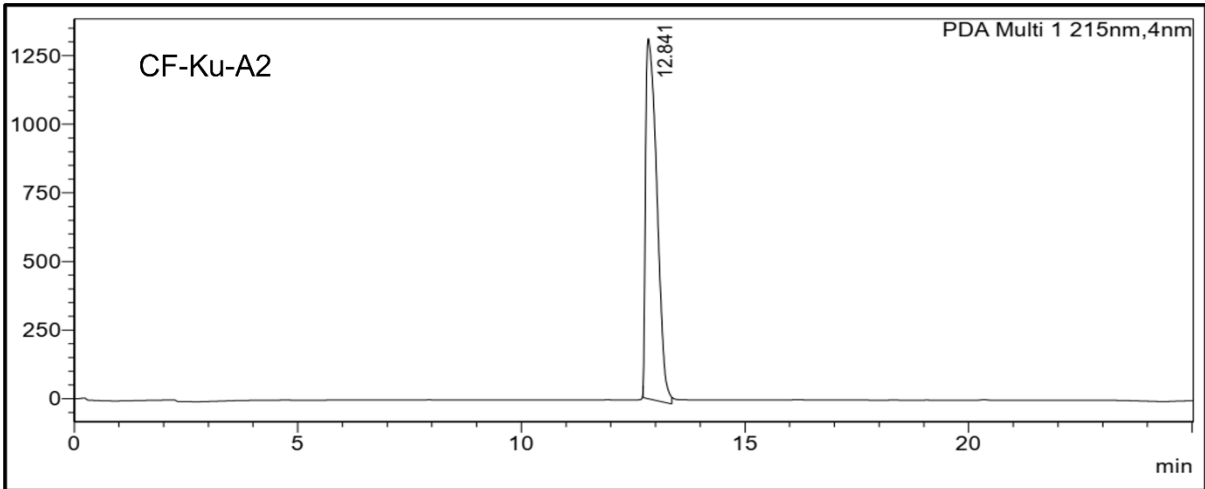
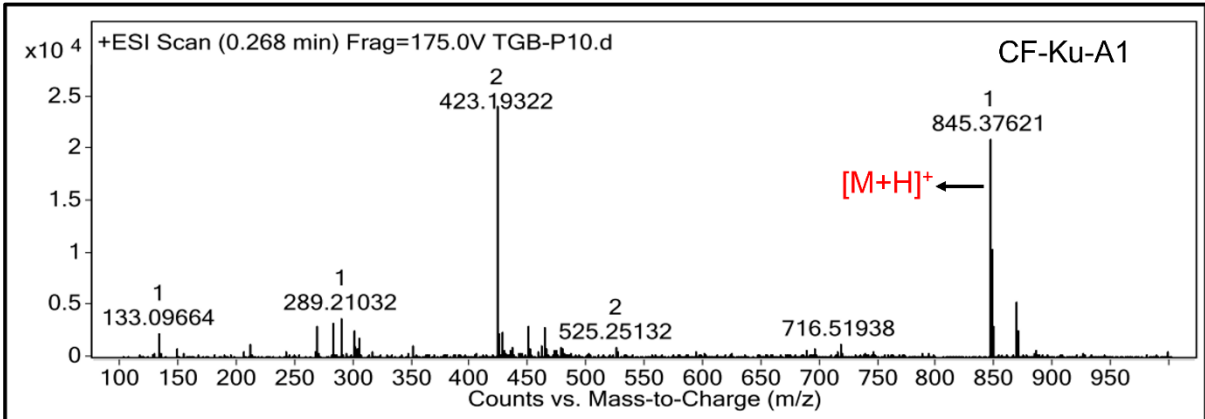
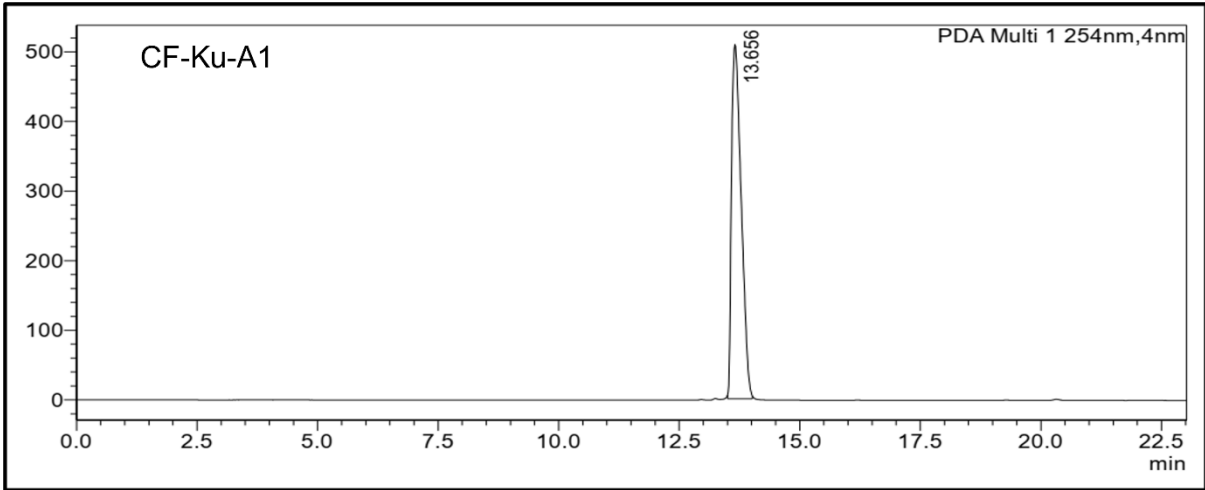
- HPLC chromatograms of peptides
- HRMS or MALDI data

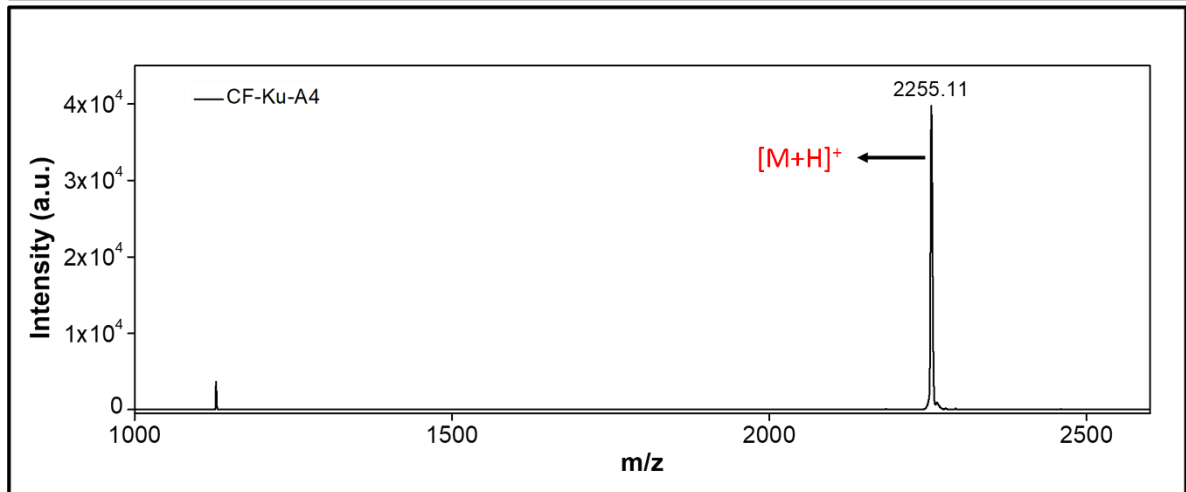
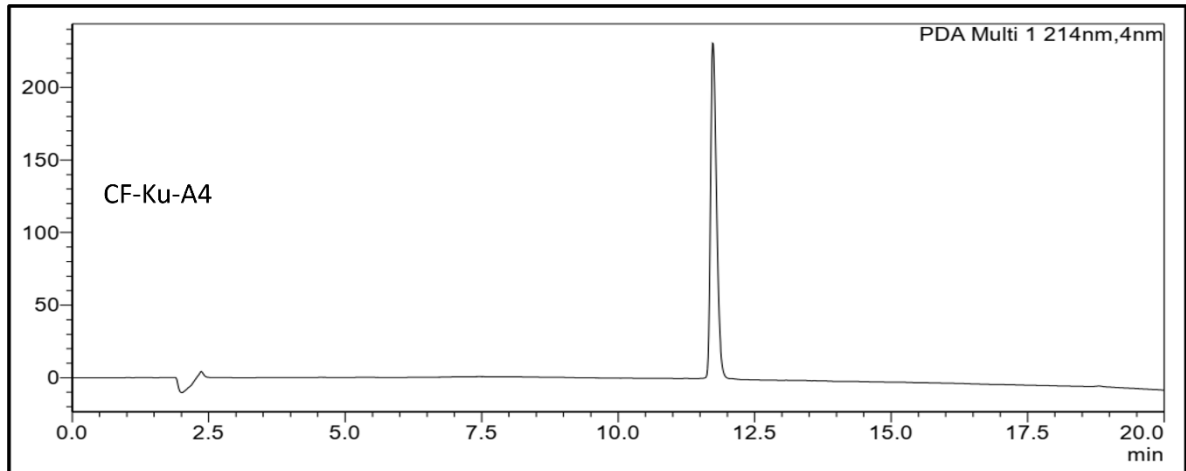
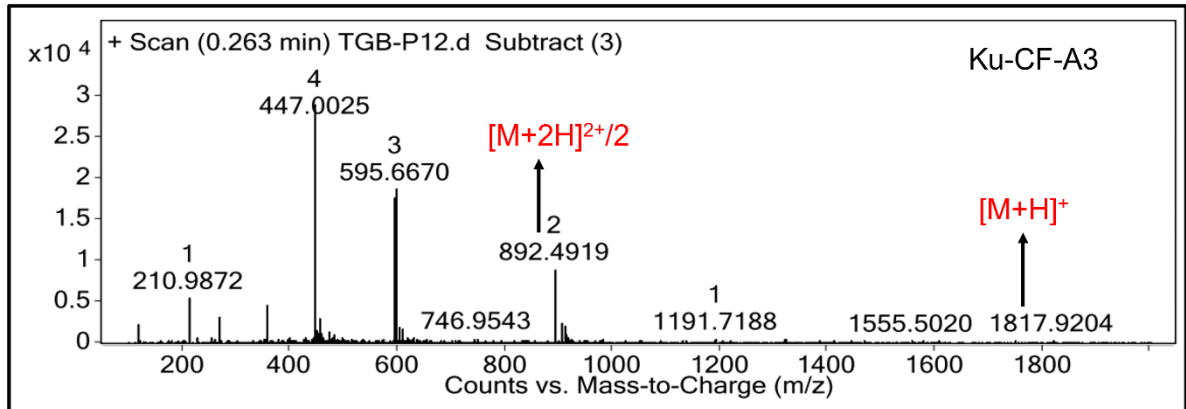
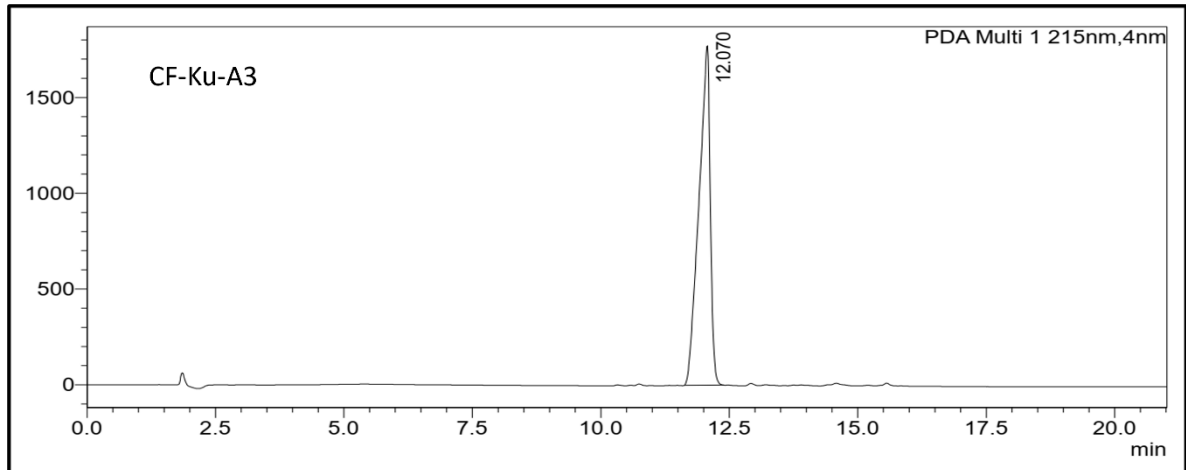


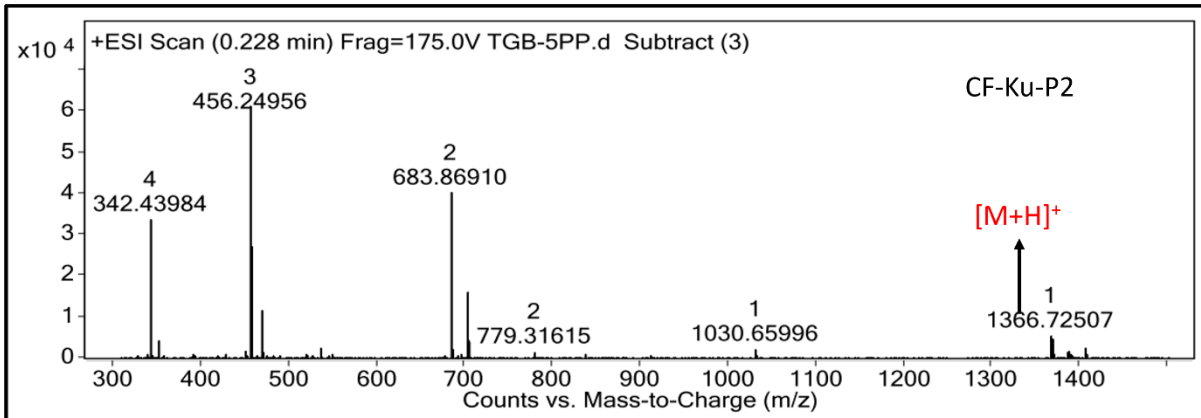
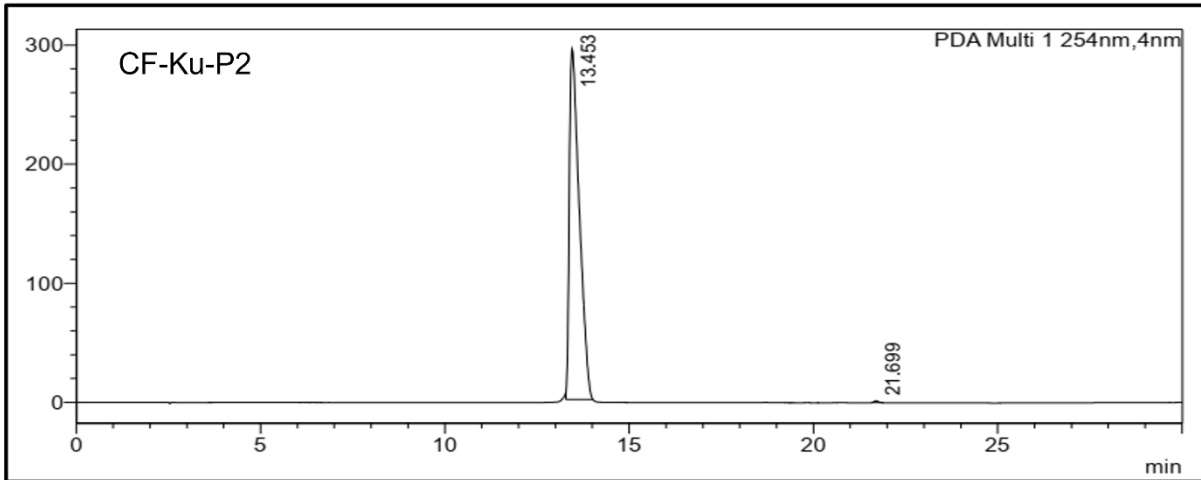
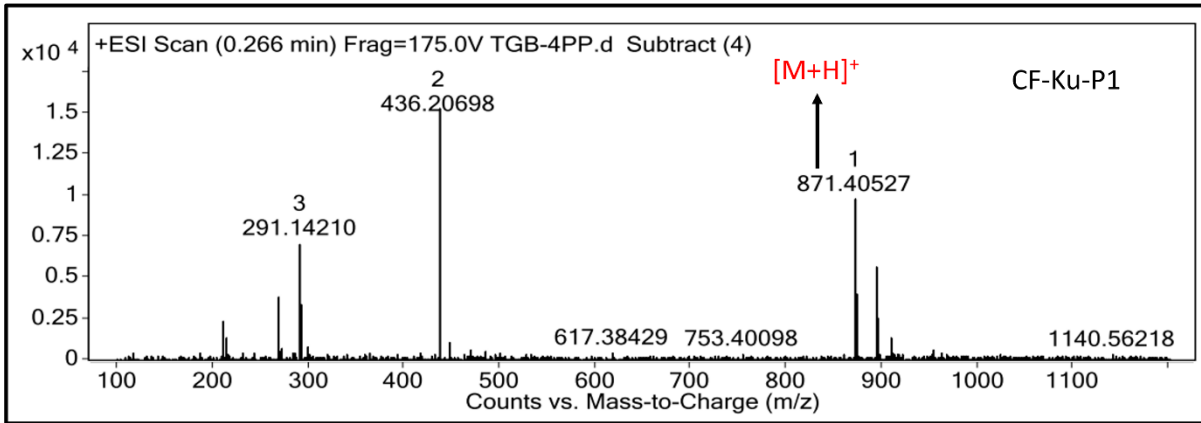
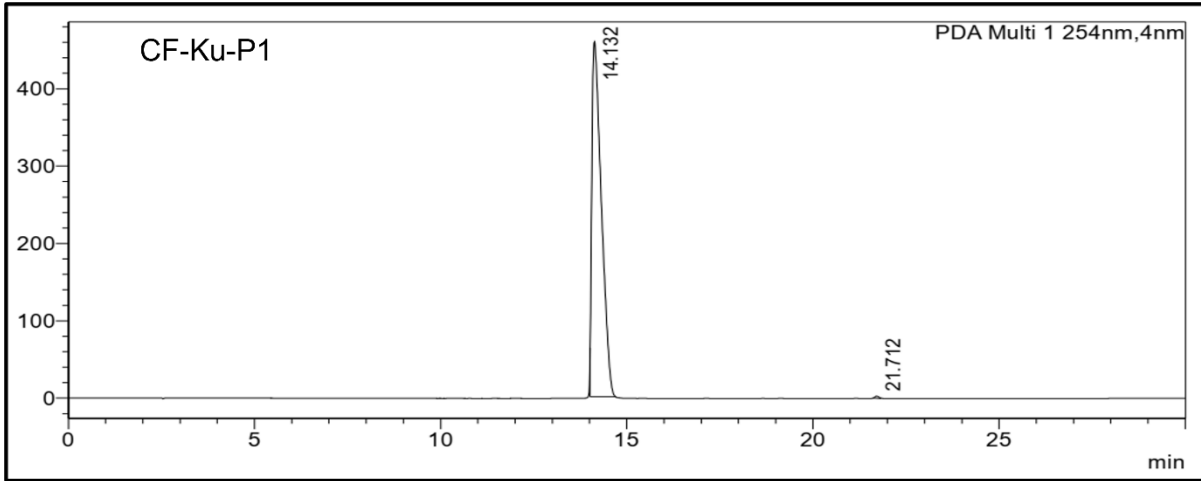


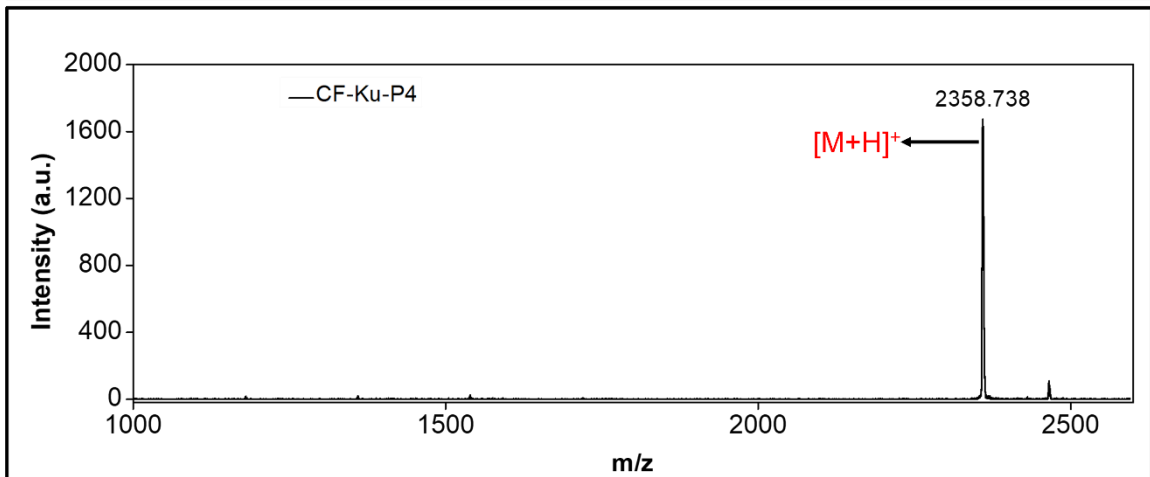
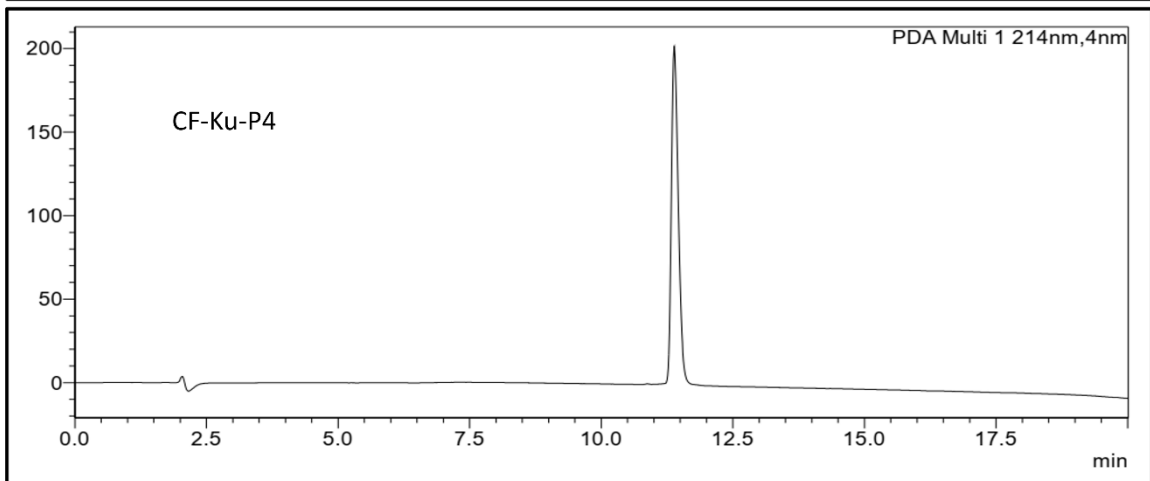
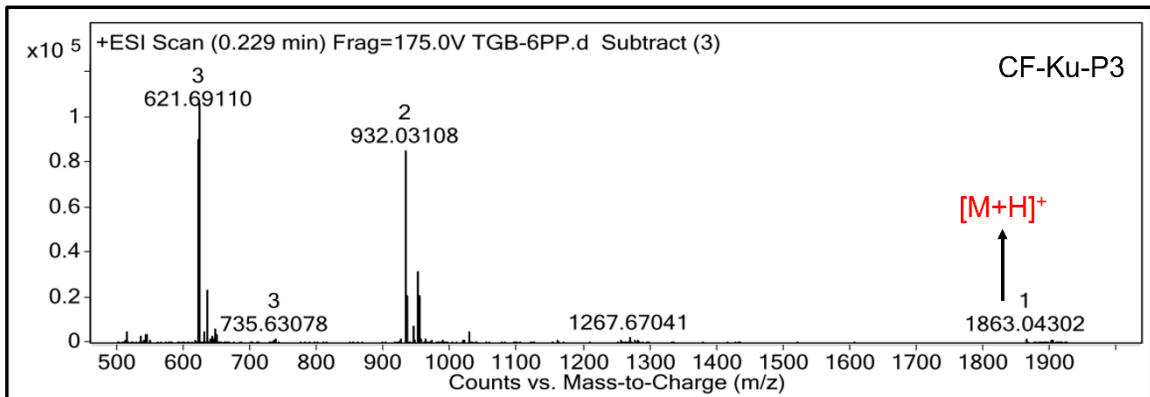
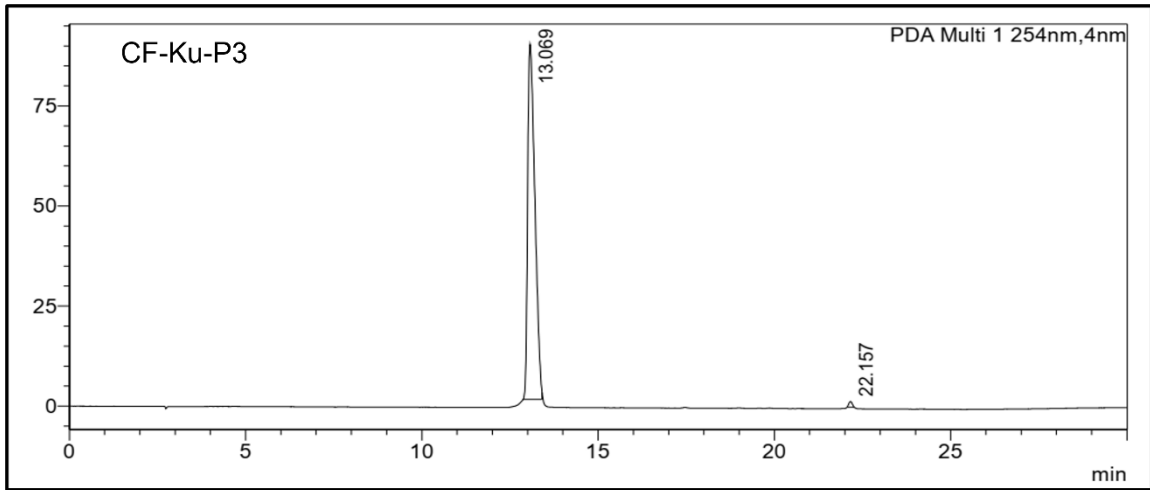












5.10 References

1. Oren, I.; Fleishman, S. J.; Kessel, A.; Ben-Tal, N. Free diffusion of steroid hormones across biomembranes: A simplex search with implicit solvent model calculations. *Biophys. J.* **2004**, *87*, 768–779.
2. Cooper, G. M. Transport of small molecules, in: *The cell: A molecular approach*, 2nd edition, Sinauer Associates, Sunderland (MA), 2000.
3. Mitragotri, S.; Burke, P. A.; Langer, R. Overcoming the challenges in administering biopharmaceuticals: Formulation and delivery strategies. *Nat. Rev. Drug Discov.* **2014**, *13*, 655–672.
4. Biffi, A.; Montini, E.; Lorioli, L.; Cesani, M.; Fumagalli, F.; Plati, T.; Baldoli, C.; Martino, S.; Calabria, A.; Canale, S. Lentiviral hematopoietic stem cell gene therapy benefits metachromatic leukodystrophy. *Science* **2013**, *341*, 1233158.
5. Yang, J.; Hendricks, W.; Liu, G.; McCaffery, J. M.; Kinzler, K. W.; Huso, D. L.; Vogelstein, B.; Zhou, S. A nanoparticle formulation that selectively transfects Metastatic tumors in mice. *Proc. Natl. Acad. Sci. U. S. A.* **2013**, *110*, 14717–14722.
6. Kirtane, A. R.; Panyam, J. Polymer nanoparticles: Weighing up gene delivery. *Nat. Nanotechnol.* **2013**, *8*, 805–806.
7. Pack, D. W.; Hoffman, A. S.; Pun, S.; Stayton, P. S. Design and development of polymers for gene delivery. *Nat. Rev. Drug. Discov.* **2005**, *4*, 581–593.
8. Pattni, B. S.; Chupin, V. V.; Torchilin, V. P. New developments in liposomal drug delivery. *Chem. rev.* **2015**, *115*, 10938–10966.
9. Yang, J.; Zhang, Q.; Chang, H.; Cheng, Y. Surface engineered dendrimers in gene delivery. *Chem. Rev.* **2015**, *115*, 5274–5300.
10. Alvarez-Erviti, L.; Seow, Y.; Yin, H.; Betts, C.; Lakhali, S.; Wood, M. J. A. Delivery of siRNA to the mouse brain by systemic injection of targeted exosomes. *Nat. Biotechnol.* **2011**, *29*, 341–345.

11. Gopal, V. Bioinspired peptides as versatile nucleic acid delivery platforms. *J. Controlled Release* **2013**, *167*, 323–332.
12. Suh, J. S.; Lee, J. Y.; Choi, Y. S.; Chong, P. C.; Park, Y. J. Peptide-mediated intracellular delivery of miRNA-29b for osteogenic stem cell differentiation. *Biomaterials* **2013**, *34*, 4347–4359.
13. Kichler, A.; Leborgne, C.; Danos, O.; Bechinger, B. Characterization of the gene transfer process mediated by histidine-rich peptides. *J. Mol. Med.* **2007**, *85*, 191–201.
14. Juliano, R. L.; Ming, X.; Nakagawa, O. Cellular uptake and intracellular trafficking of antisense and siRNA oligonucleotides. *Bioconjugate Chem.* **2012**, *23*, 147–157.
15. Torchilin, V. P. Cell penetrating peptide-modified pharmaceutical nanocarriers for intracellular drug and gene delivery. *Biopolymers* **2008**, *90*, 604–610.
16. Plank, C.; Tang, M. X.; Wolfe, A. R.; Szoka, F. C. Branched cationic peptides for gene delivery: role of type and number of cationic residues in formation and in vitro activity of DNA polyplexes. *Hum Gene Ther.* **1999**, *10*, 319–332.
17. Frankel, A. D.; Pabo, C. O. Cellular uptake of the tat protein from human immunodeficiency virus. *Cell* **1988**, *55*, 1189–1193.
18. Vives, E.; Brodin, P.; Lebleu, B. A truncated HIV-1 Tat protein basic domain rapidly translocates through the plasma membrane and accumulates in the cell nucleus, *J. Biol. Chem.* **1997**, *272*, 16010–16017.
19. Heitz, F.; Morris, M. C.; Divita, G. Twenty years of cell-penetrating peptides: From molecular mechanisms to therapeutics. *Br. J. Pharmacol.* **2009**, *157*, 195–206.
20. Habault, J.; Poyet, J. L. Recent advances in cell penetrating peptide-based anticancer therapies. *Molecules* **2019**, *24*, 927.
21. Wadia, J. S.; Stan, R. V.; Dowdy, S. F. Transducible TAT-HA fusogenic peptide enhances escape of TAT-fusion proteins after lipid raft macropinocytosis. *Nat. Med.* **2004**, *10*, 310–315.

22. Madhu, C.; Voshavar, C.; Rajasekhar, K.; Govindaraju, T. Cyclic dipeptide based cell-penetrating peptidomimetics for effective DNA delivery. *Org. Biomol. Chem.* **2017**, *15*, 3170–3174.
23. Eiriksdottir, E.; Konate, K.; Langel, U.; Divita, G.; Deshayes, S. Secondary structure of cell-penetrating peptides controls membrane interaction and insertion. *Biochim. Biophys. Acta Biomembr.* **2010**, *1798*, 1119–1128.
24. Walker, J. R.; Corpina, R. A.; Goldberg, J. Structure of the Ku heterodimer bound to DNA and its implications for double-strand break repair. *Nature* **2001**, *412*, 607–614.
25. Boehr, D. D.; Nussinov, R.; Wright, P. E. The role of dynamic conformational ensembles in biomolecular recognition. *Nat. Chem. Biol.* **2009**, *5*, 789–796.
26. Salerno, P.; Larsson, J.; Bucca, G.; Laing, E.; Smith, C. P.; Flardh, K. One of the two genes encoding nucleoid-associated HU proteins in streptomyces coelicolor is developmentally regulated and specifically involved in spore maturation. *J. Bacteriol.* **2009**, *191*, 6489–6500.
27. Vuzman, D.; Levy, Y. Intrinsically disordered regions as affinity tuners in protein–DNA interactions. *Mol. BioSyst.* **2012**, *8*, 47–57.
28. Rado-trilla, N.; Alba, M. Dissecting the role of low-complexity regions in the evolution of vertebrate proteins. *BMC Evol. Biol.* **2012**, *12*, 1471–2148.
29. Coletta, A.; Pinney, J. W.; Solis, D. W. Y.; Marsh, J.; Pettifer, S. R.; Attwood, T. K. Low-complexity regions within protein sequences have position-dependent roles. *BMC Syst. Biol.* **2010**, *4*, 1–13.
30. Uversky, V. N.; Gillespie, J. R.; Fink, A. L. Why are “natively unfolded” proteins unstructured under physiologic conditions? *Proteins: Struct., Funct., Genet.* **2000**, *41*, 415–427.
31. Jorda, J.; Xue, B.; Uversky, V. N.; Kajava, A.V. Protein tandem repeats – the more perfect, the less structured. *FEBS J.* **2010**, *277*, 2673–2682.

32. Khare, H.; Dey, D.; Madhu, C.; Senapati, D.; Raghothama, S.; Govindaraju, T.; Ramakumar, S. Conformational heterogeneity in tails of DNA-binding proteins is augmented by proline containing repeats. *Mol. BioSyst.* **2017**, *13*, 2531-2544.
33. Mukherjee, A.; Bhattacharyya, G.; Grove, A. The C-terminal domain of HU-related histone-like protein Hlp from mycobacterium smegmatis mediates DNA end-joining. *Biochemistry* **2008**, *47*, 8744–8753.
34. Bhowmick, T.; Ghosh, S.; Dixit, K.; Ganesan, V.; Ramagopal, U. A.; Dey, D.; Sarma, S. P.; Ramakumar, S.; Nagaraja, V. Targeting Mycobacterium tuberculosis nucleoid-associated protein HU with structure-based inhibitors. *Nat. Commun.* **2014**, *5*, 1–13.
35. Lima, C. S. D.; Marques, M. A. M.; Debrie, A. S.; Almeida, E. C. C.; Silva, C. M. A.; Brennan, P. J.; Sarno, E. N.; Menozzi, F. D.; Pessolani, M. C. V. Heparin-binding hemagglutinin (HBHA) of Mycobacterium leprae is expressed during infection and enhances bacterial adherence to epithelial cells. *FEMS Microbiol. Lett.* **2009**, *292*, 162–169.
36. Sadler, K.; Eom, K. D.; Yang, J. L.; Dimitrova, Y.; Tam, J. P. Translocating proline-rich peptides from the antimicrobial peptide bactenecin. *Biochemistry* **2002**, *41*, 14150–14157.
37. Lopes, J. L. S.; Miles, A. J.; Whitmore, L.; Wallace, B. A. Distinct circular dichroism spectroscopic signatures of polyproline II and unordered secondary structures: Applications in secondary structure analyses. *Protein Sci.* **2014**, *23*, 1765–1772.
38. Macarthur, M. W.; Thornton, J. M. Influences of proline residues on protein conformation. *J. Mol. Biol.* **1991**, *218*, 397–412.
39. Futaki, S.; Ohashi, W.; Suzuki, T.; Niwa, M.; Tanaka, S.; Ueda, K.; Harashima, H.; Sugiura, Y. Stearylated arginine-rich peptides: A new class of transfection systems. *Bioconjugate Chem.* **2001**, *12*, 1005–1011.

40. Jenkins, T. C. Optical absorbance and fluorescence techniques for measuring DNA-drug interactions. *In drug DNA interaction protocols*. Fox, K. R.; Ed.; Humana Press: Totowa, NY, USA, **1997**, *90*, 195–218.

41. Pratihari, S.; Suseela, Y. V.; Govindaraju, T. Threading intercalator-induced nanocondensates and role of endogenous metal ions in decondensation for DNA delivery. *ACS Appl. Bio Mater.* **2020**, *3*, 6979–6991.

42. Prevette, L. E.; Kodger, T. E.; Reineke, T. M.; Lynch, M. L. Deciphering the role of hydrogen bonding in enhancing pDNA- polycation interactions. *Langmuir* **2007**, *23*, 9773–9784.

43. Anuradha; Alam, M. S.; Chaudhury, N. K. Osmolyte changes the binding affinity and mode of interaction of minor groove binder hoechst 33258 with calf thymus DNA. *Chem. Pharm. Bull.* **2010**, *58*, 1447–1454.

44. Choosakoonkriang, S.; Lobo, B. A.; Koe, G. S.; Koe, J. G.; Middaugh, C. R. Biophysical characterization of PEI/DNA complexes. *J. Pharm. Sci.* **2003**, *92*, 1710–1722.

Chapter 6

Tumor Microenvironment Sensitive Cell Penetrating Peptidomimetics for Selective Anticancer Drug Delivery

Hypothesis: Cell penetrating peptides (CPPs) are sought-after cytosolic delivery agents and find widespread applicability in drug delivery. However, the positive charge in lysine and arginine residues induces nonselective drug delivery of cargo. We have hypothesized that replacing cationic charges in CPPs with histidine (H) and cyclic dipeptide unit (kd) comprising multiple hydrogen bonding abilities might overcome the non-specific cellular permeabilization. We have designed a decamer CPP (Hkd) to selectively deliver anticancer drugs into cancerous tissue in response to the prevailing acidic pH environment.

Cell penetrating peptides (CPPs) are sought-after cytosolic delivery agents and find widespread applicability in drug delivery.¹⁻⁵ The intrinsic cell membrane permeability of CPPs originated from their cationic or amphipathic amino acid side chains.⁶⁻⁸ Utilizing the CPPs transport ability, cellular delivery of various impermeable cargoes has been reported.^{9,10} However, the major limitation of known CPPs is target selectivity.^{11,12} The non-selectivity of CPPs is associated in the basic design of CPP models. Most CPPs possess positively charged arginine and lysine residues in their sequences. The electrostatic interactions between the cationic side chain of CPPs and anionic membrane lipids is mechanism of CPPs internalization. Thus, CPPs indiscriminately penetrate most cell types, which has become a major hurdle for selective delivery and *in vivo* applications. Therefore, local and topical administrations are the primary methods for clinical applications of CPP-based formulation and therapeutics.^{13,14}

Some of the strategies used to impart selectivity to CPPs are introduction of specific cell targeting ligands such as homing peptides and sugars.^{15,16} Although these conjugate systems have shown better selectivity, the small ligands are not sufficient to avoid the indiscriminate membrane permeability.¹⁷ The charge-masking of cationic CPPs is another strategy to minimize the non-specific membrane interaction.¹⁸⁻²⁴ However, charge-masking reduces the membrane penetration. Thus, detachment of the charge masking unit at the target site by enzymatic or photodegradation techniques could revert the membrane permeability of CPPs.^{25,26} Efficacy of these methods depends on enzymatic cleavage kinetics, enzyme abundant in the target site, and tissue permeability of light for photoactivation, which significantly limit the practical applicability. Another promising approach is utilizing the environment pH, one of the most well-known trigger signals for selective delivery of drugs to inflammatory tissues and tumors.²⁷

Uncontrolled proliferation, dysregulated energy metabolism, and insufficient perfusion collectively altered the physiochemical composition of tumor environment.^{28,29} Tumor

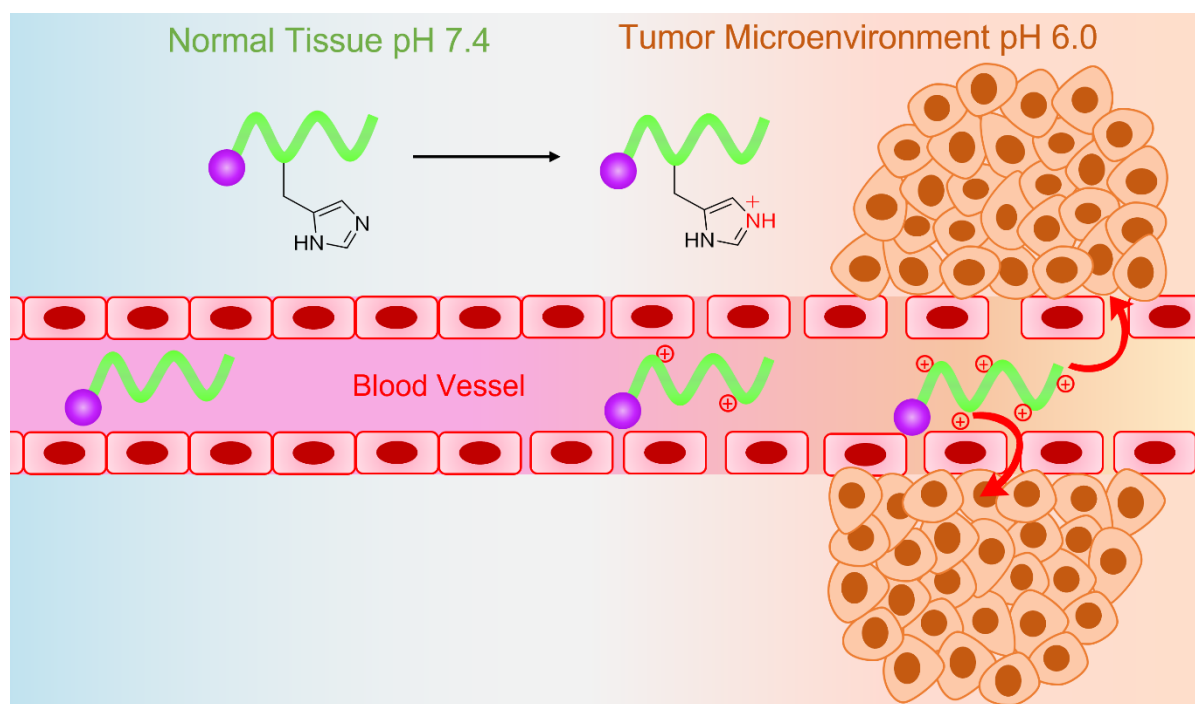


Figure 1. Schematic representation of pH-responsive uptake of **Hkd** in tumor microenvironment.

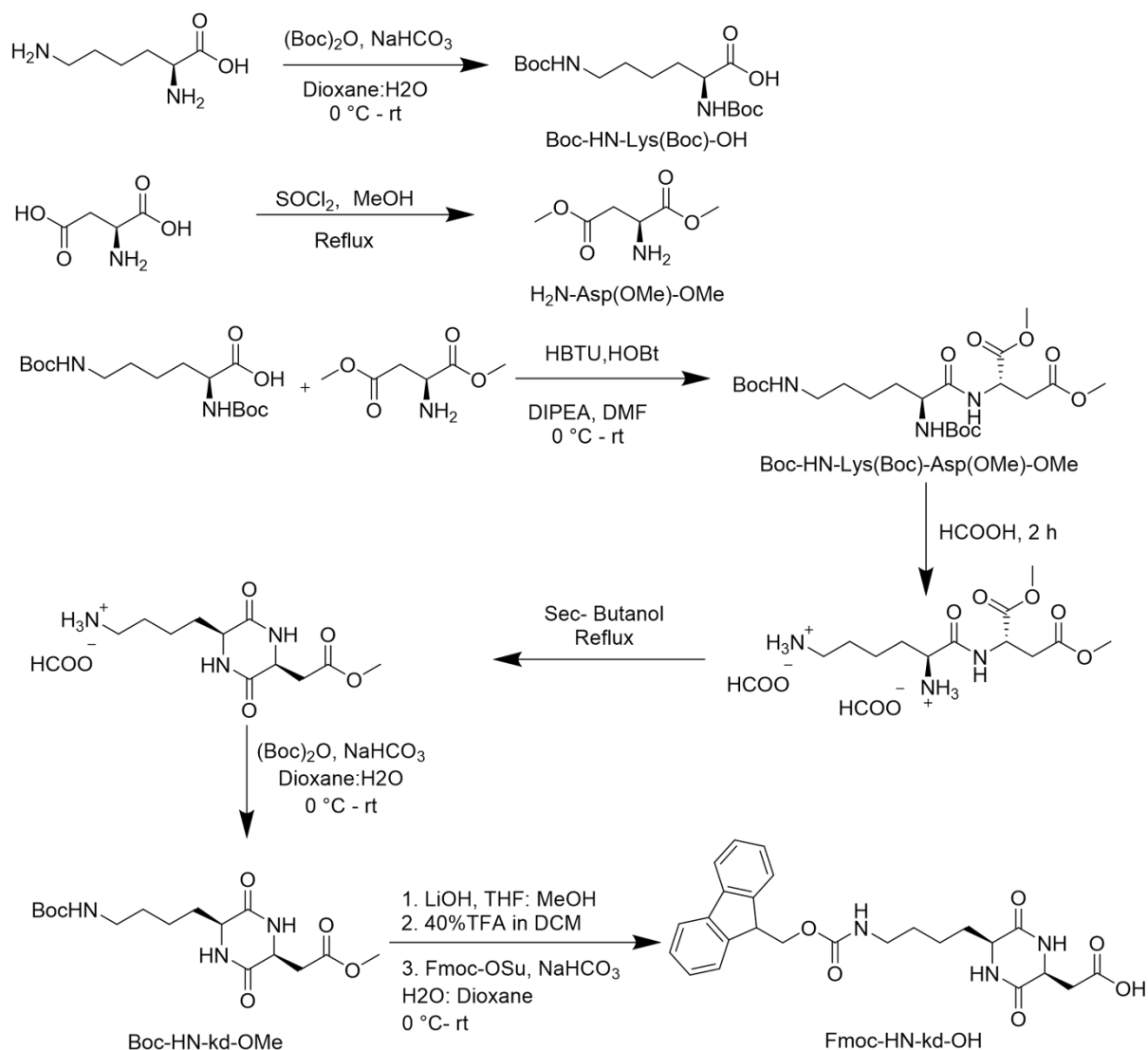
microenvironment associated with hypoxia, acidity, reduced glucose gradient, recruitment of stromal and immune cells.^{30,31} Accumulation of the acidic metabolic waste products from high metabolic activity reduces the pH of tumor microenvironments.³² The pH gradient between interstitial space and perfectly maintained intercellular pH has influential role in cell functioning, cell-cell, and cell-extracellular matrix interactions. These compartmentalized tumor microenvironments promote the cancer cell development through genetic stability, epigenetic modification, cell metabolism, cell proliferation, and survival. Thus, targeting the tumor microenvironment with pH responsive appendages significantly advances the therapeutic modalities.³³ Several pH responsive CPPs have been developed for tumor microenvironment specific delivery.³⁴⁻³⁷ However, the stability of CPPs is a major concern for *in vivo* applications.^{38,39}

In this report, we have developed a decamer CPP **Hkd** to selectively deliver anticancer drugs into cancerous tissue in response to the prevailing acidic pH environment (Figure 1). The CPP

sequence is composed of unnatural cyclic dipeptide (CDP)-based amino acid cyclo (Lys-Asp) (kd) and natural histidine. The histidine imidazole side chain is sensitive to pH and undergoes protonation in acidic environment. The rigid CDP core has multiple hydrogen bonding donor and acceptor sites, and protease stability, which helps in selective interaction driven cellular uptake. The pharmacokinetics studies unveiled the serum stability and cytocompatibility of **Hkd**. *In vitro* cellular uptake studies by FACS and confocal microscopy revealed the enhanced peptide uptake at lower pH compared to physiological pH. **Hkd** conjugation with anticancer drug camptothecin (Cpt) reduces the nonselective drug toxicity in normal cells. Thus, pH dependent uptake of **Hkd** is useful in targeting the cancer cell microenvironment for selective drug delivery to cancer cells and tissues without affecting the normal cells.

6.1 Design and Synthesis of Hkd

CDP is the simplest cyclic peptide formed by the cyclization of corresponding linear dipeptide.⁴⁰ Several natural products with CDP scaffold are the secondary metabolites with numerous biological activities such as antimicrobials, antimalarial, anticancer, hypoglycaemic agents, blood-brain barrier transporter, and drug delivery agents.⁴¹ The rigid lactam core of CDP overcomes the limitation of the linear dipeptide ranging from protease stability, conformational flexibility, and poor bioavailability. The unique hydrogen bonding pattern of the diketopiperazine core of CDP provides stable packing arrangements with numerous opportunities to construct functional materials and biomaterials.⁴² Herein, inspired by the microenvironment pH-dependent protonation of the histidine and specific hydrogen bonding interaction of rigid CDP unit we have designed a peptidomimetic system by incorporating the unnatural CDP amino acid kd at alternate position of the histidine peptide backbone. The CDP



Scheme 1. Synthesis of Fmoc-HN-kd-OH.

units will provide proteolytic stability and participates in hydrogen bonding interaction with the lipid membrane to enhance the cell permeability. The cyclo(Lys-Asp) CDP-based unnatural amino acid (kd) was synthesized as shown in Scheme 1. The amine groups of L-lysine were protected by t-butyloxycarbonyl (Boc) group, and carboxyl groups of aspartic acid were protected as methyl esters. Two protected amino acids were coupled by using HBTU/HOBt as a coupling reagent at room temperature (rt) to obtain L-lysine-L-aspartic acid dipeptide. The Boc groups of dipeptide were deprotected by formic acid and subjected to

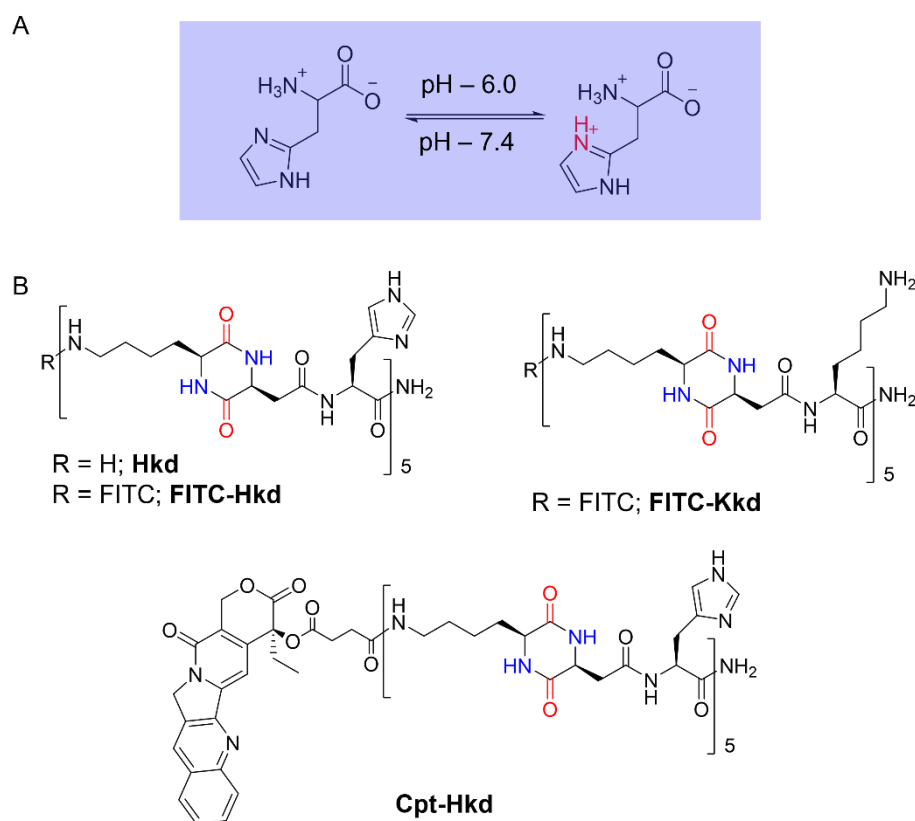


Figure 2. (A) pH dependent protonation of histidine imidazole. (B) Structure of kd incorporated peptidomimetics **Hkd**, **Kkd**, and camptothecin (Cpt) conjugated **Hkd** (**Cpt-Hkd**).

intramolecular cyclization under heating condition in excess sec-butanol as solvent. The dilution condition effectively suppresses the intermolecular reaction and promotes the intramolecular cyclization to form CDP core. The amine group of cyclized derivative was protected with Boc group. The methyl ester hydrolysed by LiOH in THF/methanol, followed by deprotection of Boc group using trifluoro acetic acid (TFA). Finally, the amine group was protected using Fmoc N-hydroxysuccinimide ester (Fmoc-Osu) to obtain Fmoc-HN-kd-OH for further utilization in solid phase peptide synthesis (SSPS). The kd unit was incorporated at the alternate position of histidine and lysine peptides to obtained **Hkd** and **Kkd** (Figure 2). The **Kkd** was synthesized to understand the relative uptake behavior at different pH conditions. Further, fluorescein isothiocyanate (FITC) fluorophore was covalently attached at N-terminal of **Hkd** and **Kkd** to understand the cellular permeability and quantification of the uptake

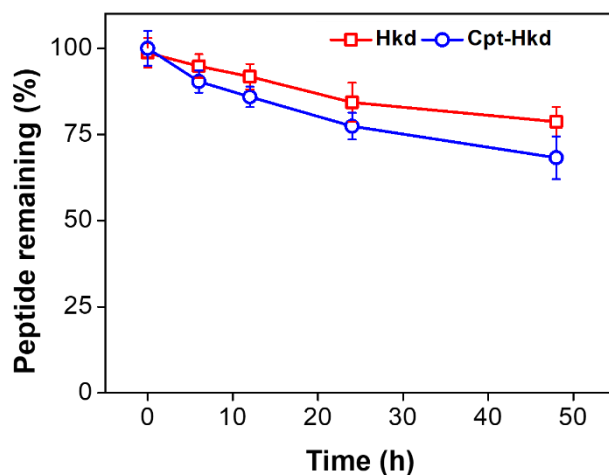


Figure 3. Proteolytic stability of **Hkd** (A) and **Cpt-Hkd** (B) with time.

profile. The anticancer drug camptothecin was covalently conjugated to **Hkd** N-terminal for the pH dependant drug delivery. All the peptidomimetics were purified by preparative HPLC, purity and integrity was ascertained by HPLC chromatogram and MALDI.

6.2 Proteolytic Stability

The synthesized peptidomimetics have unnatural amino acid kd at alternate positions in the sequence which assumed to improve proteolytic stability. Thus, the proteolytic stability of **Hkd** and **Cpt-Hkd** peptidomimetics was performed in human blood serum (HBS) to understand the role of kd in resisting proteolytic degradation. The **Hkd** treated with HBS was analyzed by analytical HPLC with time. More than 90% of the peptidomimetic remained intact even after 48 h of incubation in HBS (Figure 3). Thus, incorporation of kd imparts proteolytic susceptibility to **Hkd**. The protease stability will enhance the bioavailability of peptidomimetics. However, **Cpt-Hkd** showed low protease stability, and 70% of the peptidomimetics was remained after 48 h of incubation (Figure 3). The lower stability of **Cpt-Hkd** might be associated with the ester linkage between Cpt and **Hkd**.

6.3 Cell Viability

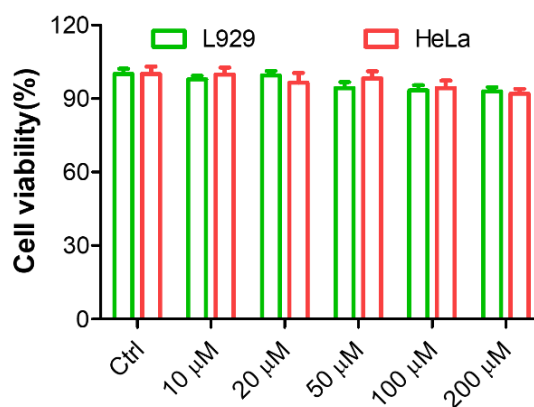


Figure 4. Viability of L929 and HeLa cells in 10 -200 μM of **Hkd** after 24 h.

The biocompatibility of the **Hkd** was evaluated in HeLa and L929 cells to assess their applicability in live cells. Cells were incubated with 10 -200 μM of **Hkd** for 24 h and cell viability was assessed by MTT assay. Cell viability remained >90% in concentration range of 10-200 μM **Hkd** (Figure 4). Thus, the kd containing histidine peptidomimetic is relatively non-toxic to cells and can be used for *in vitro* studies.

6.4 pH-dependent Cellular Uptake

The pH-dependent cell membrane penetrating ability of FITC labeled **FITC-Kkd** was

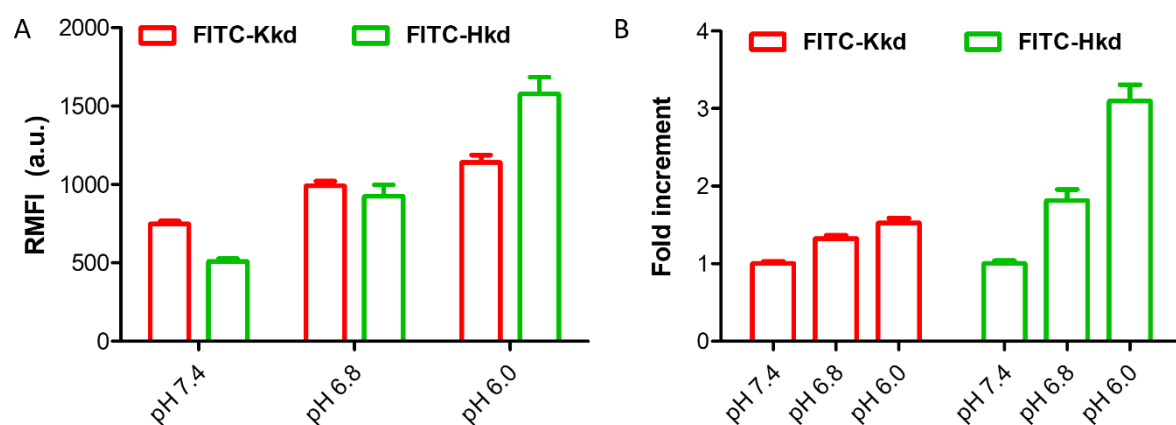


Figure 5. (A) Cellular uptake of **FITC-Kkd** and **FITC-Hkd** at pH 7.4, 6.8 and 6.0. (B) Fold increment of intracellular uptake with pH.

investigated in HeLa cells by fluorescence activated cell sorting analysis (FACS). The lysine-based peptidomimetics **Kkd** possess permanent positive charges at physiological pH. The cellular uptake of **Kkd** (10 μ M) showed efficient penetration to the membrane and exhibited good cellular internalization (Figure 5A). However, uptake remained similar with subsequent decline of pH 6.8 and 6.0. At pH 6.8 and 6.0, the fluorescence intensity increment was 1.2 and 1.5 fold, respectively (Figure 5B). In contrast, the **Hkd** showed very weak membrane permeability at physiological pH. The cellular uptake enhances by lowering the pH of the medium to 6.8 and 6.0. Cellular uptake was improved to 1.8 and 3.2 fold compared to the physiological pH of the medium. Thus, the neutral charge of the **Hkd** was not efficient in promoting the uptake at physiological pH. While lowering the medium pH, protonates imidazole side chain of histidine and stimulates the cellular uptake.

Confocal microscopy were performed to visualize the cellular uptake at different pH levels. The fluorescence inside the cells showed good cellular permeability of **Kkd** at all pH ranges (Figure 6A). The uptake was slightly increased with lowering of the medium pH. The fluorescence quantification data showed 1.2 and 1.5 folds increments in the cellular uptake (Figure 6B, 6C). While **Hkd** at physiological pH showed poor uptake with few cells had showed intracellular localization (Figure 7A). The uptake was enhanced at acidic pH 6.8, 6.0, and all cells showed **FITC-Hkd** inside. The intracellular uptake was enhanced about 1.8 and 3.2 fold at acidic pH 6.8 and 6.0, respectively (Figure 7B, 7C). The cellular uptake was further investigated in another cancerous cell line MCF-7 and similar pH-dependent uptake of **FITC-Hkd** was observed (Figure 8A). The cellular uptake was enhanced 1.9 and 3.4 fold at pH 6.8 and 6.0 respectively (Figure 8B, 8C). Thus, membrane penetration efficacy of the **Hkd** is pH dependent and can be utilize for selective drug delivery in tumor microenvironment compared to the physiological pH environments.

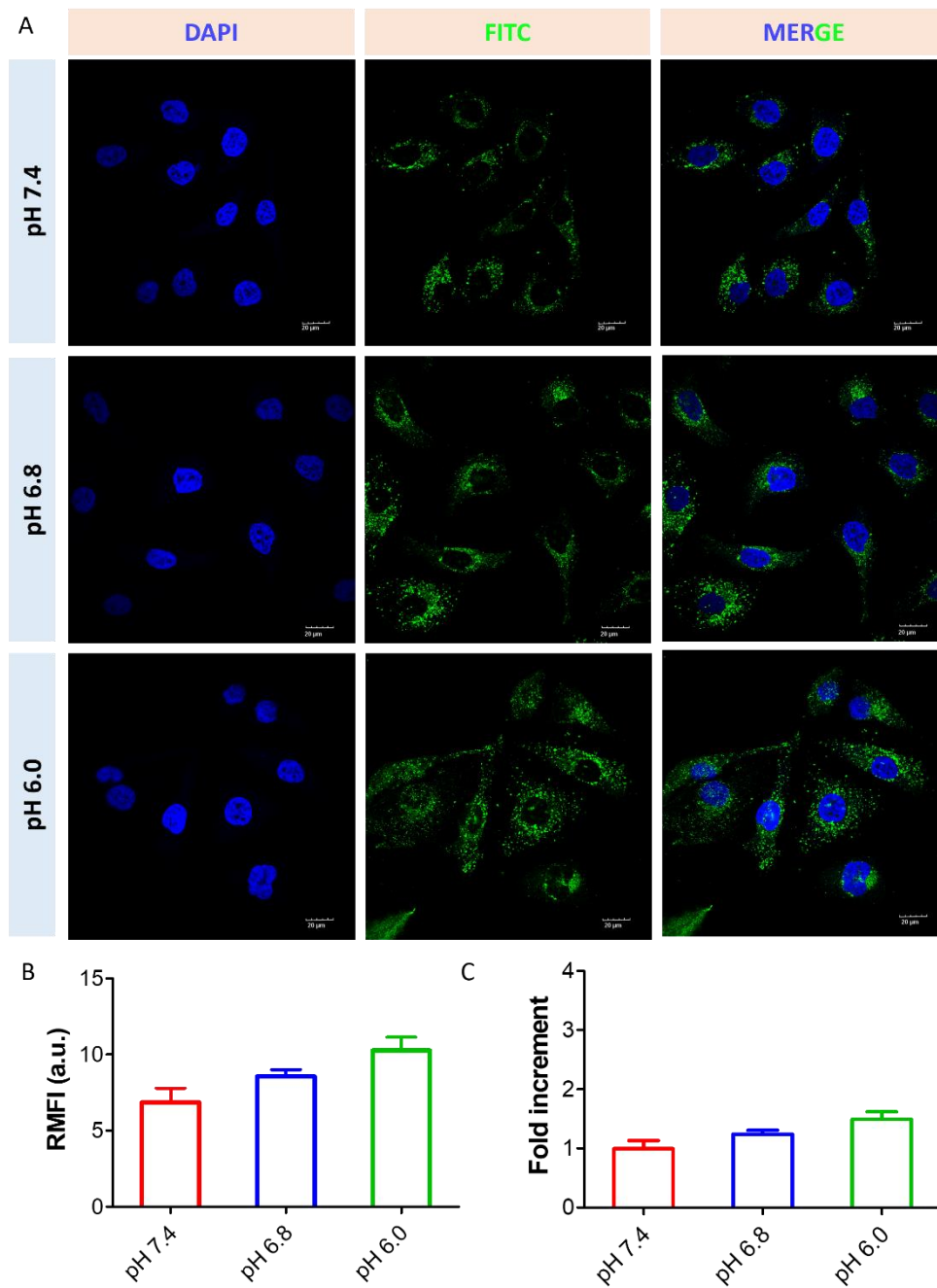


Figure 6. Cellular uptake of **FITC-Kkd** in HeLa cell. (A) pH-dependent uptake of **FITC-Kkd** (10 μ M). The cellular uptake at different pH remains similar. Cell nucleus was stained with 4',6-diamidino-2-phenylindole (DAPI). (B) Relative mean fluorescence intensity (RMFI) quantification of intracellular uptake. (C) Fold increment of **FITC-Kkd** uptake with varying pH.

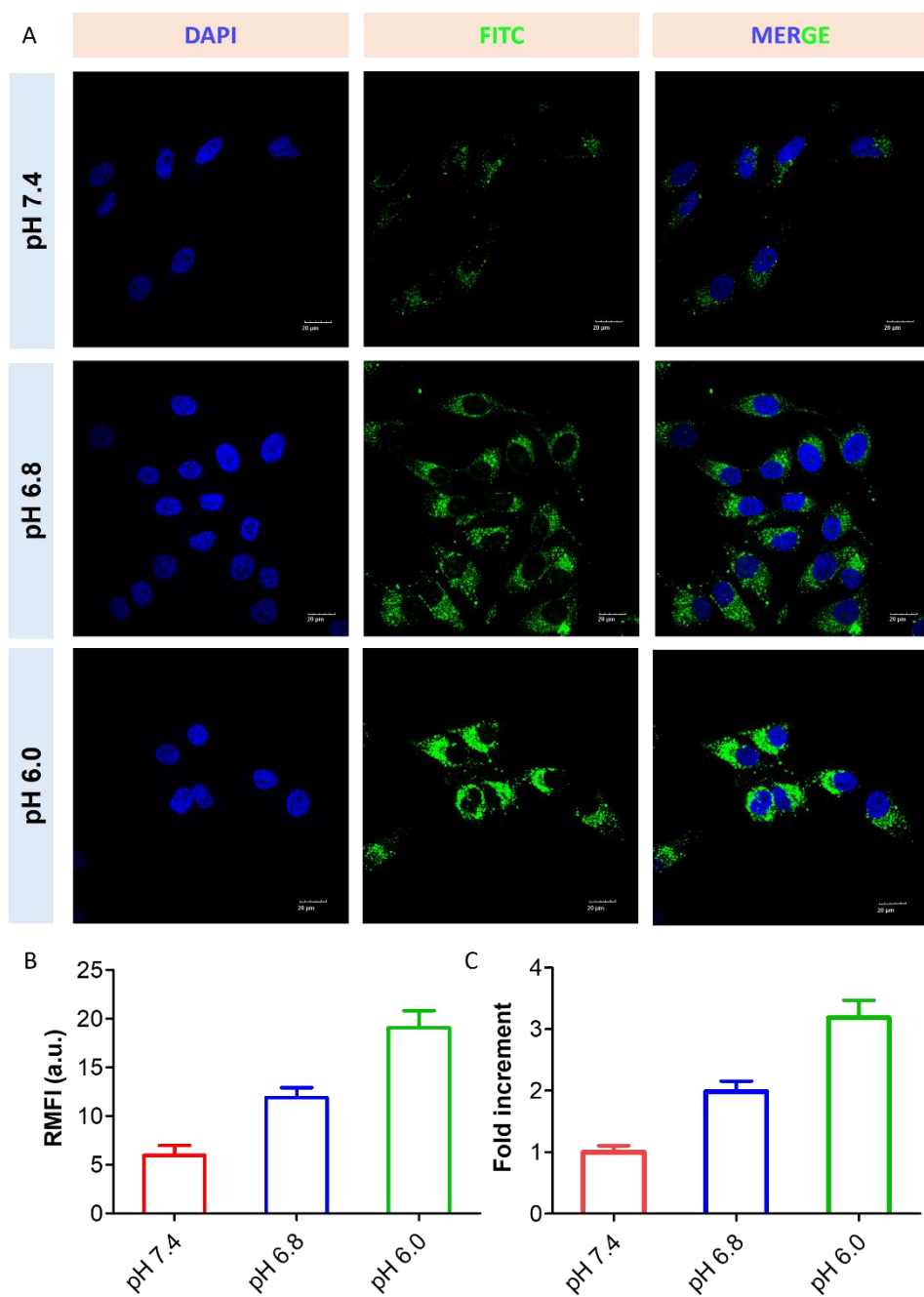


Figure 7. Cellular uptake of **FITC-Hkd** in HeLa cell. (A) pH-dependent uptake of **FITC-Hkd** (10 μ M). Cell nucleus was stained with DAPI. (B) Relative mean fluorescence intensity (RMFI) quantification of intracellular uptake. (C) Fold increment of **FITC-Hkd** uptake with varying pH.

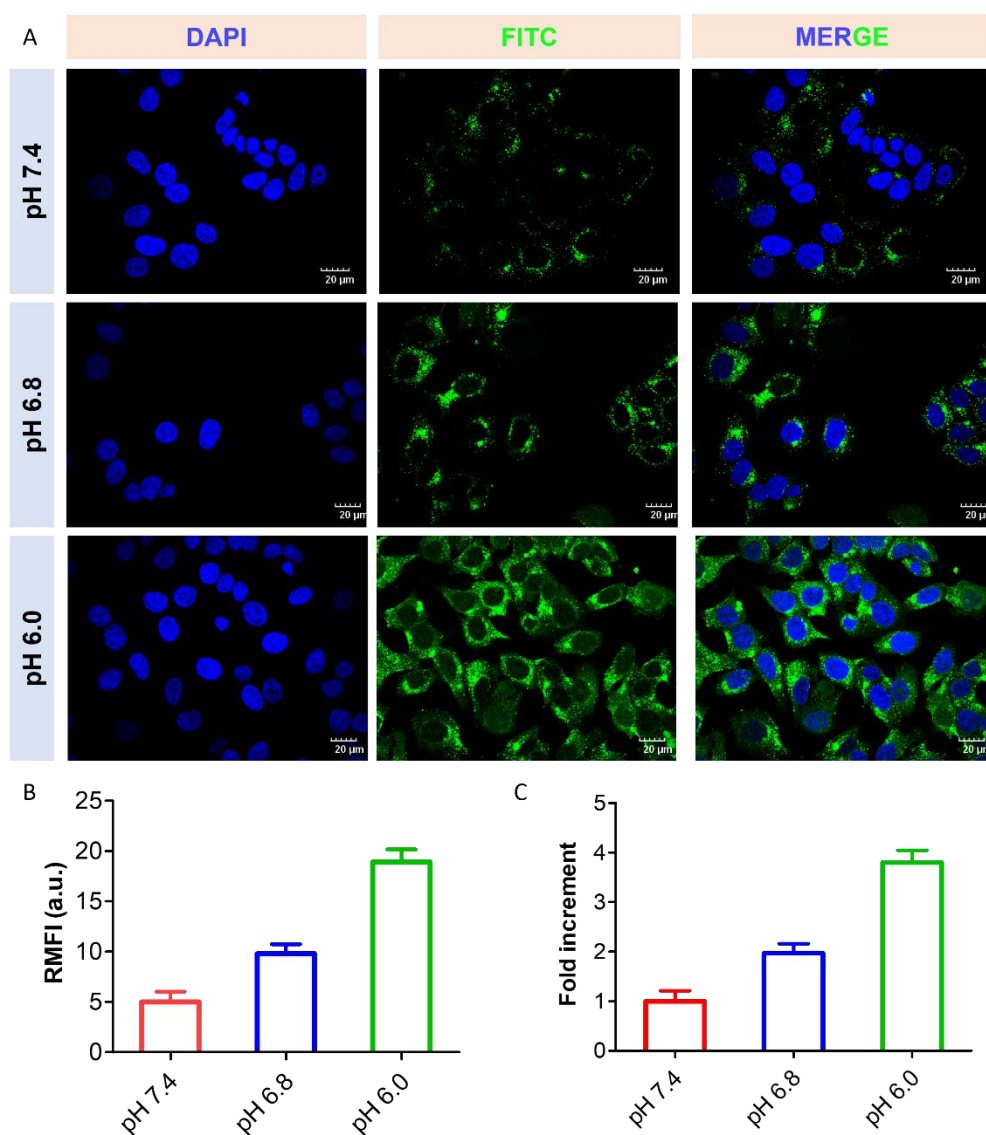


Figure 8. Cellular uptake of **FITC-Hkd** in MCF-7 cell. (A) pH-dependent uptake of **FITC-Hkd** (10 μ M). Cell nucleus was stained with DAPI. (B) Relative mean fluorescence intensity (RMFI) quantification of intracellular uptake. (C) Fold increment of **FITC-Hkd** uptake with varying pH.

The pH-dependent uptake of **Cpt-Hkd** was visualized on HeLa cells by confocal microscopy studies. The intracellular uptake at physiological pH was very marginal (Figure 9A). While cellular uptake was significantly enhanced at acidic pH 6.8 and 6.0. The drug uptake was 1.7 and 3.5 folds at pH 6.8 and 6.0 respectively (Figure 9B, 9C). Therefore, all these uptake profiles indicate that the **Hkd** has better selectivity toward the cancer cell microenvironment than the normal cells.

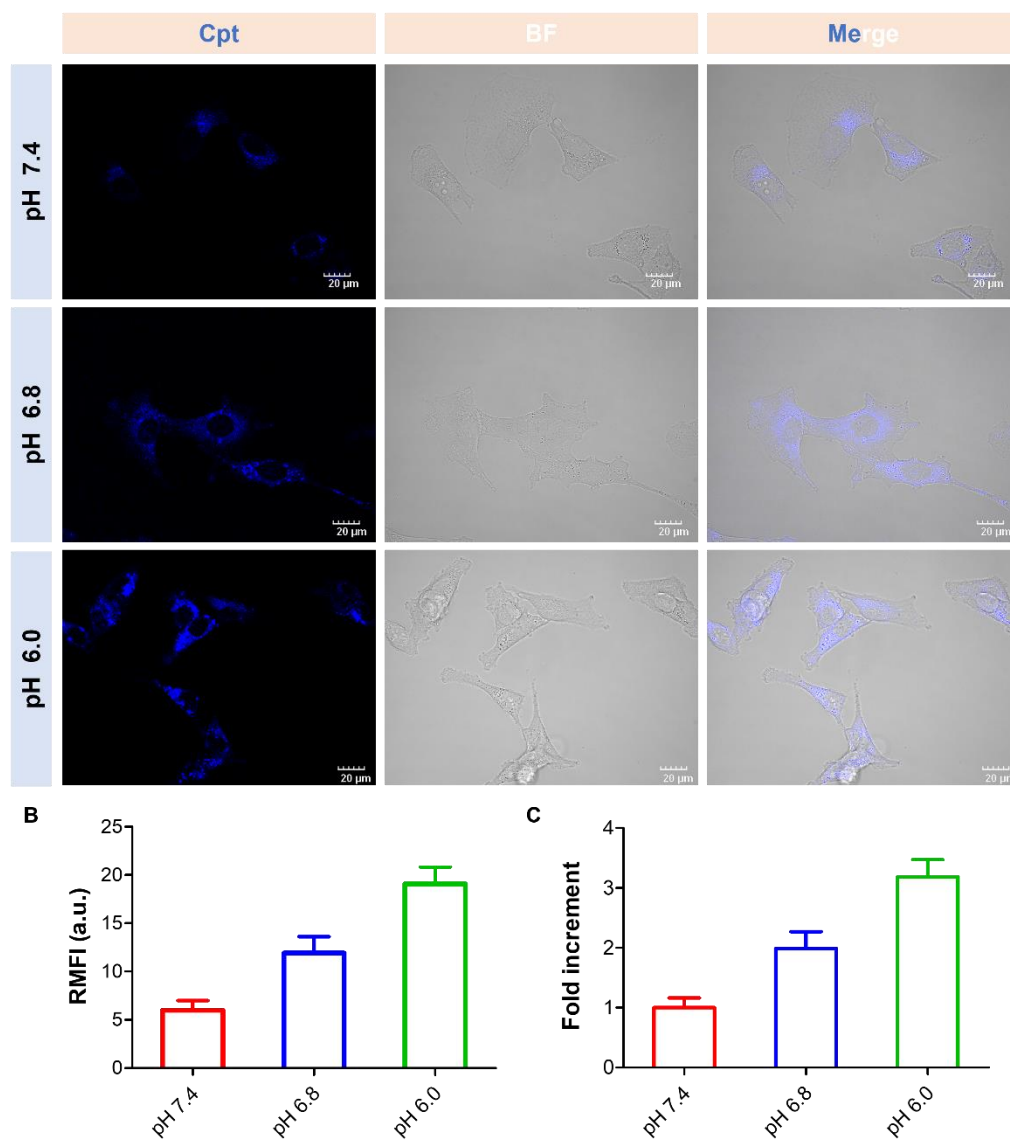


Figure 9. Cellular uptake of **Cpt-Hkd** in HeLa cell. (A) pH-dependent uptake of **Cpt-Hkd** (10 μ M). (B) Relative mean fluorescence intensity (RMFI) quantification of Cpt fluorescence. (C) Fold increment of **Cpt-Hkd** uptake with varying pH.

6.5 *In Vitro* Cytotoxicity of Cpt-Hkd

Further, toxicity profile of anticancer drug (Cpt) and drug-peptidomimetics conjugate (**Cpt-Hkd**) was evaluated in L929 cells. Cells were incubated with 0.1-20 μ M of Cpt and **Cpt-Hkd** for 24 h at physiological pH. The free drug has shown good cytotoxicity to the L929 cells, and cell viability declined to 30% at 20 μ M of Cpt (Figure 10). While, the **Cpt-Hkd** was relatively

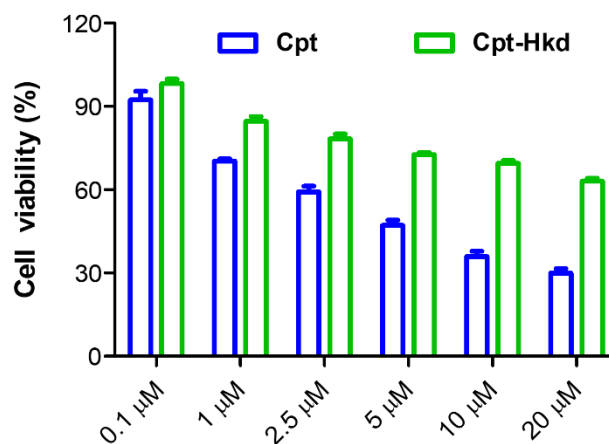


Figure 10. Viability of L929 non-cancerous cells in presence of anticancer drug Cpt and drug conjugate **Cpt-Hkd**.

less toxic to cells, and cell viability was 63% at 20 μM. The peptidomimetics conjugation brought the selectivity to anticancer drug Cpt and reduced the non-specific toxicity to normal cells. Thus, the pH-dependent uptake profile of the **Hkd** might be useful for selectively delivering the anticancer drug in cancer cells.

6.6 Conclusion

We have designed peptidomimetic **Hkd** by incorporating CDP-based unnatural amino acid kd into natural histidine peptide. The incorporation of kd unit enhanced the proteolytic susceptibility to the peptidomimetic **Hkd**. The unique hydrogen bonding ability of CDP core of kd provided multiple hydrogen bonding donor and acceptor site for interaction with membrane lipid, which helps in selective intraction driven cellular uptake. The histidine present in **Hkd** is sensitive to pH and undergoes protonation in acidic environment. Membrane permeability of the **Hkd** initiated at acidic pH. The peptidomimetic conjugation reduced the non-specific toxicity of the free drug to the normal cells. Further, we are evaluating the pH-dependent toxicity of the covalent drug conjugate in cancer cells and tumors.

6.7 Experimental Methods

6.7.1 Materials and General Methods

All Fmoc protected amino acids, Rink amide resin, and coupling reagents for peptidomimetic synthesis were purchased from Merck and Spectrochem India. Dimethyl formamide (DMF), N,N,N,N-tetramethyl-O-(1H-benzotriazol-1-yl)uranium hexafluorophosphate (HBTU), N,N-diisopropylethylamine (DIPEA), hydroxybenzotriazole (HOBt), piperidine, trifluoroacetic acid (TFA), acetonitrile and all other chemicals were purchased from Spectrochem India. Fluorescein isothiocyanate (FITC) and camptothecin were purchased from TCI (Japan). HPLC grade solvents are used for reactions, and moisture-sensitive reactions were performed under nitrogen atmosphere. Column chromatography was carried out on silica gel (100-200 mesh size). Thin layer chromatography (TLC) was carried out on silica gel plates of 60 F254 obtained from Merck. Product spots on the TLC plate were visualized using UV lamp or stained with 0.2% (w/v) ninhydrin solution in absolute ethanol, followed by charring on hot plate. Laboratory-grade reagents were used for the purification of compounds by column chromatography. NMR spectra were recorded on Bruker Av-400 spectrometer, and chemical shifts were reported as ppm (in chloroform-d₃, DMSO-d₆ with tetramethyl silane as internal standard). Peptidomimetics were purified on Shimadzu reverse-phase semipreparative HPLC system using C18 column. The integrity of the peptidomimetic system were ascertained by high-resolution mass spectra (HRMS) obtained from Agilent Technologies 6538 UHD Accurate-Mass Q-TOF. All cell lines were purchased from NCCS Pune, India. Cell culture media DMEM, fetal bovine serum (FBS), penicillin-streptomycin, and trypsin were purchased from Gibco. The MTT (3-(4,5-dimethylthiazol-2-yl) -2,5-diphenyltetrazolium bromide) were purchased from Merck.

6.7.2 Protection of Amine Groups of L-Lysine

Amine groups of the lysine were protected by t-butyloxycarbonyl (Boc) group. Lysine (5 g, 27.4 mmol) was dissolved in a mixture of water and dioxane (1:1) in ice-cold condition, and Na_2CO_3 (11.6 g, 110 mmol) was added. The mixture was stirred at ice cold conditions, and Boc-anhydride (22 mL, 95.9 mmol) in dioxane was added dropwise. The reaction was kept stirring for 12 h at room temperature. After completion, the reaction mixture was diluted with water and washed with diethyl ether (100 mL \times 3) to remove the unreacted Boc-anhydride. The aqueous layer was neutralized by concentrated HCl and further acidified by diluted HCl to protonate the carboxyl group of lysine. After acidification, DCM was poured into the aqueous phase, and the organic phase was separated. The organic phase was washed with brine solution, dried over Na_2SO_4 , and evaporated under vacuum to get colorless viscous liquid product Boc-HN-Lys(Boc)-COOH.

$^1\text{H-NMR}$ (400 MHz, CDCl_3): δ_{ppm} 6.05 (s, 1H), 5.65 (s, 1H), 5.06 (s, 1H), 3.95 (s, 1H), 3.63 (s, 2H), 2.99 (s, 2H), 1.69 (m, 1H), 1.49 (m, 1H), 1.33 (s, 18H), 1.27 (m, 2H).

6.7.3 Esterification of Aspartic Acid

The carboxylic acid group of the aspartic acid was protected through methyl ester formation. Aspartic acid (3 g, 22.5 mmol) was dissolved in methanol and kept for stirring under ice-cold conditions. Thionyl chloride (8 mL, 67 mmol) was dropwisely added into the reaction mixture. After addition of thionyl chloride, reaction mixture was reflux at 65 °C for 12 h. Solvents were evaporated under vacuum, and toluene was poured and co-evaporated to remove the residual thionyl chloride. The colorless semisolid product $\text{H}_2\text{N-Asp(OMe)-OMe}$ was used for further reaction.

$^1\text{H-NMR}$ (400 MHz, D_2O): δ_{ppm} 4.42 (m, 1H), 3.37 (s, 3H), 3.68 (s, 3 H), 3.09 (m, 2H). $^{13}\text{C-NMR}$ (100 MHz, D_2O): δ_{ppm} 171.6, 169.3, 53.9, 52.9, 49.1, 33.6.

6.7.4 Synthesis of Dipeptide

To a stirred solution of Boc-HN-Lys(Boc)-COOH (1 g, 2.85 mmol) in DMF (15 mL) at 0 °C, DIPEA (1.73 g, 10.1 mmol), HBTU (1.31 g, 3.46 mmol) and HOBt (0.53 g, 3.46 mmol) were added. The reaction mixture was kept stirring for 15 min under an inert nitrogen atmosphere. NH₂-Asp(OMe)-OMe (0.56 g, 3.4 mmol) was added to the above activated reaction mixture and stirred for 24 h. Completion of the reaction was monitored by TLC. Solvents were evaporated under vacuum, and residues were mixed into ethyl acetate (EtOAc). The combined organic phase was washed with 1N HCl (50 mL ×2), the organic layer was collected, dried over anhydrous Na₂SO₄, and the solvent was evaporated. The crude reaction mixture was purified by column chromatography, and dipeptide product Boc-HN-Lys(Boc)-Asp(OMe)-OMe was eluted at 50: 50 hexane: ethyl acetate.

¹H-NMR (400 MHz, CDCl₃): δ_{ppm} 6.89 (d, 1H) 5.1 (s, 1H), 4.75 (m, 1H), 4.6 (s, 1H), 4.01 (t, 1H), 3.69 (s, 3H), 3.62 (s, 3H), 3.03 (m, 2H) 2.94 (m, 1H), 2.74 (m, 1H), 1.72 (m, 1H), 1.58 (m, 1H), 1.46 (m, 2H), 1.44 (s, 18H), 1.41 (m, 2H). ¹³C-NMR (100 MHz, CDCl₃): δ_{ppm} 170.9, 170.3, 169.8, 155.1, 76.2, 51.8, 51, 47.4, 38.9, 35, 31.1, 28.6, 27.4, 27.2, 21.4.

6.7.5 Boc Deprotection and Cyclization.

The Boc-protection groups of the dipeptide was remove prior to the cyclization. Dipeptide (2 g, 4 mmol) was dissolved in formic acid (30 mL) and stirred for 3 h at room temperature. Formic acid was evaporated under vacuum and further co-evaporated with toluene for complete removal of acid. Boc deprotected dipeptide was dissolved in sec-butanol (200 mL), reflux at 110 °C about 4 h to subject the intramolecular cyclization. The high dilution reduced the possibility of intermolecular reaction and facilitated the intramolecular cyclization to H₂N-kd-OMe.

6.7.6 Boc Protection of H₂N-kd-OMe

The crude cyclized product was dissolved in 1:1 dioxane/water (40 mL), stirred at ice cold condition and NaHCO₃ (1.25 g, 14.3 mmol) was added. Boc-anhydride (2.5 mL, 10.2 mmol) was drop wisely added into the reaction mixture and stirred at room temperature for 24 h. Unreacted Boc-anhydride was washed out by diethyl ether, and water layer was mixed with DCM. The organic layer was collected and dried with anhydrous Na₂SO₄, and solvent was evaporated under vacuum. The crude product was purified by column chromatography using DCM and methanol as eluent to get Boc-HN-kd-OMe.

¹H-NMR (400 MHz, DMSO-*d*₆): δ_{ppm} 8.13 (s, 1H), 8.08(s, 1H), 6.72 (t, 1H) 4.21 (t, 1H) 3.88 (t, 1H) 2.87 (m, 3H) 2.68 (m, 2H) 1.66(m, 2H), 1.37 (s, 9H), 1.25 (m, 2H). ¹³C-NMR (100 MHz, DMSO-*d*₆): δ_{ppm} 170.2, 168, 167.3, 155.5, 77.3, 53.7, 51.4, 50.8, 36.4, 31.2, 29.2, 28.2, 21.3.

6.7.7 Ester Hydrolysis and Boc Deprotection of Boc-HN-kd-OMe

Next, the methyl ester group of the Boc-HN-kd-OMe was removed by LiOH. Boc-HN-kd-OMe (1.2 g, 3.3 mmol) was treated with LiOH (0.3 g, 6.6 mmol) in THF/Methanol (20 mL) for 2 h at room temperature. Methanol and THF were removed by vacuum. The dried Boc-HN-kd-COOH was treated with TFA solution in DCM (TFA: DCM = 60:40) for 2 h and evaporated to get H₂N-kd-COOH.

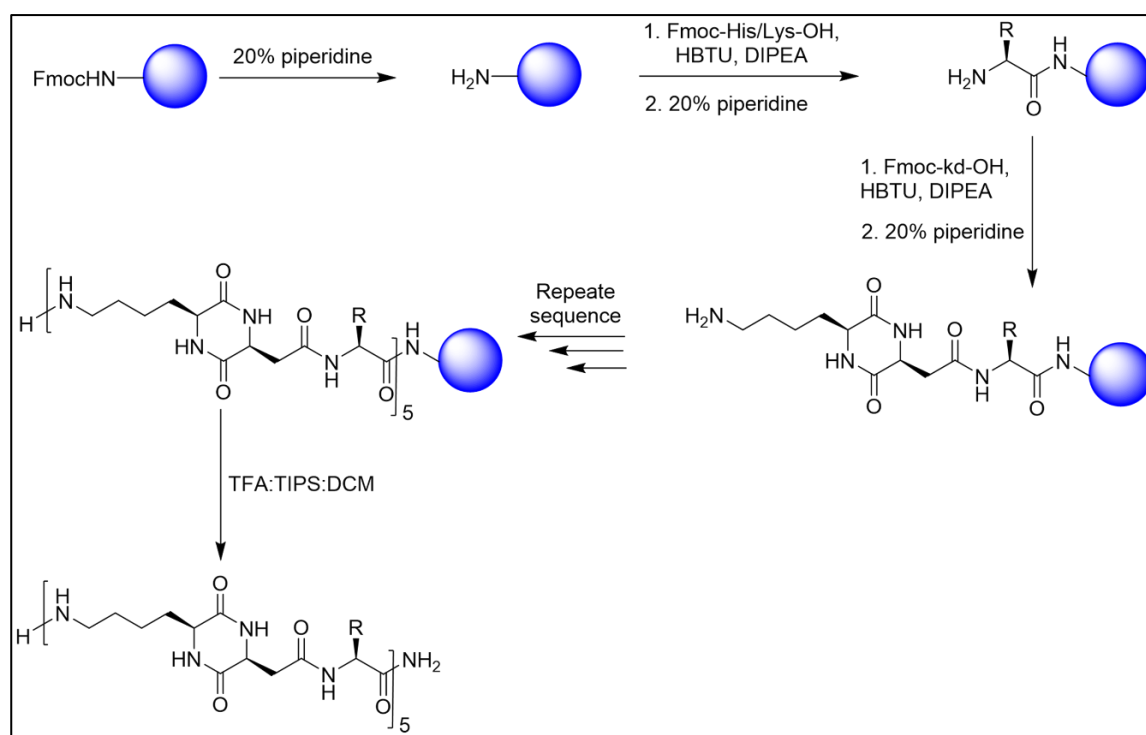
6.7.8 Fmoc Protection of H₂N-kd-COOH

The amine group of the H₂N-kd-COOH was further protected with the Fmoc group for utilization in Fmoc-chemistry protocol during solid phase peptide synthesis. The H₂N-kd-COOH (0.8 g, 3.3 mmol) was dissolved in 1: 1 water/dioxane (30 mL) at 0 °C. Na₂CO₃ (1.06 g, 9.9 mmol) and Fmoc-OSu (1.67 g, 4.95 mmol) were added to the reaction mixture and stirred for 24 h. After completion of the reaction the reaction mixture was diluted with water, and excess Fmoc-OSu was removed using diethyl ether (50 mL×3). The aqueous layer was

neutralized by 1N HCl to obtain the white precipitation. The precipitation was filtered out and dried to acquire the Fmoc-HN-kd-OH.

$^1\text{H-NMR}$ (400 MHz, $\text{DMSO-}d_6$): δ_{ppm} 12.304 (s, 1H), 8.09 (s, 1H), 8.004 (s, 1H), 7.87 (d, 2H), 7.67 (d, 2H), 7.39 (t, 2H) 7.31 (t, 2H) 7.22 (t, 1H), 4.2 (d, 2H), 4.17 (m, 2H), 3.87 (t, 1H), 2.94 (t, 2H), 2.61 (m, 2H), 1.68 (m, 2H), 1.37 (m, 4H). $^{13}\text{C-NMR}$ (100 MHz, $\text{DMSO-}d_6$): δ_{ppm} 171.3, 168, 167.6, 156, 143.9, 140.7, 127.5, 127, 125.1, 120, 65.16, 53.8, 50.8, 46.7, 36.5, 31.3, 29.1, 21.4, 15.1.

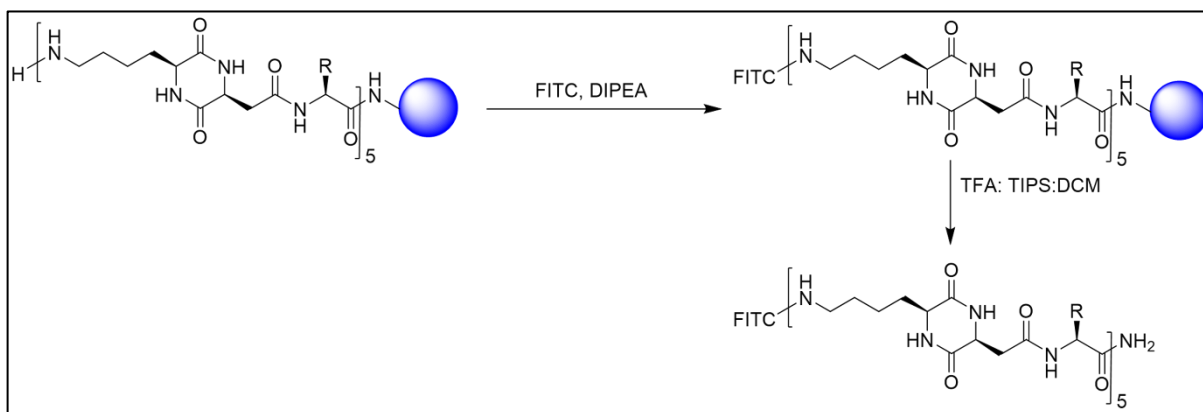
6.7.9 Peptidomimetics Synthesis



Peptidomimetics were synthesized following standard 9-fluorenylmethoxycarbonyl (Fmoc) SSPS protocols. The kd incorporated peptidomimetics were synthesized in SYRO II automated peptide synthesis system. Fmoc protected amino acid with suitable amino acid side chain protecting group was used for the solid phase synthesis. Fmoc protected Rink amide resin was used as solid support for the peptidomimetics synthesis. Resin (150 mg/vial) was swelled in DCM before starting the synthesis. Deprotection of Fmoc group was carried out by 40%

piperidine in DMF for 4 min, followed by 20% piperidine for 10 min. Amino acids coupling was performed using HBTU/HOBt as the -COOH activating reagent, DIPEA as a base in DMF solvent. HBTU, HOBt, Fmoc-amino acid in DMF and DIPEA (in NMP) were used for the coupling stage. The unnatural kd unit was incorporated by using the same coupling reagents. After completion of each sequence, the Fmoc group at N-terminal was deprotected to obtain the free N-terminal. The free N-terminal group was conjugated with fluorescein isothiocyanate (FITC, 1.5 eq) and DIPEA (5 eq) in DMF for 6 h. After completion of the sequences, peptidomimetics were cleaved from the resin bead using 95% TFA cocktail solution (TFA: TIPS: DCM = 95: 2.5: 2.5) for 3 h. The solution was poured into chilled ether to obtain the precipitation, which was further centrifuged, and solvents were discarded. Peptidomimetics were purified in reverse phase semi-preparative HPLC on C18 column in acetonitrile: water as elutant. Product purity was ascertained by HPLC chromatogram and integrity of the peptidomimetics were analyzed by HRMS (Q-TOF).

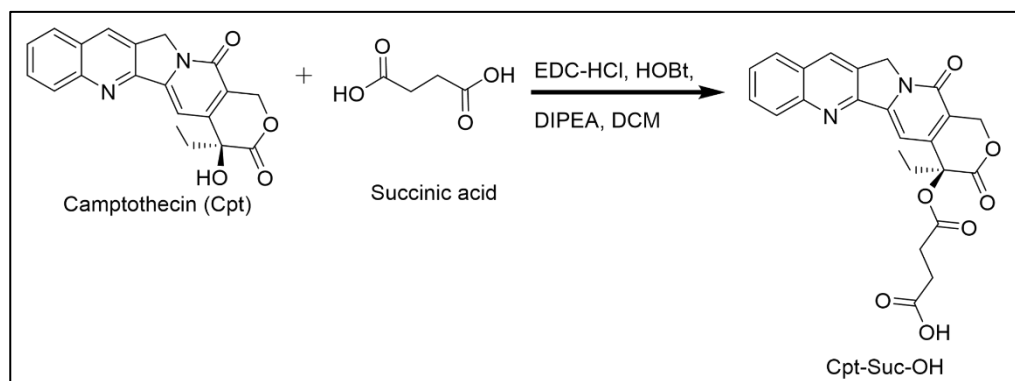
6.7.10 FITC Conjugation to Peptidomimetics



To understand cell membrane permeability of peptidomimetics, fluorescein isothiocyanate was conjugated at N-terminal. The resin bound peptidomimetics was treated with fluorescein isothiocyanate (FITC, 1.5 eq), DIPEA (5 eq) in DMF for 6 h. Resin was washed with solvents, and peptidomimetics were cleaved from the resin bead using 95% TFA cocktail solution (TFA:

TIPS: DCM = 95: 2.5: 2.5) for 3 h. The solution was poured into chilled ether to obtain the precipitation. Peptidomimetics were purified in reverse phase semi-preparative HPLC on C18 column in acetonitrile/water as eluent. Product purity was ascertained by HPLC chromatogram and integrity of the peptidomimetics were analyzed by MALDI.

6.7.11 Synthesis of Camptothecin and Succinic Acid Conjugate Cpt-Suc-OH



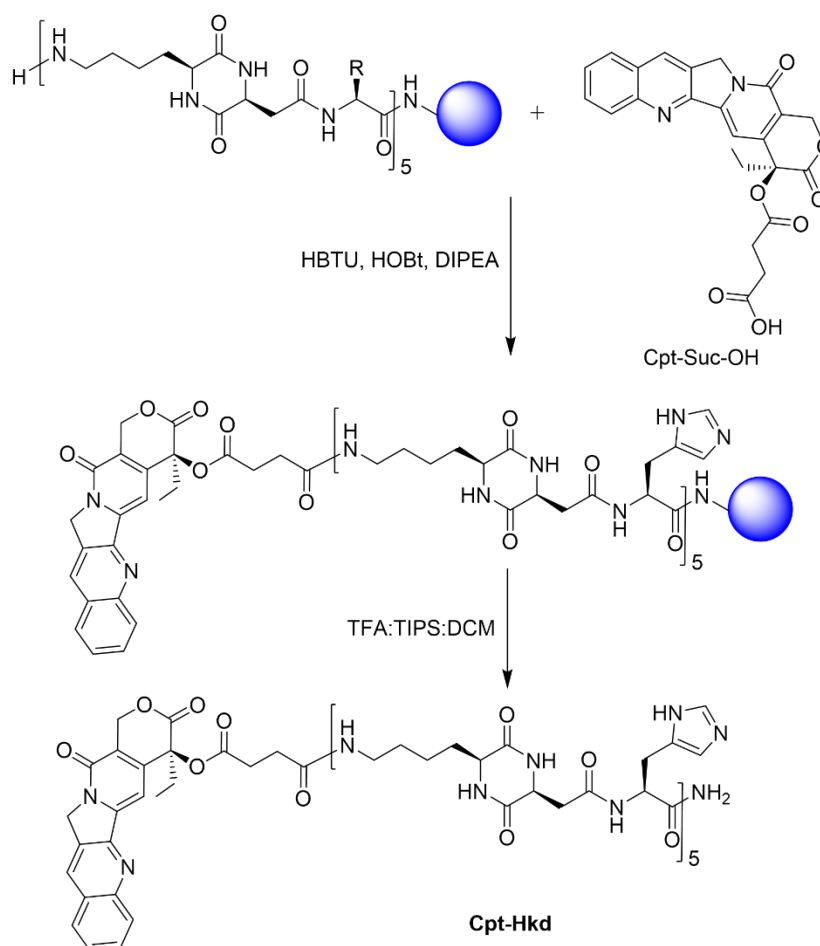
Camptothecin (Cpt) was attached at one terminal of succinic acid for further conjugation with the peptidomimetic system. To a stirred solution of succinic acid (0.116 g, 1.16 mmol), 1-Ethyl-3-(3'-dimethylaminopropyl) carbodiimide (EDC-HCl, 0.445 g, 2.32 mmol), 4-dimethylaminopyridine (DMAP, 140 mg, 1.16 mmol), and diisopropylethylamine (DIPEA, 400 μ L, 2.32 mmol) in dry DCM, Cpt (100 mg, 0.29 mmol) was added at room temperature. The reaction mixture was refluxed under nitrogen atmosphere for 24 h at 40 °C. Reaction mixture was cooled down, and DCM was poured into the mixture. The solution was washed with 1N HCl (100 mL \times 3), brine, and dried over Na₂SO₄, and solvent was evaporated under vacuum. Column chromatography was performed to purify the desired product Cpt-Suc-OH. Product was eluted at 5:95 methanol/DCM.

¹H-NMR (400 MHz, DMSO-*d*₆): δ_{ppm} 12.23 (s, 1H), 8.69 (s, 1H), 8.17 (s, 2H), 7.88 (s, 1H), 7.73 (s, 1H), 7.13 (s, 1H), 5.48 (s, 2H), 5.31 (s, 2H), 2.76 (m, 2H), 2.16 (s, 2H), 0.922 (m, 3H).

¹³C-NMR (100 MHz, DMSO-*d*₆): δ_{ppm} 173.1, 171.3, 167.1, 156.5, 152.3, 147.8, 145.9, 145.2,

131.5, 130.3, 129.7, 128.9, 128.5, 127.9, 127.6, 118.9, 95, 75.8, 66.2, 50.1, 30.3, 28.6, 28.5, 7.5.

6.7.12 Cpt-Hkd Synthesis



Cpt was conjugated into the **Hkd** by amide coupling reaction. The resin-bound peptide N-terminal Fmoc was deprotected by piperidine solution. The solution of Cpt-succinic acid, HBTU, HOBT, and DIPEA in DMF was mixed with resin matrix and kept under vortex conditions. After 12 h, the resin beads were thoroughly washed with DMF and DCM to remove unreacted reagents. The product was cleaved from the resin by cocktail solution of TFA, TIPS, and DCM (95:2.5:2.5). The solution was collected and treated with chilled ether to get the precipitation. The product was purified by reverse phase semi-preparative C18 column. The

purity of the product was determined by HPLC chromatogram, and integrity of the conjugate was analyzed by MALDI.

6.7.13 Peptidomimetic Stability

Stability of the peptidomimetics was assessed in human blood serum (HS). 100 μM of **Hkd** and **Cpt-Hkd** were incubated in serum at 37 °C. 100 μL of aliquots were removed at 6, 12, 24, and 48 h time and treated with 50 μL of 6 M urea solution and incubated at 4 °C for 10 min. The urea treatment disrupted the solubility of proteins and precipitated the serum proteins. Next, 40 μL of TFA (20%) was mixed with the above samples and incubated for 10 min at 4 °C, leading to the precipitation of serum proteins. Samples were centrifuged for 10 min and analyzed on analytical RP-HPLC system. The solution removed at 0 h was considered as the control for the experiments. The percentage of the remaining peptidomimetics was plotted against time.

6.7.14 Cell Viability

The compatibility of the **Hkd** peptidomimetics was analysed in HeLa (cancer cell) and L929 (non-cancer) cell lines. Both the cells were cultured in Dulbecco Modified Eagle Media (DMEM) supplemented with 10% Fetal bovine serum (FBS) and 1% penicillin-streptomycin (PS). Cells were seeded at cell density of 1×10^4 in a 96-well plate and cultured for 24 h. Cells were treated with 10 to 200 μM of peptidomimetic solution and incubated for 24 h. 10 μL of 0.5% MTT solution was added and further incubated for 4 h. The supernatant was removed carefully without disturbing the formazan crystals. The formazan crystals were dissolved in 100 μL of 1:1 dimethyl sulfoxide and methanol. The absorbance of the formazan dye was measured in the SpectroMax i3x microplate reader at 570 nm wavelength, followed by background correction at 690 nm.

6.7.15 *In Vitro* Cell Penetration

Human cervical cancer (HeLa) and Michigan cancer Foundation-7 (MCF-7, human breast cancer cell) cells were seeded at 12 well plates at cell density of 1×10^5 per well in DMEM supplemented with 10% FBS and 1% PS. The cells were cultured for 24 h at 37 °C with 5% CO₂. The culture medium was replaced with fresh medium with 10% FBS, and 1% PS, treated with **FITC-Kkd**, **FITC-Hkd** (10 μM) and cultured for 6 h. For pH adjustment of the culture medium, 1 M of HCl was added to the medium, and pH was measured. After 6 h, the medium was removed, and cells were washed with phosphate buffer saline (PBS, pH=7.4) three times. Wells were treated with trypsin-EDTA and incubated at 37 °C for 5 min to separate from wells. Further fresh medium was treated to wells, and cells were collected and centrifuged to get the cell palette. Cells were resuspended in PBS and washed 3 times. The extent of cellular uptake was analyzed by Flow cytometry analysis. Cellular uptake was performed thrice for each group, and the extent of cellular uptake was plotted and compared with the untreated cells.

6.7.16 Confocal Microscopy

Cells were seeded at cell density of 15000 cells/dish on a 35-mm glass bottom confocal dish (20 mm glass bottom size) and cultured for 24 h. The cultured medium was replaced with fresh medium and treated with **FITC-Kkd**, **FITC-Hkd** (10 μM). pH was adjusted with 1 M HCl and incubated for 6 h. The cultured medium was removed, and cells were washed with PBS thrice. Cells were fixed by 4% paraformaldehyde solution in PBS for 15 min and washed with the PBS. The cell nucleus was stained with 500 nM of DAPI and washed. The images were acquired using Olympus confocal microscope.

6.7.17 Cpt-Hkd Uptake in HeLa Cell

HeLa cells were seeded at a cell density of 15000 cells/dish on a 35-mm glass bottom confocal dish (20 mm glass bottom size) and cultured for 24 h. The cultured medium was replaced with a fresh medium and treated with **Cpt-Hkd** (10 μM) . pH was adjusted with 1 M HCl and

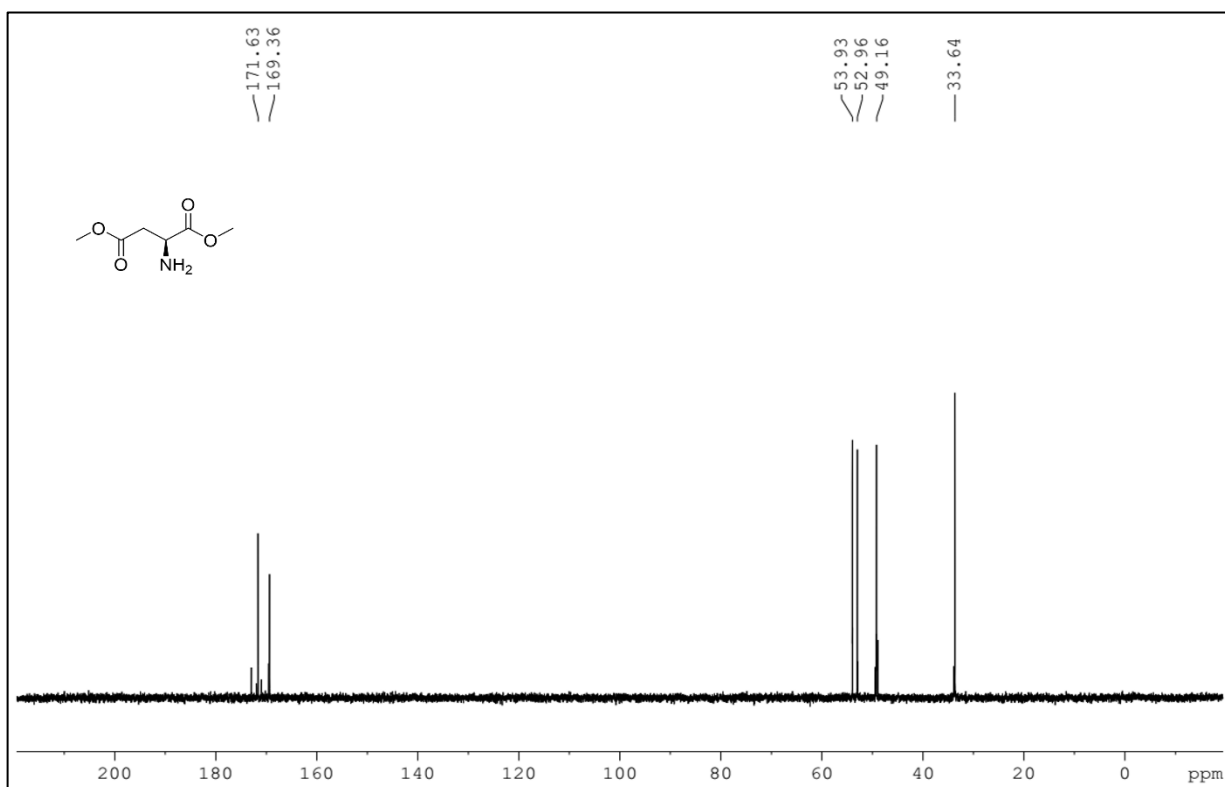
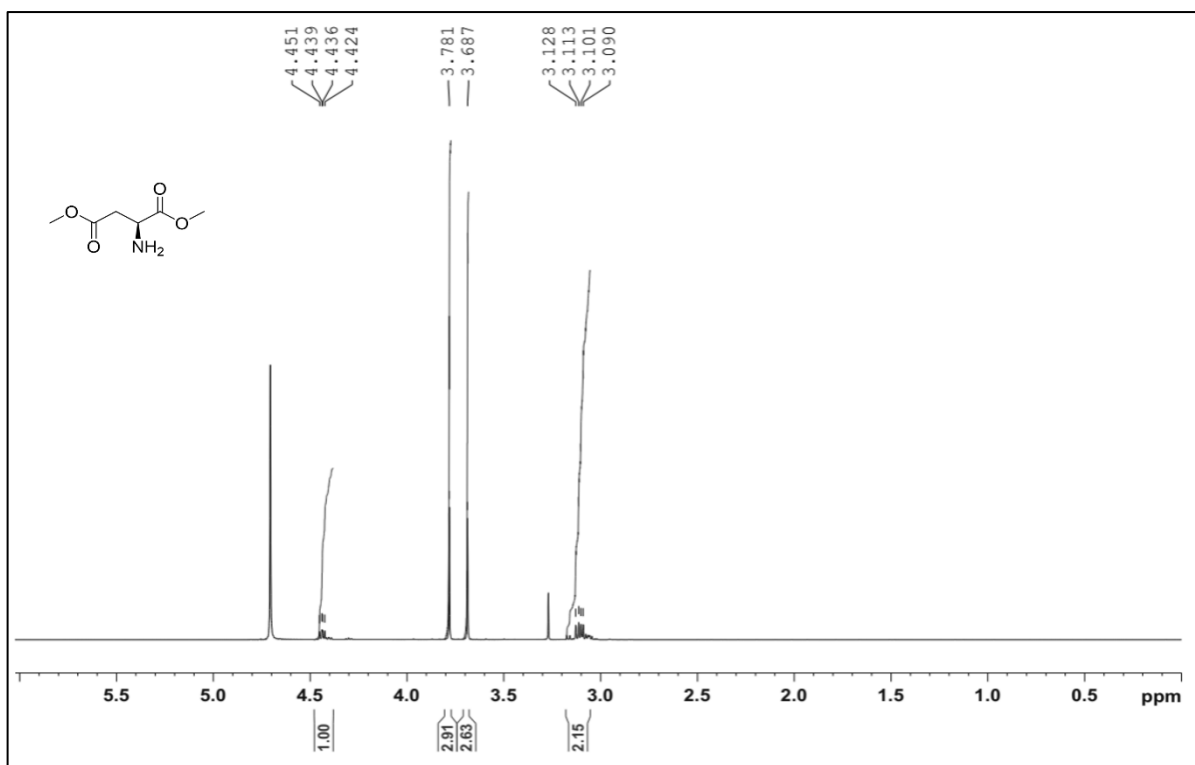
incubated for 4 h. The cultured medium was removed, and cells were washed with PBS thrice. Cells were fixed by 4% paraformaldehyde solution for 15 min and washed with PBS. The images were acquired using Olympus confocal microscope.

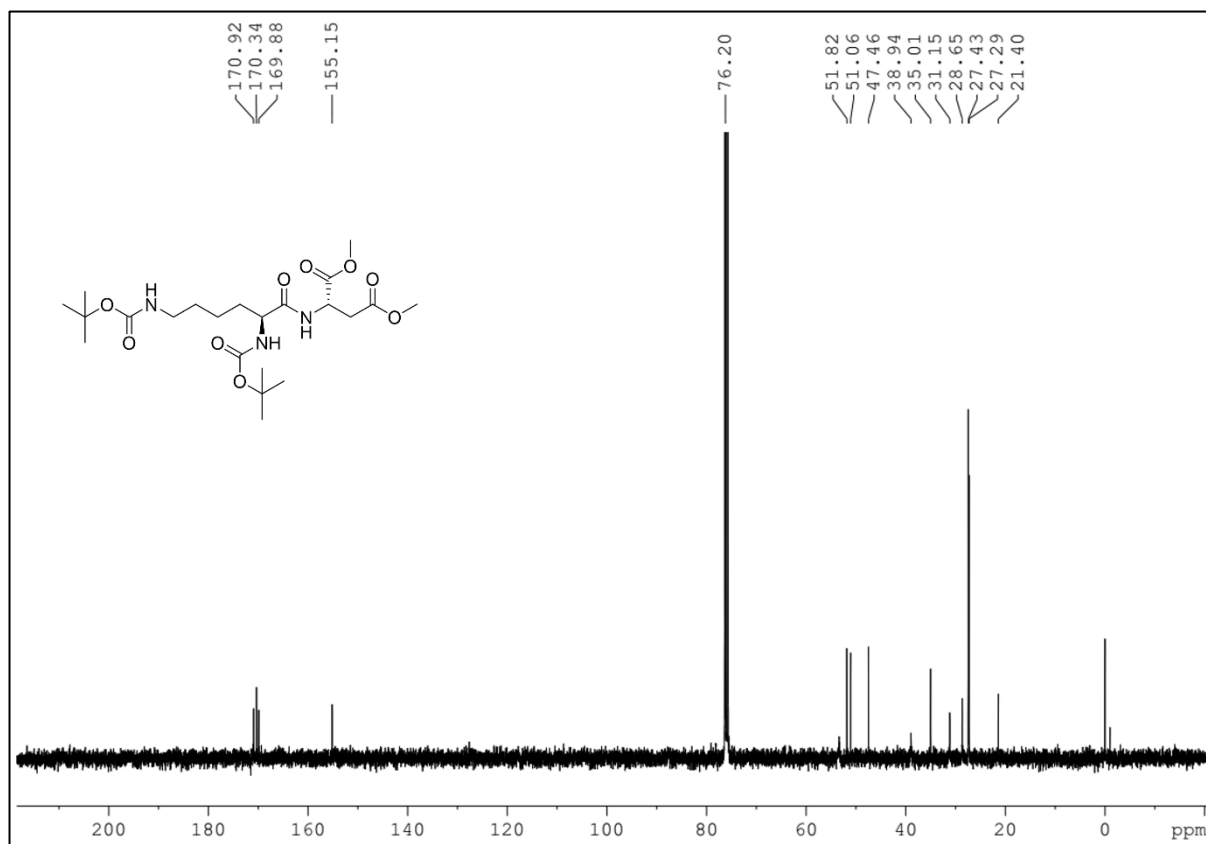
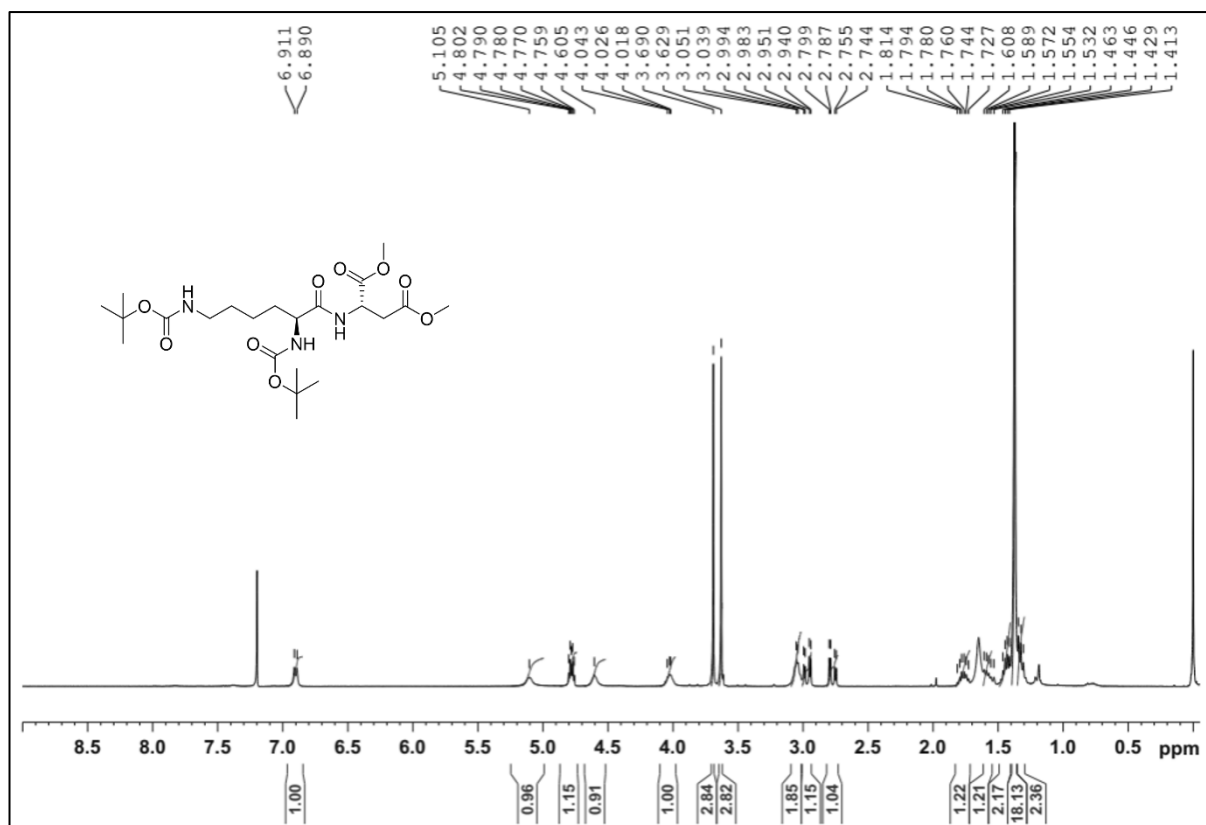
6.7.18 *In Vitro* Cytotoxicity of Cpt and Cpt-Hkd in L929 Cell

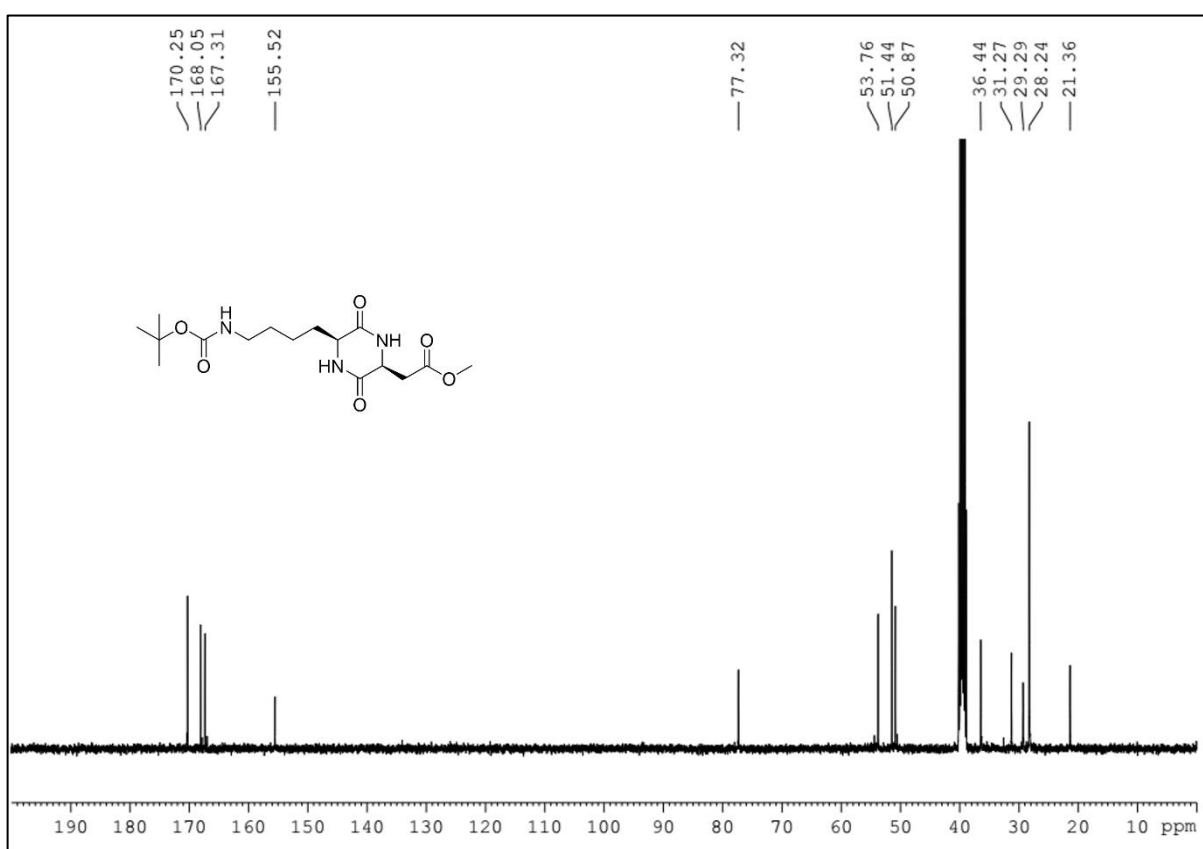
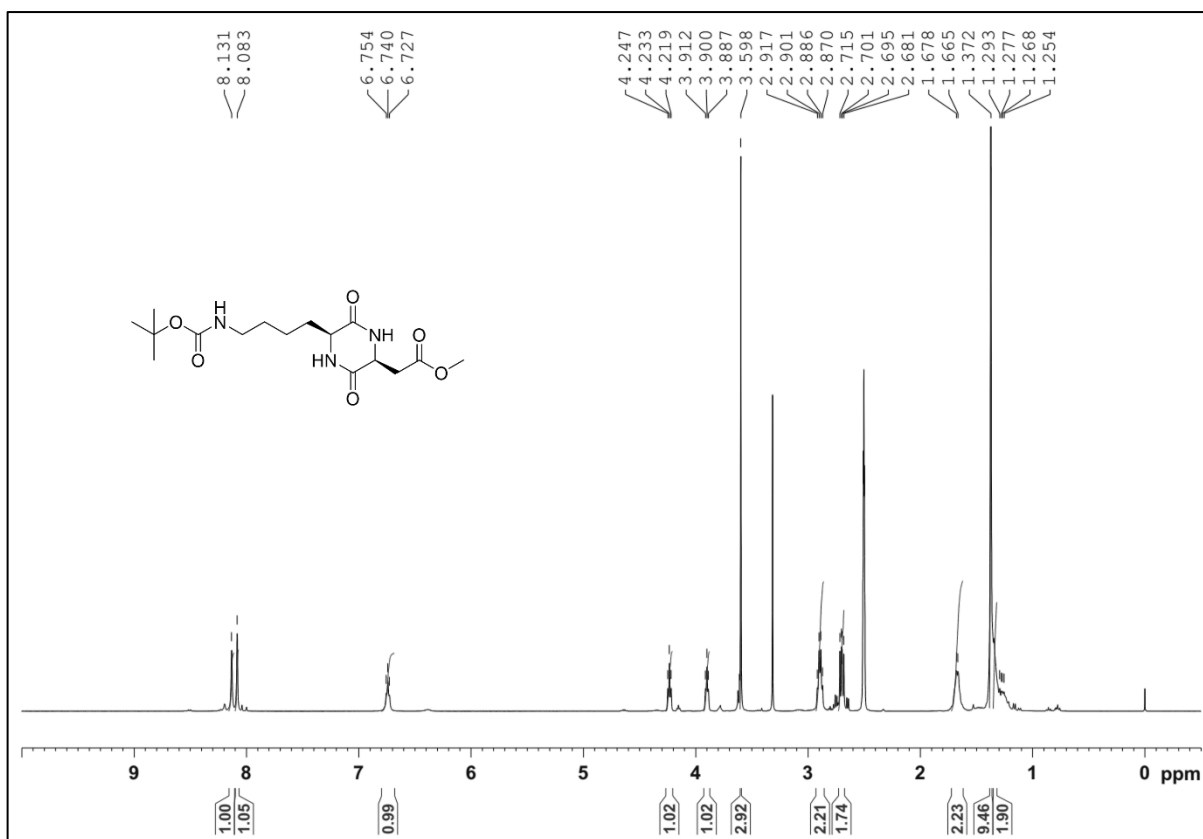
The cell viability of free Cpt drug and **Cpt-Hkd** was evaluated in non-cancerous L929 cell line. Cells were cultured in DMEM supplemented with 10% FBS and 1% PS. Cells were seeded at a cell density of 1×10^4 in a 96-well plate and cultured for 24 h. Cells were treated with 0.1 to 20 μ M of Cpt and **Cpt-Hkd** solution and incubated for 24 h. The cultured medium was exchanged with fresh medium. 10 μ L of 0.5% MTT solution was added and incubated for 4 h. The supernatant was removed carefully without disturbing the formazan crystals. The formazan crystals were dissolved in 100 μ L of 1:1 dimethyl sulfoxide and methanol. The absorbance of the formazan dye was measured in SpectroMax i3x microplate reader at 570 nm.

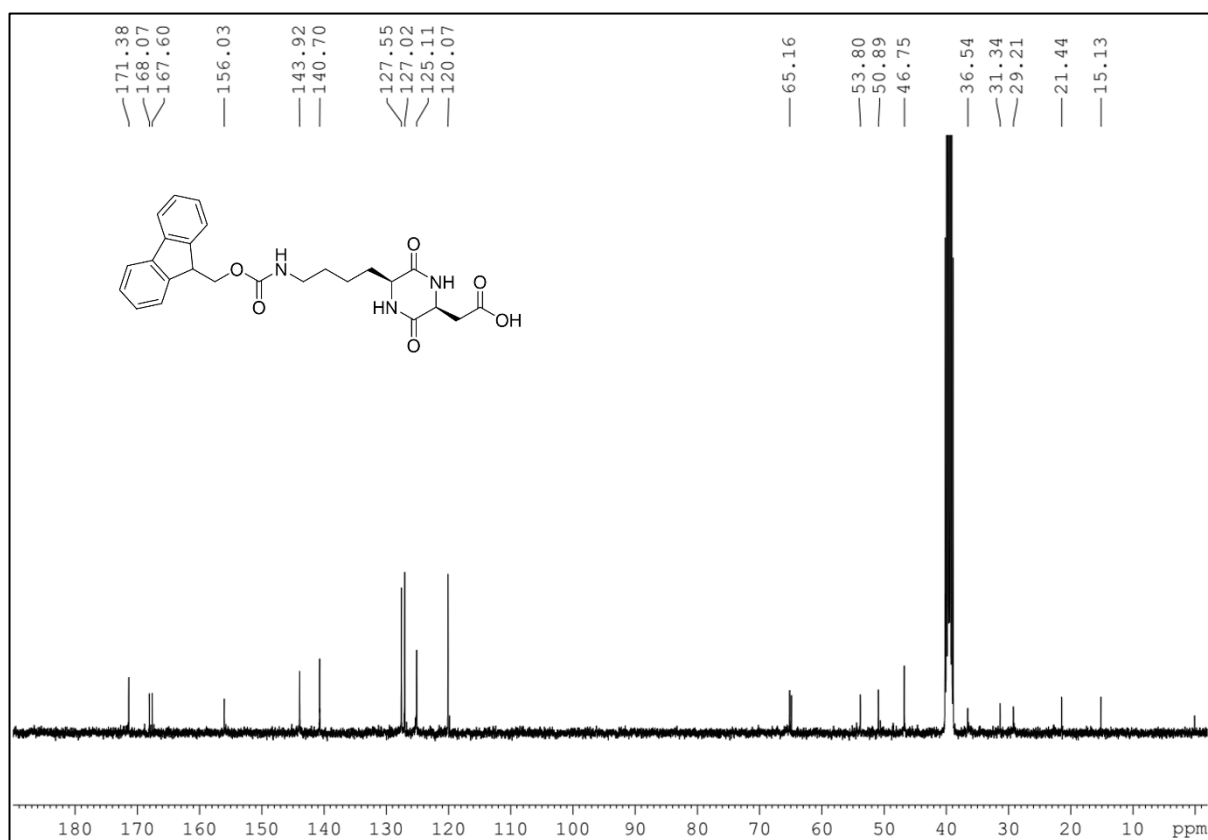
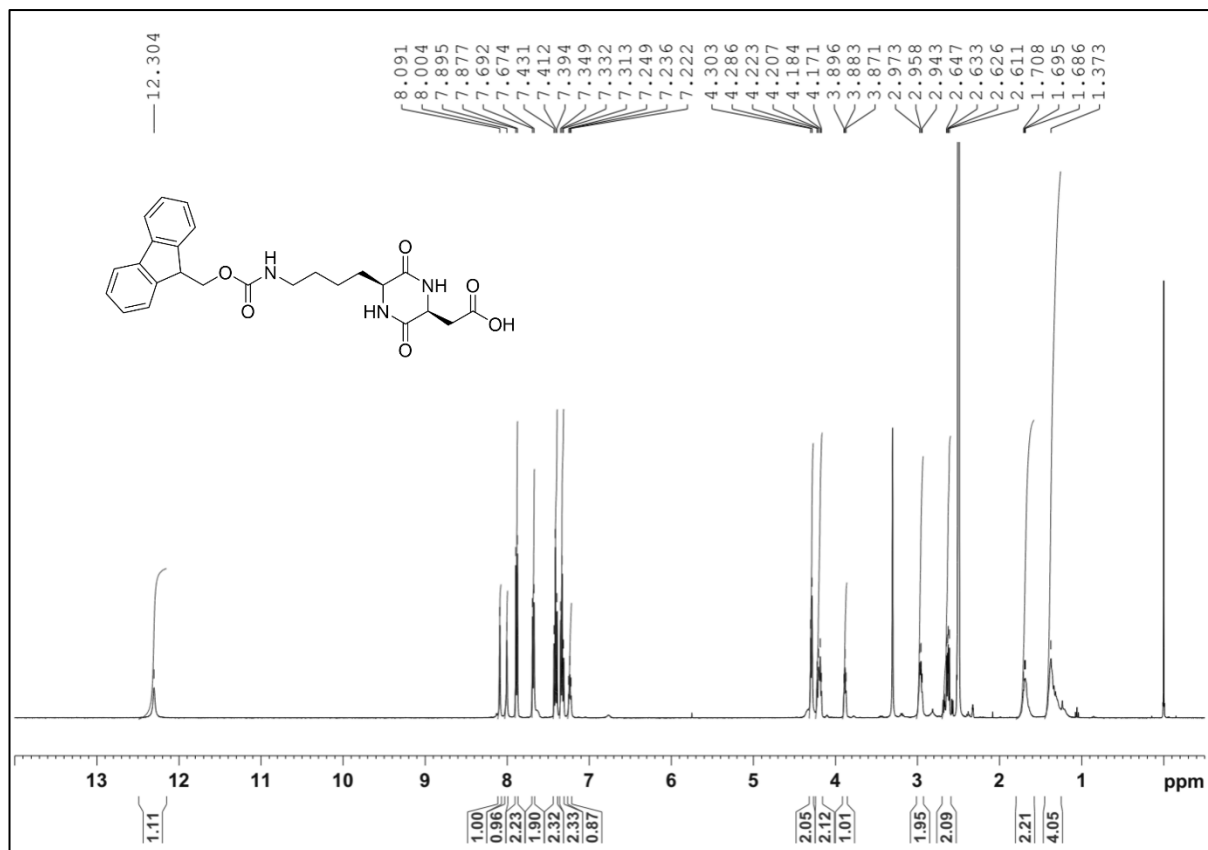
6.8 Appendix

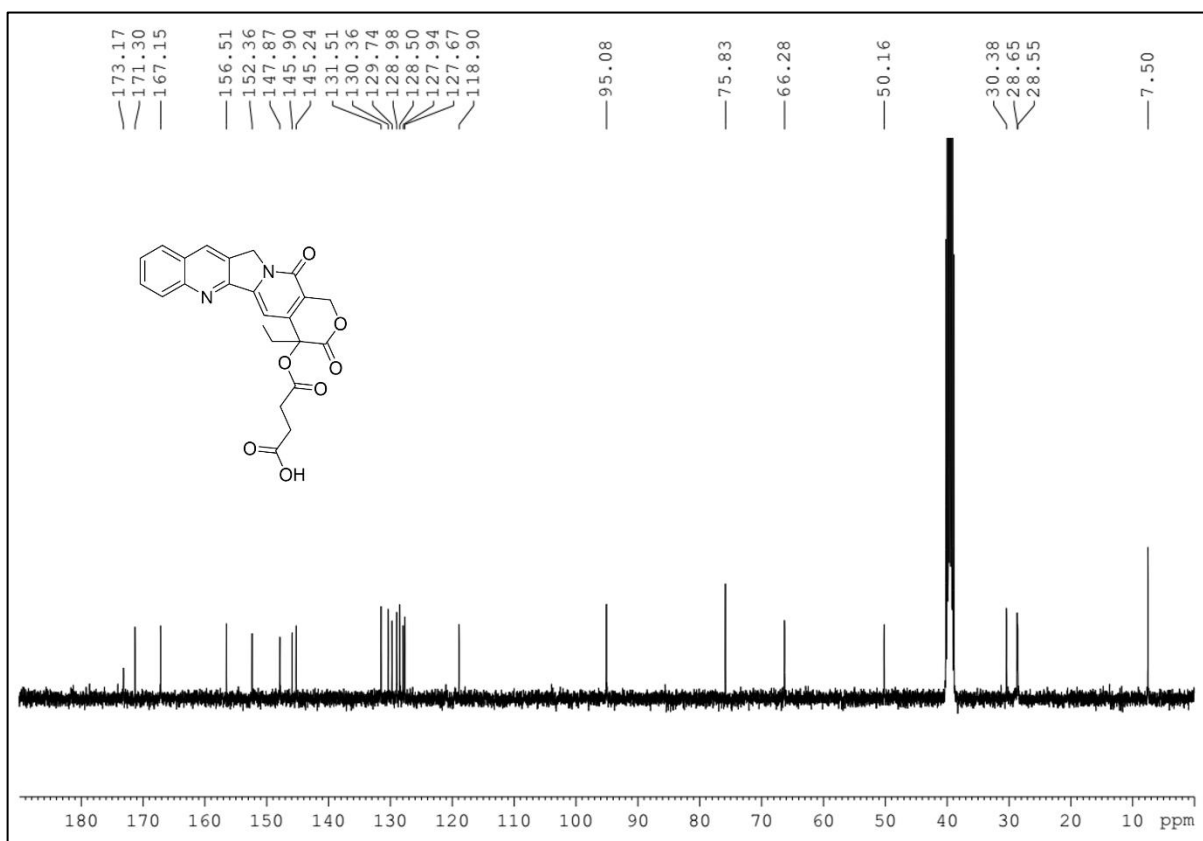
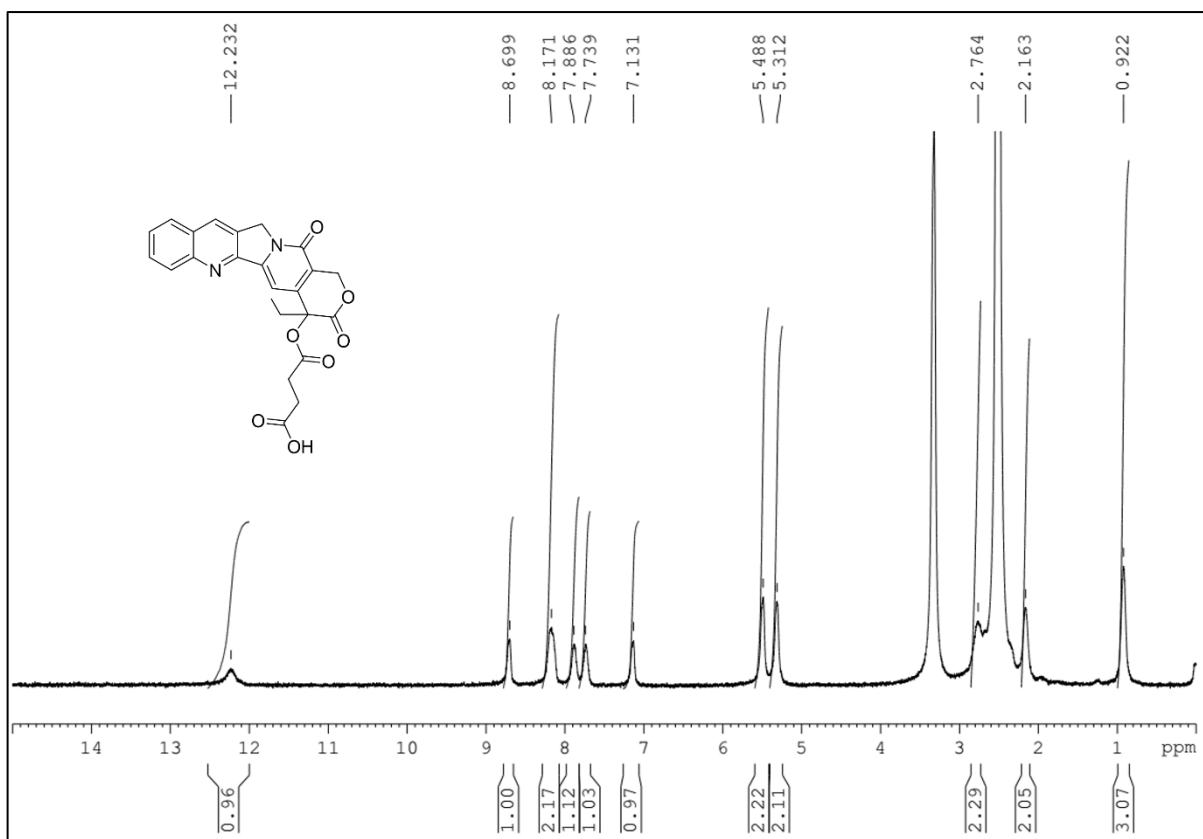
- ^1H NMR analysis of Boc-HN-Lys(Boc)-OH
 - ^1H and ^{13}C NMR analysis of $\text{H}_2\text{N-Asp(OMe)-OMe}$
 - ^1H and ^{13}C NMR analysis of Boc-HN-Lys(Boc)-Asp(OMe)-OMe
 - ^1H and ^{13}C NMR analysis of Boc-HN-kd-OMe
 - ^1H and ^{13}C NMR analysis of Fmoc-HN-kd-OH
 - ^1H and ^{13}C NMR analysis of Cpt-Suc-OH
 - HPLC and MALDI analysis of **Hkd**
 - HPLC and MALDI analysis of **FITC-Hkd**
 - HPLC and MALDI analysis of **Cpt-Hkd**
 - HPLC and MALDI analysis of **FITC-Kkd**
-

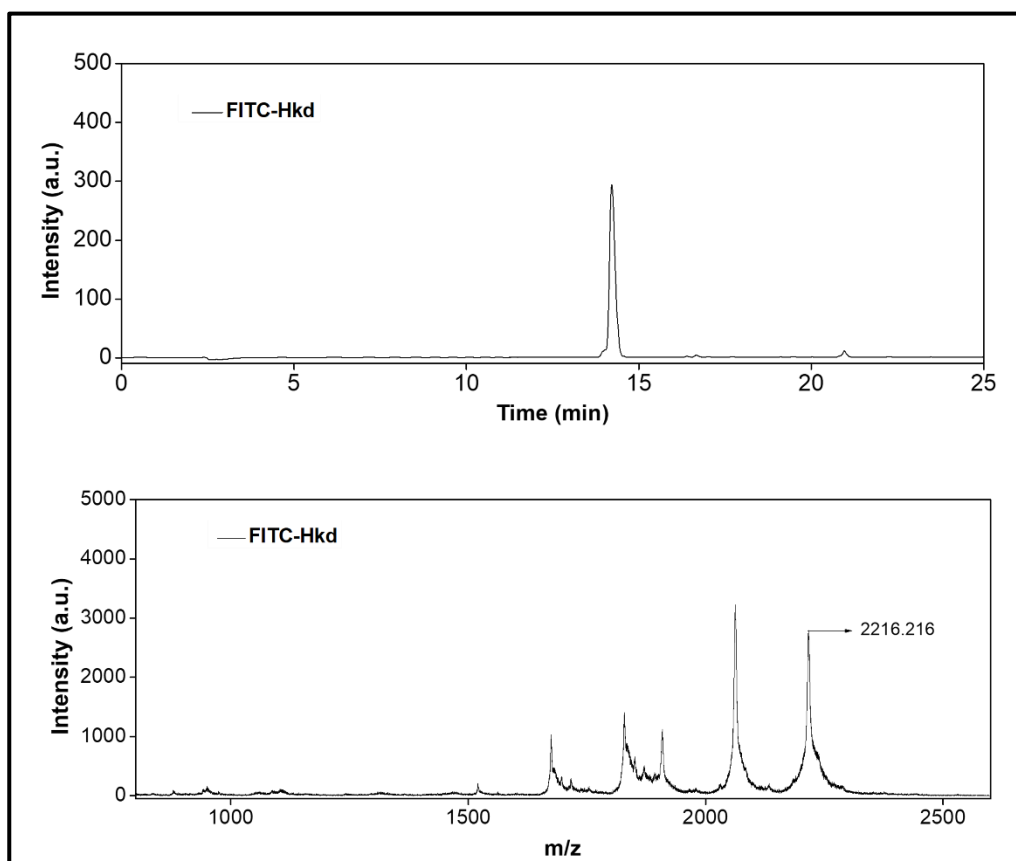
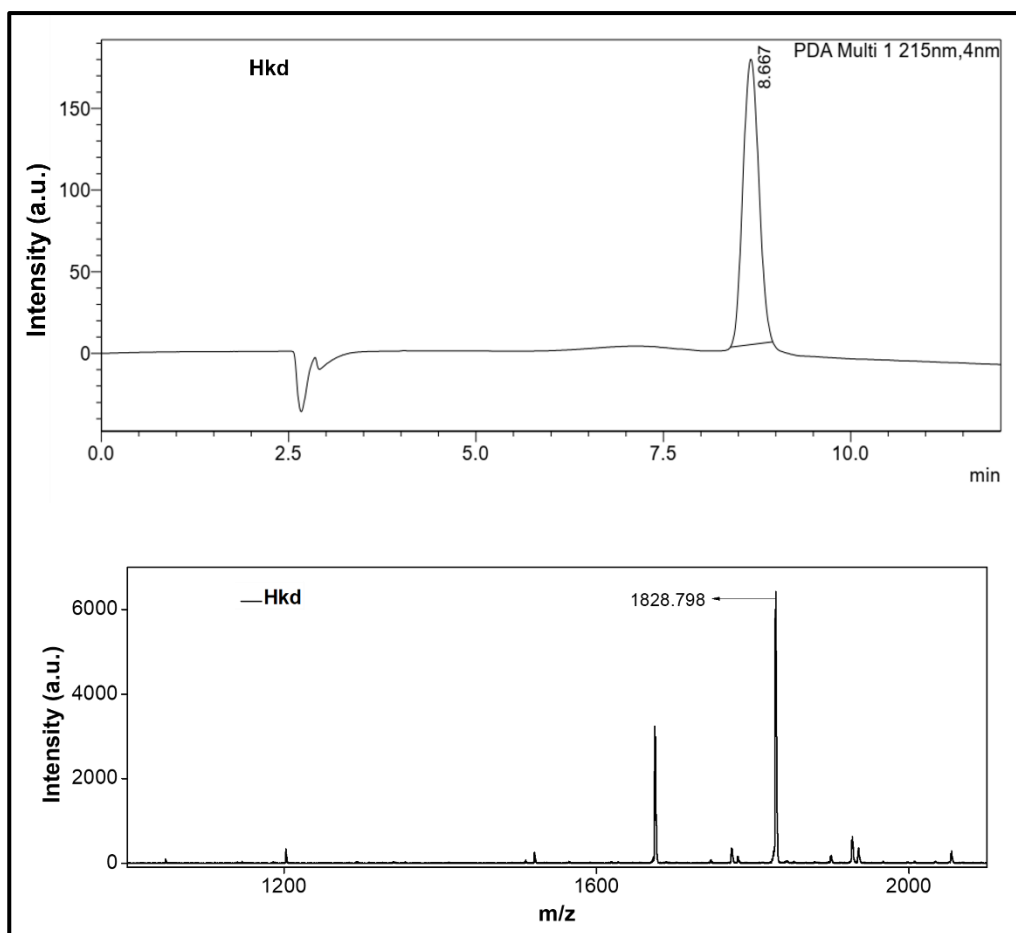


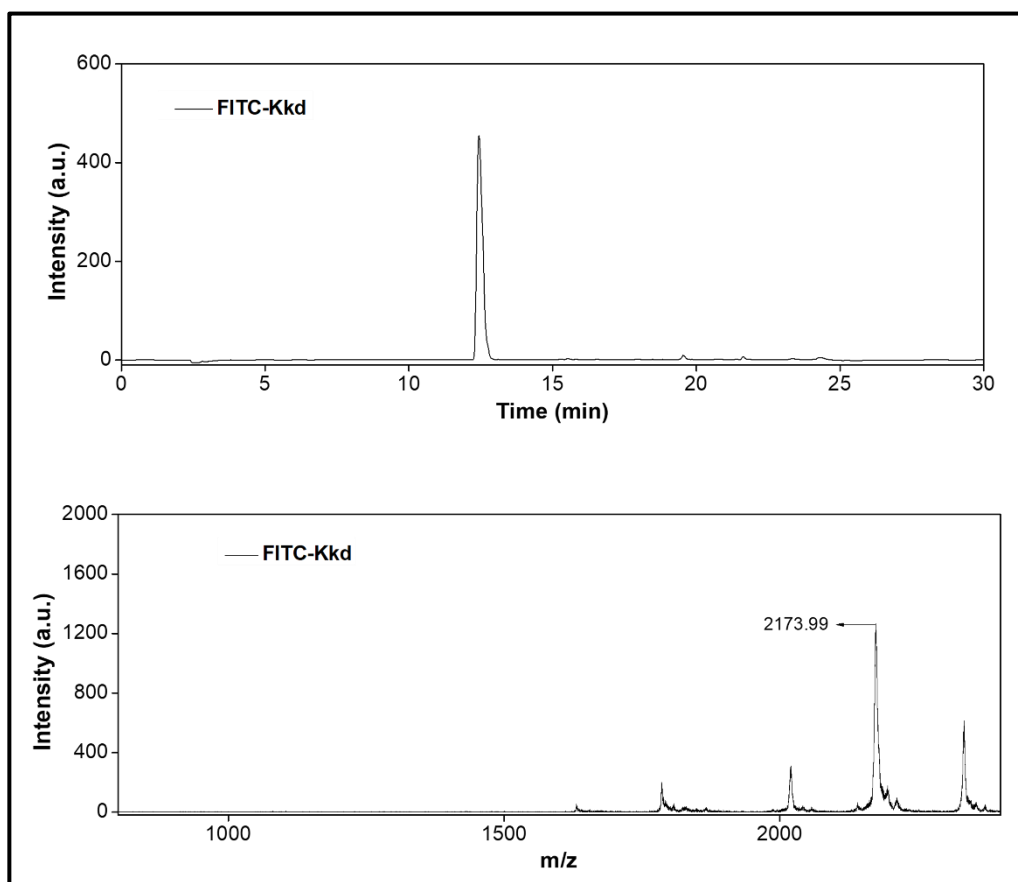
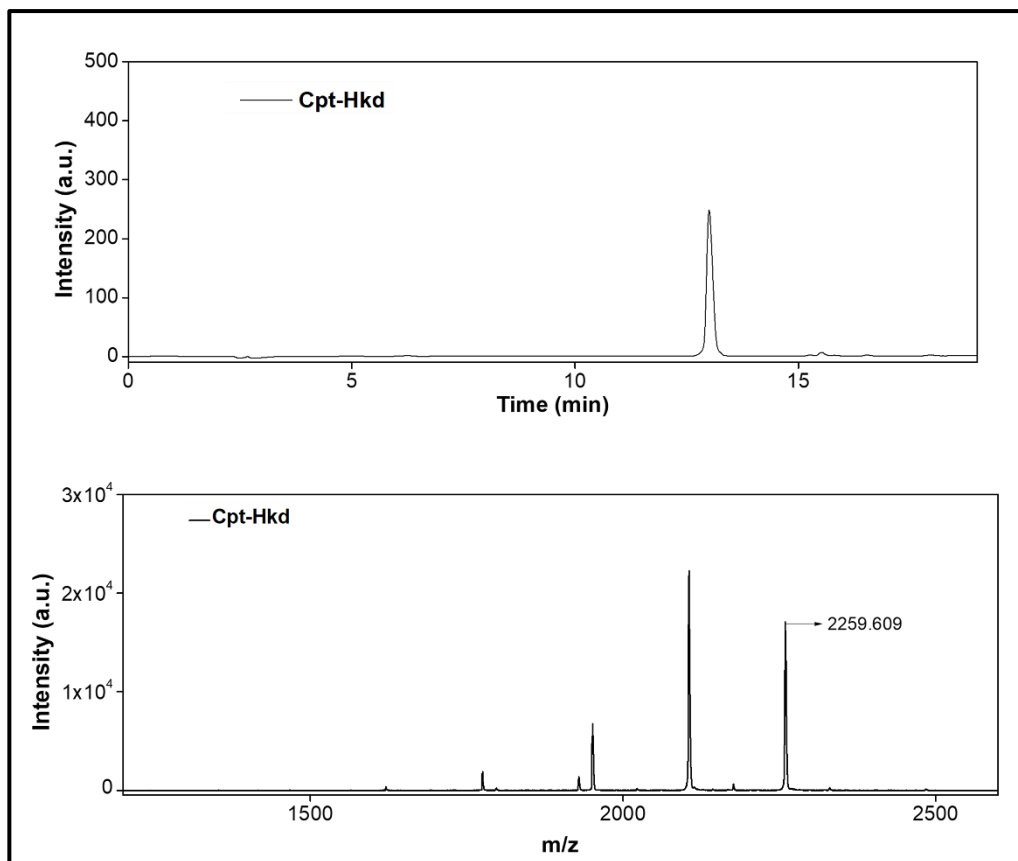












6.9 References

1. Brooks, H., Lebleu, B.; Vives, E. Tat peptide-mediated cellular delivery: Back to basics. *Adv. Drug Del. Rev.* **2005**, *57*, 559–577.
 2. Schwarze, S. R., Ho, A., Vocero-Akbani, A.; Dowdy, S. F. *In vivo* protein transduction: Delivery of a biologically active protein into the mouse. *Science* **1999**, *285*, 1569–1572.
 3. Pei, D.; Buyanova, M. Overcoming endosomal entrapment in drug delivery. *Bioconjug. Chem.* **2019**, *30*, 273–283.
 4. Tietz, O.; Cortezon-Tamarit, F.; Chalk, R.; Able, S.; Vallis, K. A. Tricyclic cell-penetrating peptides for efficient delivery of functional antibodies into cancer cells. *Nat. Chem.* **2022**, *14*, 284-293.
 5. Herce, H. D.; Schumacher, D.; Schneider, A. F. L.; Ludwig, A. K.; Mann, F. A.; Fillies, M.; Kasper, M.-A.; Reinke, S.; Krause, E.; Leonhardt, H. et al. Cell-permeable nanobodies for targeted immunolabelling and antigen manipulation in living cells. *Nat. Chem.* **2017**, *9*, 762-771.
 6. Morris, M.C.; Vidal, P.; Chaloin, L.; Heitz, F.; Divita, G. A new peptide vector for efficient delivery of oligonucleotides into mammalian cells. *Nucleic Acids Res.* **1997**, *25*, 2730–2736.
 7. Peraro, L.; Kritzer, J. A. Emerging methods and design principles for cell-penetrant peptides. *Angew. Chem. Int. Ed.* **2018**, *57*, 11868–11881.
 8. Brock, R. The uptake of arginine-rich cell-penetrating peptides: Putting the puzzle together. *Bioconj. Chem.* **2014**, *25*, 863–868.
 9. Tesauro, D.; Accardo, A.; Diaferia, C.; Milano, V.; Guillon, J.; Ronga, L.; Rossi, F. Peptide-based drug-delivery systems in biotechnological applications: recent advances and perspectives. *Molecules* **2019**, *24*, 351.
 10. Guidotti, G.; Brambilla, L.; Rossi, D. Cell-penetrating peptides: From basic research to clinics. *Trends Pharmacol. Sci.* **2017**, *38*, 406–424.
-

11. Reissmann, S. Cell penetration: Scope and limitations by the application of cellpenetrating peptides. *J. Pept. Sci.* **2014**, *20*, 760–784.
12. Shi, N.-Q.; Qi, X.-R.; Xiang, B.; Zhang, Y. A survey on “Trojan horse” peptides: Opportunities, issues and controlled entry to “Troy”. *J. Control. Release* **2014**, *194*, 53–70.
13. Pescina, S.; Ostacolo, C.; Gomez-Monterrey, I.; Sala, M.; Bertamino, A.; Sonvico, F.; Padula, C.; Santi, P.; Bianchera, A.; Nicoli, S. Cell penetrating peptides in ocular drug delivery: State of the art. *J. Control. Release* **2018**, *284*, 84–102.
17. Dissanayake, S.; Denny, W. A.; Gamage, S.; Sarojini, V. Recent developments in anticancer drug delivery using cell penetrating and tumor targeting peptides. *J. Control. Release* **2017**, *250*, 62–76.
15. Vives, E.; Schmidt, J.; Pelegrin, A. Cell-penetrating and cell-targeting peptides in drug delivery. *Biochimica et Biophysica Acta (BBA)-Reviews on Cancer* **2008**, *1786*, 126–138.
16. Araste, F.; Abnous, K.; Hashemi, M.; Taghdisi, S. M.; Ramezani, M.; Alibolandi, M. Peptide-based targeted therapeutics: Focus on cancer treatment. *J. Control. Release* **2018**, *292*, 141–162.
17. Ruoslahti, E. Tumor penetrating peptides for improved drug delivery. *Adv. Drug Del. Rev.* **2017**, *110*, 3–12.
18. Bernkop-Schnürch, A. Strategies to overcome the polycation dilemma in drug delivery. *Adv. Drug Del. Rev.* **2018**, *136*, 62–72.
19. Fei, L.; Ren, L.; Zaro, J. L.; Shen, W. C. The influence of net charge and charge distribution on cellular uptake and cytosolic localization of arginine-rich peptides. *J. Drug Target* **2011**, *19*, 675–680.
20. Zhang, M.; Chen, X.; Li, C.; Shen, X. Charge-reversal nanocarriers: An emerging paradigm for smart cancer nanomedicine. *J. Control. Release* **2020**, *319*, 46–62.
21. Zhu, L.; Kate, P.; Torchilin, V. Matrix metalloprotease 2-responsive multifunctional liposomal nanocarrier for enhanced tumor targeting. *ACS Nano* **2012**, *6*, 3491–3198.

22. Kuai, R.; Yuan, W.; Qin, Y.; Chen, H.; Tang, J.; Yuan, M. Zhang, Z.; He, Q. Efficient delivery of payload into tumor cells in a controlled manner by TAT and thiolytic cleavable PEG co-modified liposomes. *Mol. Pharm.* **2010**, *7*, 1816–1826.
23. Huang, Y.; Jiang, Y.; Wang, H.; Wang, J.; Shin, M. C.; Byun, Y.; He, H.; Liang, Y.; Yang, V. C. Curb challenges of the “Trojan Horse” approach: Smart strategies in achieving effective yet safe cell-penetrating peptide-based drug delivery. *Adv. Drug Deliv. Rev.* **2013**, *65*, 1299–1315.
24. Bernkop-Schnurch, A. Strategies to overcome the polycation dilemma in drug delivery. *Adv. Drug Del. Rev.* **2018**, *136*, 62–72.
25. Jiang, T.; Olson, E. S.; Nguyen, Q. T.; Roy, M.; Jennings, P. A.; Tsien, R. Y. Tumor imaging by means of proteolytic activation of cell-penetrating peptides. *Proc Natl Acad Sci USA* **2004**, *101*, 17867-17872.
26. Zhang, M.; Chen, X.; Li, C.; Shen, X. Charge-reversal nanocarriers: An emerging paradigm for smart cancer nanomedicine. *J. Control. Release* **2020**, *319*, 46–62.
27. Kato, Y.; Ozawa, S.; Miyamoto, C.; Maehata, Y.; Suzuki, A.; Maeda, T.; Baba, Y. Acidic extracellular microenvironment and cancer. *Cancer Cell Int.* **2013**, *13*, 89.
28. Boedtkjer, E.; Pedersen, S. F. The acidic tumor microenvironment as a driver of cancer. *Annu. Rev. Physiol.* **2020**, *82*, 1–21.
29. Boedtkjer, E.; Bunch, L.; Pedersen, S. F. Physiology, pharmacology and pathophysiology of the pH regulatory transport proteins NHE1 and NBCn1: Similarities, differences and implications for cancer therapy. *Curr. Pharm. Des.* **2012**, *18*, 1345–1371.
30. Vaupel, P.; Kallinowski, F.; Okunieff, P. 1989. Blood flow, oxygen and nutrient supply, and metabolic microenvironment of human tumors: A review. *Cancer Res.* 1989, *49*, 6449–6465.
31. Gillies, R. J.; Brown, J. S.; Anderson, A. R. A.; Gatenby, R. A. Eco-evolutionary causes and consequences of temporal changes in intratumoural blood flow. *Nat. Rev. Cancer* **2018**, *18*, 576–585.
-

32. Huber, V.; Camisaschi, C.; Berzi, A.; Ferro, S.; Lugini, L.; Triulzi, T.; Tuccitto, A.; Taqliabue, E.; Castelli, C.; Rivoltini, L. Cancer acidity: An ultimate frontier of tumor immune escape and a novel target of immunomodulation. *Semin. Cancer Biol.* **2017**, *43*, 74–89.
33. Kwon, I. K.; Lee, S. C.; Han, B.; Park, K. Analysis on the current status of targeted drug delivery to tumors. *J. Control Release* **2012**, *164*, 108–114.
34. Fei, L.; Yap, L. -P.; Conti, P. S.; Shen, W.-C.; Zaro, J. L. Tumor targeting of a cell penetrating peptide by fusing with a pH-sensitive histidine-glutamate cooligopeptide. *Biomaterials* **2014**, *35*, 4082–4087.
35. Yeh, T.-H.; Chen, Y.-R.; Chen, S.-Y.; Shen, W.-C.; Ann, D. K.; Zaro, J. L.; Shen, L.-J. Selective intracellular delivery of recombinant arginine deiminase (ADI) using pH sensitive cell penetrating peptides to overcome ADI resistance in hypoxic breast cancer cells. *Mol. Pharm.* **2015**, *13*, 262–271.
36. Nam, S. H.; Jang, J.; Cheon, C. H.; Chong, S.-E.; Ahn, J. H.; Hyun, S.; Yu, J.; Lee, Y. pH-activatable cell penetrating peptide dimers for potent delivery of anticancer drug to triple-negative breast cancer. *J. Controlled Release* **2021**, *330*, 898–906.
37. Zhang, Q.; Tang, J.; Fu, L.; Ran, R.; Liu, Y.; Yuan, M.; He, Q. A pH responsive α -helical cell penetrating peptide-mediated liposomal delivery system. *Biomaterials* **2013**, *34*, 7980–7993.
38. Lenci, E.; Trabocchi, A. Peptidomimetic toolbox for drug discovery. *Chem. Soc. Rev.* **2020**, *49*, 3262–3277.
39. Avan, I.; Hall, C. D.; Katritzki, A. R. Peptidomimetics via modifications of amino acids and peptide bonds. *Chem. Soc. Rev.* **2014**, *43*, 3575–3594.
40. Balachandra, C.; Padhi, D.; Govindaraju, T. Cyclic dipeptide: A privileged molecular scaffold to derive structural diversity and functional utility. *ChemMedChem*, **2021**, *16*, 2558–2587.
41. Borthwick, A. D. 2,5-Diketopiperazines: Synthesis, reactions, medicinal chemistry, and bioactive natural products. *Chem. Rev.* **2012**, *112*, 3641–3716.
-

42. Manchineella, S.; Govindaraju, T. Molecular self-assembly of cyclic dipeptide derivatives and their applications. *ChemPlusChem* **2017**, 82, 88–106.

43. Lee, E. S.; Na, K.; Bae, Y. H. Super pH-sensitive multifunctional polymeric micelle. *Nano Lett.* **2005**, 5, 325–329.

7.1 Conclusions

In this thesis, we have addressed the possible applications of the silk fibroin protein and cell penetrating peptides for controlled release and delivery application. One of the main contributions of our work is tuning hydrogelation of the silk fibroin protein to prepare injectable, stimuli responsive hydrogel for the biomedical implication of the bulk material silk fibroin. We further investigated the functional application in vivo system to understand the applicability of the hydrogel for application.

An innovative approach was presented to prepare injectable hydrogel of bulk material silk fibroin quickly. The controlled release of the blood glucose lowering hormone insulin was observed from the injectable hydrogel. In vivo validation of controlled insulin release from hydrogel-depot was shown in the diabetes type 1 Wistar rat model.

The chemically engineered silk fibroin protein was designed to induce quick hydrogelation with injectable behavior. The stimuli responsive release of encapsulated therapeutic insulin was achieved from the engineered silk fibroin hydrogel.

The combination of antioxidant melanin and berberine with silk fibroin can apply to the topical site of the wound. The dressing material showed effective cellular migration and provided support for tissue regeneration. The anti-inflammatory and antimicrobial berberine lowers bacterial infection and prolongs inflammatory response at the wound site. Which effectively promotes wound healing in the diabetes type I model.

The new biomimetic cell penetrating peptide was designed to promote the effective penetration of the impermeable drug into the cell. The proline-rich peptide maintained the intrinsic disorder structure and no toxicity to the cell. The peptide showed effective DNA binding and delivery of the DNA inside the cell.

Finally, we have designed a cell penetrating peptidomimetics whose cellular uptake depends on the environment's pH. The stable peptidomimetic enhances the cellular delivery of drugs into the lower pH environment and effectively reduces the risk of non-selective drug delivery.

From an experimental point of view, our contribution lies in developing silk fibroin materials and cell penetrating peptides for the controlled delivery of the drug in healthcare applications to enhance the quality of life. We have validated the applicability of the materials from biophysical, in vitro, and in vivo animal models. Our designed materials showed promising efficacy in their respective applications. These designed materials can be further translated into healthcare applications or provide the future design strategy for functional biomaterials.

7.2 Future Scope

Although we have presented the applicability of some of our designed materials, many experiments are pending. Future work will address detailed biocompatibility evolution for the applicability of the materials. Further, the following concepts can be undertaken.

1. An innovative approach of SF injectable hydrogel can be tested for the controlled local delivery of anticancer or anti-inflammatory drugs. The quick gelation and injectable behavior of hydrogel may be useful in 3D printing technology.
2. The SF protein self-assembles and undergo quick hydrogelation with injectable behavior. In the future, such hydrogel can be combined with microneedle technology for painless insulin therapy. The hydrogel displays good viscoelastic profile, porous morphology, and excellent stability. Thus, the pancreas beta cell can be encapsulated for cell-based insulin therapy in regenerative medicine. The effect of substituted phenylboronic acid on glucose responsive drug release can be pursued.

3. The combinatorial therapeutic approach in dressing material enhances wound closure and cell regeneration in diabetic rats. The adhesive properties of the SF hydrogel can be modified to expand the applicability in stretched sites and diabetic foot ulcers.
4. The peptides derived from intrinsic disordered Ku-P4 show efficient cell membrane permeability. The lysine containing peptide sequence can be modified with a minimum number of arginine residues to further enhance the membrane permeability with retention of cell viability.
5. In our design, we have tagged the drug molecules by covalent conjugation with peptidomimetics, which may reduce the anticancer drug binding with the target. The target-responsive labile conjugation can be designed for better efficacy of the conjugated therapeutics.

Although we have performed the biocompatibility of materials in vitro, the future applicability of these materials requires extensive cytocompatibility studies for translational utility. We believe that the bulk scale availability and biological origin of our peptide and protein-based molecular and materials systems have the potential to be used in various human healthcare applications.

List of Publications

- **Maity, B.;** Samanta, S.; Sarkar, S.; Alam, S.; Govindaraju, T. Injectable silk fibroin-based hydrogel for sustained delivery of insulin in diabetic rats. *ACS Appl. Bio Mater.* **2020**, *3*, 3544–3552.
- **Maity, B.;** Alam, S.; Samanta, S.; Prakash, R. G.; Govindaraju, T. Antioxidant silk fibroin composite hydrogel for rapid healing of diabetic wound. *Macromol. Biosci.* **2022**, 2200097.
- **Maity, B.;** Moorthy, H.; Govindaraju, T. Glucose responsive self-regulated injectable silk fibroin hydrogel for insulin delivery (Under preparation).
- **Maity, B.;** Govindaraju, T. Cell penetrating peptides derived from intrinsically disordered Ku- protein for DNA delivery (Under preparation).
- **Maity, B.;** Govindaraju, T. Tumor microenvironment sensitive cell penetrating peptidomimetics for selective anticancer drug delivery (Under preparation).

Patent

- Injectable silk composition and process of preparation thereof. Govindaraju, T.; **Maity, B.;** Samanta, S. Indian Patent Application Number: 202041015174; (Year 2020); PCT/IN2021/050337.

Brief Curriculum Vitae



Biswanath Maity was born on 2nd January 1994 at Thakurchak, West Bengal, India. He obtained his Bachelor's degree in Chemistry from Midnapore College under Vidyasagar University, India in 2014. He obtained his Master degree in Chemistry from Department of Chemistry, Indian Institute of Technology Guwahati (IITG), Assam, India in 2016. He joined the New Chemistry Unit (NCU), Jawaharlal Nehru Centre for Advanced Scientific Research (JNCASR), Bangalore, for the Ph.D. program in August 2016 under the guidance of Prof. T. Govindaraju. His research interest focuses on developing cell penetrating peptides, protein, and peptide-based biomaterials for drug delivery and healthcare applications.

